Nanostructured materials for photoelectrochemical hydrogen production using sunlight

Author:
Glasscock, Julie Anne

Publication Date:
2008

DOI:
https://doi.org/10.26190/unsworks/17525

Nanostructured materials for photoelectrochemical hydrogen production using sunlight

Julie Anne Glasscock

A thesis submitted in fulfilment
of the requirement for the degree of
Doctor of Philosophy

School of Chemical Sciences
and Engineering

University of
New South Wales

I hereby declare that this submission is my own work and to the best of my knowledge it contains no material previously published or written by another person, nor material which to a substantial extent has been accepted for the award of any other degree or diploma at UNSW or any other educational institution, except where due acknowledgement is made in the thesis. Any contribution made to the research by others, with whom I have worked at UNSW or elsewhere, is explicitly acknowledged in the thesis.

I also declare that the intellectual content of this thesis is the product of my own work, except to the extent that assistance from others in the project's design and conception or in style, presentation and linguistic expression is acknowledged. Some of the content of this thesis has been published in journal articles.

I hereby grant the University of New South Wales or its agents the right to archive and to make available my thesis or dissertation in whole or part in the University libraries in all forms of media, now or here after known, subject to the provisions of the Copyright Act 1968. I retain all proprietary rights, such as patent rights. I also retain the right to use in future works (such as articles or books) all or part of this thesis or dissertation. I also authorise University Microfilms to use the 350 word abstract of my thesis in Dissertation Abstract International. I have either used no substantial portions of copyright material in my thesis or I have obtained permission to use copyright material; where permission has not been granted I have applied/will apply for a partial restriction of the digital copy of my thesis or dissertation.

I certify that the Library deposit digital copy is a direct equivalent of the final officially approved version of my thesis. No emendation of content has occurred and if there are any minor variations in formatting, they are the result of the conversion to digital format.

Signed

J.A. Glasscock

for CMM

O Star (the fairest one in sight),
We grant your loftiness the right
To some obscurity of cloud -
It will not do to say of night,
Since dark is what brings out your light.
Some mystery becomes the proud.
But to be wholly taciturn
In your reserve is not allowed.
Say something to us we can learn
By heart and when alone repeat.
Say something! And it says "I burn".
But say with what degree of heat.
Talk Fahrenheit, talk Centigrade.
Use language we can comprehend.
Tell us what elements you blend.
It gives us strangely little aid,
But does tell something in the end.
And steadfast as Keats' Eremite,
Not even stooping from its sphere,
It asks a little of us here.
It asks of us a certain height,
So when at times the mob is swayed
To carry praise or blame too far,
We may choose something like a star
To stay our minds on and be staid.

Robert Frost

Abstract

Solar hydrogen has the potential to replace fossil fuels with a sustainable energy carrier that can be produced from sunlight and water via "water splitting". This study investigates the use of hematite (α-Fe_2O_3) as a photoelectrode for photoelectrochemical water splitting. α-Fe_2O_3 has a narrow indirect band-gap, which allows the utilization of a substantial fraction of the solar spectrum. However, the water splitting efficiencies for α-Fe_2O_3 are still low due to poor absorption characteristics, and large losses due to recombination in the bulk and at the surface.

The thesis investigates the use of nanostructured composite electrodes, where thin films of α-Fe_2O_3 are deposited onto a nanostructured metal oxide substrate, in order to overcome some of the factors that limit the water splitting efficiency of α-Fe_2O_3.

Doped (Si, Ti) and undoped α-Fe_2O_3 thin films were prepared using vacuum deposition techniques, and their photoelectrochemical, electrical, optical and structural properties were characterised. The doped α-Fe_2O_3 exhibited much higher photoelectrochemical activity than the undoped material, due to an improvement of the surface transfer coefficient and some grain boundary passivation. Schottky barrier modeling of α-Fe_2O_3 thin films showed that either the width of the depletion region or the diffusion length is the dominant parameter with a value around 30 nm, and confirmed that the surface charge transfer coefficient is small. An extensive review of the conduction mechanisms of α-Fe_2O_3 is presented.

ZnO and SnO_2 nanostructures were investigated as substrates for the α-Fe_2O_3 thin films. Arrays of well-aligned high aspect ratio ZnO nanowires were optimised via the use of nucleation seeds and by restricting the lateral growth of the nanostructures.

The geometry of the nanostructured composite electrodes was designed to maximise absorption and charge transfer processes. Composite nanostructured elec-

trodes showed lower quantum efficiencies than equivalent thin films of α-Fe_2O_3, though a relative enhancement of collection of long wavelength charge carriers was observed, indicating that the nanostructured composite electrode concept is worthy of further investigation. The rate-limiting step for water splitting with α-Fe_2O_3 is not yet well understood and further investigations of the surface and bulk charge transfer properties are required in order to design electrodes to overcome specific shortcomings.

Acknowledgements

There are numerous people I would like to thank for getting me to this point; not only to the end of my PhD thesis, but to where I am in life today. Hopefully I can express my gratitude to you all in person.

I am very grateful to my supervisors, Dr Ian Plumb (CSIRO) and Prof. Rose Amal (UNSW), for their guidance and support over the last three years. Very special thanks go to Ian Plumb for providing daily advice, mentoring and motivation, and for sharing his passion for science. Thanks also to Piers Barnes for numerous contributions to this work, and his wit and humour that made every day in the lab enjoyable.

My great appreciation to all the past water-splitters, and other that have helped scientifically along the way; Lakshman Randeniya, Tony Murphy, Peter Vohralik, Nick Savvides, Avi Bendavid, Phil Martin and Ian Grey. I would like to thank CSIRO for its continued support of my education, and all the quirky staff at Lindfield for making work-life so entertaining.

Thank you to all my family and friends for helping me through life's adventures. To Mum, Dad, Kerri, and all of my wonderful family; most of whom have no idea what I do all day, but are still my most ardent supporters! To Chris, for everything, who deserves more thanks than I could ever express. And finally, thanks to my wonderful friends; Angela, Adam, Andy, Lindsey and Steve for moral support, coffees, cocktails, swims and other needed distractions.

Papers

Much of the research undertaken for this thesis has been published in peer-reviewed journal articles and presented at various international conferences, as listed below. These publications will be referred to throughout this thesis were relevant. In the case of the manuscripts and presentations where I appear as first author, I was primarily responsible for the preparation of the manuscripts, fabrication and characterisation of the samples, and the data anlaysis, unless otherwise stated. The majority of the optical and electrical measurements in Papers 1 and 2 and Proceeding 1, and the photoelectrochemical measurements in Paper 1, were undertaken by P.R.F. Barnes. The XPS and hardness measurements in Paper 2 were undertaken by A. Bendavid. The gravimetric measurements in Paper 2 were undertaken by I.C. Plumb. Some of the optical and photoelectrochemical measurements for Presentation 4 were undertaken by L.K. Randeniya. My contribution to Papers 3 and 4 was limited to some sample preparation and manuscript editing.

Journal publications

1. J.A. Glasscock, P.R.F. Barnes, I.C. Plumb, N. Savvides, The enhancement of photoelectrochemical hydrogen production from hematite thin films by the introduction of Ti and Si, *J. Phys. Chem. C*, 111, 16477-16488, 2007.

2. J.A. Glasscock, P.R.F. Barnes, I.C. Plumb, A. Bendavid, P.J. Martin, Structural, optical and electrical properties of undoped polycrystalline hematite thin films produced using filtered arc deposition, *Thin Solid Films*, (in press), 2007.

3. A.B. Murphy, P.R.F. Barnes, L.K. Randeniya, I.C. Plumb, I.E. Grey, M.D. Horne, J.A. Glasscock, Efficiency of solar water splitting using semiconductor electrodes, *Int. J. Hydrogen Energy*, 31:1999-2017, 2006.

4. P.R.F. Barnes, L.K. Randeniya, A.B. Murphy, P.B. Gwan, I.C. Plumb, J.A. Glasscock, I.E. Grey, C. Li, TiO_2 photoelectrodes for water splitting: Carbon doping by flame pyrolysis? *Dev. Chem. Eng. Mineral Process*, 14, 1/2, 51-70 2007.

Conference proceedings

1. J.A. Glasscock, P.R.F. Barnes, I.C. Plumb, A. Bendavid, P.J. Martin, Photoelectrochemical hydrogen production using nanostructured α-Fe_2O_3 electrodes, in *Solar Hydrogen and Nanotechnology*, edited by Lionel Vayssieres. Proc. SPIE (SPIE, Bellingham, WA), 6430:N1-N12, 2006.

2. P.R.F. Barnes, D. Blake, J.A. Glasscock, I.C. Plumb, P.V. Vohralik, A. Bendavid, and P.J. Martin, Charge transport in Fe_2O_3 films deposited on nanowire arrays, in *Solar Hydrogen and Nanotechnology*, edited by Lionel Vayssieres. Proc. SPIE (SPIE, Bellingham, WA), 6340:P1-P8, 2006.

Conference presentations

1. J.A. Glasscock, P.R.F. Barnes, I.C. Plumb, A. Bendavid, P.J. Martin, Photoelectrochemical hydrogen production using nanostructured α-Fe_2O_3 electrodes, SPIE Solar Hydrogen and Nanotechnology Conference, San Diego USA, August 2006 (invited talk).

2. J.A. Glasscock, P.R.F. Barnes and I.C. Plumb, Photoelectrochemical hydrogen production using coated nanostructured electrodes, 16th International Conference on Photochemical Conversion and Storage of Solar Energy, Uppsala Sweden, July 2006 (poster presentation).

3. J.A. Glasscock, P.R.F. Barnes, I. C. Plumb, L.K. Randeniya and A.B. Murphy, Photoelectrochemical hydrogen production, 16th World Hydrogen Energy Conference, Lyon, France, June 2006 (oral presentation).

4. J.A. Glasscock, P.R.F. Barnes and I. C. Plumb, Photoelectrochemical water splitting using nanostructured α-Fe_2O_3 electrodes, 16th World Hydrogen Energy Conference, Lyon, France, June 2006 (poster presentation).

Contents

List of Figures

List of Tables

Chapter 1

Introduction

"How far must suffering and misery go before we see that even in the day of vast cities and powerful machines, the good earth is our mother and that if we destroy her, we destroy ourselves?"

P.B. Sears

Nano-star

1.1 Solar Hydrogen

Our current global economy is heavily dependent on fossil fuels which are integral to industry, agriculture, transport and everyday life. Access to high-energy fossil fuel sources such as coal, oil and gas facilitated the Industrial Revolution and the economic growth of developed nations worldwide. Unfortunately, the rampant exploitation of fossil fuels has had adverse effects on the environment. Some of the gaseous by-products of fossil fuel extraction and combustion (for example carbon dioxide and methane) are greenhouse gases which contribute to global warming. Other environmental problems that arise with fossil fuel use, such as air pollution, pose health risks to the population. Reliance on fossil fuels can also have negative

political and social consequences as a result of the economic dependence of the world on oil-producing countries. The challenge is to maintain and improve the standard of living of the world's population and support economic growth while utilising energy sources that are renewable and do not adversely affect the environment. The move towards a "hydrogen economy" is being driven by the potential economic and environmental benefits of replacing fossil fuels with hydrogen.

Many technical, political and economic challenges need to be overcome before a hydrogen economy can be realised. Some technical problems include producing hydrogen efficiently using renewable energy sources, storage of hydrogen (particularly for automotive uses), development of efficient, economically viable fuel cells, and the development of suitable infrastructure. There is a huge amount of on-going scientific research on hydrogen production, storage, utilisation and transport. Such research is building the expertise and technology required to achieve a hydrogen economy. A study undertaken in 2002 (8) calculated the cost of solar hydrogen as 20-30 Ecu/GJ compared to current oil and gas prices of 5 Ecu/GJ. The cost of hydrogen production must be greatly reduced in order for this technology to be competitive with other energy sources.

Currently hydrogen is primarily produced from fossil fuels and hence is not a sustainable energy source. Hydrogen is the most abundant element in the universe, yet the vast majority of hydrogen present on Earth is locked up in the form of water. The electrolysis of water to produce hydrogen is easily achieved using an electrochemical cell. If a voltage is applied between two electrodes submerged in an acidic or basic aqueous solution, water is split (electrolysed) into hydrogen and oxygen gases. The water splitting reaction will only take place when external energy is applied (in this case in the form of electricity). If the energy required to split water electrochemically can be supplied by a renewable source, solar energy for example, then hydrogen can be produced sustainably.

Solar hydrogen is a versatile energy carrier that can be used as a liquid fuel or converted to electricity (via heat from combustion, or reaction in a fuel-cell). Solar hydrogen can be produced anywhere that water and sunlight are available, enabling distributed energy generation and reducing the dependence on countries

rich in fossil-fuels for energy supplies. Other renewable technologies, such as solar, wind, tidal, and hydrothermal have intermittent supply, so storage of the produced electricity is required. The energy is often produced in remote areas, far from urban centres where the energy demand is highest. Australia has ideal climatic conditions for the production of solar hydrogen and has the potential of being a world leader in a hydrogen economy. The by-product of hydrogen combustion, or the reaction between hydrogen and oxygen in a fuel cell, is theoretically only water. However, in practice small amounts of nitrogen oxides (NO_x) can be produced during combustion. Unlike fossil fuel reactions no carbon dioxide, carbon monoxide, sulphur dioxide or particulates are produced (9). Hence the replacement of fossil fuels with hydrogen will result in the reduction of greenhouse gas emissions and improved air quality, which in turn will greatly improve the health of the environment and the population.

The solar spectrum contains enough energy to split water, but this reaction does not occur spontaneously due to the optical absorption characteristics of water. The absorption coefficient of water is very low ($\sim 10^{-2}$ m^{-1}) in the UV-visible region of the electromagnetic spectrum, where single photons have adequate energy to split water; hence an enormous path length would be required for significant absorption. However, sunlight can be used to excite a semiconductor, which acts as a catalyst for the water splitting reaction in an electrochemical cell. This thesis describes the development of semiconducting photoelectrode materials that may be used in a photoelectrochemical cell to efficiently produce solar hydrogen. Direct water splitting is currently far less efficient than electrolysing water using electricity produced using photovoltaics. The advantage of photoelectrochemical water splitting is the potential of very low material and processing costs compared to photovoltaic technologies.

The aim of water splitting research is to produce hydrogen from water using sunlight as the energy source, with efficiencies high enough to allow production of hydrogen on a commercial scale. A target hydrogen production efficiency of 10 % has been quoted for water splitting technology to be commercially viable (10). This goal is based on current fuel and infrastructure costs and is likely to change depending on future economic and political conditions.

1.2 Research design

This section outlines the reasons for investigating α-Fe_2O_3 with respect to the requirements of a water splitting photocatalyst. The limitations of hematite will also be discussed, along with hypotheses for improving the photoconversion efficiency of hematite. The technical terms used here will be defined and described in more detail in Chapters 2 and 3.

A suitable semiconductor material for use as a water splitting photocatalyst should ideally possess the the following properties:

- A band-gap energy around 2 eV;
- Strong optical absorption for all wavelengths up to the band-gap energy;
- Efficient separation (long lifetime) of charge carriers in the semiconductor;
- Conduction and valence band edges straddling water redox potentials;
- Efficient charge transfer between the semiconductor and electrolyte;
- Stability in strong electrolytes;
- Good catalytic properties for the water splitting reaction;

For practicality of technology uptake it would also be advantageous if the material had low raw material and manufacturing costs, and was non-toxic (11).

The ideal material for use as a photocatalyst for water splitting would have a band-gap energy E_g around 2 eV. Theoretically 1.23 eV is required to split water (Section 2.1). However, in practice more energy is required due to unavoidable losses within the system. The band-gap energy of a semiconductor determines the fraction of the solar spectrum that can be utilised by the material; only photons with energy greater than or equal to the bandgap energy will excite valence band electrons to the conduction band. In other words, only wavelengths of light below the wavelength corresponding to the bandgap energy, λ_c (nm) = $1241/E_g$ (eV), will generate photons which can contribute to the water splitting reaction. Hence

Material	**Band-gap energy (eV)**	**Band-gap wavelength (nm)**	**Maximum efficiency (%)**
Rutile TiO_2	3.00	413	2.2
WO_3	2.70	459	4.8
α-Fe_2O_3	2.20	564	12.9
Ideal material	2.03	610	16.8

Table 1.1: Maximum theoretical water splitting efficiencies for semiconductors of different band-gaps, illuminated with the AM1.5 solar spectrum.

narrower band-gap semiconductors are preferable as a greater fraction of the solar spectrum can be used.

Table 1.1 compares the maximum theoretical water splitting efficiencies for semiconductors of different band-gaps, illuminated with the AM1.5 solar spectrum (12). The maximum efficiencies represent the thermodynamic limit and cannot be exceeded. These values have been calculated assuming ideal conditions; however, practically achievable efficiencies will be significantly lower due to imperfect absorption, reflection losses, recombination, and the need to apply a bias voltage to the material (12). Such losses can reduce the efficiency for solar hydrogen generation by a factor of up to three (13). It can be seen that the target photoconversion efficiency of 10 % will never be achieved with materials such as TiO_2 and WO_3 (unless their band gaps can be reduced), and it will be very challenging even with materials such as α-Fe_2O_3 given the efficiency losses in a real system. Much research has been undertaken to reduce the band-gap of TiO_2 (usually by doping with C, N or S), to allow visible light absorption (14–19). The dopants act as recombination sites as well as absorption centres, enhancing charge carrier recombination and reducing the water splitting efficiency (20).

The maximum water splitting efficiency values shown in Table 1.1 were calculated assuming that every available photon up to the cut-off wavelength λ_c is absorbed and generates an electron-hole pair which contributes to current in the photoelectrochemical cell. In reality the absorption coefficient α (m^{-1}) of a material determines the number of the incident photons absorbed at each wavelength. In order to utilise

sunlight as the energy source, the photocatalyst material needs to absorb strongly up to the cut-off wavelength. Many semiconductors such as TiO_2 and α-Fe_2O_3 have absorption cross-sections $\alpha(\lambda)$ that fall off rapidly approaching the band-gap wavelength. This means that a large volume of material will be required to absorb the longer wavelength radiation. Only a small fraction of solar energy lies within the UV region, so a material that absorbs well in the visible region can better utilise the solar spectrum (21).

For efficient water splitting a large proportion of the generated charge carriers must be able to travel from the semiconductor to the external circuit without recombining. The electron-hole pairs need to be separated quickly and the charge carriers need to have a long lifetime in the semiconductor. In addition to recombination losses in the bulk, charge carriers will also recombine at the surface if the charge transfer kinetics with the electrolyte are slow.

The positions of the conduction band and valence band edges of the semiconductor are important as they determine whether spontaneous water splitting will occur and whether the material will be stable in a photoelectrochemical cell. A much higher hydrogen production efficiency can be achieved if spontaneous water splitting occurs, without the need to apply an electrical bias. A semiconductor capable of spontaneous water splitting has a band-gap ≥ 2 eV with a conduction band energy higher than that of the H^+/H_2 redox potential, and a valence band energy lower than that of the O_2/H_2O redox potential as shown in Figure 1.1. Under these conditions charge transfer between the semiconductor and the electrolyte is energetically favourable. Most metal oxides have a valence band edge at a similar energy, well below the H_2O/O_2 potential (20). Therefore, to have a conduction band edge above the H^+/H_2 potential, the material will have a wide band-gap (over 3 eV). Narrower band-gap materials with band edges that straddle the water splitting redox potentials (such as CdS and CdSe) are unstable. Maeda and Domen (20) suggest that oxynitride and oxysulphide materials may be more suitable for spontaneous water splitting than metal oxides, as their valence band edges are closer to the H_2O/O_2 potential, and those with a a suitable band-gap around 2 eV are able to have band edges that straddle the water splitting potentials.

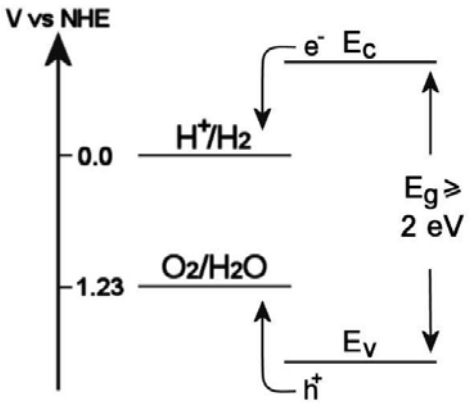

Figure 1.1: A semiconductor capable of spontaneous water splitting has a band-gap $\geq$ 2 eV with a conduction band energy E_c higher than that of the H^+/H_2 redox potential, and a valence band energy E_v lower than that of the O_2/H_2O redox potential.

A semiconductor suitable for use as a photoelectrode for water splitting must be resistant to corrosion and photocorrosion in the presence of the electrolyte in the photoelectrochemical cell. Strong electrolytes are required to minimise resistive losses (provide good charge conduction) between electrodes in the cell. Corrosion can be described as an increased reactivity of the surface atoms which increases the interaction with reagents in the electrolyte, resulting in dissolution of the semiconductor (1). A material will corrode if the free energy (Fermi level) of electrons or holes exceeds the value where cathodic and anodic processes would be in equilibrium (1). Under illumination, decomposition is also possible due to photogenerated minority carriers. Figure 1.2 shows the stability conditions for electrolytic decomposition of semiconductors (reproduced from Gerischer, 1985 (1)), illustrating the relationship between, the decomposition energy of the electrons (nE_{decomp}), the decomposition energy of the holes (pE_{decomp}), the conduction band energy (E_c), and the valence band energy (E_v), for materials that are (A) stable, (B) unstable, (C) stable against cathodic decomposition, (D) stable against anodic decomposition. In reality few semiconductors are totally stable against anodic photodecomposition and the situation shown in Figure 1.2 (C) is the most common (1).

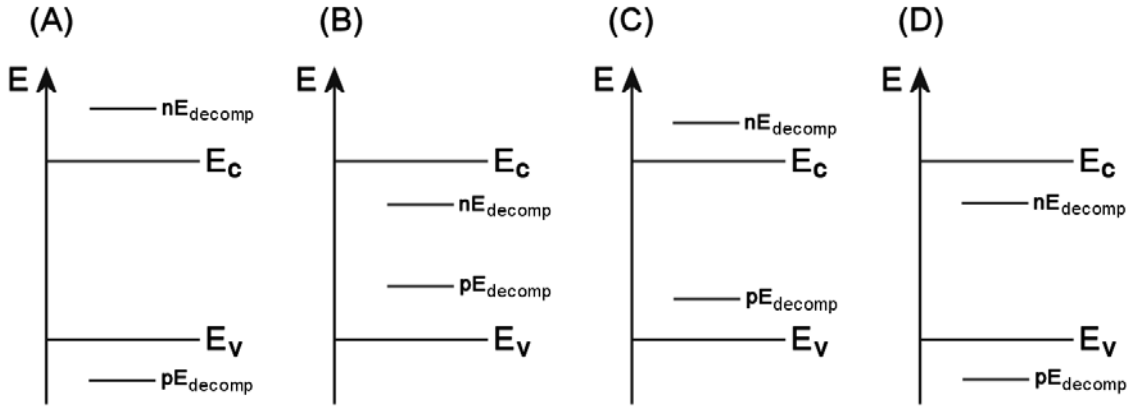

Figure 1.2: Stability conditions for electrolytic decomposition of semiconductors, reproduced from Gerischer, 1985 (1). (A) stable, (B) unstable, (C) stable against cathodic decomposition, (D) stable against anodic decomposition.

Long-term stability of an electrode is required for a water splitting technology to be commercially viable. Many oxide materials such as TiO_2, titanates and WO_3 are corrosion-resistant. Small and medium band-gap materials such as CdS, CdSe and Cu_2O experience severe photocorrosion (13, 22). Sulphide materials such as CdS and PbS are also very toxic. Hodes *et al.* (23) used the following criterion for stability: one element should be able to reversibly change its valance state to accommodate a hole without decomposing, *e.g.* $Ti^{3+} \longrightarrow Ti^{4+}$. Materials such as CdS and ZnO only have one stable valence state and are therefore decomposed by holes, while materials such as TiO_2 and WO_3 satisfy this condition. Practically, a system would need to be stable for years. Often sacrificial *hole-scavengers* are added to prevent the dissolution of the photoelectrode. This is undesirable as the sacrificial agent is often degraded in preference to the water splitting reaction occuring. Many of these agents also emit CO_2 gas and would also add cost and complexity to the technology as the chemicals would need to be replaced as they are consumed.

Probably the most important requirement of a photocatalyst (though the most complex and difficult to define) is that is must be a good catalyst for the water splitting reaction. Tributsch (13) defines a photocatalyst as a "system that energetically improves photoinduced electron transfer by introducing chemical interactions into

interfacial processes". A photocatalyst reduces the activation energy for electron or hole transfer, and its catalytic activity depends on several chemical and physical properties including, the band-gap energy, interfacial chemistry (which determines the activation energy), and the intensity of the illumination (13). The photocatalytic activity can also be affected by the grain size, morphology, and the composition of the material (24). For efficient water splitting to occur it is important that the photogenerated electrons and holes do not recombine (13, 25). Hence the material must have good electrical properties (including high conductivity and a long diffusion length of charge carriers) to allow effective separation and transport of electrons and holes. Catalytic activity of semiconductor materials can be improved by coupling transition metal catalysts (such as Ru and Pt compounds) to the surface to mediate charge transfer (13).

Hematite (α-Fe_2O_3)

Hematite (α-Fe_2O_3) has been selected as the photocatalyst material for this study as it has the potential to split water with a theoretical maximum efficiency of 12.9% (12), as a result of its band-gap around 2.2 eV. The reported water splitting efficiencies for α-Fe_2O_3 are currently much lower than its theoretical maximum and the target water splitting efficiency of 10 % (8). Figure 1.3 shows the proportion of the solar radiation being utilised to split water for the current state-of-the-art hematite (2) compared to what could be utilised by an ideal hematite sample (100% absorption and utilisation of photons up to band-gap wavelength of 564 nm). It is obvious that there is much room for improvement, particularly at wavelengths approaching the band-gap cut-off.

The poor performance of α-Fe_2O_3 has been shown to be due to a number of factors including: poor visible absorption characteristics, rapid electron-hole recombination resulting in short diffusion lengths of charge carriers (26), slow surface reaction kinetics (27), and unfavourable band-edge positions which mean that spontaneous water splitting is not possible and a bias voltage must be applied to generate hydrogen (reducing the overall efficiency) (11). The poor visible absorption of α-Fe_2O_3 means that a thick film is required so a significant fraction of the incident

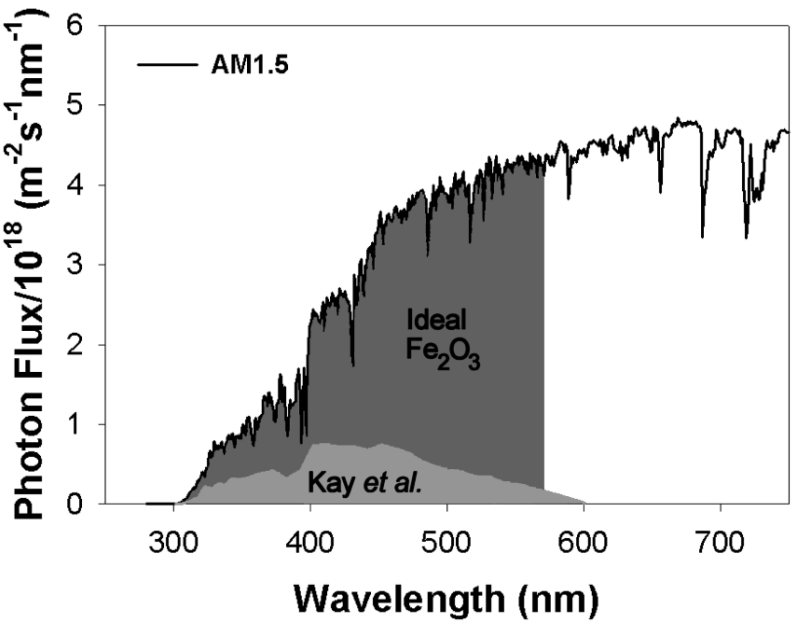

Figure 1.3: Solar photon flux as a function of wavelength, where the black curve represents the AM1.5 standard solar spectrum. The shaded regions represent the amounts of solar photon flux absorbed and used to generate charge carriers for an ideal α-Fe_2O_3 film (100 % absorption and 100 % conversion efficiency) and the current state-of-the-art α-Fe_2O_3, calculated from IPCE values published by Kay *et al.* (2).

solar radiation is absorbed. But in order for generated charge carriers with a short diffusion length to be utilised, a thin film is required to minimise the distance the charge carriers must travel to participate in the water splitting reaction. These competing requirements contribute to the poor photoelectrochemical performance of α-Fe_2O_3 films.

In order to combat the short diffusion lengths of charge carriers in α-Fe_2O_3, recombination can be minimised by reducing the distance that holes and electrons need to travel to reach the surface of the semiconductor to participate in the water splitting reaction. This can be achieved by restricting the α-Fe_2O_3 to a very thin film (28), or via nanostructuring (2, 7, 29). However, in the case of very thin films, the absorption of the solar photon flux is severely limited, and nanostructuring provides a long path length for absorption. Itoh and Bockris (28, 30) showed theoretically and experimentally that an increase in the photocurrent can be achieved by reducing the thickness of α-Fe_2O_3 films below that of the depletion layer width. In order to provide sufficient absorption, a number of thin film electrodes ($\sim$ 100 nm α-Fe_2O_3 deposited onto conducting glass) were stacked one behind the other. The electrodes were electrically connected and all of the α-Fe_2O_3 films were in contact with the electrolyte. Hence photons not absorbed by the first film were transmitted through the transparent substrate to be absorbed by the film behind, and so on. Their model showed that ten stacked films each 60 nm in thickness increase the photocurrent compared to a thick ($\sim$ 1 μm) electrode by a factor of up to four.

The concept that will be investigated in this thesis is that of a composite nanostructured electrode, as shown in Figure 1.4. α-Fe_2O_3 (or equally another low mobility photoactive material) is coated onto a nanostructured transparent conducting substrate (for example an array of nanowires or nanotubes). Wavelengths below the band-gap cut-off are absorbed by the photoactive material and longer wavelengths penetrate. Such an electrode can be used as the front-half of a tandem cell or multilayered electrode, where a photovoltaic cell behind the photoelectrochemical cell can utilize the longer wavelengths to provide an electrical bias to drive the photo-electrochemical cell. A cross-section of a single coated nanowire illustrating the charge transfer mechanism is shown in Figure 1.4. The incident light

($h\nu$) is absorbed by the semiconductor and produces an electron-hole pair ($e - h$). In the case of an n-type semiconductor such as α-Fe_2O_3, the holes migrate to the semiconductor-electrolyte interface and participate in the oxygen-production half of the water splitting reaction. The electrons are transferred to the core material and travel to the back contact, where they are conducted around the circuit to the counter-electrode to participate in the hydrogen production reaction at the counter-electrode. By restricting the absorbing coating material to a thin film, the distance that electrons and holes need to travel in the semiconductor to reach the electrolyte or the underlying conducting substrate is minimized. Similar "core-shell" structures have previously been fabricated for photovoltaic applications (31) and theoretically examined for water splitting (32) (although in this case narrow band-gap materials, acting as the anode, were coated with a cathode material to protect them from corrosion in the cell).

A modification to the composite electrode structure that may be necessary, is the deposition of an inter-layer between the α-Fe_2O_3 and the nanostructured substrate. It is possible that a nanostructured material with all the required properties (discussed next) may be difficult to fabricate. Hence a material that is easily nanostructured could provide a template for a film of a conducting material that will effectively transfer electrons from the α-Fe_2O_3. A schematic of this three-layered structure is shown in Figure 1.4 (B).

The nanostructured composite electrode concept will be investigated experimentally through the development of doped α-Fe_2O_3 thin films and nanostructured substrates, which will be combined to fabricate the electrodes. The design of the composite electrode will also be explored theoretically to optimise the geometry of the nanostructured substrate, given the restriction of the α-Fe_2O_3 film thickness and the requirement of long absorption paths.

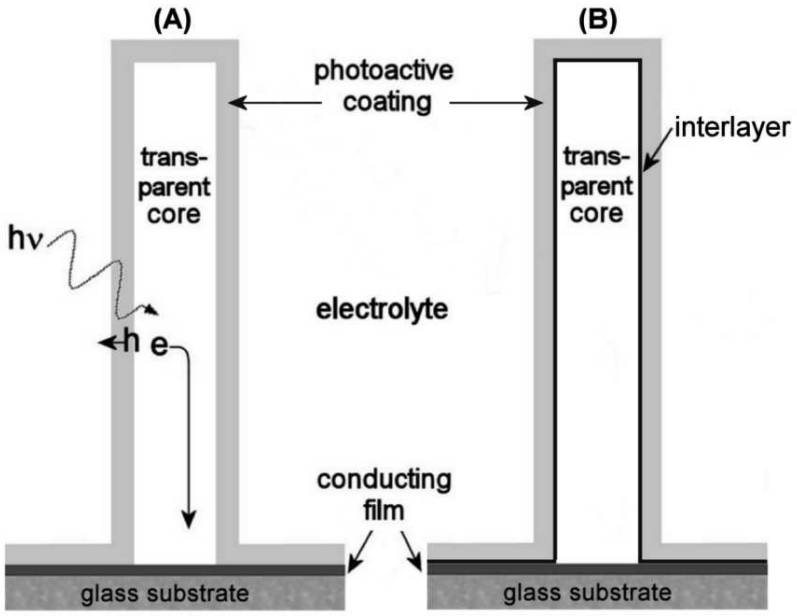

Figure 1.4: Composite nanostructured electrode design. (A) Cross-section of a single coated nanowire showing charge transfer mechanism. A narrow band-gap photocatalyst is coated onto a nanostructured substrate to optimize the absorption and charge transfer properties. Photons (hν) are absorbed by the photoactive layer, producing electron (e) and hole (h) pairs. The holes have only a short distance to travel to reach the electrolyte. The electrons are conducted through the core material to the conducting substrate. (B) Three-layer concept showing an interlayer between the α-Fe_2O_3 film and the nanostructured substrate.

Nanostructured substrates

The ideal material to be used as a nanostructured substrate for α-Fe_2O_3 thin films has to satisfy a number of challenging requirements, as listed below.

- Wide band-gap (> that of α-Fe_2O_3) with conduction and valence band edges below those of α-Fe_2O_3.
- Good electron conductivity.
- Electrochemically and chemically stable.
- Crystal structure and lattice spacings similar to that of α-Fe_2O_3.
- Easily nanostructured.

Although α-Fe_2O_3 has an almost ideal band-gap for water splitting, its conduction band energy is below the H^+/H_2 redox potential, and so spontaneous water splitting is not possible. A bias voltage must be applied in order to increase the energy of the photo-generated electrons. This reduces the overall water splitting efficiency of the system unless a tandem-cell or built-in photovoltaic configuration can be used, where the bias is applied by a photovoltaic cell behind the photoelectrochemical cell. The photovoltaic cell is able to utilize part of the remaining solar spectrum not absorbed by the photoelectrochemical cell. Hence the substrate material must have a wide band-gap (much greater than the $\sim$ 2 eV band-gap of α-Fe_2O_3) to minimise absorption in the substrate.

The conduction band edge of the substrate material must be below that of α-Fe_2O_3 in order to facilitate electron transfer. This concept is illustrated schematically in Figure 1.5 using ZnO and SnO_2 as example substrates. ZnO has a conduction band edge higher than that of α-Fe_2O_3. Hence there exists a potential barrier for electrons moving from the α-Fe_2O_3 to the substrate. In the case of the SnO_2/α-Fe_2O_3 interface, the energy levels of the conduction bands are similar, so efficient electron transfer is possible. The band-gaps of both ZnO and SnO_2 are wider than that of α-Fe_2O_3, with valence band edges below that of α-Fe_2O_3. Hence any holes

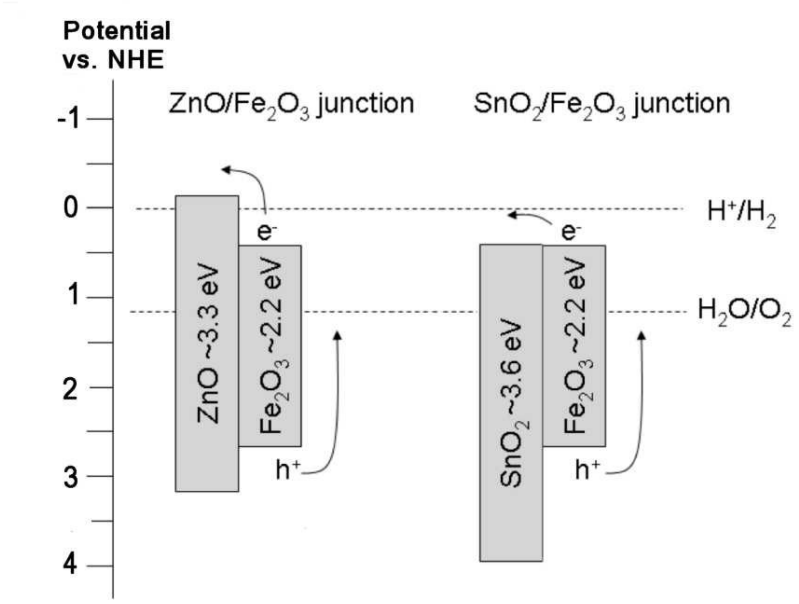

Figure 1.5: Band-edges of example substrate materials (ZnO and SnO_2) compared to those of α-Fe_2O_3. Both ZnO and SnO_2 have valence band edges below that of α-Fe_2O_3 so hole transfer is facilitated. However, the conduction band-edge of ZnO is above that of α-Fe_2O_3, so there is a potential energy barrier to electron flow; whereas the CB edges of SnO_2 and α-Fe_2O_3 are similar so electron transport should be more energetically favourable.

generated in the core (which would not occur in an ideal system) can transfer to the α-Fe_2O_3.

Figure 1.6 shows the band edges of various metal oxides (sourced from the literature (5, 11, 33, 34)) compared to those of α-Fe_2O_3 and the H^+/H_2 and O_2/H_2O redox potentials. Those materials with a conduction band edge at a lower (or similar) energy than that of α-Fe_2O_3 are shown in bold. There are a range of conduction band edges quoted for many of these materials, for example those of SnO_2 shown in Figure 1.6 have a spread of 0.6 V/NHE. This must be considered when band-edge positions are compared. Of course, the conduction band edge is not the only selection criterion and many of the materials shown can be eliminated due to poor stability (*e.g.* Cd compounds and PbO) or having too small a band-gap (*e.g.* Cu compounds). Some materials with suitable band-edge positions and stability include SnO_2, In_2O_3, and Bi_2O_3.

Heavily doping the nanostructured substrate material could sufficiently reduce the width of any potential barriers resulting from misaligned band-edges to allow charge transfer via tunneling. Doping can also be required to improve the conductivity of wide band-gap metal oxide materials. The substrate needs to have high electron mobility so electrons are removed without significant potential drops. However the introduction of a dopant may complicate fabrication and potentially affect other desirable properties of the material.

There are several nanostructured transparent conducting oxide (TCO) semiconductors being developed that may be suitable substrate materials. The most common are fluorine-doped tin oxide (FTO), tin-doped indium oxide (ITO) and aluminium-doped zinc oxide (AZO). Both FTO and ITO are used extensively as coatings to produce conducting glass which is used for a variety of commercial and research applications. Much research has already been undertaken on doped tin oxide materials, and the optical and electrical properties are well known. ITO is an expensive product due to the rarity of indium. Aluminium-doped zinc oxide (AZO) is being investigated as a cost-effective replacement for ITO (35).

The substrate material forms part of the photoelectrode in the photoelectrochemical cell and needs to be electrochemically and chemically stable. Hematite

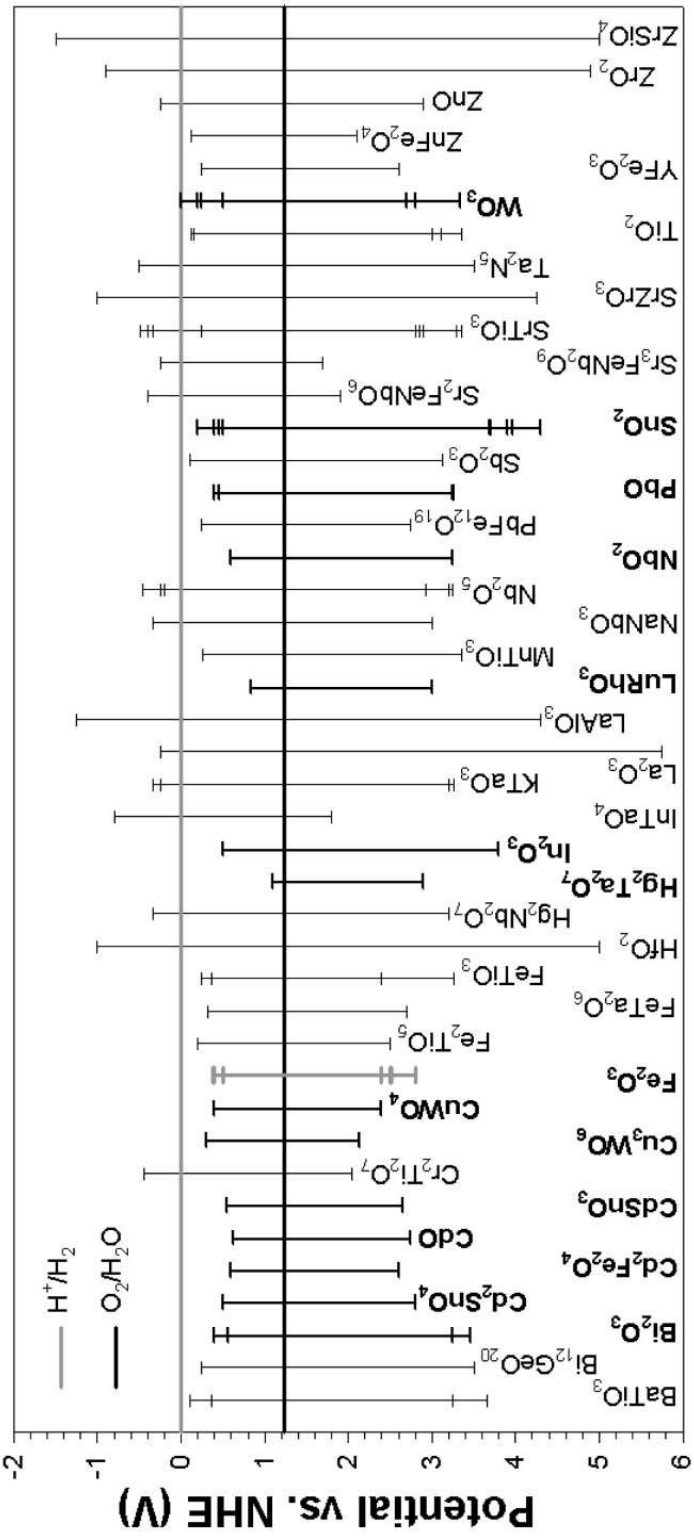

Figure 1.6: Conduction and valence band edge positions of various metal oxides compared to those of α-Fe_2O_3 and the H^+/H_2 and O_2/H_2O redox potentials. Those materials with a conduction band edge energy lower than that of α-Fe_2O_3 are shown in bold.

electrodes are usually operated in electrolytes of pH around 14, and hence the substrate material will need to be stable in a highly corrosive alkaline environment. Materials that degrade when a voltage is applied to them are not suitable *e.g.* most Pb- and Cd-based materials. The stability of water splitting electrodes will be a critical issue in determining the viability of the technology. Materials known to have poor stability must be avoided because, even though the material is coated with α-Fe_2O_3, a completely uniform coating of a very thin film is unlikely.

The quality of the substrate-α-Fe_2O_3 interface will be affected by differences in the crystal structure between the two materials. If epitaxial growth of the α-Fe_2O_3 is not possible, other iron oxides or intermediate phases may be formed as an interlayer. Such a layer may impede charge transfer and may also be photocatalytically inactive. The substrate may require pre-treatment, such as the deposition of an intermediate layer to improve charge transfer from the α-Fe_2O_3 to the core material. Hence it is desirable that the substrate material have a similar crystal structure (and preferably similar lattice spacings) to the hexagonal close-packed corundum structure of α-Fe_2O_3.

It is unlikely that an existing material will satisfy all the criteria for an ideal nanostructured substrate. Introducing nanostructure to some materials may not be easily achieved and the resulting properties may be very different to the bulk or thin films of the material. Two materials have been selected for further investigation, SnO_2 and doped-ZnO. Tin oxide has a conduction band-edge similar to that of α-Fe_2O_3, and is very stable and well-investigated as a transparent conducting oxide material. As shown in Figure 1.5, the conduction band-edge of ZnO is higher than that of hematite, meaning electron transfer will be impeded. In this sense, ZnO is not the ideal substrate material. However, much research has been undertaken producing nanostructured ZnO, and it has been shown that doping ZnO with Al can greatly enhance its conductivity. Relevant literature relating to the fabrication of such nanostructures is discussed in Chapter 4.2.

1.3 Overview of the study

The motivations and aims of this thesis have been presented in this chapter. The development of the composite nanostructured electrode for water splitting can be viewed as three bodies of work. Firstly, the development and characterisation of doped α-Fe_2O_3 thin films; secondly, the fabrication of nanostructured substrates; and thirdly, the design, modelling and fabrication of the composite electrodes. The *Literature, Methods* and *Results and discussion* Chapters will address these topics in separate sections. Chapter 2 introduces relevant theory relating to semiconductors and their interaction with the electrolyte when used as photoelectrodes in a photoelectrochemical cell. Chapter 3 describes the water splitting efficiency measurements undertaken in a photoelectrochemical cell. Chapter 4 examines the literature relating to the conduction mechanisms of α-Fe_2O_3 and its use for water splitting, along with techniques for preparing selected nanostructured metal oxide materials. Chapter 5 describes the experimental methods used to fabricate and characterise the electrodes. The results of the characterisation are discussed in Chapter 6 and finally conclusions of the thesis and recommendations for further work are presented in Chapter 7. Information about the crystal structure of α-Fe_2O_3 is presented in Appendix A. Further discussion of the conduction mechanisms of α-Fe_2O_3 is included in Appendix B.

Chapter 2

Theory

"...man will occasionally stumble over the truth, but usually manages to pick himself up, walk over or around it, and carry on."

W. Churchill

Nano-doughnut

There are many theoretical concepts that underpin the development of photocatalyst materials for water splitting. This chapter presents some important theory relating to semiconducting materials and their interaction with the electrolyte when used as photoelectrodes in a photoelectrochemical cell, along with an introduction to the solar spectrum. These concepts will be further discussed during the analysis of the hematite electrodes.

2.1 Water splitting

Water can be split into hydrogen and oxygen gases by illuminating a semiconductor photoelectrode in a photoelectrochemical cell. Equations 2.1 to 2.4 describe the water splitting reaction for the case of an n-type semiconductor photoanode and a metal counter-electrode (cathode) in an alkaline electrolyte. The absorption of n photons $h\nu$ of energy ≥ 1.23 eV produces n electron-hole pairs (Eq. 2.1). The electron-hole pair must separate and migrate to the surface of the semiconductor (hole) and to the counter-electrode (electron) without recombining. At the photoanode, adsorbed OH^- ions from solution react with the holes forming oxygen gas and water molecules (Eq. 2.2). At the cathode (counter-electrode), the free electrons react with water molecules to produce hydrogen gas and OH^- ions (Eq. 2.3). Note that the absorption of n photons generating n electron-hole pairs produces only $n/2$ H_2 molecules. The overall water splitting reaction is shown by Eq. 2.4, which requires four photons with energies greater than or equal to the band-gap energy of the semiconductor to produce a single molecule of oxygen and two molecules of hydrogen, i.e. two photons per H_2 molecule. The water splitting reaction requires an energy (Gibb's free energy at 298 K) of 237.141 kJ mol^{-1}, or 2.4578 eV per H_2 molecule produced. Therefore the water splitting energy is 1.2289 eV (usually rounded to 1.23 eV) per electron. A photon with energy of 1.23 eV has a wavelength around 1000 nm (near infra-red), so theoretically the entire ultraviolet and visible parts of the solar spectrum are available for solar water splitting. However in practice around 2.0 eV (cut-off wavelength around 620 nm) is required. The extra energy is to account for unavoidable loss mechanisms such as electrode overpotentials.

$$4h\nu \longrightarrow 4e^- + 4h^+ \qquad \text{Photon absorption} \qquad (2.1)$$

$$4h^+ + 4OH^- \longrightarrow O_2 + 2H_2O \qquad \text{Anode} \qquad (2.2)$$

$$4e^- + 4H_2O \longrightarrow 2H_2 + 4OH^- \qquad \text{Cathode} \qquad (2.3)$$

$$2H_2O + 4h\nu \longrightarrow O_{2(g)} + 2H_{2(g)} \qquad \text{Overall} \qquad (2.4)$$

2.2 Semiconductor theory

The band theory of solids defines the available energies for electrons in solids. The *valence band* is the highest energy band (in a semiconductor or insulator) that is fully occupied by electrons at 0 K, its upper edge labelled E_v. The next energy band above the valence band is referred to as the *conduction band*, its lower edge labelled E_c. The energy gap between the valence band and the conduction band is known as the *band-gap*, E_g. Electrons in the valence band are bound to the atoms in the solid and cannot conduct unless they are excited to the conduction band. Electrons promoted to the conduction band leave behind empty states in the valence band not occupied by electrons which are known as *holes*. These act essentially as positive charges. In conducting materials, such as metals, the valence and conduction bands overlap. Insulating materials have a very large band-gap, too large for any valence electrons to be thermally excited into the conduction band. Semiconductors have a small band-gap (0.2 - 3.5 eV) (3) that allows thermal and optical excitations of valence band electrons into the conduction band.

In the case of *direct* band-gap semiconductors, the bottom of the conduction band and the top of the conduction band occur at the same position in wavevector momentum $\boldsymbol{k}$ *space*, $k = 0$. The absorption of a photon, with an energy greater than or equal to the band-gap energy will generate an electron-hole pair. The electron is excited to the conduction band, leaving a hole in the valence band. This is known as the direct or optical transition. In *indirect* band-gap semiconductors, the bottom of the conduction band is shifted in k space (by k_c) and no longer matches up with the top of the valence band. The indirect transition involves both a photon, to excite an electron the the conduction band energy level, and a phonon (lattice vibration), to move the electron across k space. Schematic diagrams of the direct and indirect processes are shown in Figure 2.1.

All real crystal lattices deviate from ideal atomic structures and possess defects which influence various physical properties of the material, including the electrical conductivity (36). *Intrinsic* semiconductors (such as very high-purity Si) have a negligible number of impurities, while *extrinsic* semiconductors have impurities that

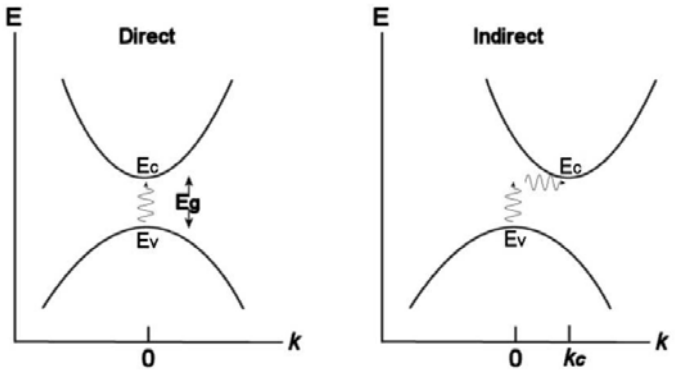

Figure 2.1: Schematic diagrams of the direct and indirect band-gap transition processes, where E is energy and k is the wavevector. The direct transition requires a photon to excite the electrons across the band-gap. The indirect transition also requires a phonon to move the electron across k space by an amount k_c. Reproduced from Kittel (3)

"donate" electrons to the conduction band, or "accept" electrons from the valence band. Usually intrinsic semiconductors are "doped" with foreign impurities to produce an extrinsic semiconductor. *Donor* or *acceptor* energy levels are formed just below the conduction- band edge or just above the valence-band edge, respectively. Donor impurities result in *n-type* conductivity, where conduction is dominated by electrons, the negative charge carriers. Alternatively, acceptor impurities result in *p-type* conductivity, where conduction is dominated by holes, the positive charge carriers. In the case of an *n*-type semiconductor, such as α-Fe_2O_3, the dominant charge carriers (electrons) are known as *majority* carriers and the holes as *minority* carriers.

In the case of an intrinsic semiconductor thermal excitation of electrons from the valence band to the conduction band occurs, leaving behind an equal number of holes as electrons, $n = p = n_i$ (intrinsic carrier density). The "mass action law" shown in Eq. 2.5 shows that the product of the electron concentration (n) and the hole concentration (p) is equal to the intrinsic carrier concentration (n_i) squared, where N_c and N_v are the number of charge carriers in the conduction band and

valence band respectively.

$$n \cdot p = N_c N_v \; exp\left(-\frac{E_g}{kT}\right) = n_i^2 \tag{2.5}$$

Metal-oxide semiconductors are generally of much lower purity than traditional semiconductors, such as Si and Ge, and often possess lattice defects (such as vacancies and interstitials) that act as donors or acceptors. Ionic defects such as vacancies and interstitials are known as point defects. Electronic defects, such as extra electrons from dopants and polarons (electron and local lattice distortion created by the charge carrier) are electrically active, and can introduce charge carriers into mid-bandgap energy levels (36). Metal-oxide semiconductors cannot be thought of as intrinsic semiconductors. However, as the intrinsic carrier density is highly temperature dependent, there exists a high temperature range where the concentration of intrinsic charge carriers exceeds that of the extrinsic carriers, so the electrical properties of the semiconductor are independent of the impurities within the material and the semiconductor exhibits intrinsic behaviour (3). At lower temperatures, the conductivity is dominated by impurity conduction mechanisms (3) resulting from the largely temperature-independent extrinsic defects (36).

For oxides such as hematite, that have transition metal ions with incompletely filled $3d$ shells, conduction can be achieved through the introduction of vacancies or impurity ions into the lattice (4). The deviation in valency as a result of the introduction of a dopant (either point defects or foreign ions) is compensated by a neighbouring parent metal ion. For example the substitution of Fe^{3+} with Ti^{4+} ions, produces a Fe^{2+} to compensate (as shown in Eq. 2.6), producing an n-type semiconductor. The metal ion that has undergone a valency change as a result of the dopant (to retain charge neutrality) is referred to as a donor centre, or more specifically as a majority centre or a minority centre depending on valence change (4).

$$Fe^{3+} + Ti^{3+} \longrightarrow Fe^{2+} + Ti^{4+} \tag{2.6}$$

The Fermi function (Eq. 2.7) describes the probability $f(\mathrm{E} - \mathrm{E_F})$ that a given available energy state will be occupied at a given temperature T (K), where E is

the energy, E_F is the Fermi level and k is Boltzmann's constant.

$$f(E - E_F) = \left[1 + exp\left(\frac{E - E_F}{kT}\right)\right]^{-1} \tag{2.7}$$

The Fermi level is the energy at which the probability of an energy level being occupied by an electron equals one half. The Fermi level can also be defined as the electrochemical potential of the electron in a material (37). In semiconductors the Fermi level is within the band-gap. For intrinsic semiconductors E_F is around the midpoint between E_c and E_v. In the case of an n-type semiconductor, E_F is shifted towards E_c and is often between the donor level and the conduction band.

An electronic band structure (*e.g.* for the case of n-type Ti-doped hematite (4)) is shown in Figure 2.2. The impurity ions produce a donor level E_D just below the empty conduction band. The Fermi energy has been shifted towards the conduction band edge.

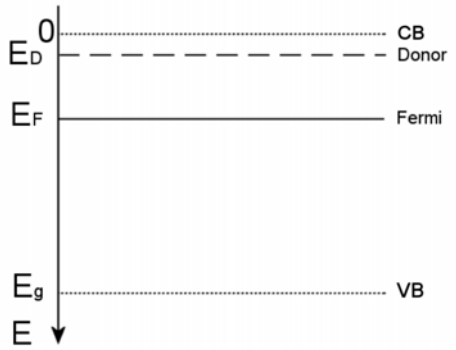

Figure 2.2: Electronic energy diagram of doped, n-type α-Fe_2O_3 showing localised energy levels (reproduced from Jonker and van Houten (4)). The conduction band edge (CB) and valence band edge (VB) differ by the band-gap energy E_g. The dopants introduce a donor level E_D below the conduction band. The Fermi energy has been shifted towards the conduction band edge.

The diffusion length L of the minority carriers in a semiconductor can be defined by Eq. 2.8 where D is the diffusion coefficient and τ is the lifetime of the minority carriers.

$$L = (D \cdot \tau)^{1/2} \tag{2.8}$$

The diffusion coefficient D is related to the mobility μ by Eq. 2.9, known as the Einstein relationship.

$$D = \left(\frac{kT}{e}\right)\mu \tag{2.9}$$

By combining Eq. 2.8 and Eq. 2.9, the mobility can be expressed in terms of the diffusion length of charge carriers, as shown by Eq. 2.10.

$$\mu = \frac{L^2 e}{kT\tau} \tag{2.10}$$

The electrical conductivity σ (Ω^{-1} m^{-1}), is given by Eq. 2.11 where e is the electronic charge (C), n and p are the electron and hole concentrations respectively and, μ_e and μ_h are the mobilities (m^2 V^{-1} s^{-1}) of electrons and holes respectively (3). Hence charge carrier mobilities and diffusion lengths can be calculated from measured conductivity values (38). The electrical resistivity ρ (Ω m) is the reciprocal of the conductivity.

$$\sigma = e(n\mu_e + p\mu_h) \tag{2.11}$$

For the case of intrinsic conductivity n_i (Eq. 2.5) can be substituted into Eq. 2.11 to give an expression for the intrinsic conductivity (Eq. 2.12).

$$\sigma = e(\mu_e + \mu_h)(N_c N_v)^{\frac{1}{2}}\ exp\left(\frac{-E_g}{2kT}\right) \tag{2.12}$$

The conductivity can be determined experimentally by measuring the d.c. resistivity and the thermopower α (mV K^{-1}) (also known as the Seebeck coefficient θ). Measurements are performed at elevated temperatures under a controlled atmosphere to ensure equilibrium conditions between the solid and gas-phase oxygen (39). For magnetic materials, experiments to determine defect and transport properties are usually undertaken above the Néel temperature (point at which the thermal energy is large enough to destroy the magnetic ordering of an antiferromagnetic material), where magnetic ordering is not an issue (40). A negative Seebeck voltage or thermopower indicates n-type behaviour and a positive value indicates p-type behaviour. The charge carrier mobilities and the intrinsic carrier concentration can be determined from the conductivity and thermopower measurements.

The d.c. conductivity of a semiconductor varies exponentially with temperature T according to Eq. 2.13, where E_a is the activation energy and k is Boltzmann's constant.

$$\sigma = \sigma_0 \; exp\left(\frac{-E_a}{kT}\right) \tag{2.13}$$

Eq. 2.14 is thought to be more appropriate for semiconductors with conduction that occurs via a hopping mechanism (discussed in Appendix B), if conductivity is dominated by one type of carrier moving by a single mechanism, rather than band conduction (4, 40). The $1/T$ term arises from the substitution of Eq. 2.15 (mobility of a thermally activated polaron) into Eq. 2.11 for conductivity.

$$\sigma = \frac{\sigma_0}{T} \; exp\left(\frac{-E_a}{kT}\right) \tag{2.14}$$

The slope of the linear region of a log σ (or $\log(\sigma T)$) vs. T^{-1} plot yields the activation energy for electrical conductivity. The E_a values calculated from the two methods differ significantly only at high temperatures (4). Often these plots show a number of distinct linear regions representing different activation energies over certain temperature regimes (41). The activation energy values provide information about the lattice traps that localise the electrons (4).

Charge carrier conduction in many transition metal oxides is often described by the *small polaron model*. The charge carriers are considered to be *polarons* (an electron or a hole and the local lattice distortion created by that charge carrier). The distortion of the lattice moves with the migrating charge carrier and so has an activation barrier associated with it. Small polarons create lattice distortions that extends over distances smaller than the lattice constant. In contrast, large polarons have wider regions of lattice distortion. A charge carrier can lower its energy by delocalising into the conduction band or by localising on a metal site inducing a distortion of the nearby lattice. The polarisation of the lattice acts as a potential well that traps the charge carrier (known as Landau trapping (4)) and reduces mobility. Small polarons move via a "thermally activated hopping process" in which thermal activation is required for the carrier to escape the trap site (42). An activation energy (arising largely from the reorganisation energy associated with the distortion or relaxation of the lattice during charge transfer) is required for a

charge carrier to hop from one site to another (43, 44). The movement of charge carriers in such a system can be considered as a diffusion process (4). The mobility of a hopping polaron can be described by Eq. 2.15, where a is the jump distance, ν is the jump frequency, E_a is the activation energy for conductivity, T the temperature and k is Boltzmann's constant (4).

$$\mu = (a^2 e\nu/kT)\ exp(-E_a/kT) \tag{2.15}$$

2.3 The semiconductor-electrolyte interface

In semiconductor physics, the vacuum level is usually used as a reference energy. However in electrochemistry a number of different energy scales are used where the electrical potentials are reversed with respect to the vacuum scale as it is the potential of the electrons that is of interest. Figure 2.3 shows a number of electrochemical energy scales, where H^+/H_2 and O_2/H_2O represent the hydrogen production and oxygen production redox potentials respectively. The normal hydrogen electrode (NHE) potential is defined as that of a platinum electrode at 298 K at pH 0 (in equilibrium with 1 atm of H_2). The reversible hydrogen electrode (RHE) potential differs from the NHE potential by +59.2 mV/pH at 25 °C. The saturated calomel electrode (SCE) is often used as the reference electrode in three-electrode photoelectrochemical cells. Details regarding photoelectrochemical cells and associated measurements will be presented in Chapter 3 and Section 5.2.1.

When a semiconducting electrode comes into contact with electrolyte in a photoelectrochemical cell a complex interface is formed. The properties of this interface are critical to the cell performance and various photoelectrochemical experiments can be performed to elucidate the nature of the interface. Several review articles give detailed descriptions of the semiconductor-electrolyte interface (11, 45, 46).

The semiconductor-electrolyte interface will be discussed with respect to an n-type semiconducting electrode (photoanode) submerged in an electrolyte with a metal electrode acting as the counter-electrode (cathode), as shown in Figure 2.4, reproduced from Nozik and Memming (5). The vertical axis represents potential

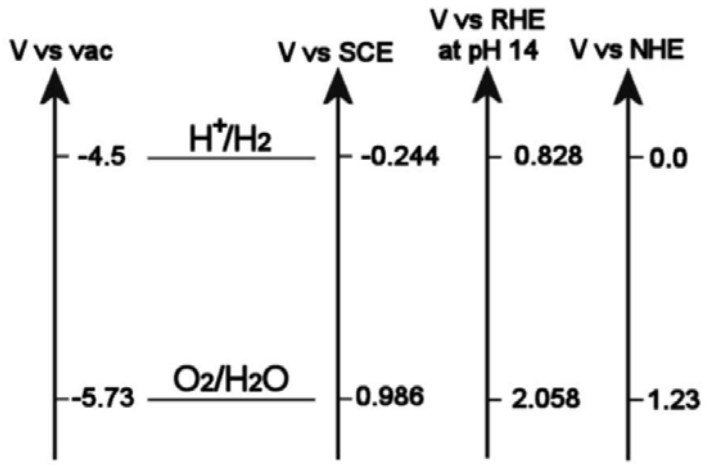

Figure 2.3: Water splitting redox potentials with respect to the reversible hydrogen electrode (RHE), normal hydrogen electrode (NHE), saturated calomel electrode (SCE) and vacuum reference levels.

energy, and the three sections horizontally in each image show the semiconductor electrode, electrolyte and metal counter-electrode respectively. The *flat band potential*, V_{fb} is the potential of the semiconductor when at a condition of zero charge (analogous to the potential of zero charge for metals). V_{bias} is the bias voltage applied to the cell and V_B is the band bending.

Four electrochemical conditions are shown in Figure 2.4: (A) initial condition before equilibrium is reached, (B) equilibrium condition in the dark, (C) illuminated condition, and (D) illuminated condition with a bias voltage applied.

Initially the Fermi level of the electrolyte can be anywhere between the two water splitting redox potentials, the exact position depending on the concentration of hydrogen and oxygen in the electrolyte (5). In Figure 2.4 (A) it is assumed that the metal cathode is in equilibrium with the electrolyte, therefore the Fermi levels of the electrolyte and metal are the same. At equilibrium in the dark (Figure 2.4 (B)) the Fermi level of the semiconductor (electrochemical potential of the electrons (13)) equilibrates with that of the electrolyte by flow of electrons from the semiconductor to the electrolyte, resulting in a region depleted of electrons at the semiconductor surface known as the *depletion layer* or *space charge layer*. This positively charged

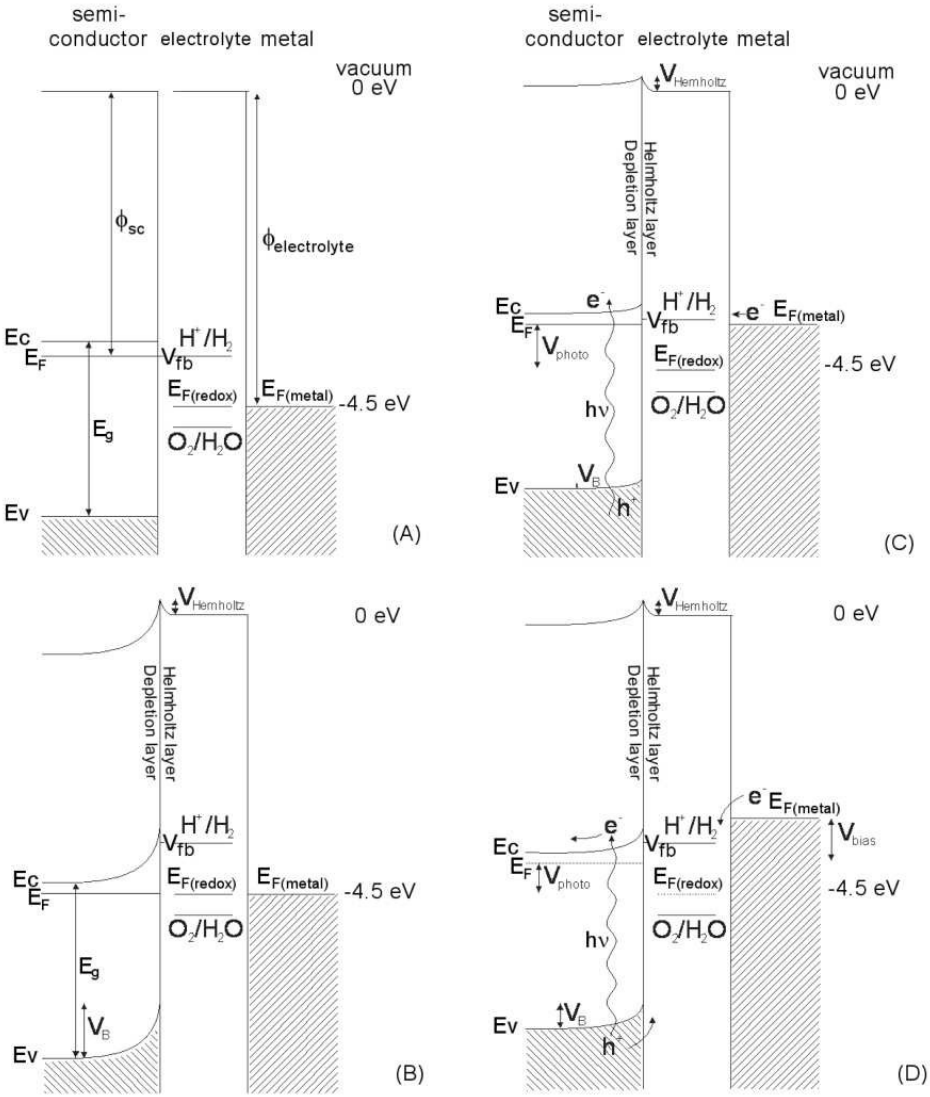

Figure 2.4: Band diagrams of a two-electrode photoelectrochemical cell. (A) The system before the semiconductor-electrolyte interface is formed. (B) The semiconductor in equilibrium with the electrolyte. (C) The semiconductor is illuminated. (D) The semiconductor is illuminated and a bias voltage is applied. E_g is the semiconductor band-gap, E_F represents the Fermi energies, V_{fb} is the flat-band potential, V_{bias} is the bias voltage, V_B is the band bending, $V_{Helmholtz}$ is the potential of the Helmholtz layer, and V_{photo} is the difference between the Fermi energies of the semiconductor and the electrolyte when the semiconductor is illuminated. Reproduced from Nozik and Memming (5).

region attracts negatively charged ions in the electrolyte, which form a very thin ($<$ 1 nm) *Helmholtz layer*. The equilibration of the electrochemical potentials of the electrolyte and the semiconductor leads to "band bending", of magnitude V_B. The potential drop across the Helmholtz layer $V_{Helmholtz}$, which increases the band bending, is determined by the interaction between the semiconductor and the electrolyte and is not greatly dependent on the applied potential.

The width of the depletion layer is represented by Eq. 2.16 where λ_D is the Debye length, the distance over which significant charge separation can occur (Eq. 2.17), ϵ_0 is the permittivity of free space, ϵ_r is the relative permittivity, N_D is the charge carrier concentration, V is the applied voltage, k is Boltzmann's constant and T is the temperature.

$$w_d = \lambda_D \left(\frac{2e|V - V_{fb}|}{kT} - 1 \right)^{1/2} \tag{2.16}$$

$$\lambda_D = \left(\frac{\epsilon_r \epsilon_0 kT}{N_D e^2} \right)^{1/2} \tag{2.17}$$

The capacitance per unit area of the space charge layer can be expressed by Eq. 2.18. Substituting w_d (Eq 2.16) into Eq. 2.18 yield the Mott-Schottky relationship (Eq. 2.19), where A is the surface area of the electrode and other symbols have been defined previously. A Mott-Schottky plot of $(A/C)^2$ as a function of applied voltage will yield a straight line. The charge carrier concentration N_D can be determined from the slope of this line and the flat-band potential determined from the intercept.

$$\frac{C}{A} = \frac{\epsilon_r \epsilon_0}{w_d} \tag{2.18}$$

$$(\mathrm{A/C})^2 = 2(\mathrm{eN_D}\epsilon_\mathrm{r}\epsilon_0)^{-1}(|\mathrm{V} - \mathrm{V_{fb}}| - \mathrm{kT/e}) \tag{2.19}$$

When the photoelectrochemical cell is illuminated, Figure 2.4 (C), charge carriers are generated, which are separated by the electric field in the space charge layer. In the case of an n-type semiconductor, the electrons move into the bulk and the holes migrate to the electrolyte interface. A photovoltage is generated and the Fermi level

is moved upwards toward the flat-band potential. The band bending is reduced as a result of electron-hole pairs being generated by the absorbed photons. Under these conditions no current is flowing. The *overpotential* of an electrode is the difference in potential of an electrode at equilibrium (with no current flowing) and when current is flowing. It is a measure of the additional energy required to drive the reaction. The value of the overpotential will depend on the magnitude of the energy barriers involved in the chemical reactions, arising from factors such as the thermodynamics, kinetics, and charge carrier concentration differences between the solution and the interface (5, 13). The total overpotential η is the sum of the overpotential across the depletion region η_d and that across the Helmholtz layer η_H. The voltage drop in the electrolyte can be assumed to be small (in concentrated solutions) and can be ignored in most cases. The interfacial activation energies for electron and hole transfer are related to the overpotentials.

Under illuminated conditions, Figure 2.4 (C), the maximum Fermi energy possible is the flat band potential, which is still below the H^+/H_2 redox potential, so hydrogen generation is not possible. When a bias voltage V_{bias} is applied, Figure 2.4 (D), the Fermi energy in the metal electrode is raised above the H^+/H_2 potential, allowing the water splitting reaction to proceed. If a bias voltage needs to be applied the efficiency of the water splitting is reduced. The properties of the semiconductor photoelectrode are critical to determining the efficiency of the water splitting process.

2.4 Schottky barrier charge transfer models

The interface formed at a semiconductor-electrolyte junction, as described in the previous section, is analogous to a Schottky barrier formed between a semiconductor and a metal. Figure 2.5 shows a schematic of such a barrier, where w_d is width of the Schottky barrier (depletion or space-charge region), L is the charge carrier diffusion length and h is the thickness of the semiconductor. The analogy with the Schottky barrier is valid, so long as the concentration of ions in the electrolyte is high enough to ensure that there is a negligible potential drop in the electrolyte (47). The analogy

is particularly valid if the reaction kinetics can be ignored (48). The analogy is less applicable to electron transfer as there is limited availability of electron states in the electrolyte compared with a metal, the ions in solution can change the Helmholtz layer, and irreversible chemical changes can occur in the electrolyte (47).

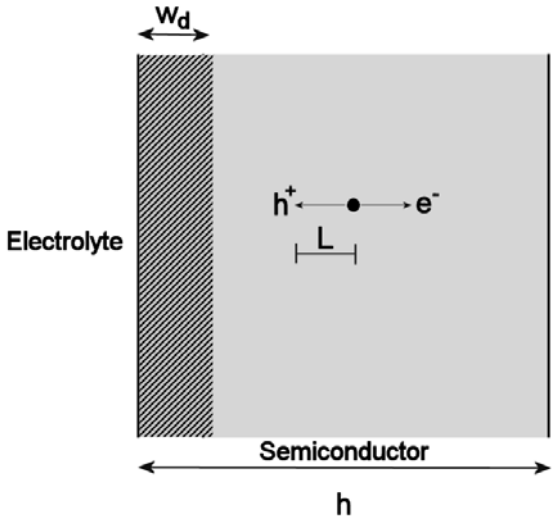

Figure 2.5: Schematic of the Schottky barrier formed at a semiconductor-electrolyte interface, where w_d is width of the Schottky barrier (space-charge region), L is is the charge carrier diffusion length and h is the semiconductor film thickness.

A number of models have been developed to describe the Schottky barrier at the semiconductor-electrolyte interface (48–55). A good review of the charge transfer processes at the semiconductor-electrolyte interface and the relevant models was presented by Wilson (47). The complexity of the models differ, although the majority are variations on the early work of Gärtner (49) and Butler (48), with different assumptions and boundary conditions applied.

Gärtner (49) considered a metal-semiconductor Schottky barrier and proposed that a fraction of the incident light (depending on the wavelength and the absorption coefficient of the semiconductor α) will be absorbed in the depletion layer. Minority carriers generated within the depletion layer of the film are assumed to be rapidly transported to the electrode surface by the strong electric field in this region. A fraction of the minority carriers generated in the bulk of the film are assumed to

diffuse to the edge of the depletion layer from where they are rapidly transported to the surface. Gärtner derived an expression (Eq. 2.20) for the generation of electron-hole pairs $g(x)$ as a function of depth in the semiconductor x, where is the photon flux and α is the absorption coefficient of the semiconductor. This expression does not consider scattering losses or optical absorption not leading to excitations across the bandgap (47).

$$g(x) = E_S \alpha \; exp\,(-\alpha x) \tag{2.20}$$

By integrating the generation rate expression (Eq. 2.20) in the depletion layer, and assuming that all carriers generated in this region contribute to the photocurrent, a current density for the depletion layer J_{dep} can be derived (Eq. 2.21).

$$J_{dep} = eE_S \;\; (exp\,(-\alpha w_d) - 1) \tag{2.21}$$

Gärtner (49) derived the diffusion current density J_{diff} (Eq. 2.22), where L is the minority carrier diffusion length, p_0 is the equilibrium hole density and D_p is the minority carrier diffusion coefficient. The boundary conditions for this solution are $p = p_0$ for $x = \infty$, and $p = 0$ for $x = w_d$.

$$J_{diff} = -eE_S \frac{\alpha L}{1 + \alpha L} \; exp\,(-\alpha w_d) - ep_0 \frac{D_p}{L} \tag{2.22}$$

Butler (48) applied Gärtner's model to a semiconductor-electrolyte system. The total current density J is the sum of the current density in the depletion layer, Eq. 2.21, and the current density in the bulk, Eq. 2.22, derived from the Gärtner-Butler expression (Eq. 2.23), where the second term is neglected (for wide band-gap semiconductors). Eq. 2.23 can be expressed as a quantum efficiency (or IPCE) by dividing J by e.

$$J = eE_S \left(1 - \frac{exp\,(-\alpha w_d)}{1 + \alpha L}\right) \tag{2.23}$$

Wilson (52) modified the Gärtner-Butler equation to consider reflection losses, surface recombination and surface electron transfer processes to yield Eq. 2.24,

$$IPCE = (1 - R) \; \frac{S_t}{S_r + S_t} \;\; \left[1 - e^{-\alpha w_d} + e^{-\alpha w_d} \frac{\alpha L}{\alpha L + 1} \frac{L_p}{L + D/S}\right] \tag{2.24}$$

where R is the reflectivity of the semiconductor surface, S_t and S_r are the rate constants for transfer and recombination, respectively, of minority carriers at the surface, D is the diffusion coefficient and S is the boundary condition shown by Eq. 2.25, where the symbols have their usual meaning.

$$S = (S_r + S_t)\ exp\left[e(V - V_{fb})/kT\right] \tag{2.25}$$

It is useful to define the direction of illumination through electrodes with transparent substrates. Commonly the abbreviations SE (substrate-electrode) and EE (electrolyte-electrode) are used to refer to back-side and front-side illumination respectively (54). Ghosh and Maruska *et al.* (51, 56, 57) derived the following equations for the IPCE for illumination from the electrolyte side (Eq. 2.26) and illumination from the substrate side (Eq. 2.27), by modifying the Gärtner-Butler expression assuming a finite semiconductor thickness. Eq. 2.20 was integrated assuming that carriers generated at distance x will have $exp[-(h - w_d)/L]$ carriers diffuse to the junction, where β is the inverse of the carrier diffusion length L, h is the film thickness and G is the surface transfer coefficient (between 0 and 1) that corrects for transport processes and photoconductive gain in the depletion layer (57).

$$\begin{aligned} IPCE_{EE} =& G\left(1 - e^{-\alpha w_d} + \left[\frac{\alpha}{(\alpha+\beta)}\right]\ e^{\beta w_d}\right) \\ & \times \left(e^{-(\alpha+\beta)w_d} - e^{-(\alpha+\beta)h}\right) \end{aligned} \tag{2.26}$$

$$IPCE_{SE} = G\left[\left(\frac{\alpha}{(\alpha-\beta)}\right)\ e^{-\beta(h-w_d)} - e^{-\alpha(h-w_d)} + \left(e^{-\alpha h}\ e^{(\alpha w_d)-1}\right)\right] \tag{2.27}$$

In Eq. 2.26, the first term describes the contribution from carriers generated in the depletion region, while the second term describes the contribution from carriers generated in the bulk. The opposite is true for Eq. 2.27 when the direction of illumination is changed.

Lindquist *et al.* (54, 55) simplified the Gärtner-Butler expression by assuming that the absorption coefficient α is small and hence $\alpha L \ll 1$. It was shown that when the $IPCE_{SE}$ is a maximum, Eq. 2.28 is true.

$$IPCE_{EE} = \frac{w_d}{h} \qquad (IPCE_{SE,\ max}) \tag{2.28}$$

Hence if the film thickness of the semiconductor can be independently determined, the width of the depletion layer can be calculated from $IPCE_{EE}$ data.

Södergren *et al.* extended this analysis under the condition that the transport is by diffusion and that the diffusion coefficient of holes is constant. By assuming that the diffusion length is shorter than the film thickness, $L < h$, the $IPCE_{SE}$ can be simplified to Eq. 2.29.

$$IPCE_{SE} = \frac{L\alpha}{1 + L\alpha} \tag{2.29}$$

A maximum for $IPCE_{EE}$ was found, assuming $(\mathrm{L}\alpha)^2 \ll 1$, when $\alpha = 1/h$. Hence an expression for $IPCE_{SE}$ as a function of the diffusion length and film thickness can be derived from Eq. 2.29 at the condition where $IPCE_{EE}$ is maximum, as shown by Eq. 2.30.

$$IPCE_{SE} = \frac{L}{h} \qquad (IPCE_{EE,\ max}) \tag{2.30}$$

These simplified expressions can only be applied to experimental data if the assumptions made in the model can be verified. This model was used to analyse nanoparticulate TiO_2, and may not be as suitable for other materials, for example where maximum values of the $IPCE_{EE}$ or $IPCE_{SE}$ do not occur.

The Schottky barrier models are based on the concepts of band-bending and a potential drop across the film (as discussed in Section 2.3). For the case of a very thin semiconducting film, or a nanostructure (where the dimensions are approaching those of the depletion region and diffusion length) these concepts no longer hold. Alternate models have been developed to describe the charge transport and photoelectrochemical response of semiconductor particles/films on the nanoscale (55, 58–60). Most of these models were developed in response to the large interest in dye-sensitised solar cells, where colloidal nanosparticles of TiO_2 are interconnected. The small particle size (5-50 nm(58)) results in no significant potential drop between the centre and the surface of the individual semiconductor particles (59), that is, no large electric fields are present. Hence charge transport in these alternate models is only diffusion.

Chapter 3

Efficiency measurements

"That orbed continent the fire
That severs day from night."

W. Shakespeare

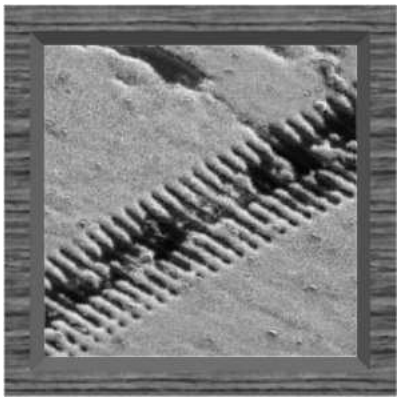

Nano-tyre-treads

This Chapter presents a summary of Paper 3 (12) which discusses some of the pitfalls of water splitting efficiency measurements, in particular the overestimation of published efficiency values as a result of using artificial light sources with spectra that differ from the solar spectrum. An extended version of Table 1.1 (showing maximum theoretical efficiency values) appears in this publication, showing data for various semiconductors using different illumination sources.

Photoelectrochemical measurements to determine the water splitting efficiency of a photocatalyst are usually undertaken in a three-electrode cell, as pictured in Figure 3.1.

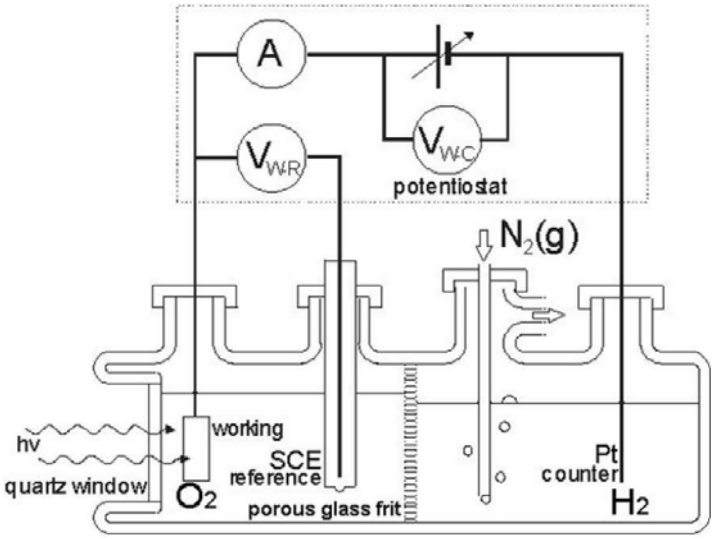

Figure 3.1: Schematic of the three-electrode cell used for photoelectrochemical measurements, showing a simplified version of the potentiostat circuit. The ammeter A measures the photocurrent. The voltages between the working and Pt counter electrodes V_{WC}, and between the working and reference electrodes V_{WR}, are labelled.

The three electrodes are the working electrode (the photocatalyst sample), a counter-electrode (often platinum wire), and a reference electrode. In this study the reference electrode is a saturated calomel electrode (SCE), though Ag/AgCl electrodes and others can also be used. The cell is filled with an electrolyte, in which the photocatalyst material of interest is stable. A simplified version of the potentiostat circuit is shown were the ammeter A measures the photocurrent. The voltages between the working and counter electrodes V_{WC}, and between the working and reference electrodes V_{WR}, are labelled.

The conversion efficiency η_c (%) of the water splitting reaction can be determined using Eq. 3.1,

$$\eta_c = \frac{j_P(V_{WS} - V_B)}{eE_s} \tag{3.1}$$

where j_P is the photocurrent produced per unit irradiated area, $V_{WS} = 1.23$ V is the water splitting potential per electron, E_s is the photon flux (photons cm^{-1}), V_B is the bias voltage applied between the working and counter-electrodes (V_{WC} in Figure 3.1) and e is the electronic charge. This relationship assumes that every electron that contributes to the current, produces half an H_2 molecule. In practice this may not be true and strictly the rate of hydrogen and oxygen production should be monitored in addition to measuring current. In the situation where gas production was not monitored (as is the case with this study), efficiency values are an upper bound for hydrogen production.

The incident photon-to-electron conversion efficiency, $IPCE$ (%), is defined as the fraction of incident photons that generate a photoelectron in the external circuit. The IPCE can be calculated using Eq. 3.2,

$$\text{IPCE} = \frac{j_P(\lambda)}{eE_s(\lambda)} \tag{3.2}$$

where $E_s(\lambda)$ is the incident photon flux at wavelength λ (within the band-pass of the monochromator) and e is the electronic charge. An IPCE of 100 % indicates that every incident photon generates an electron-hole pair, which is effectively separated and results in current flow in the external circuit. A plot of the IPCE as a function of wavelength is often referred to as an "action spectrum".

In practice, the photoelectrochemical water splitting system will be illuminated with the local solar spectrum. A common standard solar reference spectrum is the AM1.5 global solar spectrum shown in Figure 3.2. The air mass (AM) factor describes the effect of the Earth's atmosphere on the incident solar spectrum, where AM = $1/\cos(\alpha)$, where α, the zenith angle, is the angle between the overhead and actual position of the sun. The sharp dips in the spectrum are due to the absorption of certain wavelength bands by gases such as H_2O, O_3, O_2 and CO_2 in the atmosphere.

The solar spectrum reaching the surface of the Earth is dependent on the location, season, time of day and the weather. Hence most measurements of the water splitting efficiency are undertaken in laboratories using illumination from artificial light sources (*e.g.* xenon or mercury lamps). Spectral differences between

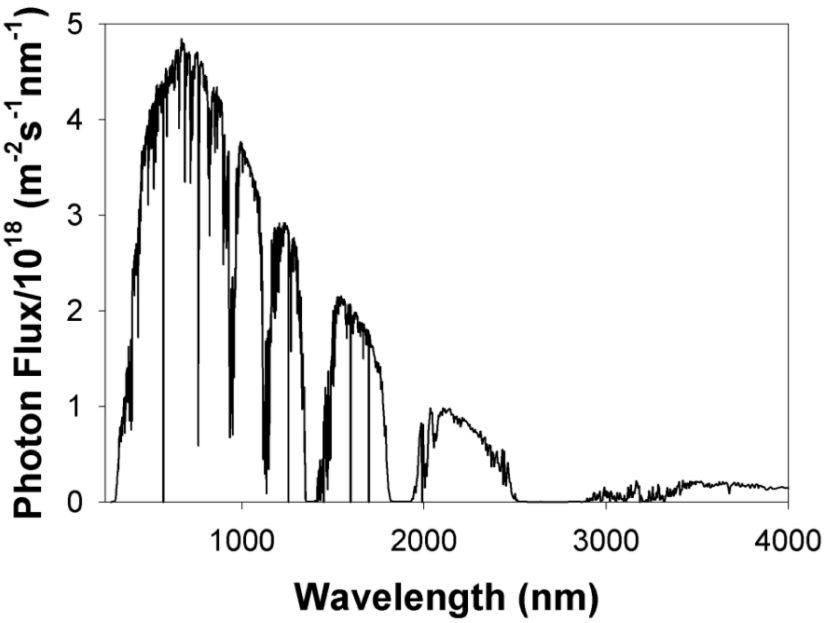

Figure 3.2: AM1.5 standard solar reference spectrum

artificial light sources and the AM1.5 reference spectrum can lead to erroneous efficiency measurements as the photocurrent generated by the photocatalyst material is highly dependent on the spectrum and intensity of the illumination source. Figure 3.3 shows the spectral photon flux for a xenon lamp compared to that of the AM1.5 global solar spectrum. The xenon lamp spectra is also shown for the case where a water filter is used to remove infrared radiation (above around 1000 nm) and UV radiation (below about 250 nm), as was the case in this study. The spectral photon flux of the xenon lamp differs from that of the AM1.5 solar spectrum, and is significantly higher at short wavelengths, particularly when the water filter is used. As a result, the use of a xenon lamp can overestimate the water splitting efficiency. Other types of lamps, such as mercury-xenon lamps have a higher photon flux in the ultraviolet region than the xenon lamp discussed here, leading to a higher overestimate of the efficiency. This effect is largest for wide band-gap semiconductors (such as TiO_2) whose photoresponse is primarily in the UV region. For example the ratio of efficiencies (AM1.5 / Xe lamp, using a water filter) for rutile TiO_2 (E_g = 3.0 eV) is 0.6, whereas the same ratio for α-Fe_2O_3 (E_g = 2.2 eV) is 0.92 (12). The

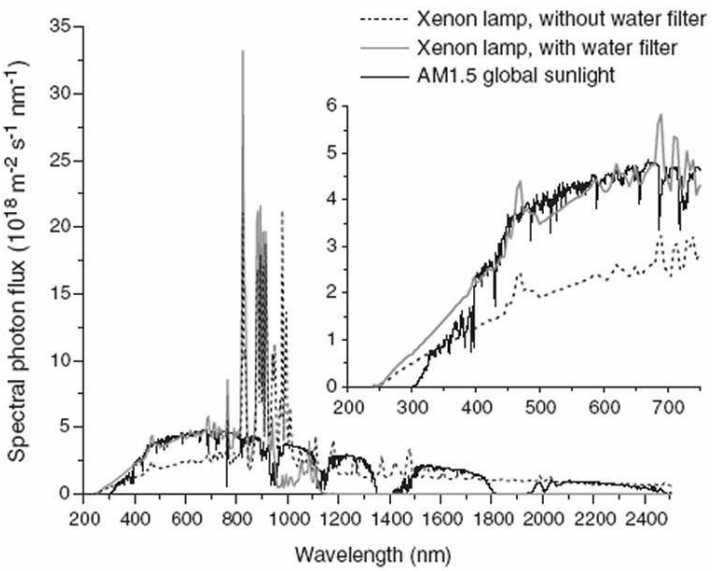

Figure 3.3: Spectral photon flux for a xenon lamp, with and without a water filter, compared to the AM1.5 global solar spectrum. The inset shows detail of the short wavelengths. The total irradiance was normalised to 1000 W $^{-2}$.

spectrum of the illumination source will also change over time. It was observed that the proportion of photon flux in the spectrum decreases as the lamp ages. There are a number of reports in the literature of efficiencies obtained using artificial illumination that are close to, or higher than, the maximum theoretical efficiency possible for the semiconductor (61–63). Losses due to non-ideal absorption, recombination of charge carriers and reflections will significantly reduce the theoretical maximum efficiency and hence such values are obviously incorrect (12).

To obtain a reliable estimate of the water splitting efficiency under AM1.5 conditions, the IPCE (measured at a bias voltage giving maximum efficiency) should be integrated over the AM1.5 standard solar spectrum (12). It should be noted however that some photocatalysts have a non-linear response with light intensity, and hence integrating the IPCE values (measured with low intensity monochromated light) may not give photocurrents representative of those under broad-band illumination.

Chapter 4

Literature

"Give me a firm place to stand and I will move the earth."

Archimedes

Nano-turtle

The pioneering work of Fujishima and Honda in 1972 (64) demonstrated that water splitting was possible by illuminating a titanium dioxide (TiO_2) electrode with sunlight. There exists an enormous body of literature regarding the development of catalyst materials for photoelectrochemical water splitting, reflecting the keen international interest in the topic over the last thirty-five years, prompted in part by the international energy crisis in the 1970s during which much interest was generated in using hydrogen as a fuel source.

The search for the ideal photocatalyst material continues and research has recently been stimulated by the advances in nanotechnology as well as the ever increasing need for a renewable energy source. The vast majority of water splitting publications present research relating to TiO_2, a popular photocatalyst for water splitting, as well as catalysis applications such as water and air purification, remediation of toxic waste and for use as a semiconductor in photovoltaic and photoelectrochemical systems. Although TiO_2 is an excellent catalyst, it will never split water with high efficiency due to its wide band-gap around 3 eV (unless the band-gap can be reduced without introducing trap states), and will not be discussed further here. Water splitting research to date has been summarised in a number of comprehensive reviews over the years including Maruska and Ghosh, 1978 (56), Nozik, 1978 (65), Somorjai *et al.*, 1984 (66), Getoff, 1990 (67), Bard and Fox, 1995 (68), Amouyal, 1995 (69), Bolton, 1996 (10), and Momirlan and Veziroglu, 2002 (8).

The review of the literature presented here is limited to those materials of direct relevance to this thesis: hematite and metal oxide nanostructures. The literature relating to the use of α-Fe_2O_3 for water splitting is discussed, with particular emphasis on the possible rate-limiting steps that prevent α-Fe_2O_3 splitting water with high efficiency. The electrical properties of α-Fe_2O_3 are critical to understanding the conduction mechanisms of this material, hence a significant part of the literature review has been dedicated to this topic. As discussed in Section 2.2, the charge carrier concentrations, mobilities, and diffusion lengths can be derived from measurements of the conductivity. Factors such as diffusion length are directly related to the quantum efficiency of the semiconductor.

An introduction to the crystal structure of α-Fe_2O_3 is presented in Appendix A, as the structure is highly relevant to the measurement of the electrical and magnetic properties. Other related areas of relevance to the conduction mechanisms of α-Fe_2O_3 (such as the anistropy and temperature dependence of the conductivity), are presented in Appendix B, along with tables summarising the results of conductivity measurements of undoped and doped α-Fe_2O_3. It should be noted that conductivity measurements primarily give information about majority carriers, whereas the minority carriers are more important in photoelectrochemical processes.

Finally, the fabrication of nanostructured metal oxides such as ZnO, SnO_2 and indium-tin oxide (ITO) will be discussed. These materials are of interest for use as the nanostructured substrate in the composite electrode structure.

4.1 α-Fe_2O_3

4.1.1 Photoelectrochemistry

The first report of α-Fe_2O_3 being used for photoelectrochemical hydrogen production was by Hardee and Bard in 1976 (70), very soon after the first report of water splitting using TiO_2 (64). The limitations of wide band-gap semiconductors (such as TiO_2) and the instability of materials such as CdS and Si with much narrower band-gaps were already being realised and hematite was being investigated as a non-reactive semiconductor with visible light photoactivity (70). However, it was quickly realised that hematite gave very low photoconversion efficiencies. This was attributed to poor optical absorption (26, 71), rapid electron-hole recombination resulting in short diffusion lengths of charge carriers (26), slow surface reaction kinetics, and unfavourable band-edge positions (27) (meaning an electrical bias is required). Hematite, in various forms, has been extensively studied for water splitting in the last thirty years. The reported water splitting efficiencies for α-Fe_2O_3, however, have not yet come close to the theoretical maximum efficiency for this material of 12.9 % (12). Some increases in the water splitting efficiency of hematite have been achieved through doping and nanostructuring, but even the performance of the current state-of-the-art material (2) is well short of the target of 10 % solar-to-hydrogen conversion efficiency (8).

Doping of α-Fe_2O_3 has been investigated in an attempt to yield a reasonable photoelectrochemical performance. The majority of dopants decrease the photocurrent (72–74). The introduction of group I A or IV B dopants such as Ge, Pb, Sn, Si and Ti produce *n*-type material while group II A, I B or VII B dopants such as Ca, Cu, Mg and Ni produce *p*-type material. Shinar and Kennedy (74) published a good review of doped hematite for water splitting, and presented photoelectrochem-

ical data for sintered polycrystalline α-Fe_2O_3 doped with ZrO_2 (IV B), HfO_2 (IV B), CeO_2, V_2O_5 (V B), Nb_2O_5 (V B), Ta_2O_5 (V B), WO_3 (VI B) and Al_2O_3 (III A), as well as sub-oxide materials.

Of the many dopants introduced into α-Fe_2O_3, Ti (26, 72, 75, 76) and Si (2, 7, 77–79) appear to be the most promising for enhancing the photoelectrochemical response. Jorand Sartoretti *et al.* (72) observed that doping α-Fe_2O_3 with around 5% of titanium produced a four-fold increase in the photocurrent of films prepared by spray pyrolysis. They proposed that this increase in photocurrent was due to improved conductivity of the iron oxide as well as stabilization of oxygen vacancies by the Ti^{4+} ions. The photocatalytic activity of the Ti-doped α-Fe_2O_3 was enhanced by the addition of 1 % Al which was attributed to the formation of Al_2O_3, itself isostructural with hematite and thereby responsible for directing the crystallinity of the films. Early research into doping polycrystalline α-Fe_2O_3 powders with group IV A elements indicated that Si is a better dopant than Ti (a group IV B element) (77, 78). It was suggested that additional energy levels introduced by the Ti metal ion centres may be acting as recombination sites, leading to lower photocurrents (78). The influence of the dopants on carrier mobility remains poorly constrained due to uncertain contributions from grain boundary resistance in polycrystalline specimens (41, 80), difficulties linked to the magnetic susceptibility of α-Fe_2O_3 during Hall measurements (81), and uncertainty in impurity quantity and type (38). The influence of Ti and Si dopants on thin film electrodes (where impurities could also affect film morphology) is even less well understood.

Hematite has been reported to have a very high recombination rate resulting in a diffusion length of holes of only 2 - 4 nm (26). Note that in TiO_2 this value is a few hundred nanometres(12). Itoh and Bockris (28, 30) presented an interesting study discussing the use of stacked thin-film electrodes of α-Fe_2O_3 deposited onto transparent conducting glass. Their hypothesis was that recombination can be reduced by making the α-Fe_2O_3 film thinner than the space-charge layer, thereby enhancing the electric field in the Schottky region and improving charge separation. It should be noted that when films are thinner than the Debye length, there is essentially no electric field in the semiconductor. Their electrodes were stacked one behind

another in order to maximise absorption. The predicted increase in photocurrent with increasing number of electrodes was verified experimentally. Another approach to combating the effect of the short diffusion length of charge carriers is through introducing nanometre-scale structure to a hematite film as a means to improve conversion efficiency. Hematite has been nanostructured to produce well-aligned nanowires by aqueous chemical growth (18, 29) and thermal oxidation of iron foil (82–86), and dendritic nanostructures using atmospheric pressure CVD and spray pyrolysis (2, 7). Nanostructures produced by thermal oxidation of Fe substrates are not ideal for water splitting applications as the metal substrate will corrode in the strong electrolytes used in the photoelectrochemical cell. Beermann *et al.* (29) showed that undoped nanorod arrays of α-Fe_2O_3 exhibit higher photocurrents than nanoparticulate films. This was attributed to better electron transfer as a result of fewer grain boundaries to act as recombination sites for charge carriers. Kay *et al.* (2) and Cesar *et al.* (7) observed high photocurrents from Si-doped dendritic nanostructured films. The formation of nanostructures was attributed to the structure-directing behaviour of the Si dopant, producing a film with preferred crystallographic orientation. It was claimed that the Si also acts as a dopant, increasing the electrical conductivity. However, it was not clear whether doping or nanostructuring is the dominant factor contributing to the observed improvement in photoelectrochemical activity.

It has been suggested that the electrical conductivity of hematite influences the photoelectrochemical performance (2, 7, 72). This is because a substantial potential drop is expected during the transport of photoelectrons through the bulk of the electrode in high resistance materials. High-purity hematite has a very low conductivity ($< 10^{-4}\ \Omega^{-1}\ \mathrm{m}^{-1}$), and doping has been shown to increase the conductivity for single crystal and bulk polycrystalline electrode samples (38, 41, 80, 87–89) (discussed further in Section 4.1.2).

It has been observed by a number of researchers that the shape of the action spectra (IPCE vs. wavelength) for hematite does not match that of the absorption cross-section (26, 29, 73, 90). Beermann *et al.* (29) compared optical and photoelectrochemical data and showed that the absorption extends out beyond 600 nm,

but the IPCE drops away quickly to almost zero beyond 500 nm. It is reasonable to expect that holes generated deep within the semiconductor (from long wavelengths) are lost by recombination before reaching the surface. However, it has been proposed that some of the absorption processes in hematite cannot generate a photocurrent (26, 27, 29), explaining the observed differences in absorption cross-sections and action spectra. Beermann *et al.* suggest that perhaps charge carrier generation is more favourable at the 3.0 eV transition (direct band-gap in α-Fe_2O_3) rather than at the indirect band-gap of 2.2 eV. Kennedy and Fresse (26) calculated an effective absorption coefficient curve from the photocurrent data using the depletion layer theory of Gärtner (49) which was significantly smaller than the measured optical absorption coefficient. It was suggested that there were two charge transfer processes occurring: an $O^{2-} \longrightarrow Fe^{3+}$ transfer that gives rise to reactive holes in the valence band (oxygen sites), and a metal-metal transfer ($2Fe^{3+} \longrightarrow Fe^{2+} + Fe^{4+}$), which produces holes on iron sites. Kennedy and Frese postulated that the Fe^{4+} hole may not be capable of participating in the oxygen evolution reaction. Dare-Edwards *et al.* suggested that this may be due to the energy mismatch between the holes in the Fe d-orbitals and the p-orbitals of the hydroxide (27). As a result of the low transfer rate of the holes to the electrolyte, positive charges build up at the surface, perturbing the space-charge layer and enhancing recombination processes. If the electron on the Fe^{2+} site is also trapped, then no current will flow (26). The surface rate constant for hole transfer has been quoted as 0.1 - 1 cm s^{-1}, a factor of 10^4 lower than for WO_3 and TiO_2 (18). Surface treatment with cobalt (2) and KI (77) have been shown to increase the photocurrent from doped α-Fe_2O_3 films.

Apart from the most recent results reported by Kay *et al.* (2), the IPCE values of nanostructured electrodes reported to date are not substantially better than those previously reported for solid polycrystalline or single crystal specimens (see IPCE data from the literature compiled in Figure 4.1, with corresponding preparation and measurement details shown in Table 4.1). It has been noted that the best performing samples are highly crystalline (72). This brings into focus the question of the relative importance of nanostructuring and morphology versus the modification of the electronic properties by dopants or the catalytic properties of the α-Fe_2O_3

surface. Improved understanding of the role of these factors in hematite photoelectrodes, and identification of the rate-limiting step will be necessary before informed progress can be made.

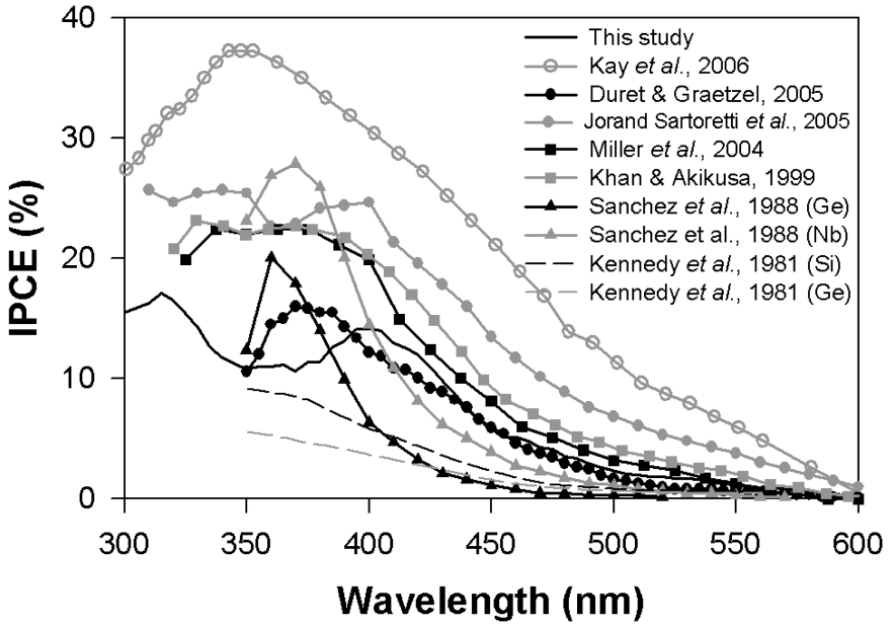

Figure 4.1: Comparison of IPCE values as functions of wavelength as presented in the literature (see Table 4.1 for sample and measurement details).

Author	**Sample**	**Dopant**	**Potential (V/RHE)**
This study (91), 2007	sputtered, polycrystalline film	Ti	1.5
Kay *et al.*, 2006 (2)	ultrasonic spray pyrolysis and CVD, nanostructured	Si	1.23
Duret and Grätzel, 2005 (92)	spray pyrolysis, nanostructured	Si‡	1.23
Jorand Sartoretti *et al.*, 2005 (72)	spray pyrolysis, polycrystalline film	5% Ti, 1% Al	1.47*
Miller *et al.*, 2004 (93)	sputtered, polycrystalline film	-	1.27*
Khan and Akikusa, 1999 (94)	spray pyrolysis, polycrystalline	-	1.67*
Sanchez *et al.*, 1988 (95)	single crystal	Ge, Nb	1.07*
Kennedy *et al.*, 1981 (78)	sintered powder, polycrystalline	Si, Ge	1.28*, 1.23*

Table 4.1: Sample properties and measurement conditions for the literature IPCE data shown in Figure 4.1. Jorand Sartoretti *et al.*, used an electrolyte of 0.1 M NaOH, all others used 1M NaOH. * Potential converted from another reference potential. ‡ Data presented as undoped, reported in a later publication(7) that samples unintentionally doped with Si.

4.1.2 Conduction mechanisms

There have been numerous experimental and theoretical studies of the conduction mechanisms of α-Fe_2O_3 from the early 1950s to today. However, the validity of much of this work has been debated and the conduction mechanisms are still not well understood. It was observed experimentally in the 1950s that α-Fe_2O_3 had quite different conduction behaviour to semiconductors such as silicon and germanium. Morin (96) observed that a much higher doping level (10^{-2} at.% Ti) was required to change the room temperature conductivity of α-Fe_2O_3 compared to a comparable change in Ge (10^{-7} at.% As). The measurement of very low mobility values (inconsistent with other transition metal oxides) and observation that the mobility had an activation energy, led Morin to suggest that conduction in hematite occurs in very narrow (highly localised) energy levels (Fe *d* levels). The density of states in α-Fe_2O_3 has been determined to be around 10^{22} cm^{-3} (approximately equal to N_0, the number of metal ions per cm^3 at room temperature), which is possible only for a system with highly localised energy levels (4).

Hematite (and most transition metal oxides) are often described by the small polaron model of conduction (39, 42–44, 97, 98) as described in Section 2.2. The movement of charge carriers through the hematite lattice is usually considered to be via the Fe sites, where electron transfer is between Fe^{3+} and Fe^{2+} states and hole transfer can be viewed as the Fe^{3+} to Fe^{4+} electron transfer (44). In hematite the localisation of an electron or hole on an iron site changes an Fe^{3+} to an Fe^{2+} or Fe^{4+} respectively resulting in a change in the ionic radius of the iron site (44). In other metal oxides such as TiO_2, the transport of electrons occurs via thermally activated hopping between metal sites, but the hole transfer occurs via the oxygen sites (band mechanism in O 2p band) (99). Morin (96) suggested that the oxygen ions in Fe_2O_3 may be expected to form 2p energy bands, which have a high mobility for holes. Jonker (4) agreed that only a small concentration of holes in the oxygen band would contribute significantly to conduction. However they commented that if there was considerable band conduction then the jump distance a (calculated from Eq. 2.15) should be large; experimental results showed otherwise. Warnes *et al.*

(38) showed that the jump frequencies of a hopping polaron in α-Fe_2O_3 were of similar magnitude to thermal atomic vibrations, suggesting thermal activation of the charge carriers, supporting the small polaron conduction mechanism. The low values of the drift mobility of α-Fe_2O_3 and its exponential increase with temperature have been used as experimental evidence for small-polaron behaviour. Bosman and van Daal (42) comment that such characteristics in the drift mobility can be due to the presence of high-ohmic grain boundary layers (non-homogeneous samples) and as such, the conclusions regarding small-polaron conductivity may be erroneous.

Conductivity experiments

This section summarises relevant experimental results of conductivity measurements (as described in Section 2.2) on hematite samples. There is a large variation in the types of materials used (polycrystalline or single crystal) and the type and quantity of dopant. The results of conductivity measurements are highly sample-dependent, so a consistent description of the properties of hematite is lacking. The experimental results must be considered in the context of the quality of the sample.

There are several factors that complicate the interpretation of results of conductivity measurements. These include the introduction of defects and formation of other phases during heating and cooling, grain boundary effects, the use of inappropriate samples, and the moisture sensitivity of hematite. Another concern with the high temperature techniques is whether the conduction mechanisms deduced from such measurements are representative of the properties of the material at room temperature. The conductivity and Seebeck voltage are highly dependent on impurity type and concentration (80, 89, 96, 100), and so there is little agreement between published values for materials with different purity (38). Further discussion of the conductivity experiments appears in Appendix B.

Conductivity measurements can yield information about both intrinsic and extrinsic conductivity. The conductivity in the high temperature intrinsic region is independent of dopant and impurity concentration as the concentration of thermally generated carriers exceeds that of the donor centres. Further discussion of intrinsic conductivity measurements is included in Appendix B. For photoelectro-

chemical applications, the extrinsic conductivity (of doped α-Fe_2O_3) is primarily of interest and will be presented here.

Jonker (4) compared the conductivity of hematite doped with various transition metals at a level of 2 at.%. The dopant elements with lower values of the fourth ionisation potential (I_4) led to doped α-Fe_2O_3 with lower resistivity values than undoped material. Little change in the resistivity was observed when α-Fe_2O_3 was doped with elements with higher I_4 values. By constructing an electronic energy level diagram it was shown that those elements that reduced the resistivity of hematite had energy levels above the empty Fe^{2+} level. These levels were not considered as donor levels as they cannot trap electrons at low temperatures, and occur at energy differences from the empty level larger than the 0.02 - 0.05 eV commonly seen with transition metal dopants. It was concluded that the donor centres are ions neighbouring the impurity. Ti ions were shown to increase the conductivity of hematite. Given the I_4 values of Si and Ge (45.1 eV and 45.7 eV) these elements would be expected to produce energy levels above the empty Fe^{2+} level and hence increase the conductivity. It should be noted that the Jonker's analysis (4) relies on the ionisation potentials of Sn and V. Values of I_4 for Sn and V of 46.4 eV and 48.0 eV respectively were used. Recent values of I_4 for Sn and V are 40.7 eV and 46.7 eV respectively (101). If the latter value of I_4 for Sn is used, then Si and Ge would not expect to lower the resistivity of hematite.

The effect on the conductivity depends on the type of impurity and the preparation of the sample. Jonker (4) comment that the concentration of impurity ions required to increase the conductivity significantly is large and hence impurities as high as 0.1 % are often of little importance. Morin (96) observed a small change in conductivity with the addition of 0.05 % Ti, while de Cogan and Lonergan (87) observed a much larger increase in conductivity with the addition of only 0.01 % Ti.

Bosman and van Daal (42) provide a good discussion of impurity conduction as a charge transfer mechanism in α-Fe_2O_3. This process occurs when thermally activated electrons hop between neighbouring Fe^{2+} sites (majority centres). An energy difference is present between occupied and neighbouring unoccupied majority centres as a result of locally varying electric fields, produced by neighbouring charged

majority and minority centres (Fe^{4+}). The partial compensation of majority centres by the presence of minority centres is critical to this charge transfer mechanism. The authors note that this process was often neglected in earlier work leading to incorrect interpretation of electrical and magnetic data which is affected by impurity conduction. The effects of impurity conduction on the resistivity of highly doped (2 at.% Ti) hematite samples as a function of temperature have been observed experimentally (42).

Ti-doped (26, 72, 75, 76) and Si-doped (2, 7, 77–79) α-Fe_2O_3 are of interest for water splitting applications and selected studies of the conductivity of such materials will be presented here. Tables summarising the experimental results of these measurements on doped α-Fe_2O_3 are included in Appendix B. There have been several studies of the electrical conductivity of Ti-doped hematite, but none relating to Si-doped hematite. Ge-doped Fe_2O_3 will be considered as an analogue system for Si-doped Fe_2O_3.

Ti-doped α-Fe_2O_3

There have been a number of studies of Ti-doped Fe_2O_3 (38, 42, 80, 87, 89, 96, 98) all showing an increase in the conductivity (reduction in the resistivity) and a decrease in the activation energy for conductivity as a result of doping. A summary of the experimental results of electrical measurements on Ti-doped hematite samples is shown in Table B.2 (Appendix B). Selected studies will be discussed here in detail.

Both Morin (89) and de Cogan and Lonergan (87) produced polycrystalline sintered samples of α-Fe_2O_3 doped with 0 - 1 % Ti (mixtures of powders), fired at 1100 °C. Morin's samples were heated in either an oxygen or a $74N_2$ + $2O_2$ atmosphere, while de Cogan and Lonergan's samples were heated in air. The purity of the α-Fe_2O_3 and TiO_2 powders used by Morin were 99 % and 98.1 % respectively. de Cogan and Lonergan did not quote reagent purity values. Conductivity measurements undertaken by de Cogan and Lonergan were restricted to the low temperature "extrinsic" region (where the effects of the dopants are the strongest) and presented resistivity and activation energy values at 100 °C. Resistivity values from Morin's data at the same temperature have been presented in Table B.2 along

with activation energy values calculated from the published data. The addition of Ti to Fe_2O_3 decreased the measured resistivity and activation energy, which de Cogan and Lonergan attributed to the formation of Ti^{4+} - Fe^{2+} pairs (substitutional doping) as proposed by Jonker (4). The resistivity and activation energy values of Morin's samples (heated in O_2) are much higher than those of de Cogan and Lonergan. The results of de Cogan and Lonergan are closer to those of Morin when the samples were heated in a reducing environment. Comparison of the undoped samples is not meaningful at 100 °C as extrinsic conductivity dominates and the electrical properties are dependent on trace impurities and defects.

Morin (89) initially interpreted the conductivity data for Ti-doped Fe_2O_3 according to the usual band theory of semiconductors. There were several inconsistencies in the analysis, including an unusually low mobility calculated using this theory and the calculated impurity concentration disagreeing with chemical analysis by several orders of magnitude. In a later publication, Morin (96) analysed the data using the model of localised energy levels (Fe *d* levels), which has since been accepted as a good model for describing hematite (4). The carrier concentration and mobility values from this later publication are presented in Table B.2. Values at 400 °C have been presented as data were available for all dopant levels. Doping Fe_2O_3 with Ti resulted in an increase in both the charge carrier concentration and the mobility. At room temperature, a sample doped with 1 at.% Ti had an electron mobility around 10^{-3} $cm^2V^{-1}s^{-1}$ and a carrier concentration around 10^{20} cm^{-3}. Morin suggests that the very low mobility values and apparent activation energy are due to the conduction electrons being confined to the narrow Fe *d* levels.

Velev *et al.* (102) have undertaken a theoretical study of transition-metal-doped hematite. They found that substitutional doping occurs with states produced by the impurities within the band gap of hematite, the position of which determines the electronic and magnetic properties of the doped material. From the density of state data it was concluded that hematite doped with Sc (group III B), Ga (III A), V (V B) and Cr (VI B) remains insulating, Cu (I B) and Zn (II B) doping produces *p*-type material (observed experimentally by Ingler *et al.* (103, 104)), doping with Ti (IV B) produces an *n*-type semiconductor and α-Fe_2O_3 doped with group VII B

elements (Ni, Mn and Co) have potentially both n and p type carriers (though carrier density and hence conductivity are expected to be low). All of the dopants other than Ti and Zn behave as D^{3+} cations which substitute for Fe^{3+}. Ti substitutes as Ti^{4+} and Zn as Zn^{2+}. In the case of Ti-doping, the "extra" electron is localised on an Fe site (Fe^{3+} to Fe^{2+}), appearing as an occupied state below the Fermi level. This electron could be thermally activated into the conduction band. However due to strong localisation, mobility could be low.

Ge-doped α-Fe_2O_3

For the measurements of conductivity Ge-doped α-Fe_2O_3 is considered analogous to Si-doped α-Fe_2O_3 (for which no studies of the conductivity could be located). Table B.3 shows the resistivity data for three studies of Ge-doped Fe_2O_3. In all cases the resistivity of the Fe_2O_3 decreased by at least four orders of magnitude with the addition of 2 % Ge. All of the samples are sintered powders (polycrystalline) except those of Sieber *et al.* which are single crystals. Sanchez *et al.* (105) produced solid solutions of GeO_2 in Fe_2O_3 (up to the solubility limit of 5 mole %, $Fe_{1.95}Ge_{0.05}O_3$) by mechanical mixing of powders and via sol-gel preparation with subsequent firing at 1000 °C. The substitution of Fe by Ge according to the Eq. 4.1 was confirmed by weight loss up to the solubility limit of GeO_2.

$$(1 - x/2)Fe_2O_3 + xGeO_2 \longrightarrow Fe_{2-x}Ge_xO_3 + (x/4)O_2 \tag{4.1}$$

The resistivity of the hematite dropped from 10^6 Ω cm for undoped material to <1 Ω cm at the solubility limit.

Sieber *et al.* (106) produced Ge-substituted Fe_2O_3 single crystals by chemical vapour transport. The exposed crystal plane was primarily the basal plane (001) and both the doped and undoped material exhibited the corundum crystal structure. A drop in the room temperature resistivity from $>10^6$ Ω cm (undoped material) to 5 ± 4 Ω cm (2 mole% Ge-doping) was observed, similar to the results presented by Sanchez *et al.* (105) and Patterson (107). An activation energy of 0.12 eV was calculated from the slope of the log σ vs. 1/T graph. In a later publication (95) a

carrier density of 1.25×10^{17} cm^{-3} was calculated (assuming a room temperature mobility of 0.1 $cm^2 V^{-1} s^{-1}$).

Primary conclusions from the literature review of α-Fe_2O_3

- α-Fe_2O_3 has been extensively investigated for water splitting, but photoconversion efficiencies are still very much lower than theoretically predicted and the rate-limiting step has not been clearly identified.
- Single crystal, polycrystalline and most nanostructured α-Fe_2O_3 samples show similar IPCE values.
- Doping appears to be essential in most cases to achieve reasonable photocurrents.
- The effect of doping is not well understood, and is complicated by some dopants affecting the morphology.
- The roles of doping and (nano)structure need to be separated in order to study the doping mechanism.
- The conduction mechanism in α-Fe_2O_3 is not well understood.
- The conductivity of hematite is highly sensitive to the quality of the sample (impurities, dopant concentration and type), and so the validity of some measurements is questionable.

4.2 Nanostructured substrates

As discussed previously, SnO_2 and doped-ZnO have been selected as materials of interest for use as nanostructured substrates. Relevant literature relating to the fabrication of these (and similar) nanostructured materials is presented here.

4.2.1 SnO_2 and ITO nanostructures

Nanorods and nanowires of tin oxide and ITO have recently been synthesised by various methods. Vayssiéres and Grätzel have recently produced arrays of ordered tin oxide nanorods using an aqueous chemical growth method (108). The nucleation and growth of the tin oxide nanorods from $SnCl_4{\cdot}5H_2O$ is controlled via the thermal decomposition of urea in an aqueous solution. The resulting films show arrays of aligned nanorods with a tetragonal "rutile" structure. These nanorods have a small aspect ratio.

Limmer *et al.* have fabricated arrays of tin oxide nanorods using a templated sol-electrophoresis technique (109–111). Electrophoretic techniques involve the deposition of sol-gel particles from solution via the application of a bias between the conducting substrate to be coated and a counter-electrode. The substrate is precoated with a porous template (polycarbonate or anodic alumina). The charged particles in the solution (in this case tin oxide nanoparticles) are attracted to the templated electrode and are deposited. The template is later removed, leaving an array of nanorods. The quality of the nanostructures is poor as the removal of template allows the rods to bend and break. The lowest resistivity achieved was around 0.01 Ωcm, which is high compared to current transparent conducting oxides. For a 100 nm thick film, a resistivity of 0.01 Ωcm is equivalent to a sheet resistance of approximately 10^3 Ω/square, whereas FTO conducting glass commonly has a sheet resistance of around 14 Ω/square.

ITO nanorod/nanowire powders have also been produced via a hydrothermal method (112). These materials are not tethered to a substrate, but the process may be able to be modified to achieve hydrothermal growth on a substrate (similar to the process of Vayssiéres and Grätzel (108)). Indium oxide (In_2O_3) nanocubes (113)

and ITO (tin-doped indium oxide) nanostructures (112) with a corundum structure have recently been fabricated and may be of particular interest if high aspect ratio features can be achieved.

4.2.2 ZnO and AZO nanowire arrays

ZnO nanowires have been fabricated using solution-based techniques, such as hydrothermal growth (114–122) and electrodeposition (86, 111, 123, 124), vapour-phase transport methods (125–133), and metal-organic chemical vapour deposition (MO-CVD) (134–136), for photovoltaic, opto-electronic, catalysis and biomedical applications. Solution-based techniques such as hydrothermal growth and electrodeposition are low-temperature methods, whereas vapour-phase transport and CVD techniques often require very high temperatures. The fluorine-doped tin oxide (FTO) glass used as a substrate for the composite electrodes cannot be heated above 550 °C, so for this study a low temperature method is required. Therefore the literature presented here will focus on the solution-based methods, in particular the "aqueous chemical growth" (ACG) technique developed by Vayssiéres (137) to produce arrays of well-aligned ZnO nanorods and nanowires.

The ACG technique was developed in order to produce purpose-built nanomaterials by controlling the thermodynamics and kinetics of the hydrothermal growth process (137, 138). The nucleation, growth and ageing processes of the system (which control the size, shape and crystal structure) can be tailored by controlling the interfacial tension. The interfacial tension is minimised by increasing the surface charge density of the system, by having a high ionic strength, and by keeping the solution pH far from the point of zero charge (the pH at which the surface charge density is zero). As a result, highly anisotropic structures such as nanowires are able to be produced. The diameter and length of the structures can be increased by increasing the reactant concentration and the growth time respectively. Vayssiéres *et al.* have used this technique to fabricate various nanostructures including ZnO nanowires (115, 137, 138), ZnO nanorods (116) and ZnO microtubes (139), Fe_2O_3 and Cr_2O_3 nanorods (137, 138), and SnO_2 nanorods (108).

Several research groups worldwide used modified versions of the Vayssiéres technique to produce arrays of well-aligned ZnO nanorods and nanowires (117–122, 140). A common variation from the original process is the application of a layer of ZnO "seed" crystals to the substrate before hydrothermal growth. Many researchers have found this to be a necessary step to producing nanowire arrays with good alignment, narrow diameter distribution, and high rod density (117, 121, 140). This is attributed to the ZnO nanoparticle crystals acting as nucleation sites for the nanorods (121, 140). Seeding is particularly important on polished substrates (such as silicon) where the nucleation density is low (121). The seed solution can be a ZnO sol-gel solution applied to a substrate by spin coating (117), dip coating (120) or electrodeposition (121), or a ZnO precursor, such as zinc acetate, which is thermally decomposed (119) to produce ZnO nano-islands. Guo *et al.* (140) presented a thorough and useful study of the hydrothermal growth conditions including substrate preparation, deposition temperature, precursor concentrations, growth time, and the effect of seed layers. It was shown that the nanoparticulate ZnO seed layer was important to nucleate the nanorod growth. This is in contrast to comments by Vayssiéres *et al.* (116) who claim that the type and crystallinity of the substrate have little effect on the resulting nanorod array. In later publications (137) they do, however, use a ZnO nanostructured thin film as a substrate for nanorod growth, which may be acting as a seeding layer. A further modification to the original process is the introduction of polyethylethenimine to restrict the lateral growth of the nanowires to achieve higher aspect ratio nanowires (119).

Cui and Gibson (121) were able to vastly enhance the nucleation and growth rate of ZnO nanowires via an electrochemical method that required no seeding. By applying a small negative potential up to -1.2 V (relative to a gold reference electrode), the growth rate of the nanowires was increased by 35 times compared to that for unbiased growth. They also observed an increase in the packing density of the nanowires due to enhanced nucleation. Cui and Gibson also demonstrated that metallic dopants (in this case Co) were able to be introduced using this technique, highlighting the possibility of modifying this technique to produce aluminium-doped ZnO (AZO) nanowires.

Aluminium-doped zinc oxide (AZO) is being investigated as a possible alternative to tin oxide- and indium oxide- based transparent conducting oxide materials. A replacement material is being sought due to the rarity (and hence expense) of indium and the toxicity of the indium precursor compounds used (particularly $InCl_3$). AZO thin films have been fabricated by solution-based techniques (141–143), pulsed laser deposition (35, 144), spray pyrolysis (145, 146) and magnetron sputtering (147). Recent developments in AZO film fabrication by pulsed laser deposition have shown resistivities and carrier concentrations comparable to those of ITO (35).

There have been only a few published reports of the fabrication of doped-ZnO nanowires (148, 149) with the study of Cui and Gibson (121) being the only one using low temperature techniques. Hsu *et al.* (148) used a vapour-liquid-solid (VLS) method to produce AZO nanowires on ZnO:Ga/glass substrates. Zinc and aluminium metal powders were heated in a tube furnace in an argon/oxygen atmosphere. An argon plasma was generated by a pulsed high-voltage bias applied to the chamber which bombarded the aluminium source, doping the ZnO nanowires as they grew. The nanowires were grown epitaxially on a gallium-doped ZnO film which was previously deposited by r.f. sputtering onto a glass substrate. The doped and undoped nanowires had a similar morphology: very well aligned and dense with an aspect ratio around 25. However, the AZO nanowires were slightly less regular. The energy-dispersive X-ray spectrum showed around 1 at. % Al, fairly well distributed throughout the rod. He *et al.* (149) produced Ni-doped ZnO nanowire arrays on sapphire substrates. The nanowires were grown using a VLS method and doped with around 6 at.% Ni using a metal vapour vacuum arc ion source doping technique. The electrical conductivity of the doped nanowires was thirty times higher than that of the undoped nanowires.

Chapter 5

Methods

"When I am working on a problem I never think about beauty. I only think about how to solve the problem. But when I have finished, if the solution is not beautiful, I know it is wrong."

B. Fuller

Nano-surfboard

This chapter describes the experimental techniques used to fabricate and characterise the α-Fe_2O_3 films, nanostructured substrates and composite electrodes.

5.1 Sample preparation

5.1.1 Sample substrates

The α-Fe_2O_3 thin films, nanostructured films and composite electrodes were fabricated using fluorine-doped tin oxide (FTO) conducting glass substrates (Pilkington TEC15 borosilicate float glass coated with a conducting FTO thin film, 14 Ω/square). The conducting glass cannot be heated above 550 °C as the conductivity of the FTO can be thermally degraded. However, the FTO is very chemically stable. The glass substrates were cleaned as follows: ultrasonic cleaning in tap water (with a few drops of Teepol detergent); rinsed well in hot water to remove detergent; rinsed in acetone; ethanol and finally de-ionised water; and dried in an air oven at 120 °C.

Substrates other than the FTO conducting glass were required by various characterisation techniques. The optical measurements and some electrical measurements required the use of quartz glass (Electron Microscopy Sciences, 1 mm thick). α-Fe_2O_3 films deposited on Silicon wafers (Silicon Wafer Enterprises N100 test wafer, 1 - 10 Ω/square, 500 $\pm$ 50 μm thick) were used for step-edge profilometry as the Si provides a much flatter uniform surface than the glass substrates. Etched titanium sheet (Aldrich, 99.7 %, 0.25 mm thick, etched in Kroll's solution for 5 s) was used as a substrate for some electrochemical characterisation. Energy-dispersive x-ray spectroscopy (EDS) measurements (Section 5.2.2), required different substrates depending on the element of interest. A substrate without the target element is preferable, for example when determining the doping levels of Si on α-Fe_2O_3, glass or Si substrates cannot be used.

5.1.2 α-Fe_2O_3 thin films

Hematite thin films have been fabricated using various techniques, including wet chemical methods (e.g. sol-gel (150–153), hydrothermal growth (18, 29, 154) and electrodeposition), spray pyrolysis (7, 72), vacuum deposition (e.g. magnetron sputtering (93)), and chemical vapour deposition (CVD) (155).

The type of fabrication process suitable for coating the nanostructured substrates will depend not only on the chemical and thermal stability of the substrate material but also its ability to conformally coat the nanostructures with a thin ($\ll$ 100 nm) film, and its ability to dope the films *in situ*, with ease, safety and efficiency. Due to the temperature restrictions of the conducting glass substrates, any very high temperature processes are unsuitable.

Vacuum deposition was chosen as the technique for depositing the α-Fe_2O_3 thin films. The laboratory where these experiments were performed has excellent facilities for techniques such as filtered arc deposition (FAD) and reactive magnetron sputtering (RMS). Both of these methods use a metallic target as the source of Fe, sputtered in an atmosphere containing oxygen. Unlike wet chemical and spray pyrolysis techniques, no precursor materials are used that may potentially contaminate the iron oxide film. Dopants can be incorporated using an alloyed target or introduced in the gas phase. The disadvantage of using alloyed targets is that dopant concentration cannot be easily changed (as with wet chemical or CVD methods). The sample composition and film thickness are easily controlled using vacuum deposition techniques. Solution-based techniques such as hydrothermal growth and electrodeposition are highly dependent on the kinetics and thermodynamics of the system, which will be changed by the introduction of a dopant phase which may lead to ineffective or inhomogeneous doping. However, it has been suggested that electrochemical deposition may aid the doping process by minimising the energy barriers to dopant incorporation (121). Solution-based techniques may also have the advantage of coating highly nanostructured substrates more easily than vacuum deposition methods.

Filtered arc deposition (FAD)

Filtered arc deposition is a vacuum arc deposition technique used to produce thin films of metals, oxides and nitrides (156–158). A plasma discharge is generated between two electrodes at low pressure ($\sim$ 0.01 Pa). The plasma contacts the cathode in small, high current density spots that move randomly around the cathode surface. The cathode material is evaporated by the "cathode spots" and liberated

from the target surface. The plasma stream is "filtered" to remove micron-sized macro-particles by being passed through a curved duct in the presence of a magnetic field. As a result, only ionic species and small charged particles reach the substrate, producing hard, smooth and dense films. An electrical bias can be applied to the substrate during deposition, which accelerates the ions, and has been shown to alter the crystal phase and crystallographic orientation of the film (156). Materials that are commonly deposited using FAD include carbon, metals such as Ni, Fe, Ti and Co, nitrides such as TiN and CN_x, oxides such as TiO_2 and others such as $AlSiO_x$. No reports of iron oxides produced by this technique have been found.

Thin films of pure and Si-doped α-Fe_2O_3 were deposited by filtered arc deposition. The system used in this study has been described in detail elsewhere (156). The deposition conditions were as follows: 99.9 %-pure iron cathode, arc current of 120 - 140 A, substrate temperature around 200 °C, 0 V applied substrate bias, Ar partial pressure of 3.9 $\times$ 10^{-3} Pa, and O_2 partial pressure of 7.3 $\times$ 10^{-3} Pa. The vacuum system was pumped by an oil diffusion pump with a water-cooled baffle and had a base pressure of 5 $\times$ 10^{-4} Pa. The temperature of the substrates was not measured directly but estimated using a sheathed thermocouple suspended in the chamber at approximately the same distance from the heating coils as the substrate holder. The chamber was left to equilibrate for one hour before deposition. Under these conditions α-Fe_2O_3 films were deposited at a rate of 70 nm/min. Various substrates were used including FTO conducting glass, quartz glass, silicon and etched titanium sheet. Silicon doping was undertaken by introducing 2.5 x 10^{-6} mbar of tetramethylsilane (TMS, $Si(CH_3)_4$) or tetraethoxysilane (TEOS, $Si(C_2H_5O)_4$) into the chamber during deposition. After deposition, all samples were annealed in air at 550 °C for one hour (heated at rate of 10 °C/min from 250 °C, cooled from 550 °C to 200 °C over 1.5 hr), to ensure any organic precursors were completely removed and to enhance the crystallinity of the film.

Figure 5.1 shows photos of the filtered arc deposition system. Figure 5.1 (A) shows the deposition chamber with the sample holder positioned in front of the inlet port for the filtered arc plasma beam. A heater coil is also visible on the left of the image and inlet pipes for gases at the top of the image. Figure 5.1 (B) shows

the iron target (35 mm diameter), the trigger wire used to start the plasma, and the shield to prevent the deposition of material behind the target and confine the arc spots to the front face of the electrodes.

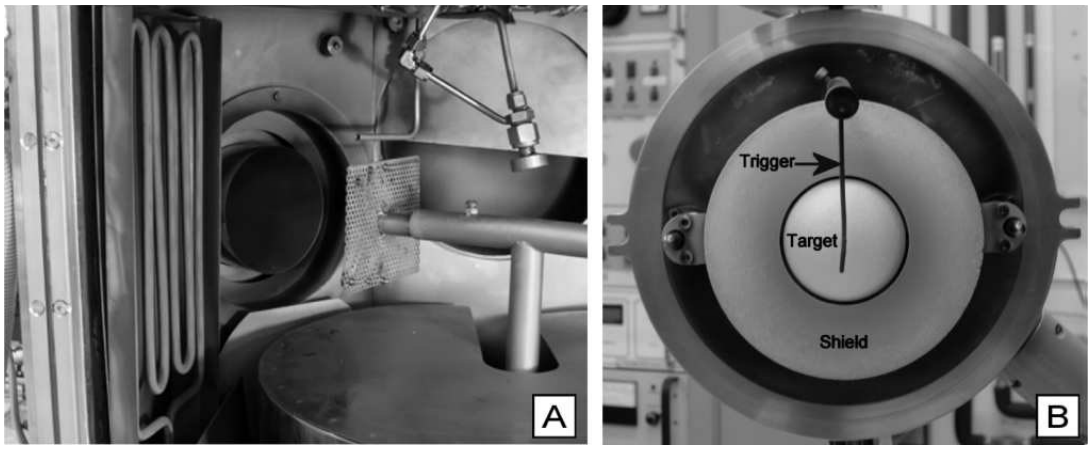

Figure 5.1: Photographs of filtered arc deposition system. (A) Deposition chamber showing the sample holder positioned in front of the inlet port for the filtered arc plasma beam. A heater coil is also visible on the left of the image and inlet pipes for gases at the top of the image. (B) Iron target, trigger wire and shield.

Reactive magnetron sputtering (RMS)

Hematite thin films were deposited using a reactive DC magnetron sputtering system described in detail by Savvides (159). Alloyed sputtering targets were used to incorporate the dopant. As a result, the dopant concentration was not easily varied. The purity and dopant level of the iron targets were selected after considering previous studies of the effects of dopants and impurities on the photoelectrochemical and electrical properties of hematite (4, 73, 78, 89). For depositing pure α-Fe_2O_3, Ti-doped α-Fe_2O_3 and Si-doped α-Fe_2O_3 respectively, the following sputtering targets were used: 99.95 % Fe, Fe with 5 at. % Ti, and transformer steel (Fe with around 5 wt % Si and <1 wt % Al). Oxygen was the major impurity in the 99.95 % Fe target with all other impurities in the parts-per-million range. The presence of around 1 % Al in the transformer iron alloy may be beneficial to the doping process. Jorand Sartoretti *et al.* (72) observed that the addition of 1 % Al to Ti-doped α-Fe_2O_3

improved the photocurrent. They attributed this to Al being a structure-directing agent (Al_2O_3 is isostructural to corundum α-Fe_2O_3) and assisting the incorporation of the dopants.

The deposition of the α-Fe_2O_3 films using the reactive magnetron sputtering system was undertaken in a vacuum chamber evacuated to a base pressure of 10^{-4} Pa. The substrates were heated to 300 °C using a heating coil within the substrate mounting block. The temperature of the substrates was measured using a thermocouple which was embedded in a copper block fixed to the substrate holder. The substrate was held at 300 °C for one hour prior to deposition. The pure and doped iron targets (75 mm diameter) were sputtered in an atmosphere of 1:4 O_2 to Ar mix at a pressure of 1 Pa. The magnetron was operated at a power of 100 W ($\sim$ 330 V and $\sim$ 0.3 A). Under these conditions films were deposited at an average rate of around 200 nm/h (approximately twenty times slower than deposition by the FAD process). Various substrates were used including FTO conducting glass, quartz glass, silicon and etched titanium sheet. After deposition the films were left to cool in the chamber, then annealed under the same conditions as the FAD films. Annealing at lower temperatures had a negative effect on the photocurrent of the α-Fe_2O_3 films. Quenching the films by removing the samples from the furnace at 550 °C to room temperature, produced the same photocurrents as samples cooled slowly.

Various deposition parameters were investigated, including lower oxygen partial pressure (1:9 O_2 to Ar ratio at 1 Pa), lower temperature (higher temperatures were not achievable with the heating system) and lower magnetron power (to reduce the deposition rate). Reducing the oxygen pressure and temperature reduced the photocurrent of the films, while the lower deposition rate did not change the photocurrents. A reduction in deposition rate was investigated, as good photocurrents have been reported for ultrasonic spray pyrolysed α-Fe_2O_3 films deposited at a low deposition rate (<1 nm/min) (7), and our experience that films deposited using filtered arc deposition at high deposition rates (70 nm/min) produced very small photocurrents. It should be noted, however, that the current state-of-the-art films produced by atmospheric CVD were deposited at a deposition rate of 100 nm/min

(2).

Part-way through the study of the RMS α-Fe_2O_3 films, intermittent problems with the film oxidation were encountered. Sometimes, instead of depositing orange transparent α-Fe_2O_3 films, metallic blue or opaque brown/black films were produced. XRD analysis showed that these films were poorly crystallised iron suboxides. After annealing, some of the samples changed to orange-brown films, that showed some photoactivity; these were inferior to those produced using the standard deposition conditions. The source of these problems was extensively investigated. The oxygen and argon gas supplies were checked which involved leak-testing and replacing suspicious valves. The chamber and target were cleaned to ensure that no contaminants were present in the chamber that may be reacting with the oxygen to reduce that available for oxidising the films. Also, the problem occurred when using other targets. The source of the poor oxidation was not identified, so the magnetron sputtering conditions had to be modified. Initially the oxygen partial pressure was increased (up to 1:1 O_2 to Ar ratio) in an attempt to oxidise the films. However, in a high-oxygen atmosphere a surface oxide can form on the metal targets, which makes the plasma less energetic and more unstable. Reproducible sputtering conditions could not be achieved with a high percentage of oxygen in the chamber. Film oxidation was achieved by increasing the total chamber pressure (but leaving the oxygen-to-argon ratio at 1:4). The sections of work affected by this change include, the surface modification experiments (Section 6.1.8), the very thin α-Fe_2O_3 films used for the Schottky barrier modelling (Section 6.1.9), and the α-Fe_2O_3 and ITO films deposited for the composite electrode study (Section 6.3.2). In the case of the surface modification experiments the oxygen partial pressure was increased to give 1:3 oxygen to argon ratio at a pressure of 1.2 Pa. For the very thin α-Fe_2O_3 films used for the Schottky barrier modelling study, and Ti-doped α-Fe_2O_3 and ITO films deposited in the composite electrode study, the chamber pressure was increased (after the gas flows were established) by throttling the turbo pump. The ITO films were deposited using a 1:3 O_2 to Ar gas ratio, throttled to a chamber pressure of 30 Pa. The Ti-doped α-Fe_2O_3 films were deposited using a 1:4 oxygen to argon ratio, throttled to a chamber pressure of 5 Pa. Unless stated otherwise all other conditions

(such as the substrate temperature) remain the same.

5.1.3 Nanostructured electrodes

This Section describes the preparation of two nanostructured materials for use as substrates in the composite electrodes: SnO_2 nanorods; and ZnO (and Al-doped ZnO) nanowires.

SnO_2 nanorods

The published method of Vayssieres and Grätzel (108) was undertaken to produce SnO_2 nanorod arrays. This hydrothermal growth process is very similar to that used to produce the ZnO nanowire arrays. However, the SnO_2 nanostructures do not self-assemble as readily as the ZnO nanowires and are far more sensitive to the preparation conditions.

The recipe as published (108) was 100 ml of aqueous growth solution containing: 0.034 g $SnCl_4{\cdot}5H_2O$, 0.92 g $(NH_2)_2CO$ (urea), and 5 ml fuming (37 %) HCl. Cleaned FTO conducting glass substrates were placed in a sealed glass bottle with the solution and heated in an oven at 95 °C for two days. The resulting films were rinsed in de-ionised water and dried.

The first several experiments failed to produce films with any structure. Although no seeding process was used in the published technique it has been shown for ZnO that such a layer is necessary to enhance the growth of well-ordered nanostructures (as discussed in Chapter 4). As a result, SnO_2 thin films (on FTO) grown from previous attempts were used as substrates to provide a seed layer.

Further modifications were made to the process after consultation with Vayssieres. Much care was taken to ensure reagent concentrations and the solution pH were correct. As $SnCl_4{\cdot}5H_2O$ is a highly hygroscopic material the weighing of small amounts (mg) may have significant error. Therefore, the $SnCl_4{\cdot}5H_2O$ was dessicated in an oven, stored in a dry environment and weighed in a glove-bag under a nitrogen atmosphere to avoid deliquescence. The order of adding the reagents was also changed: rather than adding the solids (urea and tin chloride) to the water and

then adding the HCl, the tin chloride was added last to the pH-adjusted aqueous urea solution. A preparation using 45 mg of $SnCl_4 \cdot 5H_2O$ rather than 34 mg (in case the mass of the $5H_2O$ was not taken into account in the paper) did not greatly affect the nanorod growth. Long growth times (up to several days days) were undertaken in an attempt to increase the aspect ratio of the nanorods.

ZnO and AZO nanowire arrays

Arrays of well-aligned, tethered ZnO nanowires were grown on conducting glass substrates using a two-step process: deposition of a seed layer on clean conducting glass substrates to enhance dense nucleation of the nanowires, followed by hydrothermal growth of the nanowires on the seeded substrates (using the method of Vayssiéres *et al.* (116)).

Two seeding techniques were undertaken: a sol-gel preparation of ZnO nanoparticles, and the thermal decomposition of zinc acetate to produce ZnO nanocrystals (118). Initially ZnO sol-gel solutions were prepared by adding 0.03 M NaOH (dissolved in methanol) drop-wise to 0.01 M zinc acetate dihydrate (dissolved in methanol) (117). Both solutions were kept at 60 °C and the mixture stirred for two hours. The hydrothermal growth solutions (equimolar 0.5 M zinc nitrate and hexamine) (116) were also tried as seed solutions, both in de-ionised water and in ethanol. Thin films of ZnO nanoparticulates were produced by spin-coating, dip-coating or by applying the solution by dropper onto clean conducting glass substrates. Several layers were applied to ensure adequate coverage of the nanoparticles. The substrates were annealed at 150 °C in an air oven between each seed layer application to improve adhesion. A final heat treatment of the resulting films was undertaken at 300 °C in an air oven for 10-15 minutes.

The second seeding technique involved the formation of ZnO seed particles via the thermal decomposition of zinc acetate, as reported by Greene *et al.* (118). A solution of 0.005 M zinc acetate dihydrate in ethanol was applied drop-wise to the clean conducting glass substrates. After ten seconds, the substrate was rinsed with ethanol and dried under nitrogen. The application of the zinc acetate solution was repeated four times and then the substrates were annealed at 350 °C for 20 minutes

to decompose the zinc acetate to produce ZnO nanocrystals. The entire process (four coatings of zinc acetate, followed by annealing) was repeated once to ensure an even coverage of ZnO seeds.

The seeded substrates were sealed in a glass bottle in an aqueous solution of 25 mM zinc nitrate hexahydrate ($Zn(NO_3)_2{\cdot}6H_2O$) and 25 mM hexamine ($C_6H_{12}N_4$), a well-known structure-directing agent (116). A small amount (2.5 mM) of polyethylenimine (PEI), a cationic polyelectrolyte, was added to assist the growth of high aspect ratio nanowires (120). For the preparation of AZO nanowires, $Al(NO_3)_3.9H_2O$ was added to the reagent solution. The bottle was then heated in an oven at 90 °C for up to 24 hr. For long reaction times it was necessary to refresh the solution part-way through to provide additional reagents. The resulting nanowire arrays were rinsed thoroughly in de-ionized water and annealed in air at 300 °C for 30 minutes.

Some electrodeposition experiments were undertaken, following the procedure of Cui and Gibson (121). The precursor chemistry is identical to the Vayssieres technique; but the deposition was undertaken in an open volumetric flask containing the growth solution and heated to 90 °C in a water bath. Once the temperature was stable, a cleaned substrate and a 1 mm gold wire (to act as a counter electrode) were added to the flask. The conducting glass electrode was biased at -1.2 V with respect to the gold wire. A typical reaction time was around 2 hours. The resulting nanowire arrays were rinsed thoroughly in de-ionized water and annealed in air at 300 °C for 30 minutes.

5.1.4 Composite electrodes

The composite nanostructured electrode design was discussed in Section 1.2. The fabrication of such electrodes by depositing α-Fe_2O_3 thin films (using the FAD or RMS processes previously described) on ZnO nanowire substrates is discussed here.

Since there exists a potential energy barrier to electron flow from the α-Fe_2O_3 to the ZnO (Section 1.2), it was hypothesised that the introduction of an interlayer may aid electron removal from the α-Fe_2O_3. Additional experiments were undertaken

to produce a three-layered electrode by depositing an interlayer of indium-tin-oxide (ITO) between the α-Fe_2O_3 film and the ZnO nanowires. An In-Sn target (90:10 In:Sn) was magnetron sputtered, in 1:2.5 O_2 to Ar ratio at a pressure of 5 Pa, to produce ITO films. The chamber temperature was optimised by depositing and characterising planar films. Deposition temperatures between 65 °C and 300 °C were used. The resistance of the ITO films was measured (with two DVM probes across the film about 1 cm apart) as an indicator of the quality of the films. The resistance of films deposited above 100 °C was quite low (< 50 Ω). Higher values (kΩ) were found for the films deposited at lower temperatures. After annealing at 200 °C for 1 h, all samples showed resistances around 30 Ω (similar to the FTO conducting glass substrate). The α-Fe_2O_3 films are routinely annealed at 550 °C, and hence another annealing treatment was undertaken on the ITO films at this temperature. The further annealing reduced the resistivity of the films to under 25 Ω.

5.2 Characterisation techniques

5.2.1 Photoelectrochemical characterisation

The photoelectrochemical (PEC) measurements were performed using a standard three-electrode photoelectrochemical cell, as shown previously in Figure 3.1.

The cell was constructed of Pyrex glass, with a quartz window to allow the incident radiation to enter with minimal attenuation in the ultraviolet. The three electrodes were the working electrode (the photocatalyst sample), a platinum wire counter-electrode, and a saturated calomel (reference) electrode (SCE). The working electrode was typically 1-2 mm from the window. The attenuation of light by the electrolyte and the resistance of the electrolyte were shown to be insignificant as swapping the positions of the working and reference electrodes had a negligible effect on the photocurrent (12). A Utah Electronics Model 0152 potentiostat, or a Radiometer Analytical VoltaLab® PGZ301 potentiostat was used to control the potential difference between the working and reference electrodes. The α-Fe_2O_3

electrodes were typically immersed in 1 M NaOH electrolyte. The concentration was reduced to 0.1 M when analysing the composite electrodes, as the ZnO is unstable in 1 M NaOH. A glass frit separated the counter-electrode from the working and reference electrodes. Absorbed oxygen was purged from the electrolyte in the counter-electrode compartment using a continuous flow of bubbled nitrogen gas as it has been shown that measurements performed in an oxygen-rich electrolyte can lead to erroneously large efficiency values, due to the reduction of oxygen molecules rather than the generation of hydrogen molecules at the counter-electrode (12).

The working electrode was illuminated using an Oriel 6271 ozone-free xenon lamp, fitted with an Oriel 61945 water filter). A total irradiance of 80 mW was used, measured using an Oriel 71751 sapphire window thermopile. The IPCE as a function of wavelength was measured using a monochromated beam from the xenon lamp. The pass-band of the monochromator was 12 nm (FWHM). The irradiance of the light was measured at each wavelength increment using the thermopile.

Photoelectrochemical measurements were undertaken using both electrolyte-electrode (EE) and substrate-electrode (SE) directions of illumination. EE illumination was generally used, unless otherwise stated. Illuminating an electrode from both the EE and SE sides can yield additional information about the film (as discussed in Section 2.4). This concept will be explored in more detail in Section 6.1.9 where the Schottky barrier model is applied to the photoelectrochemical data.

5.2.2 Structural characterisation

X-ray diffraction

X-ray diffraction (XRD) analyses the structure of crystalline materials by exploiting the process of x-ray scattering from crystal planes. In crystalline structures the atoms are arranged in a periodic lattice with planar spacings d. Constructive interference of x-rays of wavelength λ will occur when the Bragg condition is satisfied, Eq. 5.1,

$$n\lambda = 2dsin\theta \tag{5.1}$$

where n is an integer and θ is the angle of incidence. Hence, by scanning a range of angle of incidence, the characteristic d-spacings of the crystal can be identified.

The XRD pattern of a test material can be compared to those in a reference database to identify the component compounds. Reference patterns are generated from powder samples, where all possible crystallographic orientations are present. In the case of thin films, preferred orientation of certain crystallographic planes is common and the XRD pattern will show only some of the peaks evident in the reference pattern. Standard XRD techniques are not sensitive enough to analyse very small amounts of material. So small concentrations of secondary phases (less than a few %) will not be identified and the analysis of thin films ($<$ 100 nm) can be difficult.

Further analysis of XRD patterns can yield much information about the structure of the sample, including the crystal size, amorphous component and degree of stress in the lattice. The Scherrer equation (Eq. 5.2) can be used to calculate the crystal size t,

$$t = \frac{K\lambda}{Bcos\theta_B} \tag{5.2}$$

where λ is the x-ray wavelength (in nm), K is a constant (usually assumed to be 1), B is the full-width-half-maximum (FWHM) value of the diffraction signal (in radians), and θ_B is the angle at which the peak of the signal occurs. The width of the peak can also be dependent on instrumental effects and stress in the film. Highly crystalline materials exhibit sharp peaks, while amorphous materials show very broad features.

In this study, the crystalline structure of the α-Fe_2O_3 films was analysed over an angular range of $2\theta = 10^\circ$ to 80° using a Philips PW 1830 diffractometer (for the FAD samples) and a PANalytical X'Pert PRO 2 diffractometer (for the RMS samples), both with Cu-Kα ($\lambda = 0.1541838$ nm) x-ray sources. The XRD patterns presented in Chapter 6 have had the background (broad amorphous feature from the glass substrate) removed, have been normalised to the major tin oxide peak at $2\theta = 37.8^\circ$, and smoothed using the diffractometer software. The XRD patterns presented for the magnetron sputtered films have also been corrected for x-ray attenuation in

the hematite film, so that the peak intensity for films of different thicknesses can be compared.

Raman spectroscopy

Raman spectroscopy is used to study vibrational modes in a material, via inelastic (Raman) scattering of a laser beam which interacts with phonons in the material. A Raman shift in the energy of the laser photons as a result of this interaction produces a characteristic spectrum for a particular material. Hence Raman spectroscopy can be used to identify compounds.

Raman spectroscopy was undertaken using a Renishaw inVia system. A 514.5 nm laser beam was focused on the sample to give a spot size of approximately 2 μm in diameter. Phase transformations from FeO to Fe_3O_4 (160) and from Fe_3O_4 to α-Fe_2O_3 (161, 162) have been observed in iron oxide films as a result of laser heating at high laser powers. Hence the Raman spectra of the FAD α-Fe_2O_3 films were excited using various laser powers to determine a suitably low power for measurement. Below a power of around 1.4 mW, no change was observed in the spectra. At higher laser powers the Raman peaks broadened and shifted to lower wavenumber values as observed by others (162). A laser power of 1.36 mW was chosen, which was low enough not to degrade the sample. Spectra were excited over a range of wavenumbers 100 - 2000 cm^{-1}. The acquisition time was 10 s and ten measurements were averaged to increase the signal-to-noise ratio.

X-ray photoelectron spectroscopy

The chemical bonding of the deposited films was assessed by X-ray photoelectron spectroscopy (XPS) using a Specs 150 SAGE instrument operated with a Mg Kα X-ray source (the Mg anode operated at 10 keV and 10 mA). The energy scale was referenced to the Ag $4d_{3/2}$ and Au $4f_{7/2}$ peaks from pure elemental reference materials and the binding energies of the photoelectron peaks from the films were referenced to the adventitious C1s peak at 284.6 eV to compensate for any surface charging. No etching was undertaken prior to analysis. XPS investigates chemical

bonding, but is difficult to uniquely identify compounds, for example distinguish between α-Fe_2O_3 and Fe_3O_4. However, it can be a useful technique for identifying the presence of dopants.

Electron microscopy

Scanning electron microscopy (SEM) was undertaken using a high-resolution JEOL 6300 field emission microscope. Energy-dispersive X-ray spectroscopy (EDS) was undertaken using an Oxford Instruments system integrated into a JEOL 5400 scanning electron microscope. EDS is used to identify and quantify elements present in a sample. A nickel reference was used to calibrate the EDS quantification analysis program.

Focused ion beam milling and high-resolution SEM were undertaken using a dual-beam FEI Nova microscope equipped with a scanning electron microscope and Ga ion source for milling. The high energy gallium beam can be used to mill a trench at an angle of 52° to the vertical and the film cross-section can be imaged using the electron beam.

Profilometry

The thickness of planar thin films was measured using a Sloane Instruments Dektak 3030 surface profilometer. This is a surface contact technique in which a small stylus is moved across the sample and changes in height are detected. A clean film edge and a flat substrate are required in order obtain an accurate measurement of the step height. A step in the films was produced by masking a section of the substrate before deposition, either by covering with aluminium foil or by applying ink dots that can later be removed with solvent. Applying ink dots is a preferable technique, however thicker films (*e.g.* of α-Fe_2O_3) can prevent the ink from being removed.

Micro-indentation

The hardness of the films was measured using a CSIRO UMIS 2000 ultramicroindentation system (163), fitted with a diamond Berkovich indenter. Tests over a load

range of 1 mN to 10 mN suggested an optimum indentation load of 3 mN. At this load, the penetration depth did not exceed 10 % of the film thickness (to minimise the effect of the substrate) so that the hardness of the film was measured.

AFM

Surface roughness measurements were undertaken using an atomic force microscope (Autoprobe M5 AFM, Park Scientific Instruments) fitted with a boron-doped silicon probe of tip radius 10 nm operated in contact mode. The root-mean-square roughness was calculated over regions of α-Fe_2O_3 film (deposited on silicon) of dimensions between 7 μm ^{2} and 25 μm ^{2}, avoiding pinholes and dust particles on the surface. The influence of measurement noise and the roughness of the silicon wafer substrate were removed from the measured roughness ($r_{measured}$) using the relation $r_{film} = (r^2_{measured} - r^2_{substrate})^{1/2}$ assuming that the roughness of the substrate ($r_{substrate}$) and that of the deposited film (r_{film}) are uncorrelated. Large scale roughness of the substrate is likely to be correlated with that of the film, however this correction is valid for small measurement areas as used.

Density measurements

In order to determine the density of selected hematite thin films, the masses and film thicknesses of the films were carefully determined. Gravimetry experiments were undertaken by weighing the glass substrates before and after both film deposition and annealing. Weighing was undertaken using a Sartorius 30 g single-pan balance with a stated standard deviation of 2.4 μg. The back and sides of the substrates were masked with aluminium foil prior to deposition to ensure that only the front faces of the substrates were coated. The mass of the glass substrate, which was typically 2.5 g, was measured with an uncertainty of 4 - 5 μg. For a 1 μm coating, the change in mass was typically 1 mg, and this was determined with an uncertainty of 6 - 7 μg, or less than 1%. A control sample was included throughout the process (fully masked during deposition) to ensure that the heating during deposition and annealing did not change the mass of the substrate. The optical thickness was determined from

transmittance and reflectance measurements (described in the next section), and compared to results from profilometry and SEM of film cross-sections.

5.2.3 Optical characterisation

Direct transmittance (T) and total (diffuse plus specular) reflectance (R) measurements were made over a wavelength range of 250 - 2000 nm using a Cary 5 spectrophotometer. Reflectance measurements were calibrated using gold and silicon reference surfaces. Infrared spectroscopy was undertaken using a Digilab FTS40 FTIR spectrometer operated at 4 cm^{-1} resolution, over a wavenumber range of 500 - 5500 cm^{-1}. To determine the refractive index n, extinction coefficient κ and film thickness, a Cauchy model (164) was fitted to the spectrophotometer and FTIR data at wavelengths exceeding the band-gap value using WVASE software (WVASE32 TM, J.A. Woollam Co. Inc.) Additionally, the optical constants were calculated explicitly using the formulation of Szczyrbowski (165). This approach considers a slightly rough film on a transparent substrate polished on both sides with known optical constants and includes the effects of thin-film interference and multiple reflections. Szczyrbowski calculated a number of parameters in addition to n and κ, such as film thickness, roughness and variation in thickness, by minimizing the expression over the whole measured absolute reflectance and transmittance wavelength range. In contrast, we solved explicitly (using a numerical solver developed by P.R.F. Barnes) for n and κ at each measured wavelength given the film thickness (from WVASE), the measured surface roughness, and the measured reflectance and transmittance of the films on quartz slides. The optical constants at more strongly absorbing wavelengths were thus determined. The absorption coefficient α was calculated from the extinction coefficient using Eq. 5.3.

$$\alpha = \frac{4\pi\kappa}{\lambda} \tag{5.3}$$

The band-gap energy of a semiconductor can be estimated from the measured absorption coefficient using the Tauc relationship (166–168). This relationship assumes that the conduction and valence band edges are parabolic functions of crystal

momentum and thus is only valid for photon energies exceeding the band-gap where this approximation holds. There is a discrepancy in the literature over the appropriate form of the Tauc relationship. For example, Davids and Mott (166) and Moss (167) who reference the work of Hall *et al.* (168) use the general relationship shown in Eq. 5.4,

$$\alpha = [A(h\nu - E_g)^m]/(h\nu) \tag{5.4}$$

where A is a constant related to the density of electronic states above and below the band-gap, $h\nu$ is the absorbed photon energy, and E_g is the optical band-gap relating to direct allowed transitions ($m = 1/2$) or indirect phonon-assisted transitions ($m = 2$). However, an alternative expression is presented by Pankove (169) (who also references the work of Hall *et al.*) in Eq. 5.5.

$$\alpha = A(h\nu - E_g)^m \tag{5.5}$$

Both forms of the expression appear to be widely used in the literature, and in practice the choice does not have a large influence on the optical band-gap value derived. We use the former expression to estimate the optical band-gap for both indirect and direct transitions. The Tauc relationship can also be applied to photoelectrochemical data by replacing the absorption coefficient with IPCE(λ). This is valid because the IPCE is proportional to the absorption coefficient, in the limit that collection of charge is from a column in which attenuation of the incident radiation is negligible.

5.2.4 Electrical characterisation

Electrical measurements were undertaken on FAD and RMS α-Fe_2O_3 thin films deposited onto specially prepared substrates, as shown in Figure 5.2 (A) and (B) respectively. For analysis of the FAD α-Fe_2O_3 films, a shallow cross was cut through the FTO film of the conducting glass using a diamond saw to create four isolated pads of conducting film. For analysis of the RMS films the conducting glass was prepared slightly differently; a strip of the FTO film around 4 mm wide was removed from the centre of the conducting glass substrate (40 mm × 10 mm) by etching with

Zn powder and fuming (37 %) hydrochloric acid to create two isolated pads of conducting film each about 18 mm × 10 mm. Removing the FTO by etching is thought to be preferable to sawing the substrate, as a cleaner edge is produced, reducing the stress on the film at the step-edge. The substrates were masked at both ends before deposition (to leave areas clear for making contacts), resulting in a central pad of α-Fe_2O_3 film. Metal clips were used to make contact with the conducting glass.

Lateral conductivity measurements were undertaken with the FAD α-Fe_2O_3 films in air (50 % humidity at 294 K) as a function of temperature between 294 K and 421 K by measuring the current due to an applied potential difference between sets of co-planar FTO contacts. Similar measurements were undertaken with the RMS α-Fe_2O_3 films in air and argon gas over a temperature range of 294 K - 460 K.

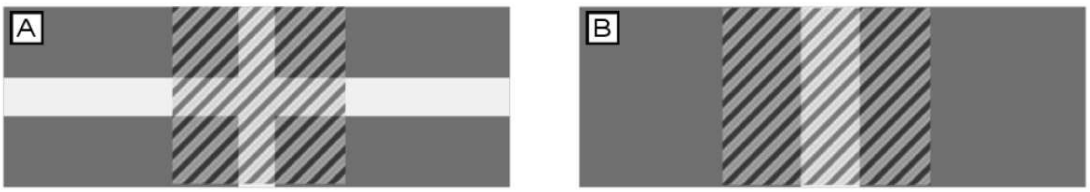

Figure 5.2: Schematic diagrams of the substrates used for the electrical measurements of (A) the FAD α-Fe_2O_3 films and (B) the RMS α-Fe_2O_3 films. The dark-grey area is the conducting glass substrate, the light-grey region is where the FTO has been removed, and the hatched area represents the α-Fe_2O_3 film.

The dielectric properties of the material were determined by evaporating a silver contact (3 mm in diameter) onto the upper surface of an FAD α-Fe_2O_3 film on an FTO substrate. The impedance of the resulting device was measured as a function of frequency and the bias voltage applied between the silver contact and the FTO substrate, using a potentiostat (Radio Analytical VoltaLab® PGZ 301) at 294 K. The measurements were corrected for both the presence of pinholes in the film and the series resistance of the conducting glass substrate using current-voltage scans (170).

Electrochemical impedance spectroscopy measurements were made using a potentiostat (Radiometer Analytical VoltaLab® PGZ 301) in the photoelectrochemical cell described previously, by sweeping both the working electrode potential (d.c. potential, 100 mV steps) and the signal frequency (100 kHz - 2.5 Hz, amplitude 10 mV). Data from the high frequency ranges (where the influence of the Helmholtz layer and surface states can be neglected (171)) were used to determine the capacitance of the space charge layer, C, at the semiconductor-electrolyte interface by fitting a simple series/parallel equivalent circuit (as shown in Figure 5.3) to the impedance values using a nonlinear least-squares routine.

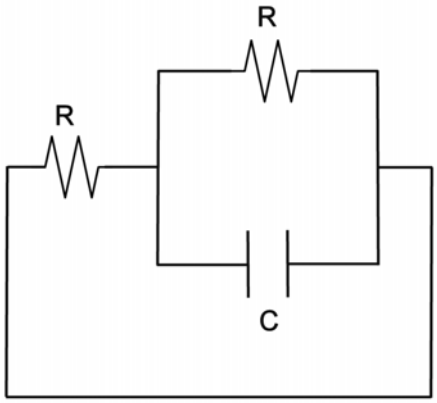

Figure 5.3: Series/parallel equivalent circuit used to model the impedance spectroscopy data.

The cell impedance Z in the chosen frequency range was modeled according to Eq. 5.6 at each applied potential, where R_s is the series resistance of the cell, R_p the resistance of the space charge layer (assumed to be in parallel to the space charge layer capacitance C), and ω is the angular frequency of the measurement.

$$\mathrm{Z} = \mathrm{R_s} + (\mathrm{i}\omega\mathrm{C} + \mathrm{R_p^{-1}})^{-1} \tag{5.6}$$

The values of C(V) were then used to determine the flatband potential, V_{fb}, and the conduction electron concentration, N_D, of the α-Fe_2O_3 of the films using the Mott-Schottky relationship (Eq. 2.19), where the dielectric constant of hematite ϵ_r was taken as 24 (27). The uncertainty range on these measurements was estimated

by calculating the spread of N_D and V_{fb} values determined from single-frequency capacitances with Mott-Schottky plots within the fitted frequency range. We note that values determined at lower frequencies than the fitting range yielded substantially higher N_D values and more positive V_{fb} values as the capacitance increased, probably due to surface states.

Models of the lower frequency impedance of semiconductor electrodes can be extremely complicated, incorporating an array of circuit elements (172, 173). In an effort to determine the approximate concentration of surface states per unit potential, N_{ss}, and the time constant, τ, for emission and capture of electrons by the states, we made the simple assumption that the frequency-dependent residual capacitance (Eq. 5.7) could be attributed predominantly to part of a continuum of electronic surface states at V within the band-gap (6), where C is the high-frequency component of the capacitance.

$$\mathrm{C_{ss}}(\omega) = \mathrm{C}(\omega) - \mathrm{C} \tag{5.7}$$

We fitted the residual capacitance due to states according to Eq. 5.8 at each measured potential (174) where the states become "frozen out" at high frequencies since τ is inversely proportional to the thermal velocity of electrons and the trap cross-section.

$$\mathrm{C_{ss}}(\omega) = (\frac{\mathrm{N_{ss}e^2}}{\omega\tau})\mathrm{arctan}(\omega\tau) \tag{5.8}$$

Chapter 6

Results and discussion

"There is nothing like looking, if you want to find something. You certainly usually find something, if you look, but it is not always quite the something you were after."

J.R.R. Tolkien

Nano-heart

The results of the fabrication and characterisation experiments outlined in Chapter 5 are presented and discussed here. This Chapter is separated into three sections, relating to the α-Fe_2O_3 thin films, the nanostructured substrates, and the composite electrodes.

6.1 α-Fe_2O_3 thin films

This section presents the results of photoelectrochemical, optical, structural and electrical characterisation of the α-Fe_2O_3 films fabricated using filtered arc deposition (FAD) and reactive magnetron sputtering (RMS). This research forms the basis of two journal publications, one relating to the FAD α-Fe_2O_3 films (175) and the other to the reactive magnetron sputtered α-Fe_2O_3 films (91). The results of modelling the IPCE of Ti-doped RMS α-Fe_2O_3 films using the Schottky barrier model described in Section 2.4 will also be presented. An additional discussion section is included to further analyse significant findings from this study.

6.1.1 Photoelectrochemical properties

The characterisation of the photoelectrochemical properties of the α-Fe_2O_3 films is critical as they will determine how effectively the material will split water. The doped and undoped α-Fe_2O_3 films fabricated using filtered arc deposition did not show significant photocurrents, and so the results presented here are limited to those of the magnetron sputtered films.

The dependence of the photocurrent on the film thickness was tested by depositing RMS α-Fe_2O_3 films of various thickness. Figure 6.1 shows the measured photocurrent as a function of film thickness for the Si-doped and Ti-doped α-Fe_2O_3 films. The electrochemical measurements were undertaken at 0.2 V vs. SCE, in 1M NaOH electrolyte, with an illuminated area of 0.5 cm^2. The photocurrent is independent of the film thickness, over the thickness range measured. Ti-doped RMS α-Fe_2O_3 films deposited at higher oxygen partial pressure and higher total chamber pressure showed an increasing photocurrent with increasing film thickness, up to a thickness of around 100 nm (Figure 6.2). It is likely that a thickness-dependent photocurrent would be observed for very thin films deposited under the standard conditions, however no films $<$ 100 nm in thickness were deposited.

The photoelectrochemical performance of the doped and undoped RMS α-Fe_2O_3 films was quantified by measuring the photocurrent density as a function of voltage vs. the SCE reference electrode, as shown in Figure 6.3 (A). The undoped hematite

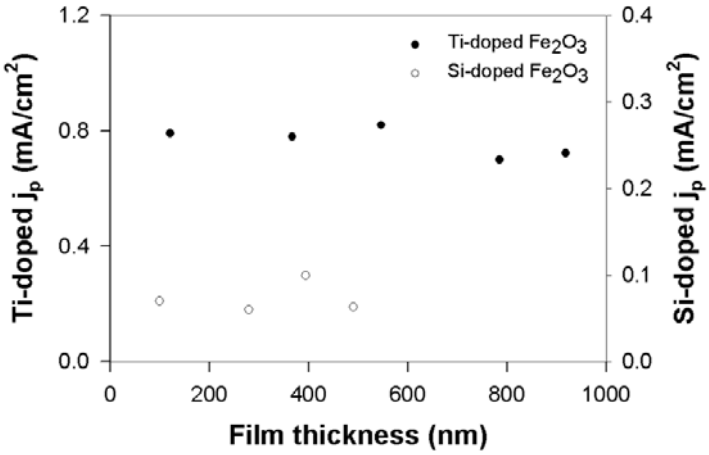

Figure 6.1: Photocurrent density j_p of doped α-Fe_2O_3 films as a function of film thickness at a potential of 0.5 V vs. SCE, in 1M NaOH.

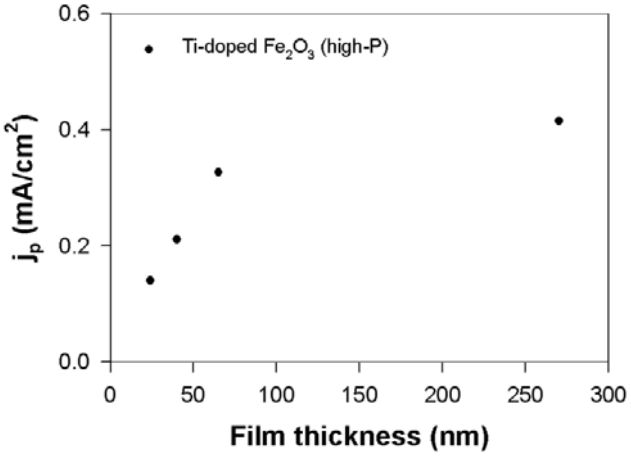

Figure 6.2: Photocurrent density j_p of Ti-doped α-Fe_2O_3 films deposited at high pressure as a function of film thickness at a potential of 0.2 V vs. SCE, in 1M NaOH

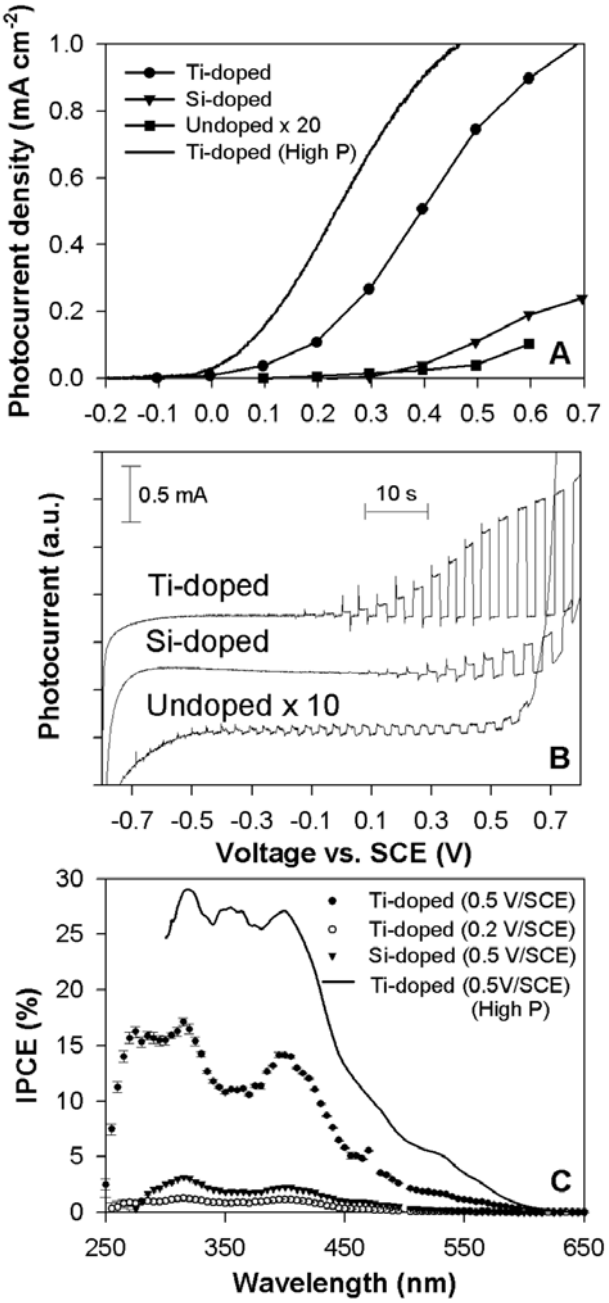

Figure 6.3: (A) Steady-state photocurrent density. (B) Chopped light potential sweep (+20 mV/s) showing transient current relaxation of the doped and undoped α-Fe_2O_3 films as a function of voltage (V vs. SCE), where the traces have been displaced for clarity. (C) IPCE as a function of wavelength of the doped α-Fe_2O_3 films at 0.5 V and 0.2 V vs. SCE. Measurements undertaken in 1 M NaOH.

shows a very small photocurrent ($< 1\ \mu\text{Acm}^{-2}$ at 0.2 V vs. SCE), with a steady state onset potential of 0.1 V vs. SCE. The doped films exhibit enhanced photocurrents compared to the undoped material, with the Ti-doped α-Fe_2O_3 having the highest photocatalytic activity. Ti-doping resulted in a significant shift of the steady state onset potential to lower voltages (-0.15 V vs. SCE), while Si-doping increased the onset potential to 0.2 V vs. SCE. Our RMS α-Fe_2O_3 films exhibit onset potentials similar to those of polycrystalline films (doped and undoped) presented in the literature (2, 92, 94). Doped single crystal α-Fe_2O_3 samples (95, 106) showed much lower onset potentials, around -0.5 V/SCE (at a pH of 14), than polycrystalline films. This may indicate differences in surface recombination rates (27) as discussed later.

A film deposited in a 1:4 oxygen to argon gas mix at a chamber pressure of 5 Pa is also shown ("Ti-doped α-Fe_2O_3 (High P)"), which has a photocurrent 1.7 times higher than that of the Ti-doped film (at an applied voltage of 0.2 V) deposited under standard conditions (1:4 oxygen to argon gas ratio at a pressure of 1 Pa). Films deposited at lower oxygen pressure (1:9 oxygen to argon gas ratio at a pressure of 1 Pa) showed less than 5% of the photocurrent (results not shown) of those deposited under standard conditions.

A reduction in deposition rate using the RMS process was investigated as good photocurrents have been reported for ultrasonic spray pyrolyzed α-Fe_2O_3 films deposited at a low deposition rate (<1 nm/min) (7), and given that the FAD films deposited at high deposition rates (70 nm/min) produced very small photocurrents. It should be noted, however, that the current state-of-the-art films produced by atmospheric CVD were deposited at a deposition rate of 100 nm/min (2). The RMS deposition rate scales approximately linearly with power, so a set of films was prepared at half of the standard power setting of the magnetron (*i.e.*, at approximately half the deposition rate). The photocurrents generated by the Si-doped and Ti-doped α-Fe_2O_3 films deposited at half the magnetron power (lower deposition rate) did not show a significant change in photocurrent or onset potential relative to films of similar thickness deposited at the higher deposition rate.

Potential sweeps of the electrodes under chopped illumination are shown in Fig-

ure 6.3 (B), where the traces have been displaced for clarity. All films showed transients (high frequency oscillations as a result of chopping the light source) in the photocurrent, though these were small in the case of the undoped α-Fe_2O_3. The relaxation of the transient photocurrents for the electrodes were analysed at a number of fixed potentials, and were found to be composed of two relaxation processes, τ_1 and τ_2, (as shown in Table 6.2). The transient photocurrents (not shown) from which the time constants were calculated, were measured at a single potential for around 30 s following the cut-off of the radiation. The two time constants were determined by first fitting one exponential curve to the tail of the decay, subtracting this component, and then fitting the second additional exponential term to the beginning of the decay. The faster process had mean time constants of 0.20 $\pm$ 0.09 s and 0.11 $\pm$ 0.03 s for the Ti-doped and Si-doped films respectively and a slightly slower process (considering the large uncertainty) of 0.3 $\pm$ 0.2 s for the undoped film. The photocurrents also displayed a second, slower relaxation with a time constant of approximately 3 s for the doped films and around 6 s for the undoped film. The chopped sweeps in Figure 6.3 (B) were also used to determine the transient photocurrent onset potential which is thought to be closely related to the flat-band potential of the electrode (27). As listed in Table 6.2 these values are -0.7, -0.1 and -0.25 V vs. SCE for the undoped, Si-doped and Ti-doped hematite films respectively. Surprisingly the undoped sample showed the most negative measurable transient onset.

Action spectra (IPCE as a function of wavelength) of the doped films, measured at potentials of 0.2 and 0.5 V vs. SCE are shown in Figure 6.3 (C). The undoped film had a negligible response at these potentials and is not shown. The Ti-doped film has a substantially higher response than the Si-doped film at all wavelengths. The drop-off in the IPCE at short wavelengths has been observed previously for hematite (see Figure 4.1) and other materials such as TiO_2 (176). Wilson (47) suggests that this may be due to hot electron processes, recombination of charge carriers in the depletion layer, or changes in the absorption coefficient. The IPCE values of the magnetron sputtered films are broadly similar to those presented by others (see Figure 4.1), however, due to the high onset potentials of our films, a more

positive bias voltage is required (which will limit the photo-conversion efficiency).

Integrating the product of the IPCE, the photon flux of an illuminating spectrum, and the electronic charge over wavelength yields the expected photocurrent density generated by the film in broadband illumination if the photo-response is assumed linear with intensity. This photocurrent density can be compared with direct measurement under broadband illumination. At 0.5 V vs. SCE the integrated photocurrent for the xenon lamp photon flux spectrum yields 0.62 $\mathrm{mAcm^{-2}}$ for the Ti-doped sample shown in Figure 6.3 (C), which is slightly lower than the directly measured 0.75 $\mathrm{mAcm^{-2}}$ at this potential. The discrepancy could be linked to variation in the lamp spectra with time or non-linearity of the electrode photo-response at low intensities (as discussed in Chapter 3). Similarly the Si-doped sample yields an integrated photocurrent of 0.10 $\mathrm{mAcm^{-2}}$ in reasonable agreement with the directly measured value of 0.11 $\mathrm{mAcm^{-2}}$. Performing the same integration using the solar AM 1.5 photon flux spectrum gives photocurrents of 0.57 $\mathrm{mAcm^{-2}}$ and 0.10 $\mathrm{mAcm^{-2}}$ for the Ti- and Si-doped electrodes respectively at 0.5 V vs. SCE, and a photocurrent density of only 0.04 $\mathrm{mAcm^{-2}}$ for the Ti doped film at 0.2 V vs. SCE.

In order to investigate the differences in the photoelectrochemical performance between the FAD α-Fe_2O_3 films and the doped and undoped magnetron sputtered α-Fe_2O_3 films, characterisation of the structural, optical, and electrical properties was undertaken. The results of these experiments follow. Some of the characterisation techniques required the hematite films to be deposited onto substrates other than conducting glass, as described in Section 5.1.1. A potential problem with the use of various substrates is that the properties of the α-Fe_2O_3 film (in particular, the crystallographic orientation) may differ. Differences in XRD relative peak heights were observed for hematite films deposited onto conducting glass, silicon and silica substrates, consistent with small changes in crystallographic orientation. Therefore the results of the optical and electrical measurements reported below may not be truly representative of the material deposited on the conducting glass (used for the photoelectrochemical characterisation).

6.1.2 Dopant levels

The dopant levels of the hematite films were determined by EDS, where the dopant was quantified as an elemental percentage relative to iron. The Ti-doped and Si-doped RMS α-Fe_2O_3 films contained 5.0 ± 0.3 % Ti, and 5.3 ± 0.3 % Si respectively, which is in agreement with the composition of the targets, indicating that no significant preferential sputtering occurred. The Si-doped FAD α-Fe_2O_3 films (doped using tetramethoxysilane) had a dopant level of 0.5 % $\pm$ 0.08 % Si. Various concentrations of Si-dopant from < 2 % (2, 78) up to 10% (79) have been incorporated into hematite. Ti-doped α-Fe_2O_3 has been widely investigated (26, 72, 73, 76, 78), and dopant levels ranging from 0.05 % to 5 % have been used. As discussed in Section 5.1.2 the dopant levels for the RMS α-Fe_2O_3 films were selected from optimum compositions reported in the literature. A study of the dependence of the photoelectrochemical performance on doping levels was not undertaken as it would be unlikely to offer substantial insight beyond that already available from previous studies.

6.1.3 Morphology

Properties of the hematite thin films such as the microstructure and roughness are described here, and are of relevance as they can affect the interaction between the films and the electrolyte. The hematite thin films deposited using the FAD and RMS techniques ranged in color from orange to deep red, depending on the thickness of the film. The films were transparent, uniform and adhered strongly to all substrates used. The RMS Ti-doped α-Fe_2O_3 films deposited on silicon substrates exhibited some minor crazing. The films deposited using RMS at lower oxygen partial pressure (0.1 Pa O_2) were dark blue and reflective, but changed to orange-red after annealing.

The film thicknesses of the magnetron sputtered α-Fe_2O_3 films were found to have a linear relationship with deposition time (as shown in Figure 6.4). The undoped and doped hematite were deposited at rates of 3.7 nm/min and 3.1 nm/min respectively (under the conditions of 1:4 O_2 to Ar ratio at a pressure of 1 Pa). A slightly lower deposition rate of 2.8 nm/min was observed for films deposited at a

higher pressure (1:4 O_2 to Ar gas mix at a total chamber pressure of 5 Pa). The FAD process deposited films at a much higher rate of 70 nm/min.

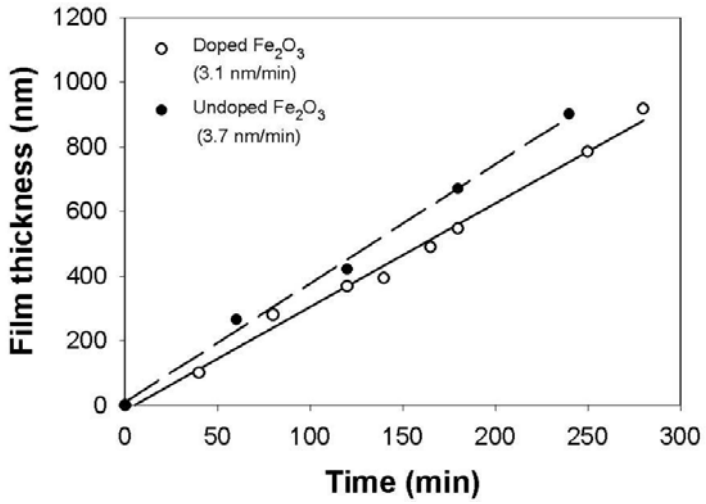

Figure 6.4: Film thickness of magnetron sputtered doped and undoped α-Fe_2O_3 films deposited under standard conditions as a function of deposition time.

Figure 6.5 shows SEM images of two FAD α-Fe_2O_3 films deposited on Si, with thicknesses of 1500 nm (A) and 130 nm (B) along with a cross-sectional image of a typical film (C) deposited on FTO conducting glass. The films are relatively smooth with little microstructure. The morphologies of the undoped and Si-doped FAD α-Fe_2O_3 films are shown in Figure 6.6 (A) and (B) respectively. The films are similar in appearance, but the grain size of the Si-doped α-Fe_2O_3 appears to be smaller than that of the undoped material.

Figure 6.7 shows SEM images of the surface microstructure of an FTO conducting glass substrate (A), and an undoped (B), Ti-doped (C) and Si-doped (D) α-Fe_2O_3 film deposited using RMS along with their respective cross-sections (E, F, G, and H). In the cross-sectional images of the magnetron sputtered films three layers are visible. The top layer is the α-Fe_2O_3 film, the middle layer is the FTO and the bottom layer is the glass substrate. Figure 6.7 (E), showing the cross-section of the bare FTO substrate, has only the glass and FTO layers.

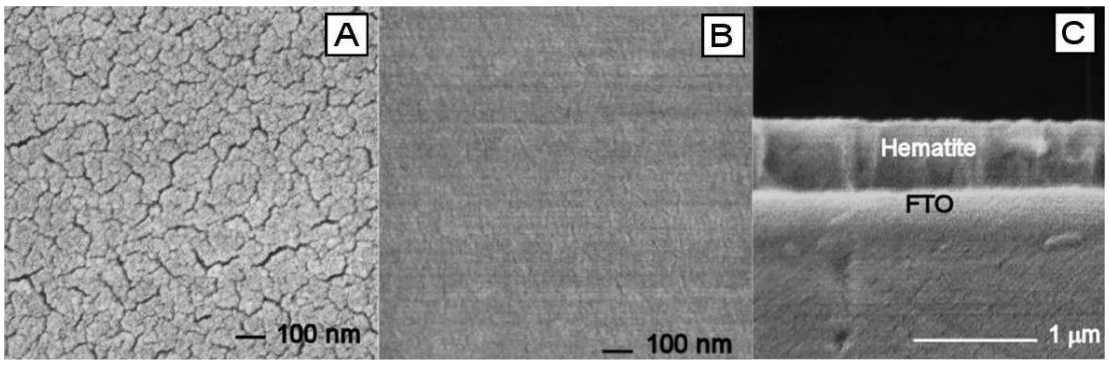

Figure 6.5: SEM images of (A) 1500 nm, and (B) 130 nm thick FAD α-Fe_2O_3 films deposited on silicon. (C) Cross-section of a typical film deposited on FTO conducting glass substrates.

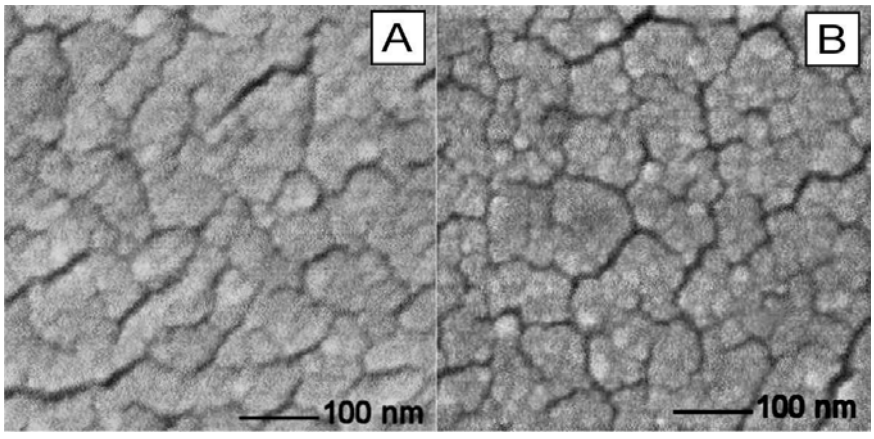

Figure 6.6: SEM images of (A) an undoped and (B) a Si-doped FAD α-Fe_2O_3 film.

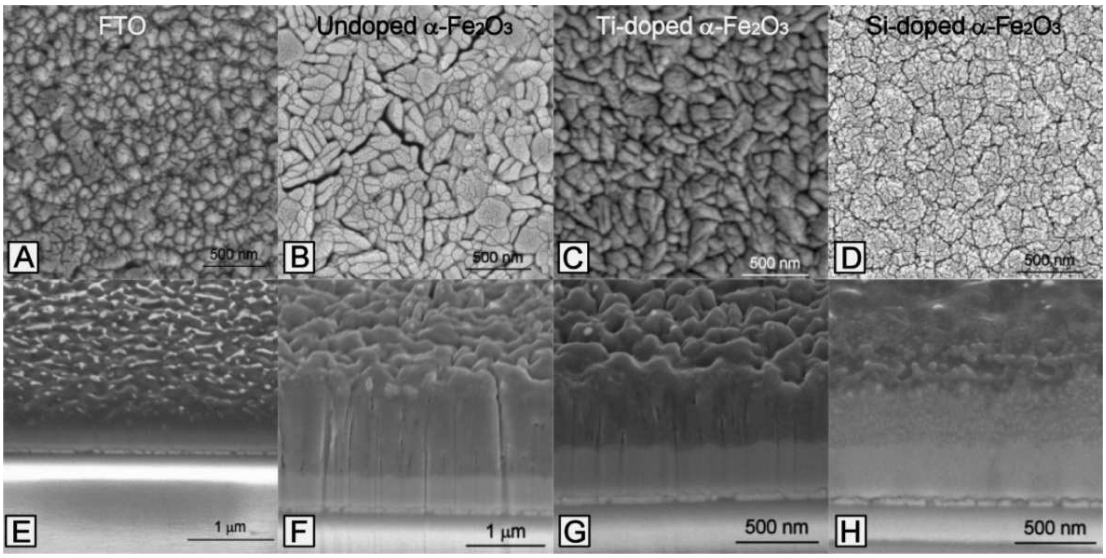

Figure 6.7: SEM images of (A) an uncoated FTO substrate, (B) undoped, (C) Ti-doped and (D) Si-doped RMS α-Fe_2O_3 films, and their respective cross-sections (E, F, G, and H).

All of the magnetron sputtered and FAD films appear to be dense, with cracking apparent in some of the films. Both the as-deposited and annealed samples exhibit cracks, most likely thermally generated during cooling (after deposition or annealing). The undoped and Ti-doped RMS α-Fe_2O_3 films have a similar surface microstructure consisting of irregular grains. From the cross-sectional images it appears that the grains have a columnar structure. The Si-doped RMS α-Fe_2O_3 film is composed of smaller grains that extend throughout the bulk of the film. Grain sizes of the undoped, Ti-doped and Si-doped α-Fe_2O_3 films, as estimated from the SEM images of the surfaces, are in the range 75 - 150 nm, 40 - 100 nm and 15 - 30 nm respectively. A reduction in the grain size with doping was observed for both the FAD and RMS films. Mörl *et al.* (177) and Miller *et al.* (93) used reactive sputtering to produce α-Fe_2O_3 films, and both observed very similar surface structure to those shown in Figure 6.7 (B) and C). Mörl *et al.* also presented cross-sectional images of fractured films that showed columnar growth.

SEM was also undertaken on the Ti-doped RMS α-Fe_2O_3 films deposited at higher chamber pressure (5 Pa rather than 1 Pa) that were used for the Schottky

barrier modelling study and for fabricating the composite electrodes. Figure 6.8 shows SEM images of these films, (A) deposited onto FTO under standard conditions, (B) deposited onto FTO under higher pressure conditions, and (C) deposited onto ITO (on an FTO conducting glass substrate). Figure 6.8 (D) shows an ITO film deposited onto an FTO conducting glass substrate, where the inset shows the structure of the underlying FTO film. The ITO film has a more structured appear-

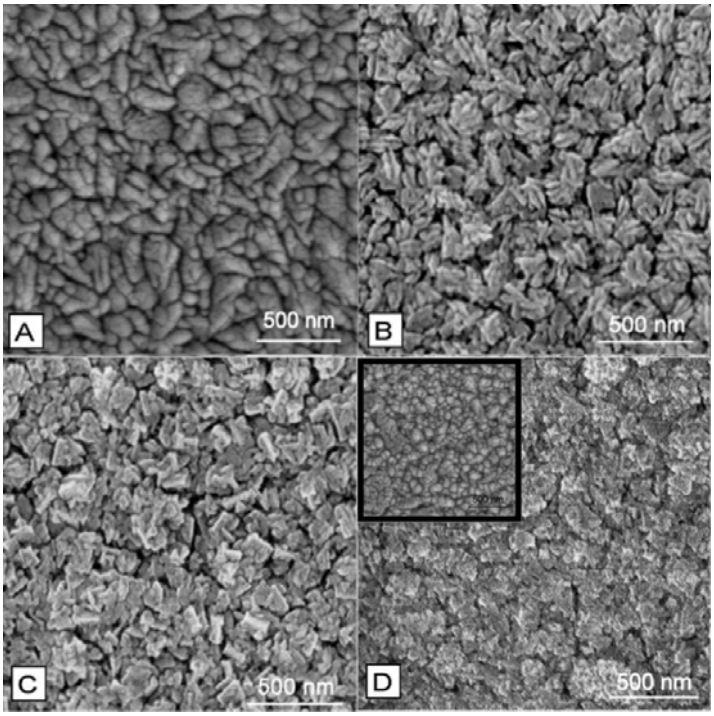

Figure 6.8: SEM images of RMS Ti-doped α-Fe_2O_3 thin films. (A) deposited onto FTO under standard conditions, (B) deposited onto FTO under higher pressure conditions, and (C) deposited onto ITO under higher pressure conditions

ance than the FTO film. The Ti-doped α-Fe_2O_3 films deposited on FTO under the two different deposition conditions have a different surface structure. The film deposited at higher pressure has finer structure, appears to be more porous, and has a similar grain size. The Ti-doped α-Fe_2O_3 films deposited onto ITO films have a broadly similar structure to the underlying ITO films and slightly larger structure than the films deposited onto FTO.

Figure 6.9 shows the r.m.s. roughness as a function of film thickness as determined by atomic force microscopy measurements of FAD α-Fe_2O_3 thin films. The surface roughness scales approximately linearly with film thickness for films between 70 nm and 600 nm thick. The roughness represents only a small fraction of the total film thickness ($\sim$ 0.5 %) in all but the initial stages of film growth. The increase in surface roughness seen as films exceed around 600 nm in thickness could be linked to cracks formed on the surface of the thicker films during annealing (see Figure 6.5 (A) and (B)).

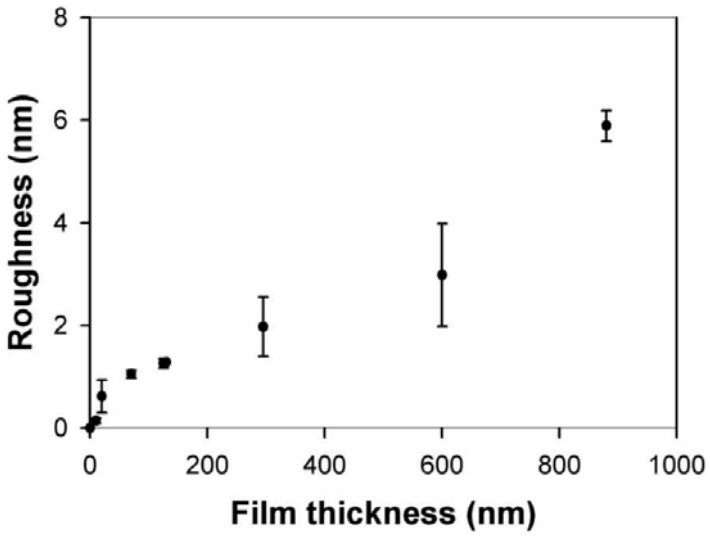

Figure 6.9: Root-mean-square roughness of FAD α-Fe_2O_3 films deposited on a silicon substrates as a function of film thickness

6.1.4 Density and hardness

The density of the α-Fe_2O_3 thin films is relevant as significant porosity can affect the behaviour of the electrode in the photoelectrochemical cell, and may influence the analysis of various characterisation experiments. The hardness is not directly relevant to photoelectrochemistry, but is an indication of the mechanical stability of the films, and it useful for other applications of α-Fe_2O_3 thin films such as optical coatings.

Sample	**Density (g cm^{-3})**	**Porosity (%)**
Bulk hematite	**5.24**	**0**
Quartz - optical thickness (mean of 6 samples)	4.75 ± 0.27	9.9 ± 5.5
Quartz - SEM thickness (single sample)	5.2 ± 1.0	1 ± 20
FTO - SEM thickness 1	3.8 ± 0.8	27 ± 15
FTO - SEM thickness 2	5.7 ± 1.2	-9 ± 22

Table 6.1: Table of density and porosity values calculated for FAD α-Fe_2O_3 films deposited on quartz and FTO conducting glass substrates.

The density and porosity of the FAD α-Fe_2O_3 films were determined using 600 - 1000 nm thick samples, deposited on quartz and FTO conducting glass substrates. The density and porosity were calculated from gravimetric mass values, film area and film thickness data as shown in Table 6.1. Thickness values were determined from optical measurements fit using the Cauchy model with WVASE software, and also from SEM images of film cross-sections. The density values calculated from thicknesses derived from the SEM cross-sections varied from 3.8 g cm^{-3} to 5.7 g cm^{-3}, corresponding to porosities of 27 % to -9 % respectively. The bulk density of hematite is 5.24 g cm^{-3} (178). The large spread in density values calculated for these samples is due to the uncertainty in the thicknesses from SEM imaging (estimated to be 20 %, although no calibration of the SEM scale was performed). The large uncertainty in the thicknesses from SEM measurements means that they are of little use for calculating the porosity of the films. Consequently, only those density values calculated from thicknesses determined from optical measurements will be considered further.

The mean density of six FAD α-Fe_2O_3 films deposited on quartz was found to be 4.75 ± 0.27 g cm^{-3}. The uncertainty in the mass and area measurements (typically around 1 %) and thicknesses from optical measurements (typically around 5 %) have been included in the uncertainty values of the density and porosity. The calculated density of the FAD α-Fe_2O_3 films is less than the bulk density of hematite of 5.24 g cm^{-3}, indicating a porosity of 9.9 ± 5.5 %. Hence it can be concluded that the maximum film porosity is around 15 %. It is likely that the porosity is due to the

thermal stress cracks observed in Figure 6.5. It is evident from the SEM images that the cracks are only visible on the surface and do not extend through the film. Any change in the thickness due to annealing was within the uncertainty of the measurement.

Figure 6.10 shows the hardness of a FAD α-Fe_2O_3 film deposited on a silicon substrate as a function of penetration depth. The hardness of the silicon substrate is also shown. The initial increase in the hardness at low penetration depths is due to the shape of the indenter tip; at this low depth the shape is initially round and so the contact is elastic (179). As the penetration depth increases, the hardness reaches a plateau region. At this point the hardness was measured to be 17.5 $\pm$ 1 GPa. At larger penetration depths the influence of the substrate is observed, with a decrease of the hardness according to the relative hardness of the film and the substrate (the hardness of the silicon substrate is about 11 GPa). The film hardness can be increased by residual stress in the film. Stress is not expected to have contributed in this case, given that the samples have been annealed. An elastic modulus value of 235 $\pm$ 5 GPa was determined by extrapolating the elastic modulus as a function of penetration depth curve (not shown) to a penetration depth of 0 nm.

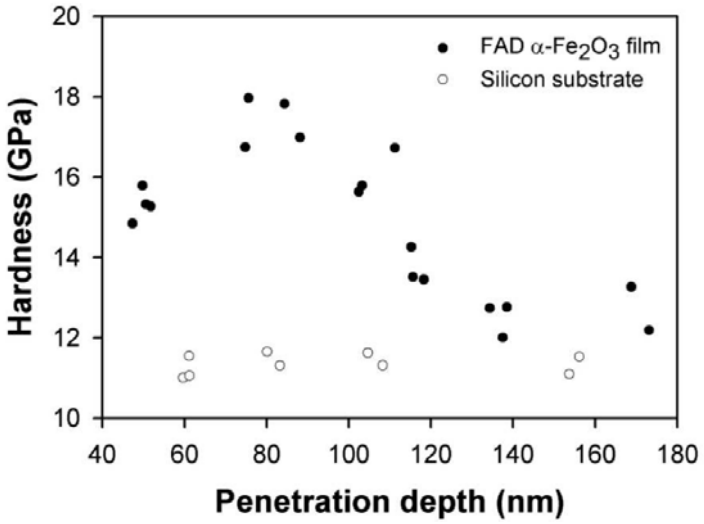

Figure 6.10: Measured hardness of a 700 nm thick α-Fe_2O_3 film deposited on silicon and that of the silicon substrate.

6.1.5 Structural properties

Hematite thin films can be contaminated by other iron oxide phases such as Fe_3O_4 (magnetite), γ-Fe_2O_3 (maghemite), FeO (wüstite) and FeOOH (goethite). Raman spectroscopy, XRD and XPS were undertaken in an attempt to identify the iron oxide phases present in the films. XRD and Raman analysis also give information about the crystal structure and crystallinity of the material. Crystalline material is critical for good photocatalytic activity (72). Also, high photocurrents of Si-doped α-Fe_2O_3 have been attributed to a specific crystallographic orientation (2).

Raman spectroscopy is often used to identify iron oxide phases. The α-Fe_2O_3 spectrum is distinctly different from that of common impurity phases such as Fe_3O_4 and γ-Fe_2O_3 (161). The Raman spectra of α-Fe_2O_3 films deposited using FAD and RMS are shown in Figure 6.11 and Figure 6.12 respectively, along with a hematite reference spectrum (RRUFF ID R050300) (180). Figure 6.11 shows Raman spectra of (A) the α-Fe_2O_3 reference compared to that of (B) an undoped FAD α-Fe_2O_3 film deposited on a quartz glass substrate and (C) a Si-doped FAD α-Fe_2O_3 film deposited on an FTO conducting glass substrate. Figure 6.12 shows Raman spectra of (A) the α-Fe_2O_3 reference compared to those of (B) undoped, (C) Ti-doped, and (D) Si-doped magnetron sputtered α-Fe_2O_3 films on FTO substrates. All of the Raman data shown were collected after the films were annealed.

The spectra of the undoped (FAD and RMS) and Ti-doped films clearly identified hematite as the only phase present and matched the reference spectrum well. Raman spectroscopy is a surface analysis technique and hence there is no contribution from the substrate in the signal. The FAD and RMS Si-doped α-Fe_2O_3 films exhibited similar Raman spectra, with very broad features that appeared to be shifted to higher wavenumbers compared to the reference spectrum. Such behaviour is characteristic of a material with very small crystals or a high amorphous content. This conclusion is discussed in further detail in Section 6.1.10.

The Raman mode around 660 cm^{-1} is present in several published hematite spectra (161, 162, 181, 182), though it has been assigned to other iron oxides that also have a peak in this region. Jorand Sartoretti *et al.* (72) assigned this mode to

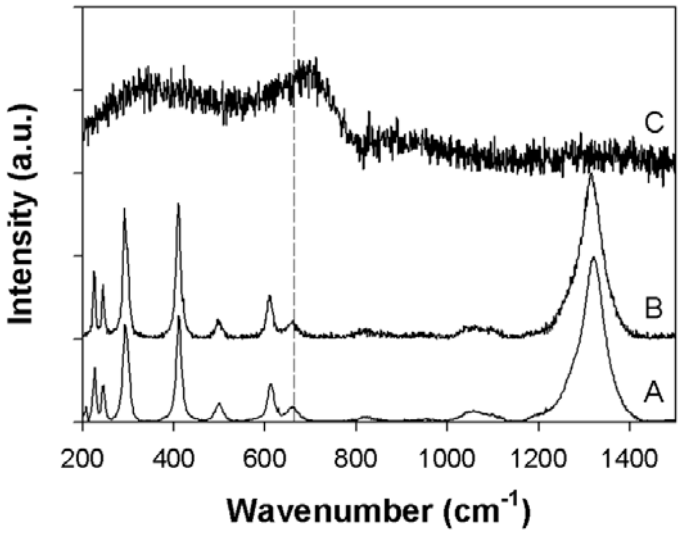

Figure 6.11: Raman spectrum of (A) a hematite reference compared to that of (B) an undoped FAD α-Fe_2O_3 film deposited on a quartz glass substrate and (C) a Si-doped FAD α-Fe_2O_3 film deposited on an FTO conducting glass substrate (after annealing).

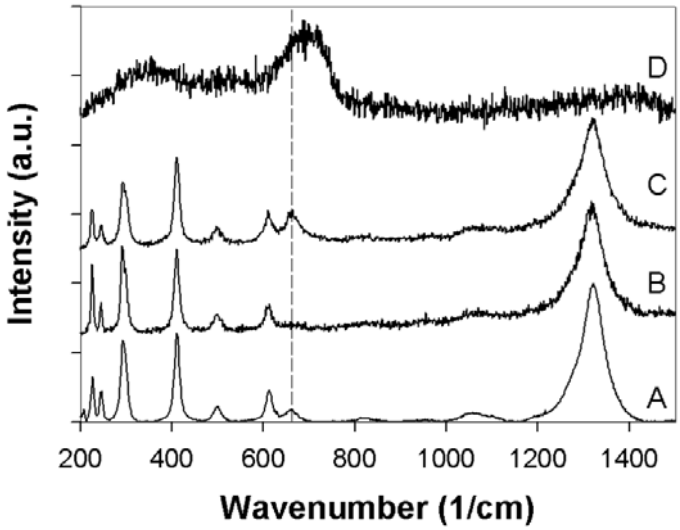

Figure 6.12: Raman spectra of (A) a hematite reference compared to that of (B) undoped, (C) Ti-doped and (D) Si-doped α-Fe_2O_3 films deposited using magnetron sputtering on FTO substrates (after annealing).

Fe_3O_4, though no magnetite was observed by XRD. There is evidence that this peak is characteristic of hematite and related to disorder (162, 182). It has been shown that large inclusions of magnetite ($\geq$ 30 %) are required (due to its weak Raman spectrum) in order for a 600 cm^{-1} magnetite peak to be discernible in the hematite spectrum (160, 162). Such significant amounts of magnetite would be identifiable by other characterisation methods such as X-ray diffraction. Bersani *et al.* (162) have also correlated crystallite size with the intensity of the mode around 660 cm^{-1}, which suggests that the mode may be related to surface and grain boundary disorder in particular. This may explain why this peak is not always observed in hematite spectra and possibly misassigned as magnetite in nanocrystalline samples (72). The doped and undoped FAD α-Fe_2O_3 films and doped RMS films exhibited a peak at 660 cm^{-1}, while the undoped RMS film did not. The very large disorder peak evident in the Raman spectrum of the Si-doped material supports the presence of significant grain boundary defects. After annealing the intensity and width of the peak at 660 cm^{-1} reduced, indicating enhanced crystallinity.

X-ray diffraction patterns of annealed FAD α-Fe_2O_3 films are shown in Figure 6.13. (A) Hematite powder reference pattern (with the crystallographic directions (h,k,l) labelled), (B) undoped FAD α-Fe_2O_3 pattern, and (C) Si-doped FAD α-Fe_2O_3 pattern. Figure 6.14 shows XRD patterns of the doped and undoped RMS α-Fe_2O_3 films. (A) reference pattern, (B) annealed undoped RMS α-Fe_2O_3 film, (C) annealed Ti-doped RMS α-Fe_2O_3 film, (D) annealed Si-doped RMS α-Fe_2O_3 film and, (E) as-deposited undoped RMS α-Fe_2O_3 film. The peaks labelled with an asterisk are tin oxide (casseterite JCPDS 21-1250) from the FTO substrate. The data in Figure 6.13 have been normalised to the major α-Fe_2O_3 peak [104] at $\theta = 33.15°$. The data in Figure 6.14 have been normalised to the major tin oxide peak at $2\theta = 37.8°$. These data have also been smoothed, and the background, containing a broad feature from the amorphous glass substrate (centred around $2\theta = 30°$) has been subtracted. All peaks not assigned to those from the substrates were identified as hematite (JCPDS 33-0664), with no other iron oxide or impurity phases identified. The XRD patterns of the magnetron sputtered films are dominated by the scattering from the substrate, with the hematite peaks small in comparison. If the hematite

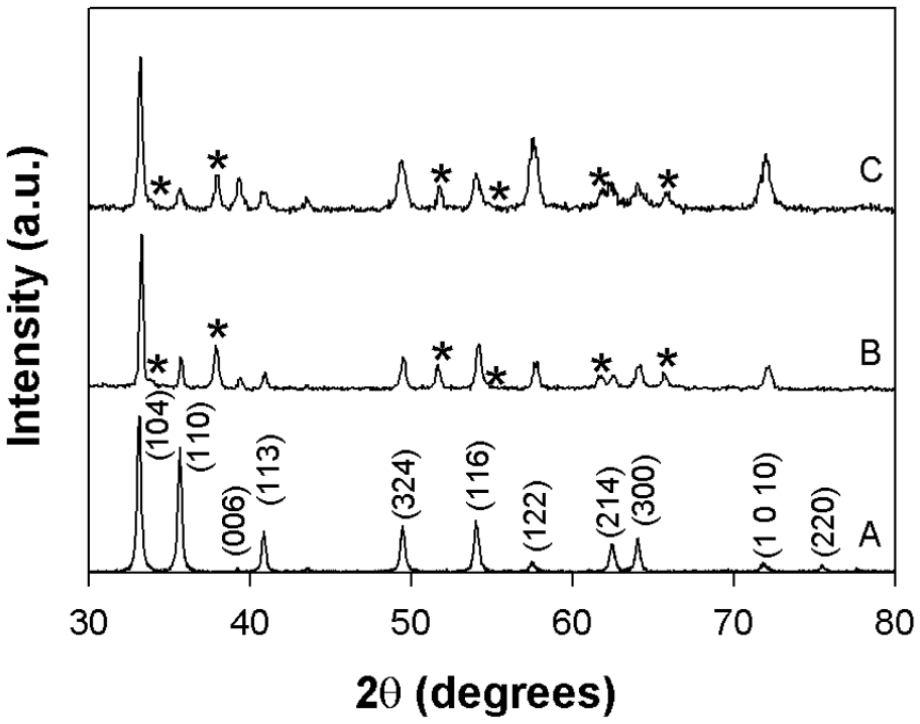

Figure 6.13: XRD patterns of (A) hematite reference powder, where the crystallographic directions (h,k,l) are labelled, (B) undoped and (C) Si-doped FAD α-Fe_2O_3 films deposited on FTO conducting glass substrates after annealing. The asterisks denote peaks from the FTO substrate.

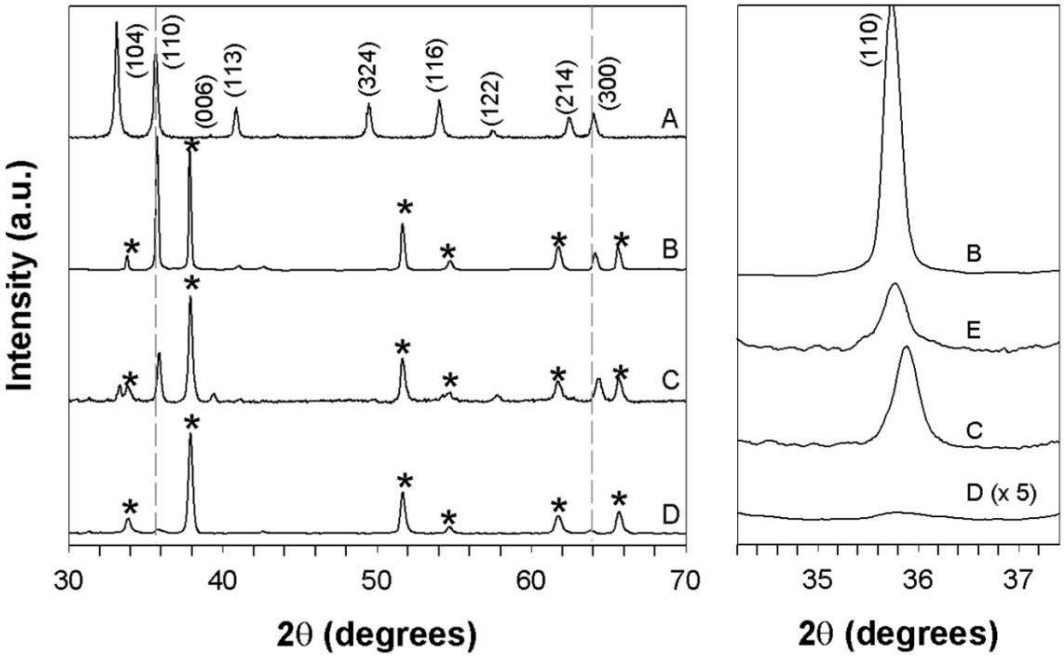

Figure 6.14: XRD patterns of (A) hematite reference powder, where the crystallographic directions (h,k,l) are labelled, and magnetron sputtered, (B) 265 nm thick undoped film, (C) 550 nm thick Ti-doped film, and (D) 755 nm thick Si-doped film on FTO substrates after annealing. The asterisks denote peaks from the FTO substrate. An expanded view of the major (110) peak of each sample is also shown.

films contain amorphous material (as suggested by the Raman spectra), it is likely that the characteristic broad features in the XRD patterns would not be discernible from those of the substrate.

The XRD patterns of the hematite films differ significantly from the hematite reference spectrum. The XRD patterns of the FAD and RMS α-Fe_2O_3 films have different relative peak heights compared to the powder reference spectrum, indicating a preferred orientation of some crystallographic planes. Powder reference samples are randomly oriented, exposing all crystallographic planes equally. However it is common for films be preferentially aligned. The undoped FAD α-Fe_2O_3 films (Figure 6.13) exhibited (110) and (113) peaks smaller than those of the reference material, whereas the (006), (018) and (1 0 10) peaks are larger. The magnitude of the latter peaks as well as the (202) and (300) peaks increased when the FAD α-Fe_2O_3 was doped with Si, indicating enhanced preferred orientation with doping.

On the whole, the XRD patterns of the RMS films (Figure 6.14) are weak, indicating a low level of crystallinity (particularly in the case of the Si-doped film). Most of the hematite peaks were present for the Ti-doped α-Fe_2O_3 film, but in the case of the undoped and Si-doped α-Fe_2O_3 films only the (110) and (300) peaks were visible. If other peaks are present they are very small. The undoped film showed a very strong (110) peak compared to the other films. Both the (110) and (300) peaks for the Si-doped film were very weak. The relative intensities of the XRD peaks compared to that of the reference spectrum, suggest that all three film-types are preferentially oriented. In contrast to the FAD α-Fe_2O_3, the magnetron sputtered films were highly oriented. If the films had a random crystallographic orientation, then the major hematite peaks, (104) and (110), as shown by the reference pattern, should be very strong, and minor peaks such as the (300) should be weak. The fact that the (104) peak is observed as a weak peak (only for the Ti-doped material) and that the (300) peak is a major peak for all samples indicates preferred orientation. The strong orientation of the (110) and (300) directions indicate that the c-axis of the hexagonal hematite unit cell is aligned parallel to the substrate (or the basal planes are aligned perpendicular to the substrate). The hematite peak positions of the Ti-doped α-Fe_2O_3 film are shifted to higher angles compared to the reference spectrum.

The magnitude of the shift increases with angle, consistent with a decrease in the lattice parameters. The FTO peak positions have not changed, indicating that the shift is not an artifact of the measurement.

Crystal sizes were calculated using the Scherrer equation from the full-width-half-maximum values of the (110) peaks from the XRD patterns of the undoped and doped FAD and RMS α-Fe_2O_3 thin films. Crystal sizes for the undoped FAD and RMS α-Fe_2O_3 films were similar, around 70 nm and 65 nm respectively. Doping the hematite resulted in a reduction of the crystal size. In the case of the Si-doped FAD α-Fe_2O_3, the crystal size decreased to 30 nm. The Ti-doped and Si-doped RMS α-Fe_2O_3 film have crystal sizes around 40 nm and 20 nm respectively. An expanded view of the (110) peak used to calculate the crystal sizes for the RMS α-Fe_2O_3 films is shown in Figure 6.14 where pattern (E) is that of an as-deposited undoped α-Fe_2O_3 film. A large increase in the intensity of the (110) (and other) peaks is observed after annealing, Figure 6.14 (B), along with an increase in the crystal size from 50 nm to 65 nm, indicating enhanced crystallinity. No compositional changes were observed after annealing. Here crystals are defined as the area of local order for diffraction purposes. Grains may be single crystals or comprise a number of crystals of the same or similar crystallographic orientation. Hence the grain size as determined from observation of SEM images is not necessarily the same as the crystal size determined by XRD. However the trend is the same, the dopants reduce the grain/crystal size and the Si dopant appears to prevent grain/crystal growth.

Figure 6.15 shows XRD patterns of annealed Ti-doped RMS α-Fe_2O_3 films deposited at higher pressure conditions, (C) deposited onto an FTO substrate and, (D) deposited onto an ITO film on an FTO substrate, compared to (B) a Ti-doped RMS α-Fe_2O_3 film deposited onto an FTO substrate under standard conditions, Figure 6.14 (B), and (A) the hematite reference pattern. The XRD patterns have been normalised, smoothed and had the background removed as for Figure 6.14. The peaks labelled with an asterisk or a cross are tin oxide or from the ITO film, respectively. The Ti-doped α-Fe_2O_3 films deposited at higher pressure have a similar diffraction pattern to the film deposited under standard conditions. In all cases most of the hematite peaks are evident. The smaller hematite peaks (such as (116),

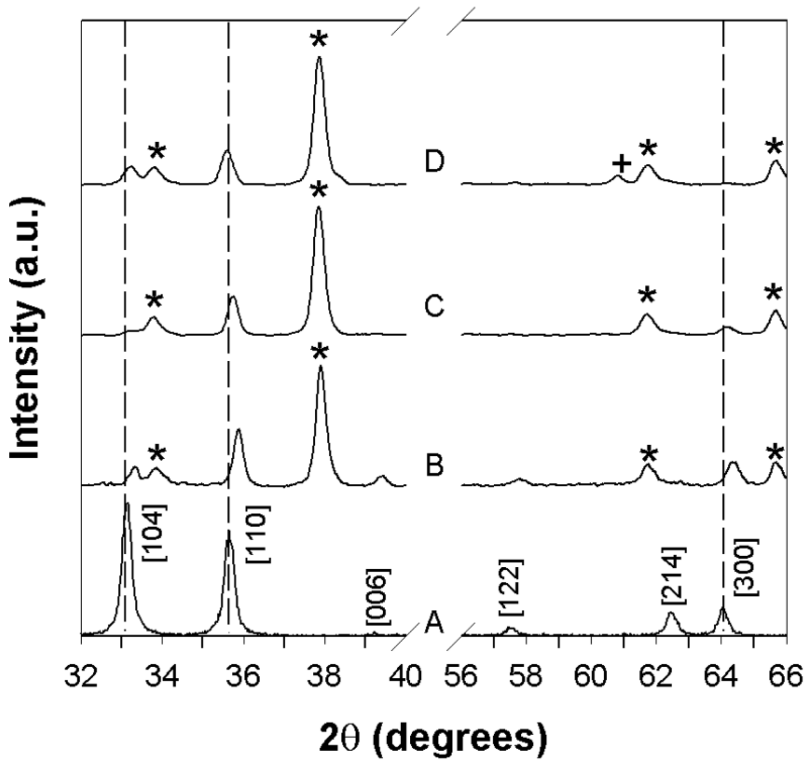

Figure 6.15: XRD patterns of a hematite reference powder and magnetron sputtered Ti-doped α-Fe_2O_3 films. (A) α-Fe_2O_3 reference powder with the crystallographic directions (h,k,l) labelled. (B) 550 nm thick Ti-doped α-Fe_2O_3 film deposited on an FTO substrate under standard conditions. (C) 250 nm thick Ti-doped α-Fe_2O_3 film deposited on an FTO substrate at higher pressure. (D) 270 nm thick Ti-doped α-Fe_2O_3 film deposited on an ITO film on an FTO substrate at higher pressure. All films have been annealed. The asterisks denote peaks from the FTO substrate and the cross denotes a peak from the ITO film.

(122) and (1 0 10), not shown here) are stronger for the film deposited under the standard conditions. The films shown by patterns (C) and (D) have weaker (110) and (300) peaks, with film (C) also exhibiting a very weak (104) peak. The crystal sizes calculated from the full-width-half-maximum values of the (110) peaks of films (C) and (D) gave values within 7 % of the value of 40 nm calculated for film (B).

The XRD patterns of the RMS α-Fe_2O_3 films deposited at a lower deposition rate (patterns not shown) showed a narrowing of the diffraction peaks (indicating larger crystals) compared with those films deposited under standard conditions. The crystal sizes of the magnetron sputtered Ti-doped and Si-doped α-Fe_2O_3 films increased from 40 nm to 50 nm, and from 20 nm to 30 nm respectively. The Ti-doped film also exhibited enhanced preferred orientation, with a 2.5 times increase in the relative magnitude of the (110) peak.

Others producing nanostructured hematite thin films for photocatalytic applications have seen different crystallographic orientations. Kay *et al.* (2) observed a very strong dominance of the (110) peak for Si-doped α-Fe_2O_3 films, (deposited by atmospheric pressure CVD), while Jorand Sartoretti *et al.* (72) observed an XRD spectrum similar to that of a hematite powder spectrum for Ti-doped Fe_2O_3 (deposited using spray pyrolysis). Kay *et al.* (2) suggested that the strong preferred orientation of their samples is induced by the Si dopant. Miller *et al.* (93) saw preferred growth in the (024) and (110) crystallographic directions (for magnetron sputtered films of pure hematite), with the (110) peak dominant in the films deposited at higher temperatures. The orientation observed by these authors consists of the basal plane of the hexagonal structure being aligned orthogonal to the substrate (or the *c*-axis parallel to the substrate). The orientation of films produced using FAD can be modified by changing the bias applied to the substrate during deposition (183); no bias was applied to films produced in this study.

The broad features evident in the XRD and Raman spectra of the Si-doped α-Fe_2O_3 suggest that the material may not be fully crystalline. Additional annealing treatments (up to 165 h at 550 °C) of the RMS Si-doped material were undertaken in an attempt to increase the film crystallinity. No change in the photoelectrochemical performance of the film was observed after the extended annealing. The annealing

temperature was limited to 550 °C due to the limitations of the FTO conducting glass substrate and may not have been high enough to produce significant crystal growth.

Figure 6.16 shows the XPS spectrum of the Fe $2p_{3/2}$ peak of a FAD α-Fe_2O_3 film (both raw data and a fitted curve are shown). The Fe $2p_{3/2}$ peak of a number of iron oxides, including Fe_2O_3, Fe_3O_4, FeO and FeOOH, is located around 710 eV, with a wide variation in the published values of this binding energy (184). For example the Fe $2p_{3/2}$ peak of Fe_2O_3 varies between 709.9 eV and 711.6 eV, while that of Fe_3O_4 varies between 708.1 eV and 711.4 eV (184). The XPS data presented here cannot uniquely identify a single iron oxide phase. It is likely that the Fe $2p_{3/2}$ peak is that of Fe_2O_3, given that this was the only phase identified by other characterization techniques.

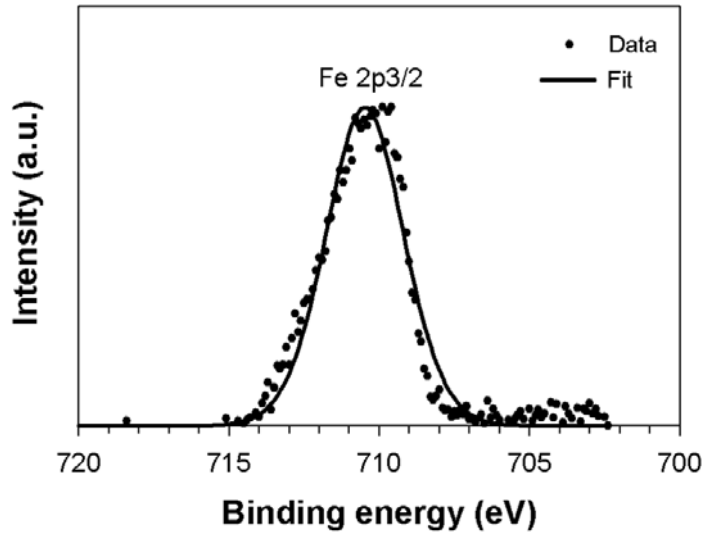

Figure 6.16: XPS spectra (raw and fitted) of an FAD α-Fe_2O_3 film deposited on an FTO conducting glass substrate.

The characterisation of the morphology and structural properties of the hematite thin films has provided a lot of information about the films, in particular the differences between the doped and undoped material. All films exhibited a preferred orientation, with the basal planes being aligned orthogonal to the substrate. The in-

troduction of dopants changed the morphology of the films, as well as decreasing the crystal size. In particular the Si-doping of both the FAD and RMS films appeared to promote a rather amorphous material, with small crystals and a high level of surface disorder. These characterisations experiments do not, however, explain why the Si-doped RMS α-Fe_2O_3 films are photocatalytically active, while the Si-doped FAD α-Fe_2O_3 films are not.

6.1.6 Optical properties

The optical properties of the α-Fe_2O_3 thin films have been carefully measured as accurate values are important for analysis and modelling of the composite nanostructured electrodes. The optical properties of α-Fe_2O_3 thin films are also of general interest for a wide range of applications, including catalysis (185), sensing (gas, alcohol and humidity) (186–188), optics (189) and electronics (190). α-Fe_2O_3 is also a major component of airborne dust in the atmosphere, and its optical properties are required for calculations of single scattering albedo (191). There are currently few data available in the literature on the properties of polycrystalline hematite thin films, and there is often considerable variation in the presented data.

The optical properties of the α-Fe_2O_3 thin films such as the refractive index n, the extinction coefficient κ, and the absorption coefficient α, are of interest for fundamental studies of hematite, as well as being useful data for the design and modelling of the composite nanostructured electrode system. The absorption coefficient determines the number of incident solar photons that will be absorbed by a film of a given thickness. The refractive index of α-Fe_2O_3 will affect the reflection of incident light within the nanostructured electrode and the effective path length for absorption. Other information such as the band-gap energy can be determined from the optical absorption values. The optical properties can also be used to determine the optical thickness of the films.

The refractive index, extinction coefficient, and absorption coefficient were calculated from ultraviolet and visible (UV-vis) transmittance and total reflectance, and FTIR diffuse reflectance data from films with different thicknesses. No changes in

the reflectance and transmittance data were observed after the films were annealed. Optical characterisation was undertaken with both the FAD and RMS α-Fe_2O_3 films.

Figure 6.17 shows examples of the reflectance and transmittance curves from a 980 nm thick FAD α-Fe_2O_3 film on a quartz substrate (grey points) along with a Cauchy model fit of the data using the WVASE software (black curves). The inset curve shows reflectance as a function of wavelength up to 4500 nm. The high visibility interference fringes indicate that the film is smooth and relatively dense. The Cauchy model does not describe the highly absorbing regions well. Therefore fitting using the WVASE software was limited to the region 600 nm - 4500 nm.

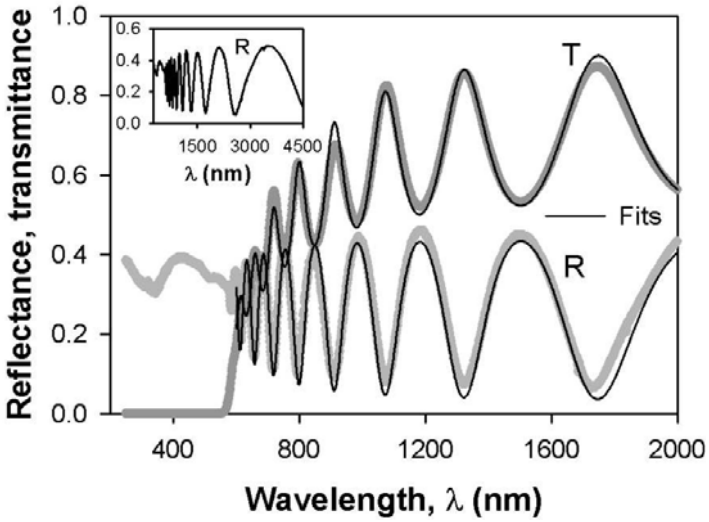

Figure 6.17: Reflectance and transmittance spectra of a 980 nm thick film deposited on a quartz glass substrate (grey curves) along with a fit using the Cauchy model (black curves). The inset shows the reflectance data up a wavelength of 4500 nm.

The refractive index and extinction coefficient of the FAD and RMS α-Fe_2O_3 films deposited onto quartz substrates are shown in Figure 6.18. Figures 6.18 (A) and (B) show n and κ data (respectively) for the FAD α-Fe_2O_3 films from the explicit calculation of the optical constants using the measured reflectance and transmittance (Szczyrbowski method), which is a compilation of both the 102 nm and 980 nm thick films, along with WVASE output for both films. For wavelengths less than 600 nm

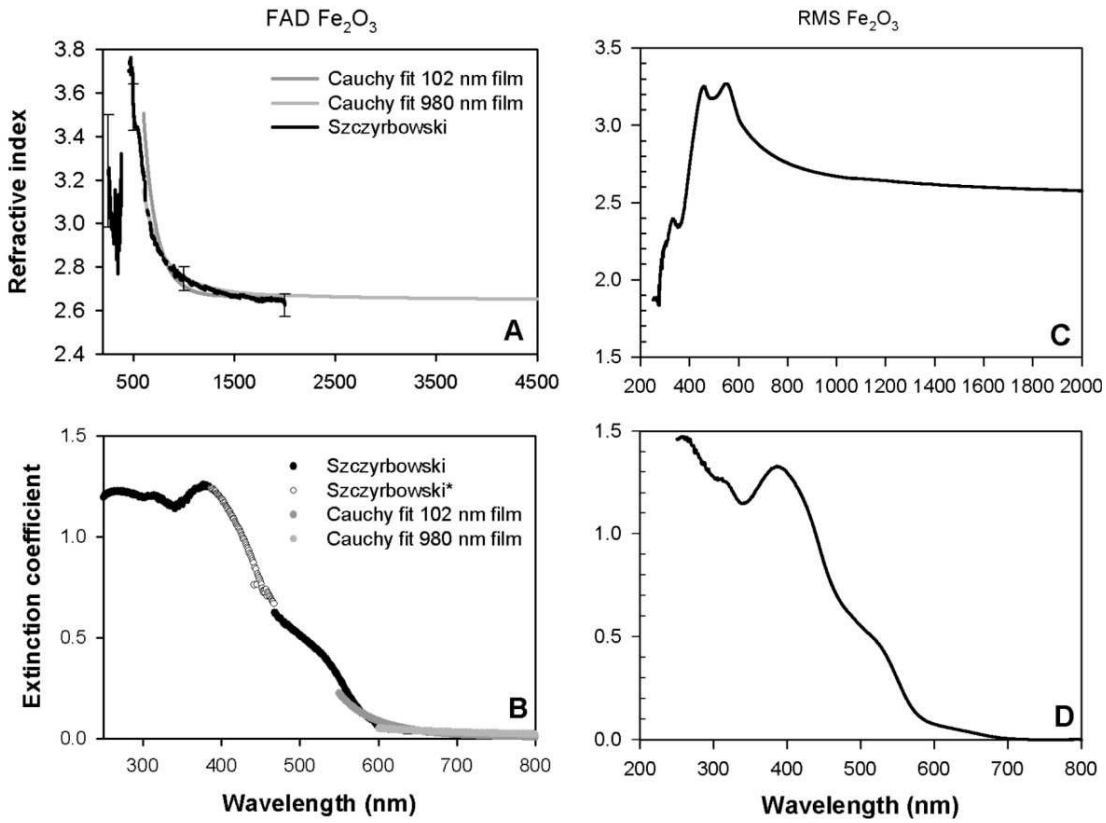

Figure 6.18: Optical constants of FAD and RMS α-Fe_2O_3 films. (A) Refractive index and, (B) extinction coefficient of undoped FAD α-Fe_2O_3 film as determined by the Szczyrbowski method (average of result from 102 nm and 980 nm films) and the Cauchy model. (C) Refractive index and extinction coefficient (κ) and, (D) absorption coefficient of a 120 nm thick RMS Ti-doped α-Fe_2O_3 film versus wavelength.

there was no significant transmission through the thick film, and so only the results from the thin film were used in this region. At some wavelengths the calculated n and κ values failed to converge to reasonable and continuously varying values; this was probably due measurement error and measurement of slightly different regions of the film for R and T (with corresponding differences in thickness). On the graphs these regions are labelled Szczyrbowski*. For wavelengths greater than 600 nm, the calculated n and κ values were averaged for the Szczyrbowski method calculation when data were available for both films. Values of n and κ derived for repeated measurements of R and T showed variation of approximately $\pm$ 8, $\pm$ 3, $\pm$ 2 and $\pm$ 2 % at 250, 500, 1000 and 2000 nm respectively. Indicative error bars are shown in Figure 6.18 (A). Good agreement between the refractive indices calculated by the Szczyrbowski method and the fitted Cauchy n values for the thick and thin films at wavelengths greater than 600 nm can be seen in Figure 6.18 (A). Figures 6.18 (C) and (D) show the refractive index and extinction coefficient respectively for a 120 nm thick Ti-doped RMS α-Fe_2O_3 film over the wavelength range of 250 nm - 2000 nm. It can be seen that the optical constants derived for the FAD and RMS α-Fe_2O_3 films are similar.

There are few sources of refractive index data in the literature for comparison with our α-Fe_2O_3 films. The refractive indices determined by Tanaka (192),for sintered polycrystalline material, and by Longtin *et al.* (193), for colloidal material (194) and hematite plate (195), are within 5% of our values beyond 600 nm. The peak in n values for the RMS α-Fe_2O_3 films at around 550 nm is similar to that reported in Tanaka (192) and Longtin *et al.* (193), however, the peak value for the FAD α-Fe_2O_3 film is about 20 % higher. The refractive indices of r.f. sputtered Fe_2O_3 thin films produced by Mörl *et al.* (177) are dependent on deposition temperature (n increases with increasing temperature) and are approximately 10 % lower than our values at wavelengths greater than 500 nm. Different refractive index values in the literature for hematite may be attributed to differences in the composition and crystallinity, and uncertainties in the optical measurements. The low porosity of the films in the present study should mean that the derived optical parameters apply well to dense polycrystalline material.

The absorption coefficients derived from the extinction coefficient (calculated directly from the reflectance and transmittance data) of the FAD and RMS α-Fe_2O_3 films are shown in Figures 6.19 (A) and (C) respectively. The κ values from the Szczyrbowski method were used rather than those from WVASE (due to the limitations of the Cauchy model in the absorbing region). For the RMS films, quantitative optical constant were derived only for a Ti-doped α-Fe_2O_3 film deposited on a quartz glass substrate. Reflectance and transmittance measurements of all three sample types (deposited on FTO conducting glass) were undertaken, which showed that, after allowance for differences in thickness, the optical properties of the undoped and Ti-doped α-Fe_2O_3 films were identical within experimental uncertainty. The optical properties of the Si-doped material were broadly similar to the other films, but showed significant differences in the absorption coefficient data (in particular slightly reduced absorption at short wavelengths), probably due to the larger disordered component. Differences in optical properties of crystalline and non-crystalline α-Fe_2O_3 have been reported (196). Figures 6.19 (B) and (D) show Tauc plots for direct and indirect optical transitions for the FAD and RMS α-Fe_2O_3 films respectively. Examples of the linear fits used to determine the band-gap energy are also shown. The optical band gap of the FAD α-Fe_2O_3 for both indirect and direct transitions was found to be around 1.9 eV and 2.7 eV respectively. The indirect band-gap values of the undoped and Ti-doped RMS α-Fe_2O_3 films were also around 1.9 eV, with the Si-doped material having a slightly lower value of 1.8 eV. Hence the improved photocurrent with doping is not due to absorption effects. Optical transitions can be assigned to the features in the extinction coefficient data at approximately 265, 320, 395, (425 possible), 530 and 650 nm. The direct band-gap values of the undoped and Ti-doped RMS α-Fe_2O_3 films were also around 2.2 eV, and that of the Si-doped material 2.4 eV. Often with Tauc plots, as is the case for the Si-doped RMS α-Fe_2O_3 film, the determination of the linear region can be ambiguous. Hence there is high uncertainty in the band-gap values for the Si-doped material.

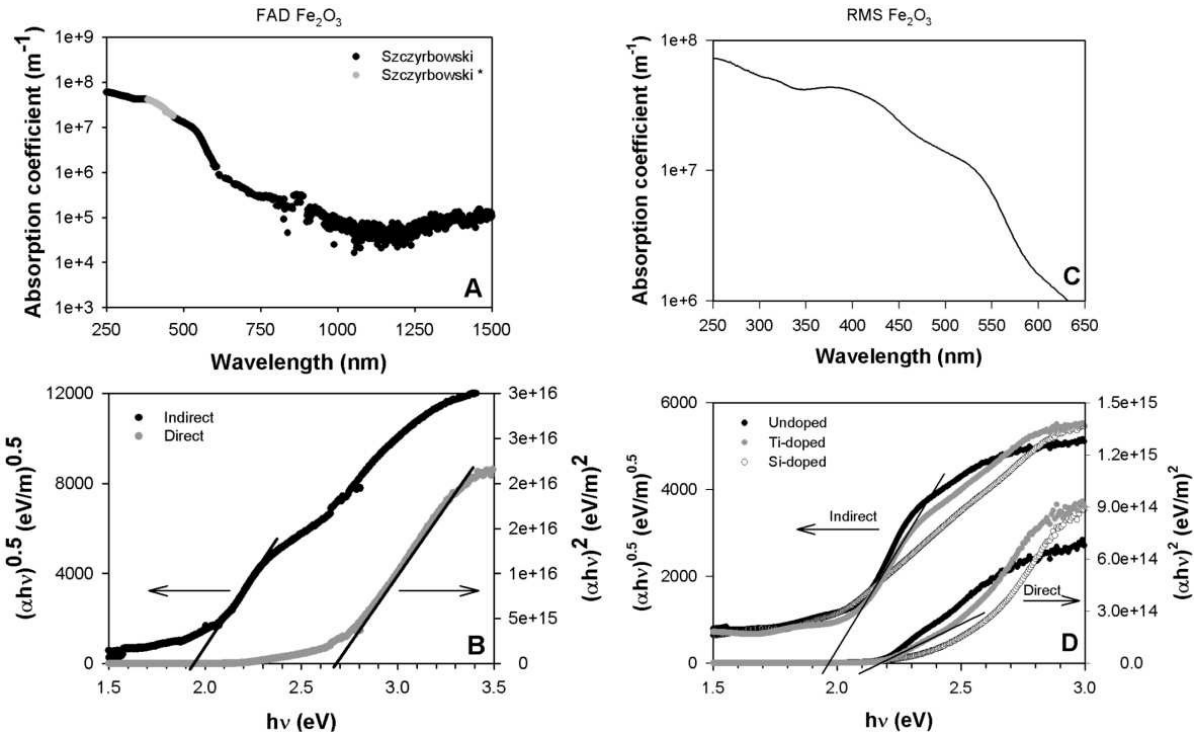

Figure 6.19: (A) Absorption coefficient as a function of wavelength of a 102 nm FAD α-Fe_2O_3 film deposited on a quartz glass substrate as determined by the Szczyrbowski method (average of result from two films) where "Szczyrbowski*" is calculated from k values where the corresponding n failed to converge to reasonable values. (B) Direct and indirect Tauc plots of a 102 nm thick FAD α-Fe_2O_3 film deposited on a quartz glass substrate. (C) Absorption coefficient and (D) direct and indirect Tauc plots for a 120 nm thick Ti-doped RMS α-Fe_2O_3 film deposited on a quartz glass substrate.

6.1.7 Electrical properties

The electrical properties of the α-Fe_2O_3 thin films can give important information about the behaviour of charge carriers in the material. Electrical characterisation can quantify the charge carrier concentrations and mobilities, which are directly related to the quantum efficiency of α-Fe_2O_3. A variety of electrical measurements were undertaken on the FAD and RMS deposited α-Fe_2O_3 films. The electrical conductivity was measured as a function of temperature, from which activation energies for the conductivity were derived. The dielectric constant was determined for an undoped FAD α-Fe_2O_3. Electrochemical impedance spectroscopy (EIS) measurements, from which values of the flat-band potential, carrier concentration and surface state density were calculated, were undertaken only with the magnetron sputtered α-Fe_2O_3 films.

Table 6.2 summarises the results of the electrical characterisation of the magnetron sputtered α-Fe_2O_3 films, allowing comparison of the doped and undoped sample-types. This Table will be referred to throughout the following discussion.

α-$\mathbf{Fe_2O_3}$ **electrode**	σ_{295K} $(\Omega\mathbf{m})^{-1}$)	$\mathbf{E}_a$ **(eV)**	$\mathbf{N}_D$ $(\mathbf{m}^{-3})$	$\mathbf{V}_{fb}$ **(V)**	μ $(\mathrm{m^2V^-s^{-1}})$	$\mathbf{V}_{onset}$ **steady (V/SCE)**	$\mathbf{V}_{onset}$ **transient (V/SCE)**	τ_1 **(s)**	τ_s **(s)**
Undoped	3×10^{-4}	0.68	$1.3^{+0.1}_{-0.7} \times 10^{24}$	$-0.84^{+0.02}_{-0.07}$	1×10^{-9}	0.10	-0.7	0.3	6
Si-doped	2×10^{-3}	0.34	$7.6^{+11}_{-0.3} \times 10^{24}$	$-0.69^{+0.12}_{-0.00}$	2×10^{-9}	0.20	-0.1	0.1	3
Ti-doped	5×10^{-2}	0.23	$3.3^{+1.4}_{-1.0} \times 10^{26}$	$-0.99^{+0.20}_{-0.01}$	1×10^{-9}	-0.15	-0.25	0.2	3

Table 6.2: Electrical properties of doped and undoped RMS α-Fe_2O_3 films determined from electrical conductivity and electrochemical impedance spectroscopy. Here σ_{295K} is the room temperature conductivity, E_A is the activation energy for the conductivity, N_D is the charge carrier concentration, V_{fb} is the flat-band potential, μ is the charge carrier mobility, V_{onset} is the onset potential, and τ_1 and τ_2 are time constants.

The temperature dependence of the electrical conductivity of an undoped FAD α-Fe_2O_3 film, and for doped and undoped RMS α-Fe_2O_3 films is shown by Arrhenius plots in Figure 6.20 (A) and (B) respectively. The results for the RMS films must be considered with caution since the resistance of the films displayed unstable behaviour during the measurements. Initial measurement of the room temperature conductivity of the RMS films (after the samples had been annealed at 550 °C and subsequently cooled) exhibited values of (10^{-4} - 10^{-5}) Ω^{-1} m^{-1} for all samples. The conductivity values showed drift over time scales of tens of minutes. The samples were then heated to determine the temperature dependence of the conductivity. The conductivity behaviour changed to a more stable regime, exhibiting much higher conductivity values, during heating (to less than 180 °C, under either argon or air). Upon cooling the results presented in Figure 6.20 were measured. The lower conductivity state could be reproduced by annealing the films again at 550 °C followed by cooling. Further heating to temperatures lower than 550 °C re-established the higher conductivity behaviour shown in Figure 6.20.

Ohmic behaviour was not observed for the undoped RMS sample despite the use of a number of contact materials in addition to the FTO contacts. The undoped α-Fe_2O_3 conductivity values plotted in Figure 6.20 were consequently derived from the linear region of the differential conductance determined at high applied voltages from the current-voltage curves of the sample. The back contact of the undoped sample may not have been ohmic, so collection of electrons may have been impeded. To check this, an undoped sample was identically prepared on a Ti substrate. This sample showed no improvement in photocurrent, whereas the native TiO_2 layer alone formed during preparation worked well.

Given the above caveats for the RMS films, the conductivity curves of the Ti-doped sample measured in air and argon atmospheres are similar. The activation energies for conductivity E_A were calculated from the gradients of linear fits to the data shown in Figure 6.20. The undoped FAD and RMS α-Fe_2O_3 films showed activation energies of 0.69 eV and 0.68 eV respectively.

Gardner et al. (41) observed an activation energy of 0.7 eV from undoped polycrystalline hematite, which was attributed to the formation of other iron oxide phases

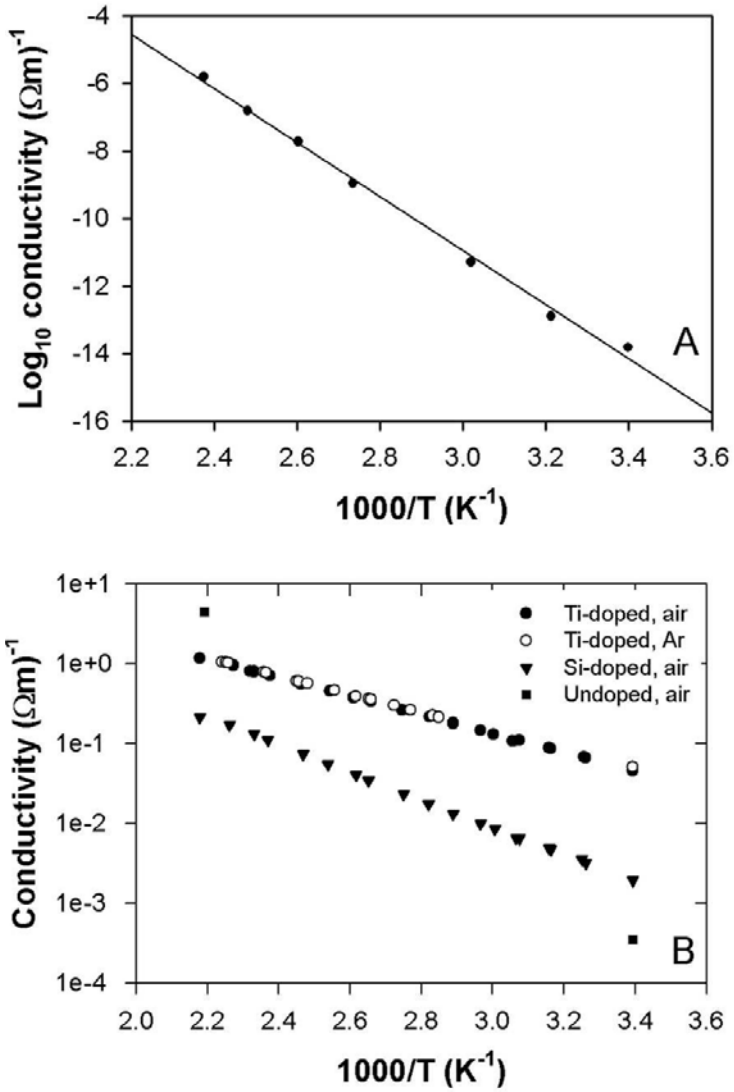

Figure 6.20: The logarithms of conductivity as functions of inverse temperature (Arrhenius plots). (A) An undoped FAD α-Fe_2O_3 film deposited on an FTO conducting glass substrate, measured in air. (B) A doped and undoped RMS α-Fe_2O_3 films deposited on an FTO conducting glass substrate, measured in air and argon atmospheres.

(such as Fe_3O_4) at grain boundaries. The narrow band gap of sub-oxide phases such as Fe_3O_4 would allow recombination pathways for photoholes. These were caused by the complete stoichiometric oxidation of Fe at grain boundaries when their specimens were slowly cooled after firing. On rapid quenching from high temperatures, insufficient time for re-oxidation at the boundaries resulted in lower activation energies. This explanation seems consistent with the gradual cooling (around 1.5 hours) experienced by the FAD and RMS films following annealing, and helps confirm that the undoped films are highly stoichiometric. Similar activation energy values were theoretically calculated for hematite (4). Hematite films produced by Miller *et al.* (93) using magnetron sputtering showed lower activation energies of 0.21 - 0.34 eV, and the authors observed a reduction in activation energy values with increasing crystal size. The activation energy of doped hematite has been shown to be highly anisotropic (100). Therefore differences in reported activation energies for hematite may be related to different crystallographic orientations. The activation energy for conductivity of the RMS hematite thin films was reduced, from 0.68 eV to 0.34 eV or 0.23 eV, by the introduction of Ti or Si respectively. This suggests a change to the bulk properties of the material, rather than just a surface effect. The Ti or Si impurities added to the RMS α-Fe_2O_3 films may segregate between the grains, passivating recombination at the grain boundaries. This would be expected to increase carrier lifetimes and consequently hole diffusion lengths. This argument is consistent with the results of Kay *et al.* (2) who showed that a thin SiO_2 layer at the base of their nanostructured photoelectrodes led to an improvement in performance.

High-purity hematite has conductivity values several orders of magnitude lower than impure material. Small inclusions of magnetite (Fe_3O_4) can greatly increase the conductivity (88); so the conductivity can be used as an indicator of the purity of the undoped hematite films. As deposited, the conductivity of the undoped FAD α-Fe_2O_3 was of the order of 1 Ω^{-1} m^{-1}. After annealing in air, the conductivity dropped to around 10^{-3} Ω^{-1} m^{-1} (measured in air). The decrease in the conductivity after annealing could be due to the completion of the oxidation process during the heat treatment. When the conductivity of the undoped FAD films was measured in a nitrogen atmosphere rather than air, the conductivity was measured

to be greater than 10^{-3} Ω^{-1} m^{-1}. The differences in conductivity as measured in air and nitrogen may be due to water adsorption on the film surface. This is a well-known property of hematite thin films, exploited for humidity sensing applications (187). The undoped magnetron sputtered material in this study showed a similar room temperature conductivity value (10^{-4} Ω^{-1} m^{-1}) to that often quoted for high-purity α-Fe_2O_3 (38, 80, 88, 106). Miller *et al.* (93) also observed a room temperature conductivity as high as 10^{-4} Ω^{-1} m^{-1} for undoped magnetron sputtered α-Fe_2O_3, and samples deposited using magnetron sputtering at lower oxygen partial pressure showed higher conductivity values, which they attributed to reduced grain boundary scattering as a result of an increase in crystal size.

The room temperature conductivity values of the RMS α-Fe_2O_3 films (as shown in Table 6.2) suggest that doping with both Si and Ti increases the conductivity of hematite. This would be expected from the results of previous studies (38, 80, 89). However, it should be noted that as the conductivity of the undoped sample was determined using a method different to that used for the doped samples it may be incorrect to directly compare the data. The conductivity of the Ti-doped film is more than one order of magnitude higher than that of the Si-doped film at room temperature. The conductivity of the Ti-doped hematite is around three orders of magnitude lower than values quoted in the literature for 1-2 % Ti-doped material (42, 87), while the conductivity of the Si-doped α-Fe_2O_3 is around two orders of magnitude higher than the largest of a range of values (105, 106) quoted for 2 mol.% Ge-doped hematite (where Ge is considered as an analogous dopant to Si). The conductivity of hematite is known to be highly dependent on the concentration and type of impurity, as discussed in Chapter 4. It is therefore difficult to compare our measurements with those from other studies when very small differences in dopant levels and types can lead to large differences in the conductivity.

The dielectric constant of the FAD hematite films was calculated from measurements of the the capacitance of metal films deposited on top of the Fe_2O_3. The capacitance of the films did not vary significantly with applied bias (-0.9 V to +0.1 V), indicating that films up to 680 nm in thickness are fully depleted of charge carriers. Measurements of films of differing thicknesses allowed the derivation of a

dielectric constant of between 32 and 57 (measured at a frequency of 100 kHz). The high uncertainty results from the influence of pinholes on the measurements, even after correction for these effects. Pinholes also prevented the derivation of a complex permittivity. Dielectric constant values quoted in the literature for α-Fe_2O_3 vary widely from 12 - 120 (101, 197–199).

Electrochemical impedance spectroscopy (EIS) measurements were undertaken only with the magnetron sputtered α-Fe_2O_3 films. Examples of the EIS data measured at -0.5 V vs. SCE are shown in Figure 6.21 in the form of Nyquist plots (A - C) and Mott-Schottky plots determined from the fitted space charge layer capacitance values at each potential (D - F) for the undoped, Si-doped and Ti-doped α-Fe_2O_3 films respectively. Carrier concentration (N_D) and flat-band potential (V_{fb}) values calculated from the impedance spectroscopy data are shown in Table 6.2, along with mobility values calculated from the room temperature conductivities and carrier concentrations. The carrier concentration of the Ti-doped material is over one order of magnitude higher than that of the Si-doped α-Fe_2O_3. The electron mobilities of the doped films are similar, around of 10^{-9} $m^2s^{-1}V^{-1}$, which are smaller than mobility values for Ti-doped hematite, of the order of 10^{-6} $m^2s^{-1}V^{-1}$ and 10^{-7} $m^2s^{-1}V^{-1}$ presented by Gardner *et al.* (80) and Morin (96) respectively, although similar to those calculated theoretically (44). If the thermally activated hopping mechanism of conduction is assumed for hematite (42, 87), where electron transport occurs via hopping between Fe^{3+} and Fe^{2+} sites, then similar mobilities for Si-doped and Ti-doped α-Fe_2O_3 may be expected. V_{fb} values for our doped and undoped α-Fe_2O_3 films tended to be more cathodic than those presented previously (26, 27, 73, 173), as shown in Table 6.3. Our Si-doped material showed a more anodic flat-band potential than a Ge-doped α-Fe_2O_3 single crystal (106) (where the Ge dopant is considered to be analogous to Si). Sastri *et al.* (73) observed a cathodic shift in the flat-band potential with increased Ti-doping, with a maximum occurring at a dopant level of 1.0 % Ti.

Figure 6.22 shows surface state densities and time constants derived from the residual capacitance not attributed to the depletion layer. Despite the unsophisticated description and assumptions a model (6) with only two adjustable parameters

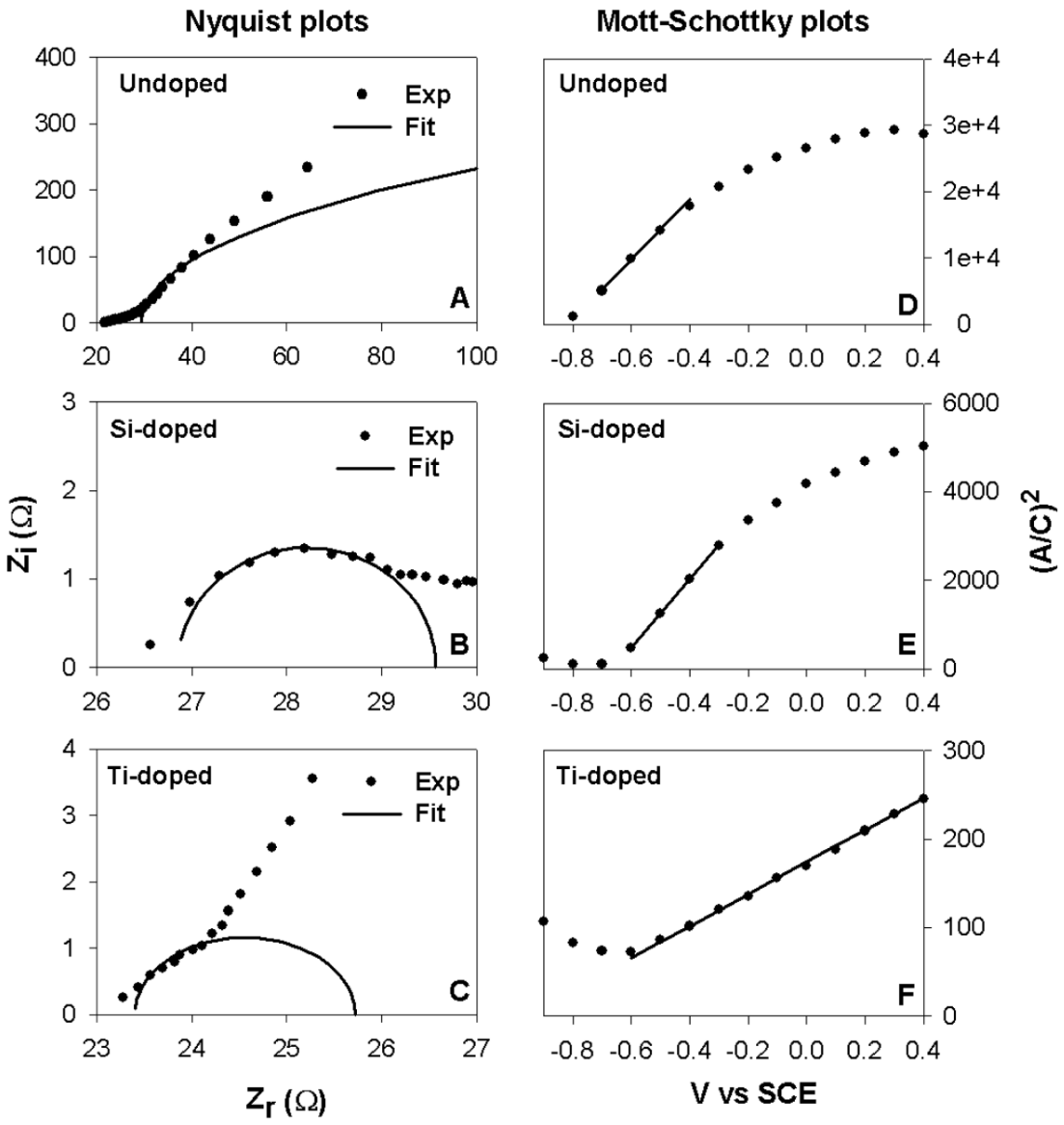

Figure 6.21: Examples of Nyquist plots showing the imaginary versus the real component of the impedance at -0.5 V vs. SCE and modeled impedance, of the (A) undoped (1 kHz - 10 kHz), (B) Si-doped (5 kHz - 32 kHz) and (C) Ti-doped (4 kHz - 25 kHz) α-Fe_2O_3 films (where Zr and Zi are the real and imaginary parts of the impedance respectively), and corresponding Mott-Schottky plots for two samples of each material (D, E, F).

Author(s)	**α-Fe_2O_3 sample**	**V_{fb} (V)**
This study	Undoped	$-0.84^{+0.02}_{-0.07}$
	5 % Si	$-0.69^{+0.12}_{-0.00}$
	5 % Ti	$-0.99^{+0.20}_{-0.01}$
Sastri *et al.*, 1980 (73)	Undoped	-0.65
	0.5 % Ti	-0.67
	1.0 % Ti	-0.80
	1.5 % Ti	-0.72
McCann and Badwal, 1982 (173)	1.0 % Ti	-0.75
Kennedy and Frese, 1977 (26)	Undoped	-0.73
Dare-Edwards *et al.*, 1983 (27)	0.15 % Ti	-0.50
Sieber, 1985 (106)	1.0 % Ge	-0.95

Table 6.3: Flat-band potential of doped and undoped α-Fe_2O_3 from the RMS deposited films in this study compared to those presented in the literature.

fits the data surprisingly well, Figure 6.22 (A) shows examples. The Si-doped film shows the highest concentration of states, around an order of magnitude higher than the Ti-doped film, and about three orders of magnitude higher than the undoped film, over most of the voltage range, Figure 6.22 (B). Figure 6.22 (C) shows the Ti-doped film to have the smallest time constants followed by the Si-doped and undoped films. These differences are likely to be inversely proportional to the capture/emission cross-section since the thermal electron velocity is expected to be constant for all the films.

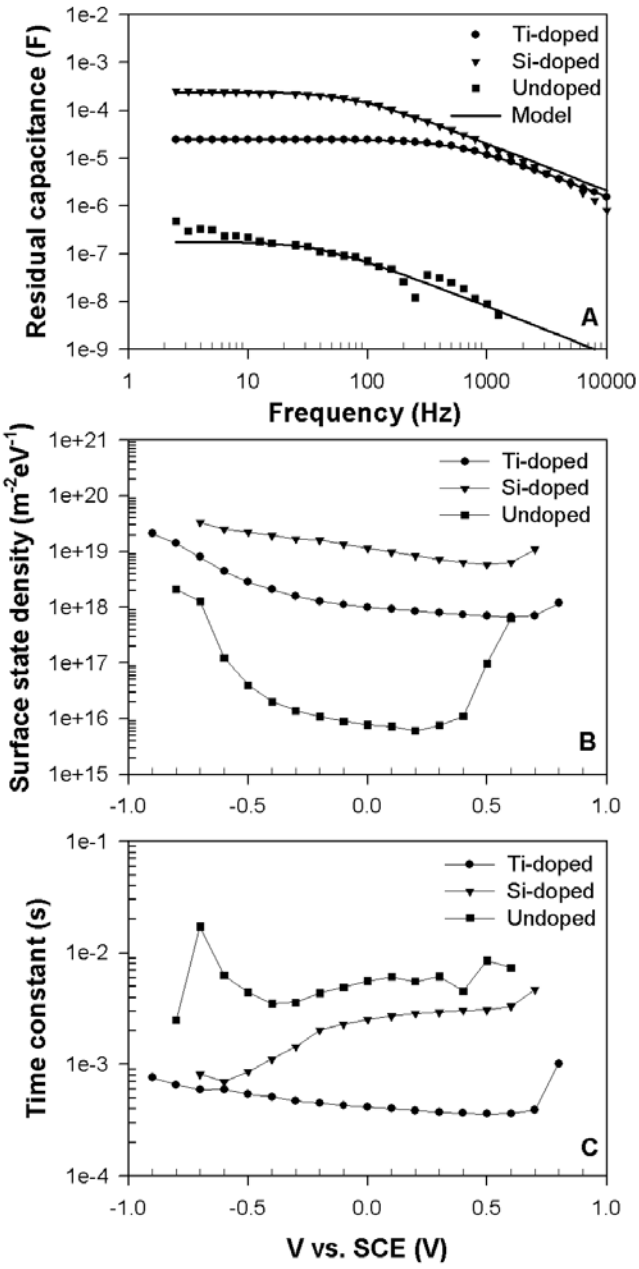

Figure 6.22: (A) Examples of the residual capacitance as a function of frequency measured at 0.5 V vs. SCE and model (6) fitted assuming this capacitance can be attributed to surface states. (B) The surface state density per unit energy determined from the fits shown in (A) at each measured potential. (C) Corresponding surface state emission/capture time constants plotted against potential.

6.1.8 Surface modification

As discussed in Chapter 4, surface recombination is thought to be a problem in α-Fe_2O_3. This has been proposed to be caused by very slow transfer of Fe^{4+} ions (holes) to the electrolyte with the consequent build-up of positive charge at the surface perturbing the space-charge layer and enhances recombination processes (27). The onset potentials of the RMS hematite films are far from the respective flat-band potentials, which has been linked to surface recombination (27). The larger onset potential and flat-band potential of the Si-doped α-Fe_2O_3 compared to the Ti-doped α-Fe_2O_3 may be explained by the presence of amorphous (disordered) material at the surface of the Si-doped film. The slow increase in the onset current evident from the IPCE curves of all three RMS sample types has also been attributed to recombination (27). Surface treatment with cobalt (2) and KI (77) have been shown to increase the photocurrent from doped α-Fe_2O_3 films. Surface modification experiments were undertaken with magnetron sputtered α-Fe_2O_3 films in order to investigate the charge transfer properties at the semiconductor-electrolyte interface.

It is possible that the enhanced photocurrent of Ti-doped hematite compared to the Si-doped α-Fe_2O_3 is due to TiO_2 (known to be a good catalyst material) forming on the surface and providing a catalytic function for the water splitting reaction. This hypothesis was tested by depositing very thin films (around 10 nm) of TiO_2 or Ti-doped α-Fe_2O_3 onto an undoped hematite film. The additional film was kept thin so that it did not contribute significantly to absorption, but could provide catalytic functionality. No improvement in the photoelectrochemical properties was observed by the addition of either of these thin films. If the undoped material does indeed have a highly defective surface layer, then perhaps the addition of a Ti-containing layer would not be expected to solve the surface transfer problems. Differences in the crystal structure between the films and the fact that Ti is a very good oxygen getter (and may be reducing the hematite film) may also have affected the results. It is also clear that the bulk properties of α-Fe_2O_3 are affected by the dopant, and that doping is required in order to generate a photocurrent. A better experiment may have been to deposit a thin TiO_2 film onto a doped α-Fe_2O_3 film, however this

Catalyst	**T_{dep} (°C)**	**P O_2 (Pa)**	**P Ar (Pa)**	**Power (W)**	**t_{dep} (s)**
Co	300	1	-	100	10
Ir	350	2.8	-	100	2
Ni	300	0.4	1.1	100	2, 10
	300	0.4	1.1	50	1
Pd	25	-	2	30	2
Pt	25	-	2	30	2

Table 6.4: Table of deposition conditions for the thin films of oxygen evolution catalysts deposited onto Ti-doped α-Fe_2O_3 films.

was not undertaken.

Further surface modification experiments were undertaken in which Ti-doped α-Fe_2O_3 films were coated with very thin layers (< 5 nm) of materials thought to be good oxygen evolution catalysts: cobalt oxide, nickel oxide, iridium oxide, Pt, and Pd. The catalyst materials were deposited by magnetron sputtering from metal targets using the deposition conditions shown in Table 6.4. The Co, Ni and Ir targets were sputtered at temperatures ≥ 300 °C in the presence of oxygen in an attempt to deposit an oxide film. The Co depositions were undertaken using a different magnetron sputtering system (reproducing the standard operating conditions as closely as possible) as the available Co target was too small for the original magnetron system. The Pt and Pd were deposited as metal films (at room temperature without oxygen present). Metals deposit at a much higher rate than oxides, so the magnetron power was reduced when sputtering the Pt and Pd, in order to accurately deposit very thin films.

Initially films several hundred nanometres in thickness were deposited on Si substrates (to determine the deposition rate via film thickness measurements), and conducting glass substrates. Depositions from the Pt, Pd, Co and Ir targets produced films metallic in appearance, whereas the nickel oxide films were transparent and slightly brown. Despite the metallic appearance of the films deposited from the Co and Ir targets, it would be expected that a film of thickness ~ 5 nm would be fully oxidised after annealing, even if full oxidisation did not occur during deposition. The

actual thicknesses of the very thin films could not be measured using our standard techniques. No structural analysis of the oxide materials was undertaken to confirm the presence of an oxide (rather than the metal). All of the films were annealed (in air at 550 °C using the procedure described in Chapter 5) after the deposition of the catalyst film. A Ti-doped α-Fe_2O_3 sample was fully masked and placed in the vacuum chamber during deposition of the catalysts (onto identical films) as a control. Hence the control sample was heated in the chamber and annealed with the modified samples.

The current-voltage curves of the surface modified Ti-doped α-Fe_2O_3 films are shown in Figure 6.23 (A) and are compared to the curve of the Ti-doped α-Fe_2O_3 control sample. It can be seen that, with the exception of the Ni coated sample (2 s, 100 W), all the catalyst materials had adverse effects on the photocurrent response: the magnitude of the photocurrent was reduced at a potential of 0.2 V and the onset potential shifted to much higher potentials. Such a shift in the onset potential means that a greater bias voltage needs to be applied to split water. The Ir and Co coatings degraded the photocurrent to the greatest extent. Further experiments were undertaken with the Ni catalyst coatings. It was suspected that the film thickness may still be too large, so a shorter deposition (1 s) at half the power (50 W) was undertaken. The deposition rate is approximately proportional to power. Figure 6.23 (B) shows the photocurrent curves of samples with Ni coatings of various thicknesses. The film with the thickest Ni coating had a reduced photocurrent with an onset potential shifted to higher potentials as before. The thinnest Ni coating appeared to increase the photocurrent slightly, however this change is well within the uncertainty of the measurements and is not considered significant.

It has been observed that heating Co-activated α-Fe_2O_3 electrodes above 250°C reduced the photocurrent, whereas the activated samples that were not heat treated increased the photocurrent, compared to non-activated films (2). This was attributed to aggregation of the cobalt oxide into larger particles, reducing the contact area with the hematite and increasing absorption by the Co. All of the surface modification results presented so far are for samples that were annealed after deposition of the catalyst (on to unannealed α-Fe_2O_3 films). The deposition of thin films of

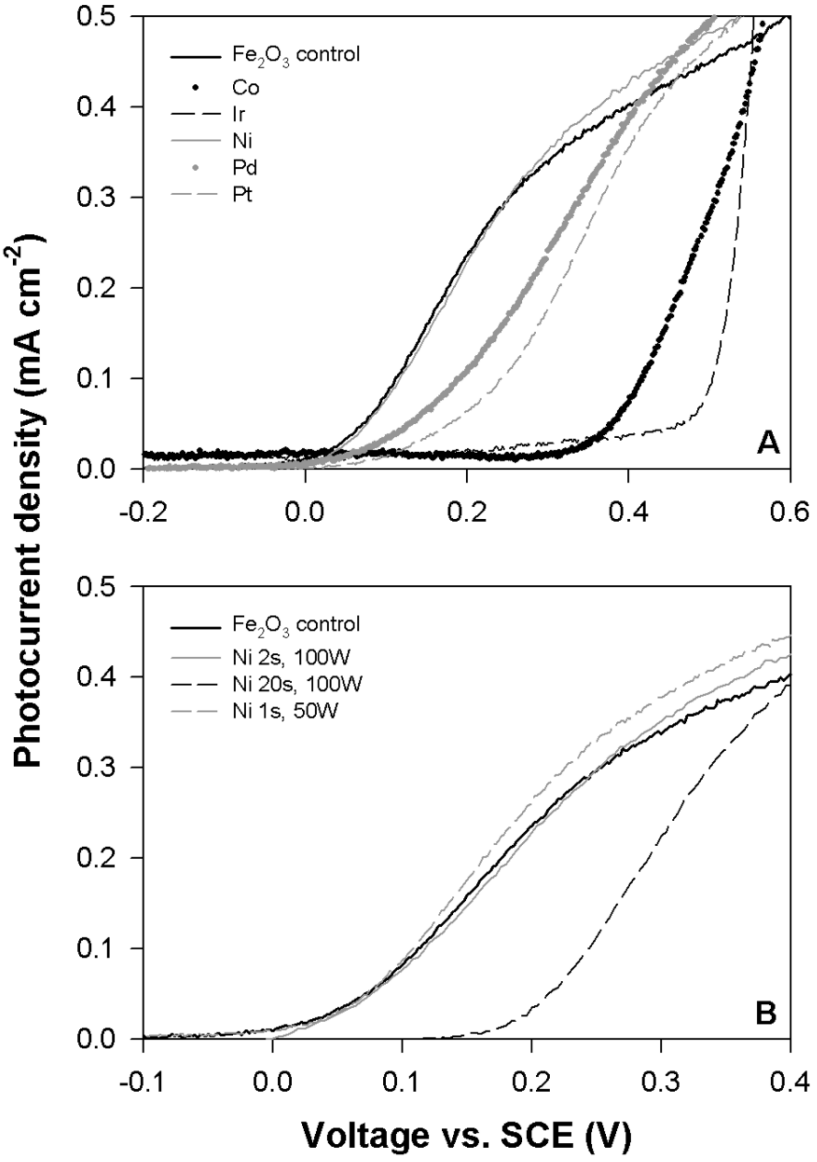

Figure 6.23: Current-voltage curves of magnetron sputtered α-Fe_2O_3 films with surfaces modified by deposition of (A) very thin films of various oxygen evolution catalysts, and (B) Ni films of varying thickness (different deposition times and power).

Ni was repeated using annealed α-Fe_2O_3 substrates, without heat-treating the Ni (although the substrate was heated to around 300 °C during deposition to ensure oxidation of the Ni). This experiment yielded similar results to those previously, where the photocurrent was reduced or not changed by the Ni film.

In this study, the deposition of known oxygen evolution catalysts on top of Ti-doped α-Fe_2O_3 had no effect, or unfavourable effects on the photocurrent. The thicker catalyst films may form a potential barrier to charge transport at the α-Fe_2O_3 surface, resulting in the reduced photocurrent, while the thinner films may have been so thin as to have no effect on the surface charge transfer mechanism. It is possible that the films were being deposited in a form that does not promote catalytic function. The fact that these surface modification experiments did not lead to any improvement in the photocurrent does not rule out poor surface charge transfer as a major limitation of hematite. Investigating the surface charge transfer properties of hematite thin films is worthy of further study. Once a greater understanding of the surface is achieved, surface modification experiments can be designed more effectively to overcome specific shortcomings.

6.1.9 IPCE analysis

The Schottky barrier model proposed by Ghosh *et al.* (51) as described in Section 2.4, has been used to model the action spectra, IPCE (λ), of the magnetron sputtered α-Fe_2O_3 thin films, in an attempt to quantify the diffusion length L, the width of the depletion layer w_d, and the surface transfer coefficient G (which scales the calculated IPCE value). All calculations used the absorption coefficient values presented in Figure 6.19 (C) corrected for surface reflectance (12).

The IPCE of the Ti-doped magnetron sputtered α-Fe_2O_3 film shown in Figure 6.3 (C) was analysed by fitting the Schottky barrier model, allowing the hole diffusion length, surface transfer coefficient and depletion layer width to vary, as shown in Figure 6.24. In the least squares fit shown, the diffusion length is very small ($<$ 0.1 nm), so the modeled fit is scaled by the width of the depletion layer (3 - 5 nm) and the transfer coefficient (0.8 - 1). This barrier layer model does not describe the

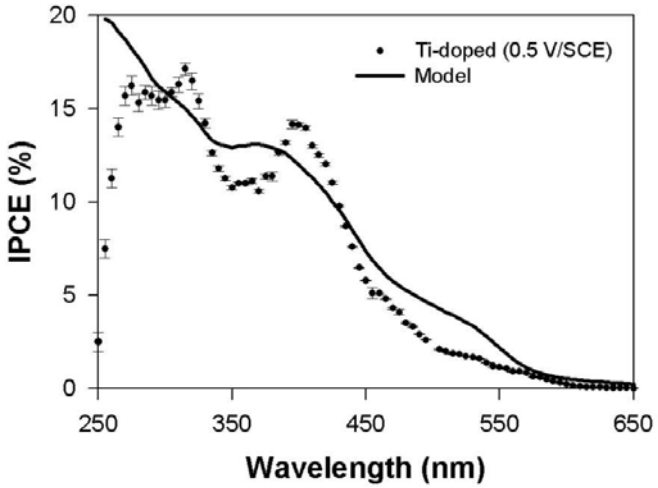

Figure 6.24: IPCE as a function of wavelength of a magnetron sputtered Ti-doped α-Fe_2O_3 films at 0.5 V vs. SCE, with a Schottky barrier model fit of the data.

observed IPCE well. In particular, the modeled IPCE is noticeably higher than the measured values at long wavelengths. If there are, as suggested (26, 27, 29), absorption processes in hematite that generate holes unable to participate in the water splitting reaction, then it is not surprising that the measured photocurrent differs from that calculated from the absorption coefficient. The Schottky barrier model assumes that all absorbed photons are capable of contributing to the photocurrent. This being said, the charge transfer model is still a useful tool for analysing (and potentially quantifying), L, w_d, and G of the doped hematite materials, and will be investigated further.

The sensitivity of the Schottky barrier model to the diffusion length and depletion layer width was explored. Figure 6.25 shows $\mathrm{IPCE_{EE}}$ values (electrolyte-electrode illumination) calculated for various conditions, where the transfer coefficient G was assumed to be 1 and the film thickness h = 121.5 nm (thickness of the α-Fe_2O_3 film from which the absorption coefficient was derived). The decrease in the IPCE values with wavelength and the features within the curves are a result of the shape of the absorption coefficient curve. When w_d is small, there are a small number of charge carriers generated in the depletion region, and diffusion from the bulk must

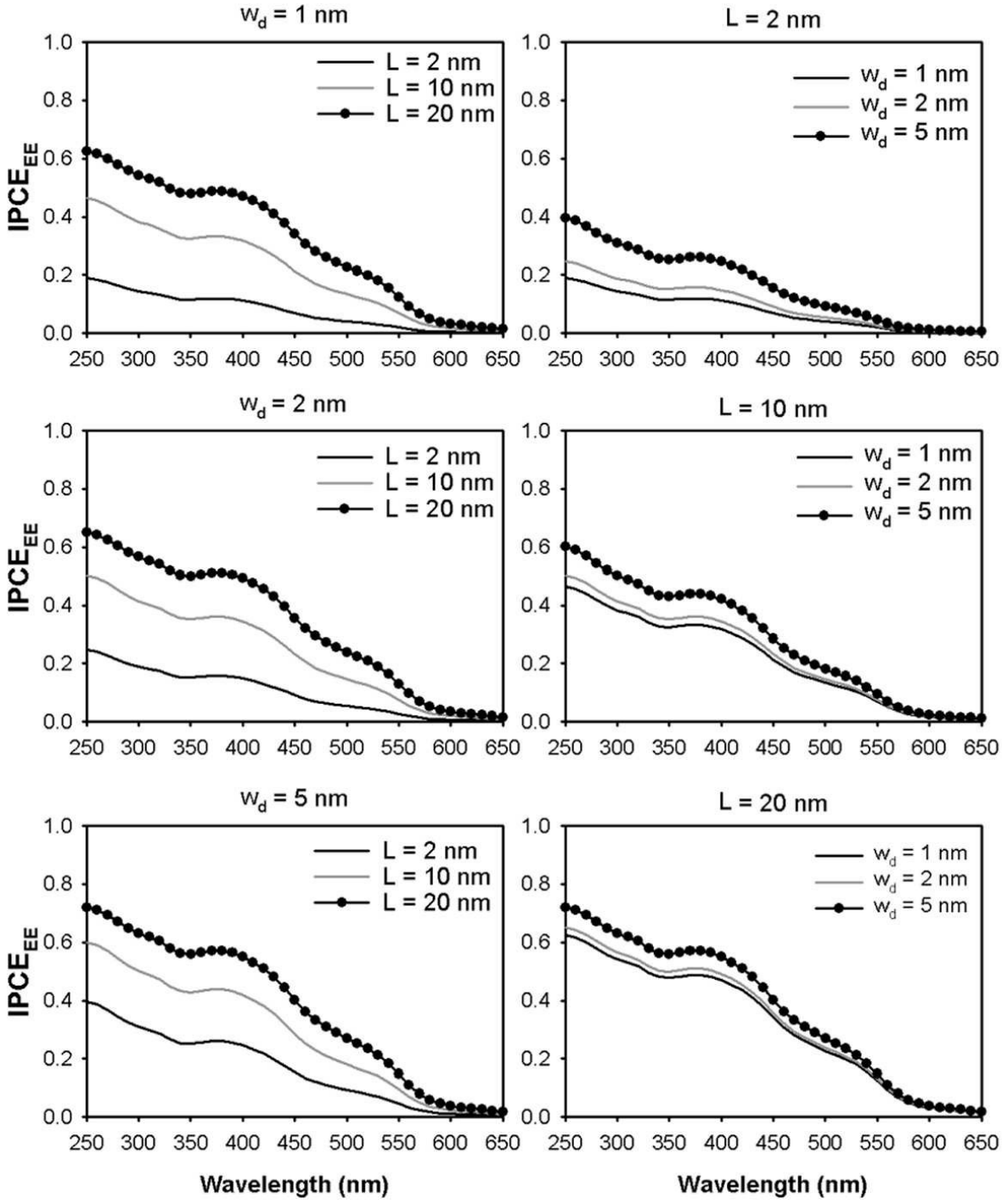

Figure 6.25: $\mathrm{IPCE_{EE}}$ (electrolyte-electrode illumination) values calculated from the Schottky barrier model using various depletion layer widths w_d and diffusion lengths L, assuming $G = 1$ and the film thickness h = 121.5 nm.

be substantial (*i.e.* a long diffusion length L) to achieve a large IPCE value. When the diffusion length is short, the proportion of charge carriers diffusing from the bulk is very small, and only charge carriers generated within the depletion region will contribute significantly to the photocurrent. Even in the best case where w_d and L are large the IPCE is low at long wavelengths. This is due in part to poor absorption in this region. Also, the long wavelengths are absorbed deeper into the bulk and the generated charge carriers having a high probability of recombining before diffusing to the depletion region.

It has been shown that the Schottky barrier model does not fit IPCE data for our α-Fe_2O_3 thin films well (Figure 6.24), and similar IPCE values can be calculated for a range of L and w_d values (Figure 6.25). The magnitude of the diffusion length cannot be determined directly from modelling the IPCE, as the width of the depletion region and the transfer coefficient G are also unknown. It is unlikely that G is unity, given that surface charge transfer is known to be low in α-Fe_2O_3 (as discussed previously). By taking the ratio of the IPCE measured when the film is illuminated from the substrate side to that measured when it is illuminated from the electrolyte side ($IPCE_{SE}/IPCE_{EE}$), the term G cancels out and can be removed from consideration, leaving only the diffusion length and width of the depletion regions adjustable parameters. Figure 6.26 shows this ratio calculated for two different film thicknesses (h = 20 nm and 100 nm) assuming a depletion layer width of 1 nm and diffusion lengths between 1nm and 10 nm. When the film thickness is large there will be significant absorption in the film and the shape of the curve is dominated by that of the absorption coefficient. When the film thickness is reduced the shape of the IPCE ratio curve flattens (because of reduced absorption) and $IPCE_{SE}$ approaches $IPCE_{EE}$. The IPCE ratios are then far more sensitive to the diffusion length. It is proposed that this characteristic may allow the diffusion length to be estimated from experimental IPCE curves of very thin films.

To this end, Ti-doped α-Fe_2O_3 films 20 - 40 nm in thickness were deposited by magnetron sputtering. In order to quantify the diffusion length from the ratio of the IPCE values, the film thickness must be determined with as little uncertainty as possible. Gravimetry measurements were undertaken, where the conducting glass

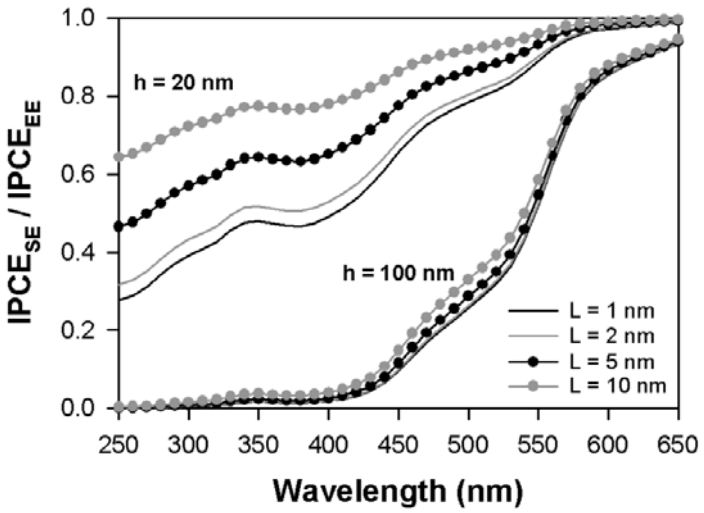

Figure 6.26: Ratio of the $IPCE_{SE}$ to the $IPCE_{EE}$ calculated for two different film thicknesses (h = 20 nm and 100 nm) assuming a depletion layer width of 1 nm and diffusion lengths between 1 nm and 10 nm.

substrates were weighed before and after deposition of the α-Fe_2O_3 in order to calculate the film thickness via a change in mass. Many of the films in fact had a negative mass change, probably due to mass changes during handling exceeding the mass gain from α-Fe_2O_3. The expected mass gain for the 20 - 40 nm films was 20-40 μg, which is reaching the limit of the precision of the scales (around 7 μg). The film thicknesses were also measured using step-edge profilometry of α-Fe_2O_3 films deposited onto silicon substrates, which gave values of 24 $\pm$ 5 nm and 40 $\pm$ 5 nm for the two films that will be discussed hereafter.

Figure 6.27 shows the ratio of the $IPCE_{SE}$ to the $IPCE_{EE}$ measured for a 24 nm and a 40 nm Ti-doped RMS α-Fe_2O_3 film. In the case of the substrate-electrode illumination, the glass substrate absorbs a significant fraction of the radiation below 350 nm. The $IPCE_{EE}$ measurements were undertaken with a bare piece of conducting glass between the monochromator and the photoelectrochemical cell to compensate for absorption in the glass substrate. Reflection corrections were undertaken as the glass substrate in the $IPCE_{EE}$ measurement was in air rather than the electrolyte, which reduced the IPCE ratio curves by around 20 % (as shown in

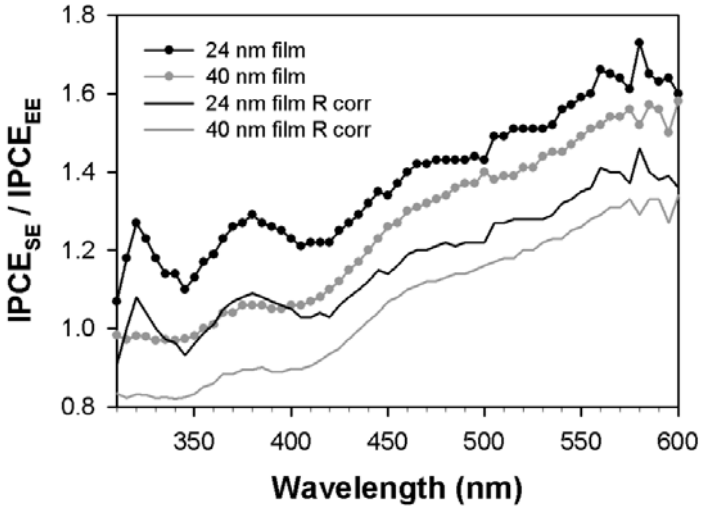

Figure 6.27: Ratio of the $IPCE_{SE}$ to the $IPCE_{EE}$ for a 24 nm and a 40 nm Ti-doped RMS α-Fe_2O_3 film. The IPCE ratios corrected for reflections are also shown.

Figure 6.27). Even after the reflection corrections, the IPCE measured from the SE side is higher than that measured from the EE side, and hence the ratio is greater than unity. The Schottky barrier model predicts that at long wavelengths, where the absorption coefficient and hence attenuation in the film is low, the IPCE is not dependent on the direction of illumination. For thin magnetron sputtered α-Fe_2O_3 films $IPCE_{SE} > IPCE_{EE}$ is consistently observed, though it is not clear why this should be the case. It is possible that the geometry of the measurement is affecting the IPCE values; the α-Fe_2O_3 film is very close to the quartz window of the cell in the EE illumination experiment and perhaps losses are arising from a concentration overpotential as a result of restricted transfer of ions in the electrolyte. There are also additional reflection terms (*e.g.* electrolyte-α-Fe_2O_3 and glass-α-Fe_2O_3) for the electrodes in the cell and these have not been considered here. Reflection corrections from the front and rear faces of the α-Fe_2O_3 films will cancel out to first order and will not be large enough to correct the IPCE ratio to unity. It is also surprising that the IPCE ratio curves of the 24nm and 40 nm films are so similar in shape and magnitude. Figure 6.26 shows that for given w_d and L values, the IPCE ratio is highly dependent on film thickness, hence the IPCE ratio for the 40 nm film should

be smaller than that of the 24 nm film, at short wavelengths.

The experimental IPCE ratios were normalised to unity at the longest wavelength in order to apply the Schottky barrier model. The experimental data is quite different to that predicted by the model, indicating that this description may not be adequate for the α-Fe_2O_3 thin films. The modeled values must be considered with this in mind. Reasonably good fits to the experimental IPCE ratios for the 24 nm and 40 nm films were achieved using the Schottky barrier model, where L and w_d were allowed to float, after the data was normalised (as shown in Figure 6.29). The modeled IPCE ratios did not yield a unique solution for L and w_d, a combination of a large depletion layer width value and a low diffusion length value (or vice versa) produced similar fits. In the case of the 40 nm film (fit over the region 340 - 600 nm) the pairs of L and w_d values that gave the best fit to the experimental data were: $L \leq 1$ nm and $w_d = 30$ nm; and $L = 25$ nm and $w_d \leq 1$ nm. For the 24 nm film (fit over the region 310 - 600 nm) these values were: $L \sim 4$ nm and $w_d = 10$ nm; and $L = 10$ nm and $w_d \leq 1$ nm. As shown previously (Figure 6.25), when one parameter is large, the model is quite insensitive to the other parameter, hence ranges of this value give a similar result. Modelling of the 24 nm and 40 nm films yielded different parameter values; the fits to the data for the 40 nm were much better and considered to be more reliable (with previous caveats still standing). The values of the dominant parameter (either w_d or L) of around 30 nm, from the modelling of the 40 nm films seem to be consistent with the photocurrent density being dependent on film thickness up to a thickness around 100 nm (Figure 6.2). If the dominant parameter was around 10 nm, as suggested by the modelling of the 24 nm film, it is likely that the dependence of the photocurrent on film thickness would be limited to thinner films. L and w_d are material properties of the α-Fe_2O_3 and should not be dependent on the film thickness. If the depletion layer width is around 30 nm, a 24 nm film would be fully depleted (have no electric field), and have no bulk region. The Schottky barrier model may not be suitable for describing such a situation.

A significant source of uncertainty in these calculations is that arising from the film thickness. Figure 6.29 shows the experimental IPCE ratios along with those calculated using the Schottky barrier model, where the error bars indicate the variation

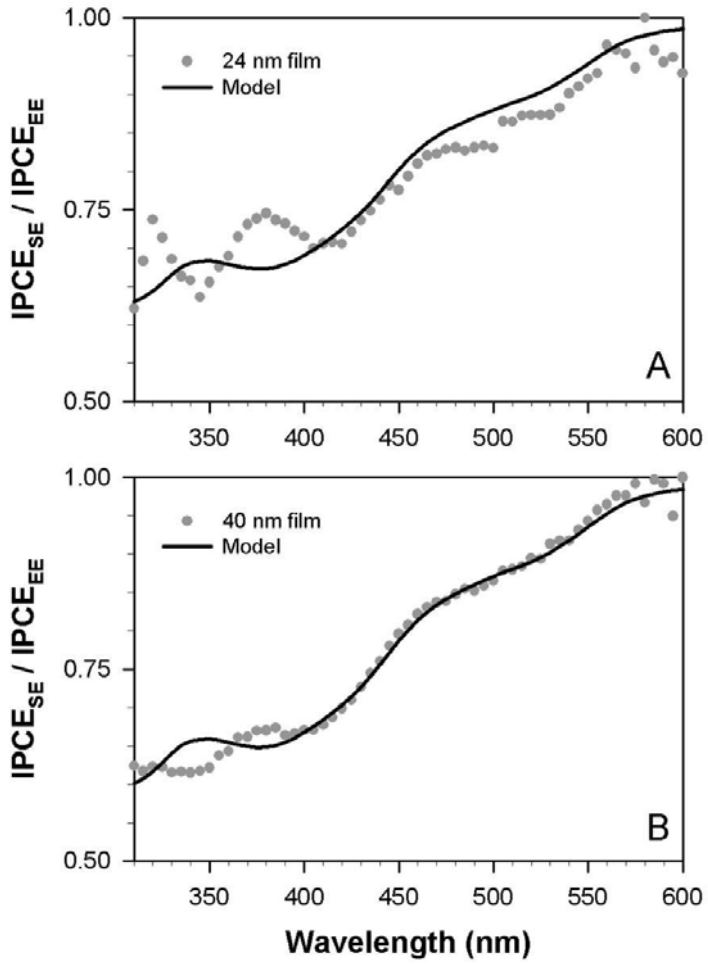

Figure 6.28: Normalised ratios of the $IPCE_{SE}$ to the $IPCE_{EE}$ for a 24 nm and a 40 nm Ti-doped RMS α-Fe_2O_3 film, and least squares fits from the Schottky barrier model, where L and w_d were allowed to float.

in the modeled IPCE ratios corresponding to the error in the thickness measurements of $\pm$ 5 nm. It is clear that there is large uncertainty associated with the values of L and w_d calculated from the model.

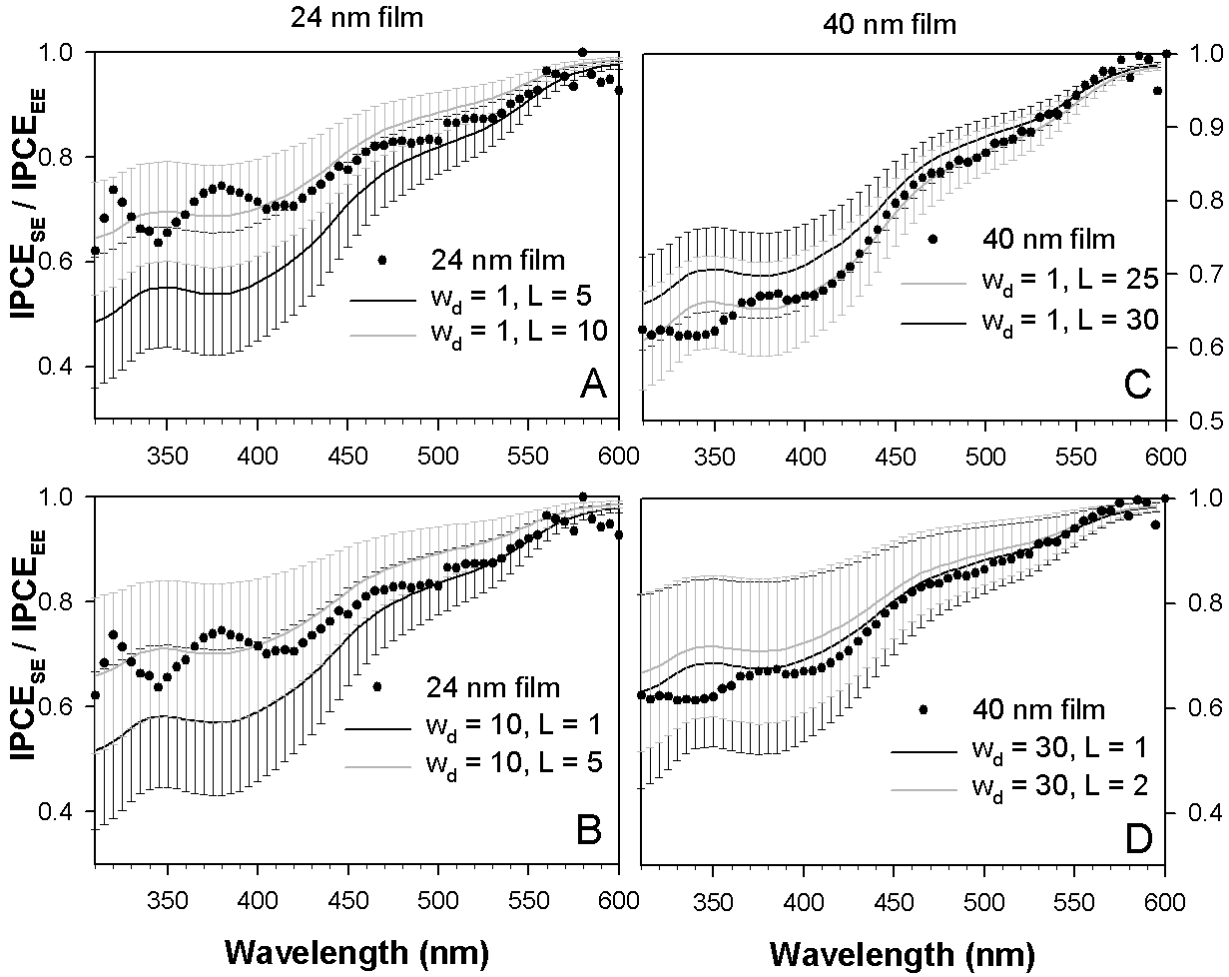

Figure 6.29: Normalised ratios of the $IPCE_{SE}$ to the $IPCE_{EE}$ for a 24 nm and a 40 nm Ti-doped RMS α-Fe_2O_3 film, and modeled curves for various L and w_d values, where the error bars indicate the variation in the modeled IPCE ratios corresponding to the error in the thickness measurements of $\pm$ 5 nm.

It should be noted that for thicker (10^2 nm) RMS α-Fe_2O_3 films, the photocurrents from SE illumination were much lower than for EE illumination. For many practical applications including tandem-cells, it is necessary to illuminate the photoelectrochemical cell from the SE side. Flat films of α-Fe_2O_3 of several hundred

nanometres in thickness are required to absorb a significant fraction of the incident radiation. In such thick films a small fraction of holes generated in the bulk will reach the electrolyte to participate in the water splitting reaction, unless the diffusion length is large. Also, in substrate-electrode illumination it is the long wavelength photons that are absorbed in the depletion region. If the long wavelength photons are absorbed via a mechanism than is unable to produce a photocurrent, then this may further decrease the photocurrent. Such practical requirements may put α-Fe_2O_3 at a very severe disadvantage for water splitting.

Under certain conditions, as described below, dividing $IPCE_{EE}$ by the absorption coefficient can yield a value equivalent to the depletion layer width. The intensity of the illumination at a depth x within a film can be expressed by Eq. 6.1, where I_0 is the incident intensity and α is the absorption coefficient. Differentiating this Equation with respect to x (Eq. 6.2) and dividing by the incident intensity yields Eq. 6.3, which is the fraction of incident photons absorbed. Assuming that all these absorbed photons produce electron-hole pairs which are effectively separated and contribute the photocurrent, then -dI/I_0 is equal to the photocurrent. Assuming a factor N which scales the fraction of absorbed photons for recombination losses, then -ndI/I_0 is equivalent to IPCE. Under the condition that $\alpha x \ll 1$, Eq. 6.6 is true, where dx can be approximated as the width of the depletion region in a simplified model where all of the photocurrent is generated from charge carriers produced in the depletion region. This may be a reasonable assumption for materials such as α-Fe_2O_3 where the diffusion length is thought to be very short.

$$I = I_0 \; e^{(-\alpha x)} \tag{6.1}$$

$$\frac{dI}{dx} = -\alpha \; I_0 \; e^{(-\alpha x)} \tag{6.2}$$

$$-\frac{dI}{I_0} = \alpha \; e^{(-\alpha x)} \; dx \tag{6.3}$$

$$-\frac{ndI}{I_0} = n\alpha \; e^{(-\alpha x)} \; dx \tag{6.4}$$

$$= \text{IPCE} \tag{6.5}$$

$$-\frac{\text{IPCE}}{\alpha} \simeq ndx \text{ if } \alpha x \ll 1 \tag{6.6}$$

$IPCE_{EE}$ values calculated from the Schottky barrier model divided by the absorption coefficient at each wavelength are shown in Figure 6.30, where $G = 1$, $h =$ 121.5 nm, and $w_d = 1$ nm (A) or 10 nm (B). In the case where the depletion region is narrow and the diffusion length is small the $IPCE_{EE}/\alpha$ value is approximately equal to the width of the depletion layer. When L is very small (*e.g.* $L = 0.1$ nm, w_d $= 1$ nm) there is no significant diffusion of carriers from the bulk and charge carriers are only being collected from the depletion region. This is the case described above and it can be seen that $IPCE_{EE}/\alpha$ is approximately equal to the depletion region width. For the case of a wider depletion region ($w_d = 10$ nm), the $IPCE_{EE}/\alpha$ values are similar to w_d for a wider range of L values (only because $L < w_d$). The upward slope is due to absorption of radiation so αx is not less than 1.

Figure 6.31 shows $IPCE_{EE}/\alpha$ curves as a function of wavelength for the 550 nm thick magnetron sputtered Ti-doped α-Fe_2O_3 and the examples from the literature shown in Figure 4.1. All IPCE values have been divided by the absorption coefficient of our RMS α-Fe_2O_3 films shown in Figure 6.19 (C). The $IPCE_{EE}/\alpha$ curve using the results of Kay *et al.* (2) is relatively flat (ignoring the drop-off in the IPCE at short wavelengths), whereas the other samples show a significant decrease at longer wavelengths. The modeled curves in Figure 6.30 are flat for small values of L and increase at longer wavelengths for larger values of L. The shape of the curves for our samples and the selected examples from the literature suggest that the diffusion length is small. However, the yield of electron-hole pairs may be less at long wavelengths.

Figure 6.32 shows $IPCE_{EE}/\alpha$ curves as a function of wavelength for a 24 nm and a 40 nm Ti-doped RMS α-Fe_2O_3 film. These curves, as well as those shown in Figure 6.31, exhibit a decrease in the $IPCE_{EE}/\alpha$ values at long wavelengths. This is indicative of the shape of the IPCE curves not matching that of the absorption coefficient, as previously discussed. However for the relatively flat region up to around 450 nm where the IPCE is proportional to the absorption coefficient, the $IPCE_{EE}/\alpha$ value is around 3 nm. Using Eq. 2.16 and Eq. 2.17, with the flat-band potential and carrier concentration values for Ti-doped RMS α-Fe_2O_3 shown in Table 6.2 a depletion layer width of 2.8 nm is calculated. This is in good agreement

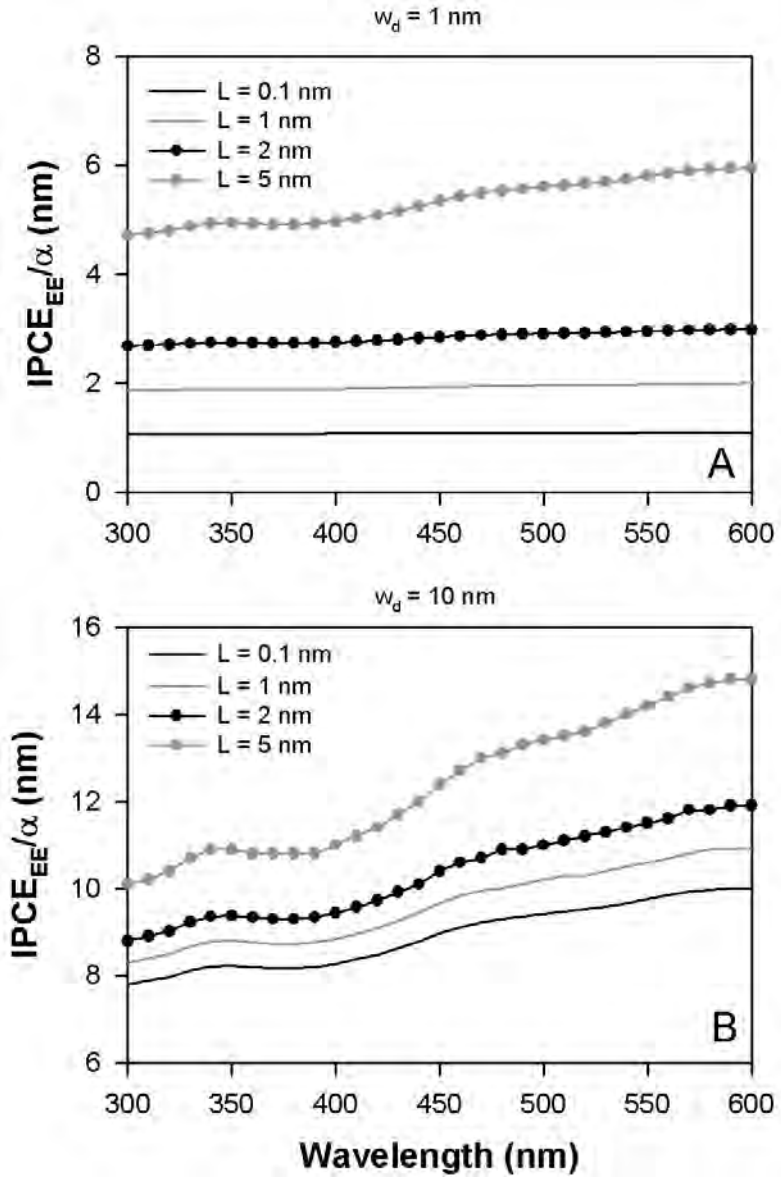

Figure 6.30: IPCE_{EE} values calculated from the Schottky barrier model divided by the absorption coefficient α, assuming a depletion layer widths $w_d = 1$ nm, $G = 1$ and the film thickness $h = 121.5$ nm.

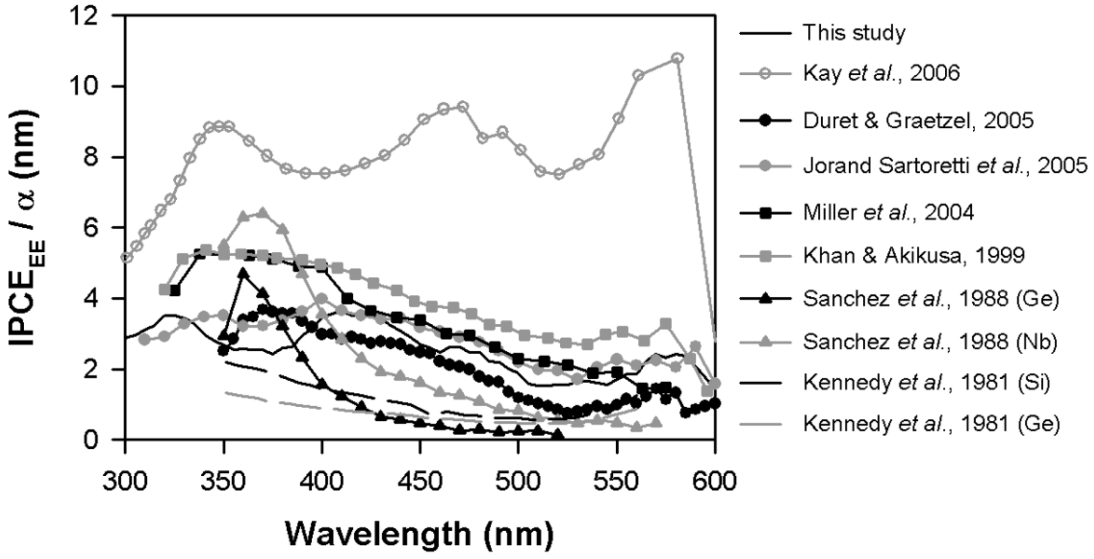

Figure 6.31: $IPCE_{EE}$ of magnetron sputtered Ti-doped α-Fe_2O_3 and IPCE values from the literature (Figure 4.1) divided by our absorption coefficient α (Figure 6.19 (C).

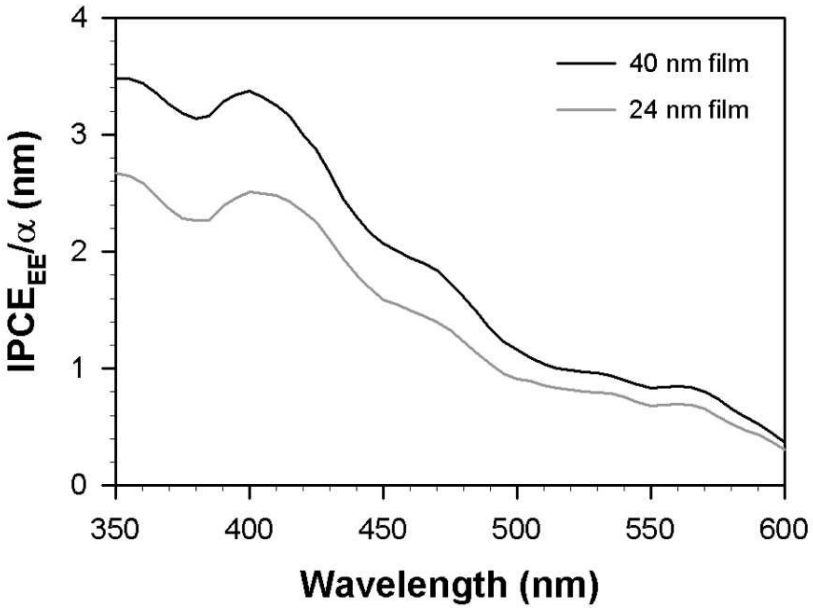

Figure 6.32: $IPCE_{EE}$ of a 24 nm and a 40 nm Ti-doped RMS α-Fe_2O_3 film divided by the absorption coefficient.

with the value from the $IPCE_{EE}/\alpha$ curve.

Using the ranges of values of L and w_d derived previously from the modelling of the $IPCE_{SE}/IPCE_{EE}$ curves, the Schottky barrier model was applied to the $IPCE_{EE}/\alpha$ curves shown in Figure 6.32 to estimate values of the surface transfer coefficient G. Under the conditions where L is small and w_d is larger, G was found to be between 0.2 and 0.25. When w_d is small and L is significant, G increases to between 0.25 and 0.35. These values are small, and similar to the quantum efficiency values at short wavelengths, supporting the conclusion that surface charge transfer is a significant limitation for α-Fe_2O_3.

In summary, extensive modelling of the IPCE values of Ti-doped RMS α-Fe_2O_3 thin films was undertaken using a Schottky barrier model, yielding a lot of interesting results, many of which are not fully understood at this stage. The modelling did not yield a unique solution for values of L and w_d, however it was only possible to get good fits of the data where one parameter was dominant and much higher than the other. The results of the modelling will be discussed further in the next Section

within the context of other characterisation experiments.

6.1.10 Discussion

In the case of the magnetron sputtered α-Fe_2O_3 films, doping was necessary to produce photocatalytically active material, with the Ti-doped α-Fe_2O_3 exhibiting a much higher photocurrent than the Si-doped α-Fe_2O_3 at the bias voltages investigated. It is not surprising then that the undoped α-Fe_2O_3 films deposited using FAD were inactive. However, it is unclear as to why the the introduction of Si into the FAD α-Fe_2O_3 films did not improve the photoresponse. It is likely that the dopant was not effectively incorporated into the α-Fe_2O_3 lattice using this technique. There was, however, evidence from the Raman and XRD that the Si was present in the doped FAD films. It is surprising that the Si-doped RMS material showed significant photoactivity, given that it appears to be highly amorphous and have a high level of surface disorder. The substantial photocurrents achieved by Si-doped α-Fe_2O_3 samples prepared by other techniques (2, 76) can probably be attributed to their material being more crystalline, and also probably some contribution from the nanostructuring. Several mechanisms have been proposed for the improvement of the photocatalytic performance of hematite with doping. We discuss these mechanisms in the context of our results and those presented in the literature.

Kay *et al.* (2) and Cesar *et al.* (7) attributed the good photocatalytic behaviour of Si-doped α-Fe_2O_3 produced by spray pyrolysis, in part, to a high degree of preferential crystallographic orientation. Strong (110) and (300) peaks were observed in the X-ray diffraction patterns, indicating that the basal planes (001) were aligned perpendicular to the substrate. It was suggested that photoelectron collection was enhanced because of the orientation of the strongly conducting basal planes, while photo-hole transfer was facilitated by the short diffusion distances from nanostructure to electrolyte. Bedwell and McCartney (200) measured the photoelectrochemical response of single crystals cut to expose different crystallographic planes to the electrolyte. They found that an electrode exposing the (001) plane showed little

photocurrent, but the (012) plane showed a good photoresponse. The difference in photocurrent was attributed to the much higher resistivity in the [001] direction, (110) plane ($10^4\ \Omega$m), compared to the [012] direction (20 Ωm). The anisotropic nature of the electrical conductivity of hematite is well-known and has been observed experimentally (100, 201) and demonstrated theoretically (44, 202) (discussed in Section B.1). However, the magnitude of the anisotropy is highly dependent on impurities. In the present study the doped and undoped films all exhibited a preferred orientation of the basal planes perpendicular to the substrate yet showed very different photocurrents. The Ti-doped α-Fe_2O_3 deposited at a lower deposition rate showed a large increase in the preferred orientation, but no change in photocurrent. Therefore it appears unlikely that crystallographic orientation is a dominant factor determining the photocatalytic performance of these films.

A simple calculation can be made to determine the expected potential drop through a film to quantify the effect of anisotropic conductivity. Considering a 1 μm α-Fe_2O_3 film with a resistivity of $10^5\ \Omega$ cm operating at the theoretical maximum photocurrent for solar illumination (assuming complete absorption and conversion of photons with energies exceeding the band gap ($j_p = 10.6$ mA cm^{-2})), there will only be a modest drop in potential (around 100 mV). In practice lower photocurrent densities are obtained with correspondingly lower potential drops, such that photoelectrode conductivity has only a minor direct influence on thin film performance. Thus lowering ohmic drops in the electrode by increasing the conductivity can not explain the large improvements in the photocurrent due to doping. Also, changes in conductivity will not shift the onset potential of the material, as observed.

It is clear that the introduction of dopants affects the growth mechanism of the hematite films, resulting in different crystallinity, alignment and morphology. The Si appears to prevent the growth of highly crystalline material (small crystals and a large amorphous content), whereas the presence of Ti allows crystalline growth. Given the low partial pressure of oxygen during deposition, it is likely that Fe is deposited onto the substrates and then oxidises to form α-Fe_2O_3. The mobility of the Fe atoms will affect the crystal structure and orientation of the oxide. It has been suggested that preferential growth in the [110] direction is due to facile Fe atom

diffusion in this direction (85). It is possible that the Si is reducing the mobility of the Fe atoms during growth, which might restrict the formation of large crystallites.

In the case of the FAD and RMS films, the Raman spectrum of the Si-doped α-Fe_2O_3 is strikingly different to the spectra of the undoped FAD α-Fe_2O_3, and the Ti-doped and undoped RMS α-Fe_2O_3 respectively. In fact, it would be impossible to identify the Si-doped material as hematite without the x-ray diffraction data. In contrast, the XRD patterns of the doped and undoped materials produced by each technique are broadly similar. Raman spectroscopy is a surface measurement, while XRD analyses the entire film. Hence these results suggest that the bulk material of the doped and undoped films is similar (apart from small differences in crystallographic orientation), while the surface of the Si-doped α-Fe_2O_3 is substantially more disordered than that of the Ti-doped and undoped films. Given the smaller grain sizes of the Si-doped α-Fe_2O_3 compared to the undoped and Ti-doped material the Raman technique would be analysing a greater number of grains, with a higher surface to grain boundary contribution. The magnitude of the Raman disorder peak from the RMS Si-doped film is considerably larger than that of the Ti-doped film, consistent with the higher calculated surface state density for the Si-doped α-Fe_2O_3. The surface state density of the undoped RMS α-Fe_2O_3 film was orders of magnitude lower than that of the doped materials and did not exhibit the disorder peak in its Raman spectrum. These results support the suggestion by Bersani *et al.* (162) that this Raman peak is related to surface disorder.

The concentration of charge carrier in the Ti-doped RMS α-Fe_2O_3 is over one order of magnitude larger than that of the Si-doped RMS material. We would expect lower carrier concentrations to correspond to wider depletion layers at the electrolyte interface, thus leading to a greater harvesting of charge carriers. However, a Schottky barrier model predicts that the transit time through the depletion layer varies as the square of the Debye length (inversely with charge carrier concentration), so that the greater harvesting of charge carriers may be offset by increased recombination.

If the number of charge carriers in the Ti-doped and Si-doped RMS films is proportional to the number of dopant atoms that are substitutionally incorporated into the lattice (creating Fe^{2+} ions, inferred from N_D values) and we assume that

the remaining impurity is segregated at grain boundaries in an oxide phase, then the approximate thickness of the proposed TiO_2 or SiO_2 interfacial layers can be estimated. The percentage of dopant atoms that produce charge carriers is around 23 % and 0.6 % in Ti-doped and Si-doped α-Fe_2O_3 respectively. The resulting thickness of a TiO_2 or SiO_2 layer would be around 0.05 nm assuming a cubic grain packing. This small dimension suggests that the TiO_2 or SiO_2 phases could not exist as uniform layers between grains. However, presence of Ti and Si may still play a part in passivating grain boundaries.

The activation energy for electrical conductivity of the RMS hematite thin films was reduced by the introduction of Ti or Si. This suggests a change to the bulk properties of the material, rather than just a surface effect. As discussed, this may be due to the passivation of grain boundaries by the dopants. However, if grain boundary recombination was the rate-limiting step for hematite electrodes, then it would be expected that single crystals would perform substantially better than polycrystalline material, which is not generally true, see Figure 4.1. It is clear that α-Fe_2O_3 needs to be highly crystalline in order to produce a high photocurrent. However, it appears that surface recombination is likely to be the dominant factor limiting the performance of our hematite thin films, rather than recombination at grain boundaries.

Modelling the Ti-doped RMS α-Fe_2O_3 films using a Schottky barrier description estimated that the dominant charge transfer parameter (either L or w_d) is around 30 nm, with the other being small (< 1 nm). These values need to be considered in the context of the large uncertainties related to this analysis. Calculating the depletion layer width from $IPCE_{EE}/\alpha$ and directly from the electrical properties, gave values around 3 nm. If the depletion layer width is small, then the diffusion length would be the dominant parameter. However the large voltage dependence of the photocurrent is not consistent with charge transfer being dominated by diffusion. It is clear the the Schottky barrier model does not describe our IPCE data well and it is likely that model is too simplistic. For example the model assumes that no recombination is occuring within the depletion region; this is not a valid assumption for a low mobility material such as α-Fe_2O_3 (203). Hence the depletion layer width

may be underestimated due to recombination losses not being considered by the model. As briefly discussed in Section 2.4, the Schottky barrier model may not be entirely applicable for very thin films; a diffusion models may be more appropriate and are worthy of further investigation.

As discussed previously, a major limitation of α-Fe_2O_3 electrodes for water splitting is that a (frequently high) bias voltage is required. Hematite will not spontaneously split water due the the position of the band-edges. The required bias depends on the photocurrent onset potential and the shape of the current-voltage curve. A potential around 0.2 V/SCE is equivalent to the water splitting potential. Therefore, if a bias voltage exceeding 0.2 V/SCE is required, the water splitting efficiency of the electrode (according to Eq. 3.1) will be negative. The mechanisms related to the high onset potential of this material requires further investigation in order to design a material with smaller bias requirements. Currently hematite electrodes are only viable for water splitting when operated in a tandem-cell configuration, where a "free" bias is applied by a photovoltaic.

Significant findings from the α-Fe_2O_3 thin film study

- Doping was required to produce photocatalytically active RMS α-Fe_2O_3 films.
- Si-doped FAD α-Fe_2O_3 films probably inactive as a result of ineffective doping.
- Ti-doped RMS α-Fe_2O_3 showed significantly higher photocurrents than the Si-doped material, perhaps due to enhanced recombination at the surface and at grain boundaries.
- Both FAD and RMS α-Fe_2O_3 films exhibited preferred crystallographic orientation, with the basal plane aligned perpendicular to the substrate.
- Orientation of the films does not appear to affect the photocurrent, consistent with small differences in the potential drop in the film as a result of the resistivity.

- The poor performance of undoped RMS α-Fe_2O_3 is thought to be due to short charge carrier diffusion lengths or poor surface charge transfer.

- Increased photocurrent with doping attributed to enhanced surface charge transfer and some passivation of grain boundaries.

- Photocurrent onset potentials were reduced by doping, though still high relative to the water splitting potential. Hence the water splitting efficiency will be low unless a tandem cell configuration is used to provide a "free" bias voltage.

- Schottky barrier modelling of IPCE measurements with illumination from electrolyte and substrate sides showed that either the depletion layer width or the diffusion length is the dominant parameter, with a value around 30 nm. Calculated values of the surface transfer coefficient were similar to measured IPCE values, confirming that surface charge transfer is a major limitation for α-Fe_2O_3.

6.2 Nanostructured substrates

The second step in fabricating composite nanostructured electrodes was to develop the nanostructured substrates on which to deposit the hematite thin films. The results of the characterisation of the nanostructured SnO_2, ZnO and AZO substrates fabricated according to the processes described in Section 5.1.3 are discussed here.

6.2.1 SnO_2 nanorods

SnO_2 was selected for use as a nanostructured substrate for α-Fe_2O_3 thin films as it has a wide band-gap with a conduction band-edge below that of α-Fe_2O_3, and is electrochemically and chemically stable. The process to produce SnO_2 nanorods as presented by Vayssieres and Grätzel (138) (as described in Section 5.1.3) was undertaken, with the intention of modifying the growth process to produce high aspect ratio nanorods.

Initial attempts to fabricate the SnO_2 nanorods produced transparent, colourless films that were visible by eye (via interference fringes). SEM images confirmed that the surface was different to that of the FTO substrate, but no clear nanostructures were observed. As discussed in Section 5.1.3, consultation with Vayssieres led to several changes in the fabrication method. Some film structure was achieved by carefully preparing the growth solution, and changing the order of addition of the reagents. SEM micrographs of the most highly structured films are shown in Figure 6.33, where (A) is a top-view of the film with an inset showing square features that resemble those shown in the literature (138). In this case the structures appear

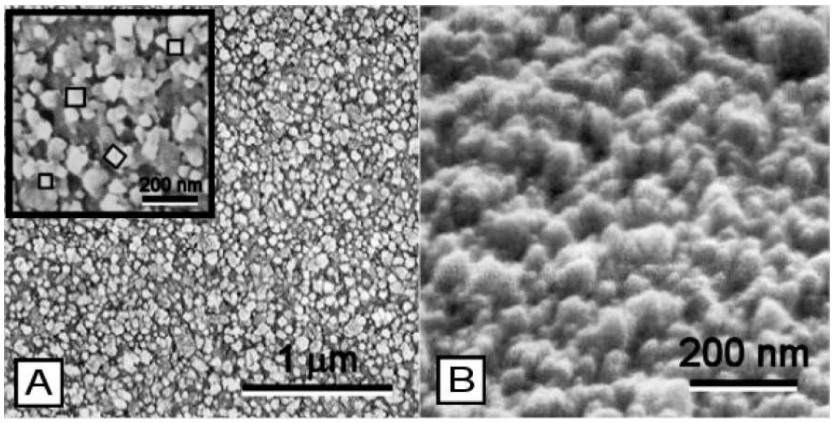

Figure 6.33: SEM micrographs of SnO_2 nanorod films: (A) top-view with inset showing square "rods" and (B) imaged at an angle of 60°.

to be clusters of square particles rather than nanorods. Figure 6.33 (B) shows the film imaged at 60°. Some columnar structure is evident, though high aspect ratio nanorods were not present. Modification of the growth solution to include slightly more tin chloride precursor produced similar films. The film shown in Figure 6.33 was grown for 2 days. Shorter growth times resulted in less visible structure. It is conceivable that very long growth times may improve the aspect ratio, but the precursor solution would require refreshing as the reactants were used up.

As discussed in Section 4.2.2, it is common for seed layers to be used to enhance the nucleation of nanostructures. In this case it might be expected that the FTO film on the glass substrate would act as a seed layer, given that it has the same

rutile SnO_2 (cassiterite) structure of the desired nanorods. However, this did not appear to be the case. SnO_2 thin films produced from previous depositions were used as seed layers for subsequent growths, but this did not improve the nucleation or growth of nanorods.

Arrays of SnO_2 nanorods were not achieved using this technique. The growth rate is slow, and at best produced nanorods with an aspect ratio of 1:10 (138). A higher aspect ratio would be required for these nanostructures to be suitable as a substrate for the hematite thin films. As discussed by Vayssieres and Grätzel, the probability of the rutile SnO_2 structure growing in the [001] direction (c-axis growth) is low, but can be increased by controlling the thermodynamics and kinetics of the synthesis process. It appears that the process is highly sensitive to the preparation conditions and is difficult to reproduce.

6.2.2 ZnO and AZO nanowire arrays

Since the SnO_2 nanorods were difficult to fabricate, ZnO nanostructures were investigated. The conduction band-edge of ZnO is higher than that of α-Fe_2O_3, so there will be an energy barrier to electron flow. This is problematic as the role of ZnO nanostructured material in the composite electrode is to conduct electrons from the α-Fe_2O_3 to the conducting substrate. The potential energy barrier to electron flow at the α-Fe_2O_3-ZnO interface could be reduced by heavily doping the ZnO. To this end, ZnO and Al-doped ZnO (AZO) nanowire arrays were fabricated. The results of the production and characterisation of the nanostructures are presented here.

Firstly, optimisation of undoped ZnO nanowire arrays was undertaken to produce nanowires of suitable diameter, length and coverage. Two very important steps in the procedure for producing high-quality nanowire arrays are the deposition of a seed layer before hydrothermal growth to assist the nucleation of the nanowires, and the addition of polyethylenimine (PEI) to restrict lateral growth of the nanowires allowing a high aspect ratio to be achieved.

Seed layers

The hydrothermal growth processes developed by Vayssieres *et al.* do not require the use of a seeded substrate. However, many researchers (117, 121, 140) have found a seed layer necessary to produce uniform, well aligned arrays of nanostructures. This was certainly the case in this study.

ZnO seed layers were applied to the conducting glass substrates by spin-coating or dip-coating ZnO sol-gel solutions, or via the thermal decomposition of zinc acetate. The ZnO nanowire arrays grown on the seeded substrates were of higher quality (greater packing density and uniformity) than those grown on unseeded substrates. Figure 6.34 shows SEM micrographs of ZnO nanowire arrays grown (A) without a seed layer, (B) from a spin-coated seed layer, (C) from a dip-coated seed layer and, (D) from seeds produced by the decomposition of zinc acetate. Films grown without first depositing a seed layer, were of very poor quality. Large diameter (> 1 μm), low aspect ratio nanorods were produced, which were poorly tethered, not aligned and sparsely distributed. The inclusion of a seed layer provides nucleation points for the nanowire growth. If the seeds are large and/or have a wide size distribution, as was the case with the dip-coated and spin-coated sol-gel seed layers (as shown in Figure 6.35), inhomogeneous nanowire growth results (Figure 6.34 (B) and (C)). Spin coating was found to produce superior seed layers to dip-coating. However, in both cases uniformity of the nanowire arrays was poor, with microrods and disordered clusters of nanorods often observed. Slow dipping rates were found to produce more uniform films than faster dipping rates. Better results were observed when spin-coating using ethanolic solutions (50 vol. %), rather than aqueous solutions, which improved substrate wetting. The film quality was improved somewhat by treating the sol-gel solutions with ultrasound (to break up particle flocs, reducing the size of the seeds). The sol-gel seed layers were often visible by eye and milky in colour. The better films were less milky and highly transparent, indicating smaller particle sizes.

The decomposition of the zinc acetate to form a nanoparticulate ZnO film produced, by far, the best seed layers. These layers consisted of very small particles

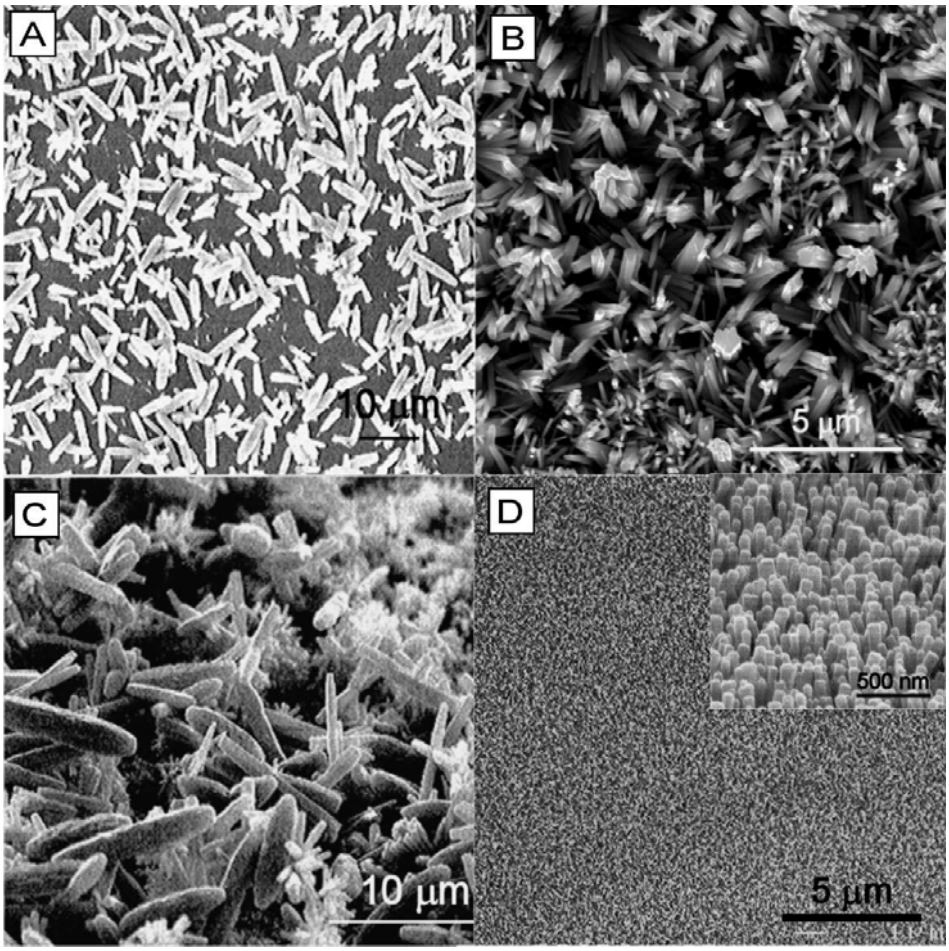

Figure 6.34: SEM micrographs of ZnO structures grown under different seeding conditions. (A) Untethered microrods grown without a seed layer. (B) Disordered nanowire arrays grown from a spin-coated seed layer. (C) Dense, untethered microrods and structures grown from a dip-coated seed layer. (D) High quality ZnO nanowire arrays grown from seeds produced by the decomposition of zinc acetate.

that were not visible by eye or electron microscopy. The nanowire arrays grown from these very small seed crystals were uniform, densely-packed, and well-aligned, as shown in Figure 6.34 (D) with excellent coverage over the several cm^2 substrate.

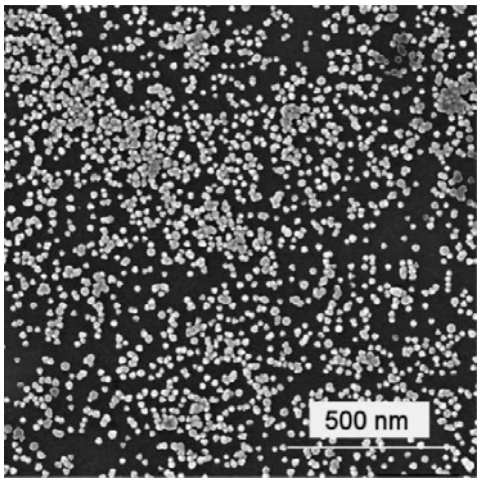

Figure 6.35: Seed layer produced from spin-coating a sol-gel solution.

The orientation of the seeded substrates in the bottles during growth of the nanowire arrays was found to have an effect on the quality of the films. Initially the substrates were placed in the bottom of the bottles, with the seeded layer upright. However, this allowed precipitate to fall on the surface during deposition, which was providing nucleation sites for the microrod and secondary nanowire growth, as shown in Figure 6.36. Leaning the substrates against the side of the bottle or fixing them to a support, to allow the seeded surface to face downwards, improved the homogeneity of the films. In this position though, bubbles can collect underneath the substrate which prevent nanowire growth (Figure 6.37). This effect was limited by periodically tapping the bottles to remove the bubbles.

PEI addition

PEI was added to the growth solution in order to restrict the lateral growth of the nanowires and allow the growth of high aspect ratio nanostructures. SEM images of the optimised ZnO nanowire arrays grown with the addition of PEI from seeds produced by the decomposition of zinc acetate are shown in Figure 6.38. A growth

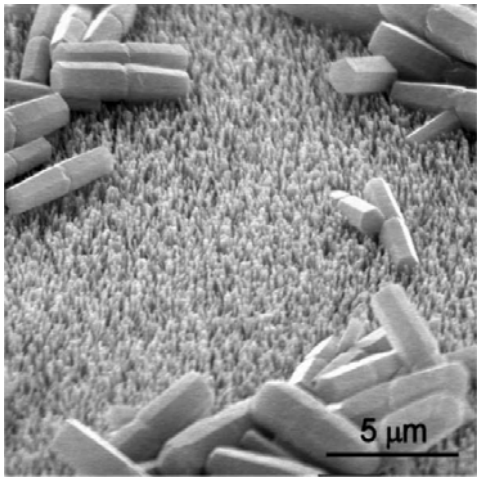

Figure 6.36: SEM micrographs of a ZnO nanowire array grown with the seed layer facing upwards. The large nanorods form as a result of precipitate from the growth solution falling on the substrate.

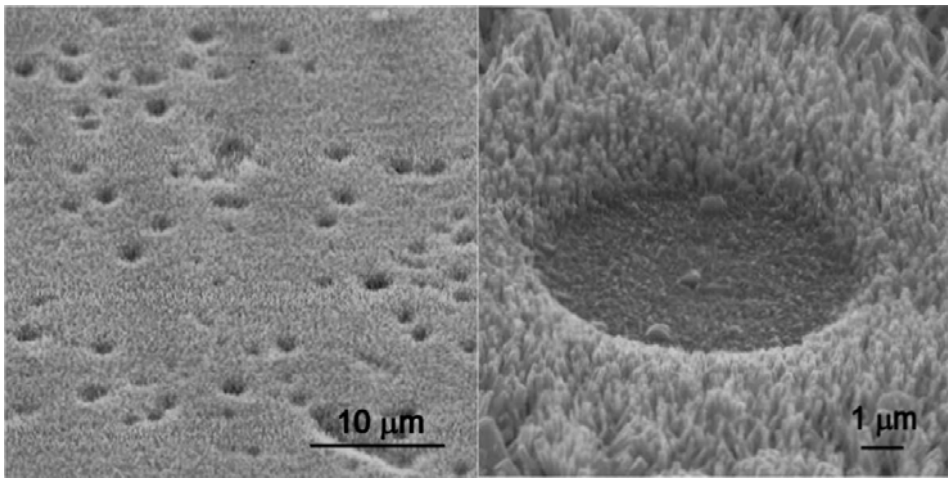

Figure 6.37: SEM micrographs of craters in the ZnO nanowire array caused by bubbles preventing nanowire growth.

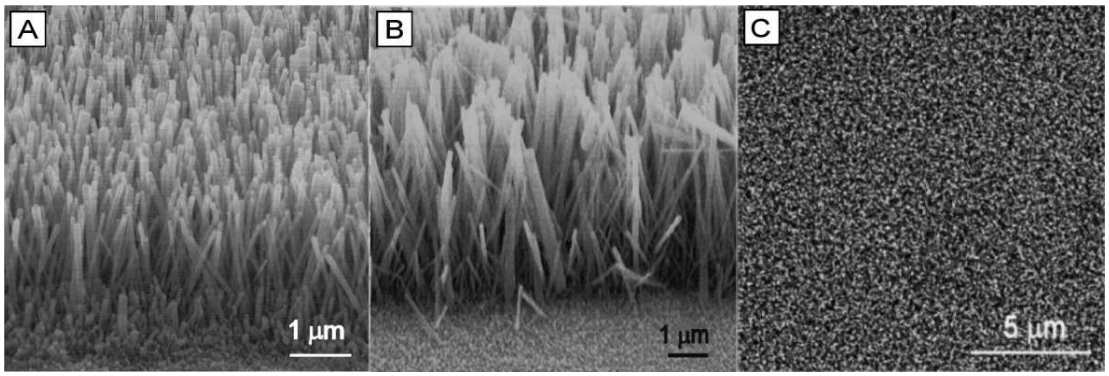

Figure 6.38: SEM micrographs of optimised ZnO nanowire arrays (A) 18 hr deposition, and (B) and (C) 24 hr deposition, grown with the addition of PEI from seeds produced by the decomposition of zinc acetate.

time of 18 hr (Figure 6.38 (A)) produced nanowires around 1.7 μm in length. Longer growth times, up to 24 hr (Figure 6.38 (B)) produced 3-4 μm long nanowires. However, it can be seen that the longer nanowires begin to clump due to nanowires not growing exactly perpendicular to the substrate.

Figure 6.39 shows histograms of the size distribution of (A) the nanowire diameter and (B) inter-nanowire spacing of the optimised ZnO nanowire arrays shown in Figure 6.38 (A). There is a wide distribution of inter-nanowire spacings, though 75% of the nanowires are spaced a distance of 1-5 times the diameter from each other. The average nanowire diameter and inter-nanowire spacing is 61 $\pm$ 23 nm, and 169 $\pm$ 106 nm respectively. The aspect ratio of these nanowires (assuming a length of 1.7 μm) is around 28, and the surface area per unit area is around 12.5.

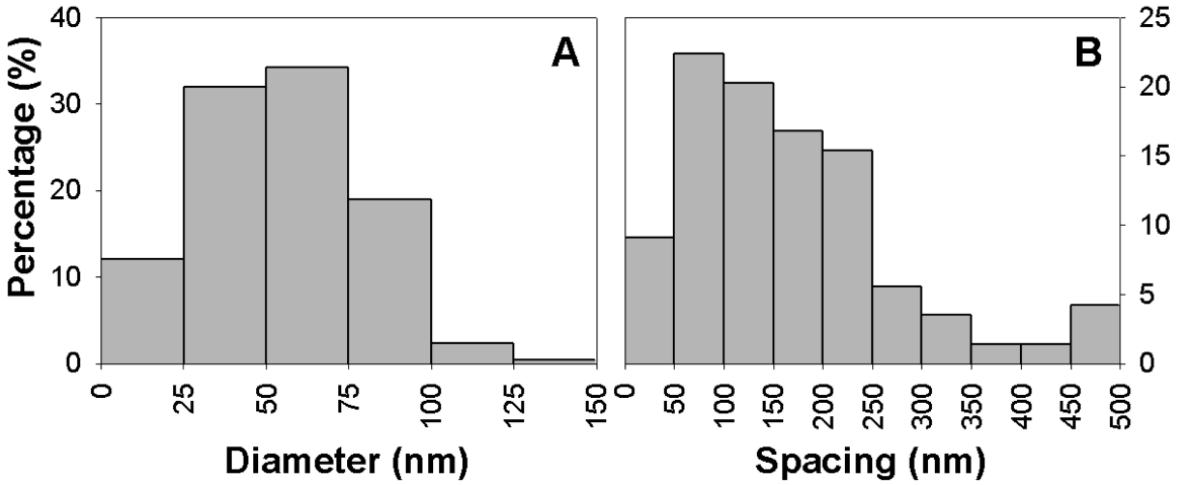

Figure 6.39: Histograms showing the size distribution of (A) the nanowire diameter and (B) inter-nanowire spacing of the optimised ZnO nanowire arrays shown in Figure 6.38.

Aluminium doping

After the procedure for producing ZnO nanowire arrays was optimised, an aluminium precursor was introduced in the growth solution to produce AZO nanowire arrays. Figure 6.40 shows SEM images of an Al-doped ZnO (AZO) nanowire array compared to an undoped sample prepared under identical conditions. It can

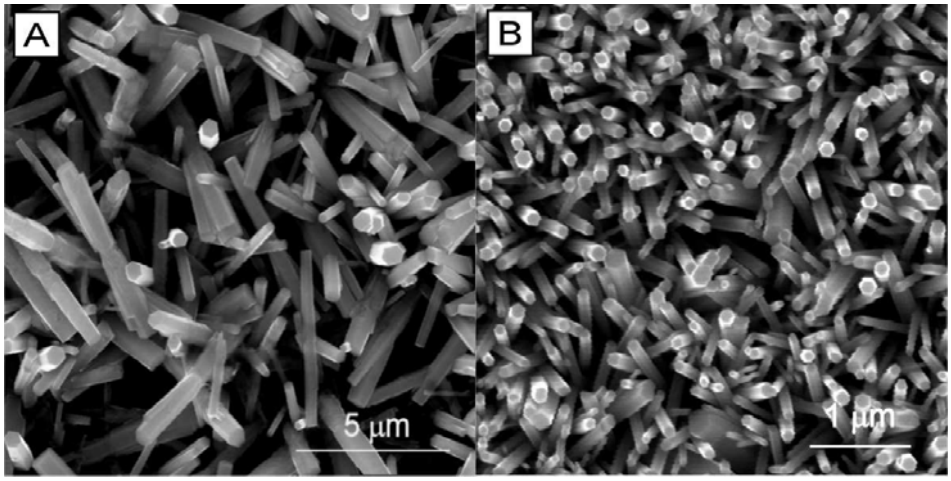

Figure 6.40: SEM micrographs of (A) an Al-doped ZnO nanowire array, showing poor alignment, packing density and uniformity, compared to (B) an undoped ZnO nanowire array prepared under identical conditions.

be seen that the addition of the dopant has a detrimental effect on the alignment, packing density and uniformity of the nanowires. This result has also been observed by others (121). The presence of aluminum was confirmed using EDS, showing an elemental doping level of 0.28 % $\pm$ 0.11 % (normalised to the percentage of Zn). The form of the Al-dopant and homogeneity of its distribution throughout the nanowires is unknown.

The electrodeposition of doped ZnO was attempted following the procedure of Cui and Gibson (121) who reported that the application of a voltage to the substrate removed the need for seeding and assisted the introduction of dopants. Poor quality nanowire arrays were formed using this process, as shown in Figure 6.41. No improvement in the film quality was achieved using seeded substrates, and the addition of Al further degraded the quality of the films.

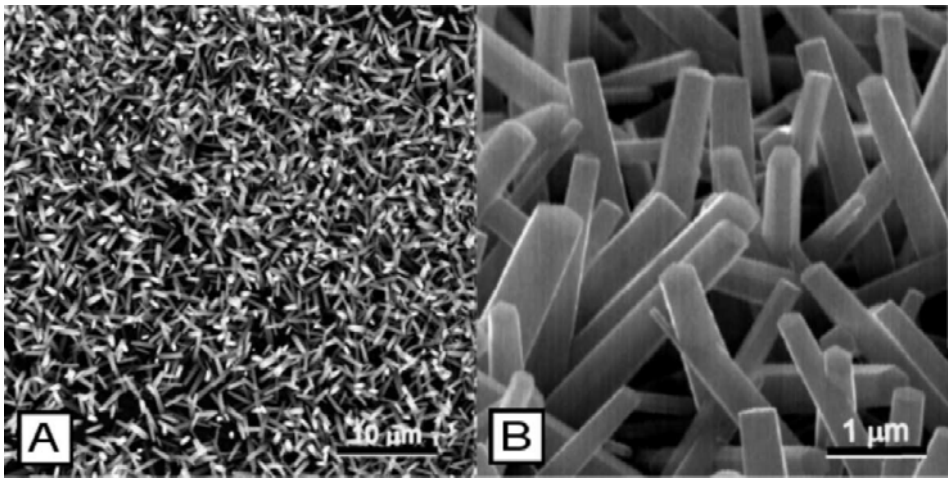

Figure 6.41: SEM micrographs of electrodeposited ZnO nanowire arrays: (A) top-view and (B) imaged at an angle of 60°.

The aspect ratio and packing density of the Al-doped ZnO nanowires is low and will not provide a high enough surface area for use as a substrate for the α-Fe_2O_3. The undoped ZnO nanowires will be used for further investigation of the nanostructured composite electrode concept. It is likely that electron transfer from the hematite to the ZnO will be difficult due to the potential energy barrier arising from the mismatch of conduction-band edges. The ZnO nanowire arrays do, however, provide a high surface-area nanostructured substrate, and can be used as the substrate for the three-layer composite electrode (as described in Section 1.2).

Significant findings from the nanostructured substrate study

- The method to fabricate SnO_2 nanorods was highly sensitive to the preparation conditions and high aspect ration nanorods were not produced.
- The growth of dense, well-aligned, high aspect ratio ZnO nanowire arrays was achieved by;
  - the deposition of a seed layer, and
  - the addition of a lateral growth restricting agent.

- Al-doping had a detrimental effect on the alignment, packing density and uniformity of the ZnO nanowires.

- The AZO nanostructures do not have high enough surface area for use as substrates for α-Fe_2O_3 thin films

- The undoped ZnO nanowire arrays will be used as nanostructured substrates for further investigation of the composite electrode concept.

6.3 Nanostructured composite electrodes

6.3.1 Design and modelling

The nanostructured composite electrode concept was devised as a method for combating the short diffusion lengths of charge carriers in α-Fe_2O_3. Very short hole diffusion lengths of 2 - 4 nm have been quoted in the literature (26). If this is the case, then it is expected that the use of very thin α-Fe_2O_3 films, of a few diffusion lengths in thickness, will reduce recombination by limiting the distance that holes need to travel to reach the electrolyte. Such films would need to be 10 - 20 nm in thickness, much too thin to absorb a significant fraction of the incident solar illumination. Hence it is hypothesised that coating thin films of α-Fe_2O_3 onto nanostructured substrates will provide a long path length for absorption, while allowing the α-Fe_2O_3 to be thin enough to efficiently extract the generated charge carriers.

In order to maximise the amount of the incident radiation absorbed by the electrode, a long path length in the α-Fe_2O_3 is necessary. This can be achieved by multiple reflections/passes through the thin film. Therefore the nanostructured substrate must provide a large surface area so that the α-Fe_2O_3 layer can be restricted to a thin film. It should be noted that if the hole diffusion length in α-Fe_2O_3 could be increased (or is not actually as short as predicted), then thicker films could be used. The thickness of a hematite film required to absorb all of the incident solar

photons was calculated using Eq. 6.7 and Eq. 6.8.

$$I_\alpha(\lambda) = I_0(\lambda)(1 - e^{-\alpha t}) \tag{6.7}$$

$$f = \frac{\int_{\lambda_0}^{\lambda_c} I_\alpha(\lambda)\, d\lambda}{\int_{\lambda_0}^{\lambda_c} I_0(\lambda)\, d\lambda} \tag{6.8}$$

The magnitude of the absorbed solar photon spectral flux (I_α) as a function of wavelength (λ) is described by Eq. 6.7, where I_0 is the incident solar photon spectral flux (photons $m^{-2}s^{-1}nm^{-1}$), α is the optical absorption coefficient (shown in Figure 6.19 (A) for our films) and t is the thickness of the film. This function can be integrated over a range of wavelengths (in this case λ_0 is 280 nm and the λ_c is the band-gap wavelength of α-Fe_2O_3 of 564 nm) to give the total number of absorbed photons. By dividing the number of absorbed photons by the total number of photons available in this range of the solar spectrum a fraction f can be calculated for a particular film thickness (Eq. 6.8).

Figure 6.42 shows a graph of the fraction of the available solar photons absorbed by a hematite film as a function of film thickness. It can be seen that a film thickness around 500 nm is required in order to absorb essentially all of the available photons up to the band-gap wavelength. In the case of the nanostructured electrode design a path length equivalent to a film thickness of 500 nm is required, rather than a 500 nm thick film. These same data are presented in Figure 6.43 as the proportion of the AM1.5 solar spectrum absorbed by films of various thicknesses as a function of wavelength. A ray-tracing model was developed by I. Plumb in order to calculate approximate path lengths in an array of coated nanowires, assuming ideal 2-D geometry. While the wavelengths of visible and near-ultraviolet radiation are greater than the lateral dimensions of the nanowire arrays being considered, so that use of geometrical optics is not justified, and the idealized geometries used by the model will not be achievable in practice, such a model is expected to provide some guidance for path lengths in proposed array structures, and should allow the main design parameters to be identified to maximize path lengths in the photo-active material. Calculations were made for a regular array of nanowires, of length 10 μm,

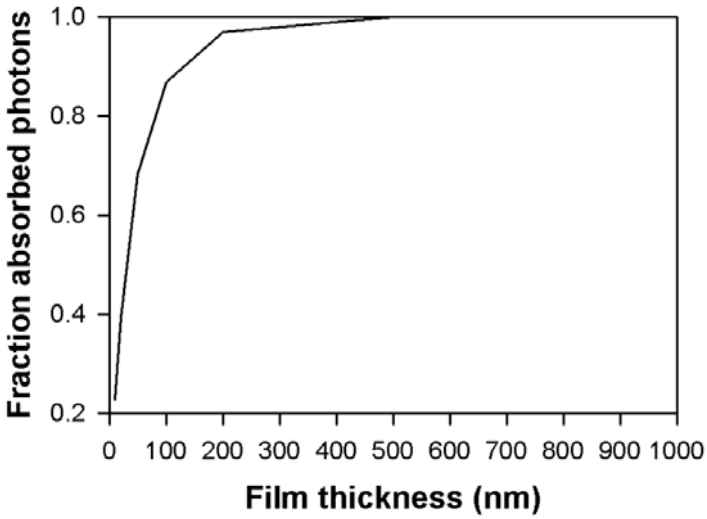

Figure 6.42: Fraction of the available solar photons absorbed by a hematite film as a function of film thickness.

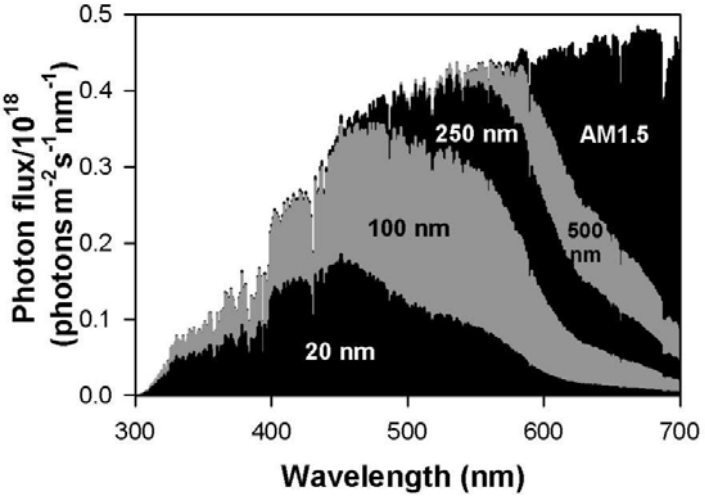

Figure 6.43: Proportion of AM1.5 solar spectrum absorbed by hematite films of various thicknesses.

diameter 100 nm, with a uniform coating of 10 nm thickness of photo-active material on the rods. The refractive indices of the rods, coating and space between the rods were assumed to be 2.0 (corresponding to ZnO), 3.0 (corresponding to α-Fe_2O_3) and 1.33 (corresponding to H_2O), respectively. Nanowire separations of 100 - 400 nm and angles of incidence of 10°- 80° were considered. Absorption in the photo-active material and in the nanowires were not considered; the model simply calculates the path lengths through different components of the structure.

For a dense array of nanowires with an average separation of 100 nm (d = 200 nm in Figure 6.44), calculated average path lengths in the photo-active material were found to range from approximately 1 μm for a 10° angle of incidence (with respect to the vertical axis of the wires) to almost 6 μm for an 80° angle of incidence. If the volume of active material on the nanorods was distributed onto the substrate as a flat film, the film thickness would be approximately 700 nm (depending on the packing geometry of the nanowires). Because of the large refractive index of the hematite, this would be close to the path length through the thin film for a range of incident angles. Hence, the path lengths through the hematite deposited on the nanowires is greater than that for a thin film containing the same volume of active material by factors of 1.4 to 8. If the nanorod separation is increased from 100 nm to 400 nm (d = 500 nm) , the calculated path lengths through the photo-active material range from 220 nm for a 10° angle of incidence to 2.5 μm for an 80° angle of incidence. In this case, the corresponding film thickness for a film containing the same volume of photo-active material is 130 nm, so the path lengths in the nanowire structure are greater by between factors of 1.7 and 19, although the overall path lengths are reduced relative to the case with 100 nm wire separation. Not surprisingly, the calculations show that dense, high aspect ratio nanowire arrays produce the longest optical paths in the nanostructured arrays. For a sparsely spaced array, much of the optical path is in the spacing between the nanowires.

Calculations were undertaken to determine the required geometry of the nanostructure for α-Fe_2O_3 films of optimum thickness (5 - 10 nm). An array of cylindrical nanowires was considered as the model geometry, as shown in Figure 6.44. (A) shows a cross-sectional view of the coated nanowires with a radius r, length l, and spacing

between adjacent nanowires d. A hematite film of thickness t is deposited uniformly over the surface of the nanostructure. Figure 6.44 (B) shows a top-view of the nanowires where a "unit-cell" is indicated by a shaded region. The surface area (per cm^2) is linearly dependent on the aspect ratio of the nanowires. From Figure 6.42,

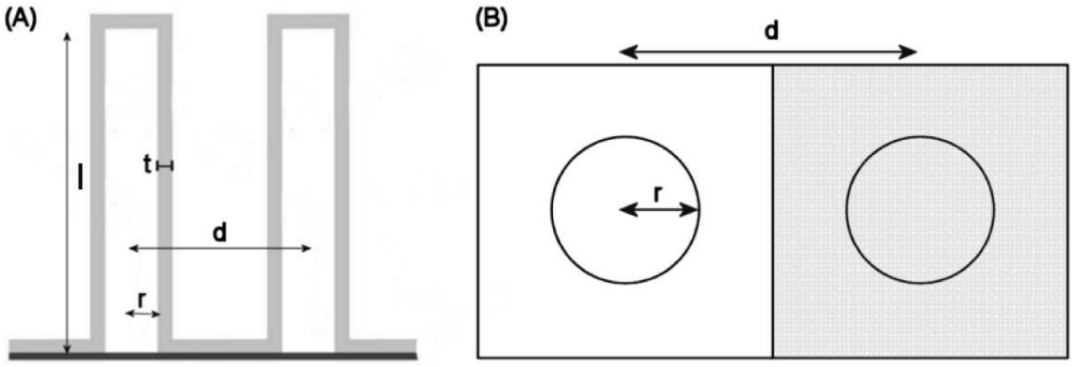

Figure 6.44: (A) cross section of nanowires and (B) top view of nanowire unit cell where r is the radius of the nanowire, d is the spacing between adjacent nanowires, l is the length of the nanowires and t is the thickness of the α-Fe_2O_3 film.

the film thickness required to absorb a certain fraction of the AM1.5 standard solar flux can be determined. For example, to absorb 98 %, 87 %, 68 % or 40 % of the solar flux up to 564 nm requires flat α-Fe_2O_3 films (or equivalent path lengths) of 250 nm, 100 nm, 50 nm or 20 nm respectively. For a given α-Fe_2O_3 coating thickness, the required surface area and aspect ratio of the nanostructured substrate can be determined (assuming a nanowire spacing of d = 4r), as shown in Table 6.5. The data shown in Table 6.5 are presented graphically in Figure 6.45. It can be seen that the thinner the hematite film, the higher the aspect ratio of the nanowires need to be to provide a sufficient path length to absorb a significant proportion of the incoming photons. The effect of nanowire packing density on the aspect ratio as a function of α-Fe_2O_3 film thickness is shown in Figure 6.46 for d = 2r, 4r and 8r. For a given α-Fe_2O_3 film thickness, the aspect ratio (AR) is related to the spacing d by a power law such $AR = Cd^2$, where the coefficient C is a constant inversely proportional to the film thickness. Hence a low packing density of nanowires has the disadvantage of requiring much higher aspect ratio features. Modelling the

α-Fe_2O_3 film thickness (nm)	**SA/cm^2 98% abs.**	**Aspect ratio 98% abs.**	**SA/cm^2 87% abs.**	**Aspect ratio 87% abs.**	**SA/cm^2 68% abs.**	**Aspect ratio 68% abs.**
2	125	316	50	125	25	61
5	50	125	20	48	10	23
10	25	61	10	23		
20	12.5	29	5	10	2.5	4
50	5	10	2	2.5	1.25	0.6

Table 6.5: Surface area per unit area and aspect ratio of a nanowire array required to provide adequate path length through α-Fe_2O_3 coatings of various thicknesses in order to absorb certain fractions of the AM1.5 standard solar spectrum.

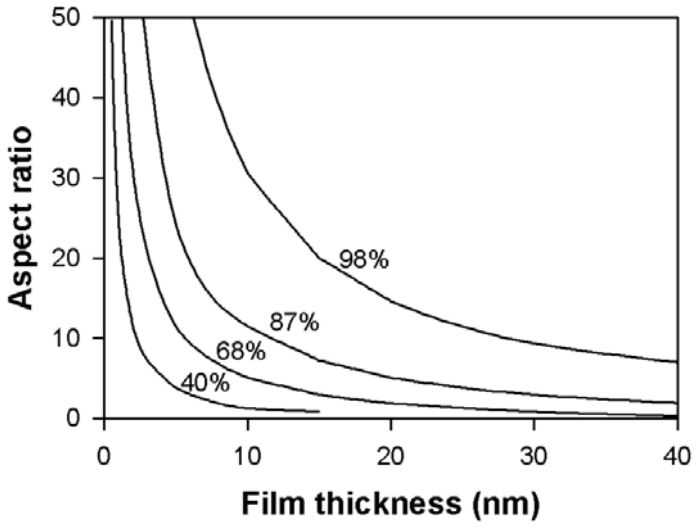

Figure 6.45: Aspect ratio of nanostructure required to absorb certain fractions of the incident solar spectrum as a function of hematite film thickness, assuming the ideal geometry shown in Figure 6.44 with a spacing d = 4 × the nanowire radius.

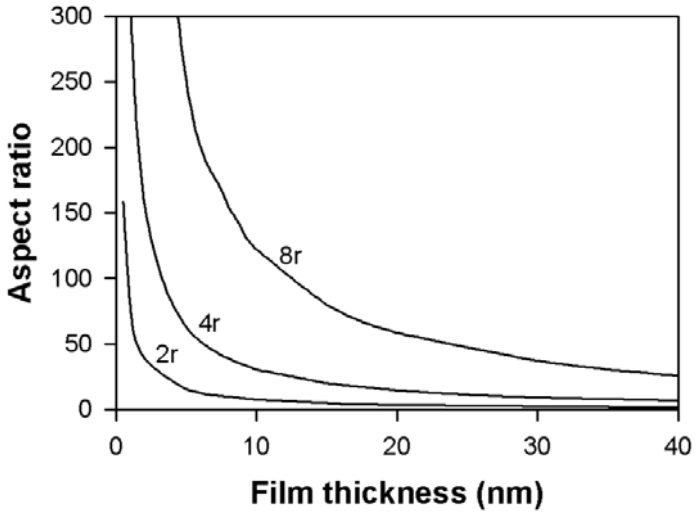

Figure 6.46: Aspect ratio of nanostructure of radius r, and inter-nanowire spacings 2r, 4r and 8r, required to absorb 98 % of the incident solar spectrum as a function of hematite film thickness, assuming the ideal geometry shown in Figure 6.44.

nanostructured electrodes showed that: close-packed, high aspect ratio nanowires are required to provide a high surface area for hematite deposition; a higher aspect ratio of nanowires is required for thinner hematite films; and a path length of over 500 nm is required to absorb essentially all of the incident solar photons. However, 100 nm will absorb 87 % of the incident photons. These conclusions raise issues regarding the process of fabricating the electrodes. It would be expected that, because of shadowing, it would be difficult to coat densely-packed, high-aspect ratio arrays with a uniform coating of α-Fe_2O_3 using vacuum deposition processes. Figure 6.47 shows schematic diagrams of some possible coating configurations. Figure 6.47 (A) shows the ideal case where a thin, uniform α-Fe_2O_3 layer is deposited over the entire nanostructured array. However, it is likely in practice that non-uniform coatings will be formed. The α-Fe_2O_3 may simply cap the nanostructured array and not penetrate between the nanowires (Figure 6.47 (B)), or partially coat the bottom of the array producing a non-uniform coating, Figure 6.47 (D). If the spacing between the nanostructures is not significantly larger than the α-Fe_2O_3 film thickness, then it is likely that the nanostructured array will be filled with α-Fe_2O_3, Figure 6.47 (C). The uniformity of the coating will depend on the aspect ratio and packing density of the nanostructure array and the characteristics of the coating technique. Non-uniform coatings would mean that the proposed advantages of the nanostructured substrate would be reduced. For instance, if the full length of the nanowire was not being utilised, then the increase in surface area would not be as great. There may also be problems with charge transfer if the α-Fe_2O_3 films are significantly thicker than the diffusion length of minority carriers.

In practice, the fabricated nanowire arrays are far from the ideal case assumed for the modelling (as seen in Section 6.2.2). In the case of the ZnO nanowire arrays the angle of nanowire growth will depend on the orientation of the seed particle. Nanowires growing at a higher angle from the normal will terminate when they reach another nanowire, allowing the more highly aligned nanowires to grow longer. This non-uniformity may reduce the quality of the α-Fe_2O_3 coating. Disorder in nanowire arrays has been shown to affect the light propagation (204). Disorder in the placement of the nanowires enhances absorption, while randomly varying the

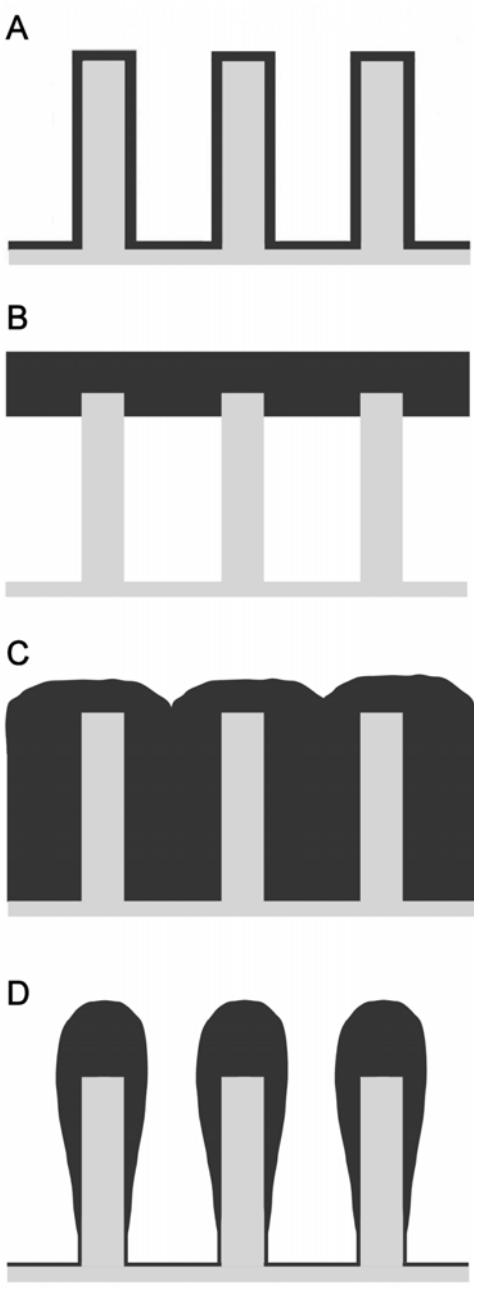

Figure 6.47: Schematic diagrams of various possible configurations of the α-Fe_2O_3 thin films coated onto the nanostructured substrate. (A) ideal coating of uniform thickness, (B) capping of the nanostructures with a thicker than desired film, (C) thick coating of α-Fe_2O_3 filling in the nanostructure array, and (D) non-uniform coating.

nanowire diameters had a smaller effect.

6.3.2 Experimental results and discussion

Initially films of α-Fe_2O_3 > 100 nm in thickness were deposited onto ZnO nanowires, in order to determine the feasibility of coating high aspect ratio structures with vacuum deposition techniques. Figure 6.48 shows scanning electron micrographs of the ZnO nanowire arrays before (A) and after (B, C) being coated with α-Fe_2O_3 using FAD. Figure 6.48 (C) shows a sample that has been sectioned using a focused ion beam mill. The sample was cross-sectioned at 52° to the vertical, hence the lower part of the image is deeper within the array. The brighter areas on the images (indicated by the arrows) are the α-Fe_2O_3 film. The FAD deposition is quite directional, hence the uneven deposition of iron oxide. The substrates were scanned back and forward across the plasma beam during deposition to minimise this difference. Samples that were not scanned had larger amount of α-Fe_2O_3 deposited on the tips of the nanowires. The RMS samples were not moved during deposition. Although not a uniform coating, these images indicate that reasonable coatings of high aspect ratio nanostructured substrates are possible with vacuum deposition techniques. The undoped ZnO nanowire arrays were the only available nanostruc-

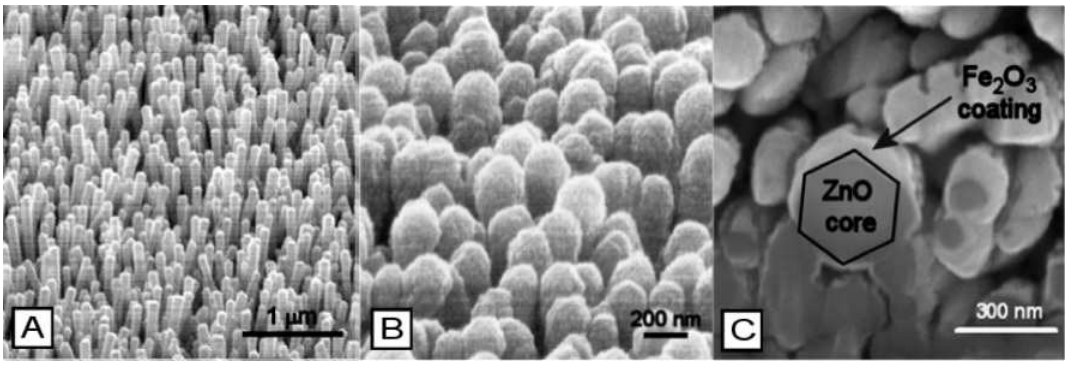

Figure 6.48: SEM images of ZnO nanowire arrays. (A) uncoated nanowires (60 nm diameter), (B) coated with α-Fe_2O_3 using FAD and (C) cross-section of coated nanowires.

tured substrate for this study, and the interface between ZnO and α-Fe_2O_3 is likely

to produce a large potential barrier for electron flow. Therefore the three-layer composite electrode design was employed in order to utilise the large surface area of the ZnO, while achieving electron conduction via a more suitable interlayer material. To this end, ITO films were deposited onto ZnO nanowire arrays, before the deposition of Ti-doped RMS α-Fe_2O_3 films.

α-Fe_2O_3 films were deposited onto nanostructured ZnO substrates as well as blank conducting glass, to fabricate composite electrodes and planar control films respectively. Control α-Fe_2O_3 films were fabricated with and without the ITO interlayer. The photoelectrochemical properties were measured throughout each stage of the depositions (uncoated ZnO, ITO coated ZnO and final composite electrode) to determine the contribution from each layer. α-Fe_2O_3 film thicknesses of 5 nm and 20 nm were deposited; 5 nm was selected because of the diffusion length of 2-4 nm quoted by Kennedy *et al.* (26), and 20 nm was selected because of the results of the Schottky barrier modelling that suggested the dominant charge transfer parameter could be around 30 nm. The surface area per cm^2 of the ZnO nanowire arrays was around 12.5. Therefore the thicknesses of the planar control films (to give an equivalent volume of absorbing material) for the 5 nm composite electrode and the 20 nm composite electrode are 62.5 nm and 250 nm respectively. The measured film thicknesses (from step-edge profilometry) of the 5nm and 20 nm control α-Fe_2O_3 films were 65 $\pm$ 5 nm and 270 $\pm$ 5 nm respectively.

Figure 6.49 shows photocurrent density as a function of voltage (vs. SCE) curves for the composite electrodes compared to the planar control α-Fe_2O_3 films, for (A) the 20 nm α-Fe_2O_3 electrodes, and (B) the 5 nm α-Fe_2O_3 electrodes. It can be seen that the addition of an ITO layer between the planar α-Fe_2O_3 control film and the FTO substrate substantially decreases the photocurrent. There is also a shift in the onset potential to higher voltages (see Table 6.6) indicating that a potential energy barrier to electron flow is present; perhaps resulting from an inadequate electron conductivity of the ITO film, or from an inferior α-Fe_2O_3 layer at the interface. Two composite electrodes were fabricated for each α-Fe_2O_3 film thickness, where the ZnO nanowire substrates were grown in different batches. The photocurrents of the composite electrodes using ZnO nanowires from one batch are a lot higher than

Sample	**Layers**	V_{onset} **(V/SCE)**
20 nm equivalent control	α-Fe_2O_3, FTO	-0.15
20 nm equivalent control, ITO	α-Fe_2O_3, ITO, FTO	-0.1
20 nm composite	α-Fe_2O_3, ITO, ZnO, FTO	-0.1
20 nm composite (no ITO)	α-Fe_2O_3, ZnO, FTO	-0.25
5 nm equivalent control	α-Fe_2O_3, FTO	-0.15
5 nm equivalent control, ITO	α-Fe_2O_3, ITO, FTO	-0.05
5 nm composite	α-Fe_2O_3, ITO, ZnO, FTO	-0.25

Table 6.6: Onset potentials from current-voltage curves of the composite electrodes and control films shown in Figure 6.49.

that of those from the other batch. SEM imaging showed that the latter batch of ZnO nanowires were less uniform and had more defects (due to bubbles collecting on the surface) than the other batch. Hence it is clear that the photocurrent of the composite electrode is highly dependent on the quality of the nanostructured substrate. A 20 nm α-Fe_2O_3 film was also deposited directly onto ZnO, without an ITO interlayer (Figure 6.49 (A)). This sample has a surprisingly high photocurrent given the potential barrier to electron flow expected at the ZnO - α-Fe_2O_3 interface. However most of this photoactivity can be attributed to the ZnO (see Figure 6.51).

IPCE curves as functions of wavelength are shown in Figure 6.50 through to Figure 6.53, where (A) in all cases is data measured with electrolyte-electrode (EE) illumination, and (B) in all cases is data measured with substrate-electrode (SE) illumination. All curves shown are raw data, with no corrections for reflection undertaken. The drop in the $IPCE_{SE}$ values at short wavelengths is predominantly due to the absorption of the conducting glass substrate.

Figure 6.50 shows the IPCE curves of the planar α-Fe_2O_3 control films, with and without an ITO interlayer. As expected from the photocurrent-voltage curves, the ITO interlayer causes a decrease in the IPCE values of the α-Fe_2O_3 films. Figure 6.51 shows the IPCE curves of ZnO nanowire substrates both uncoated and coated with ITO. The uncoated ZnO exhibits good photoactivity up to its cut-off wavelength around 400 nm. For the purposes of analysing the composite electrodes the

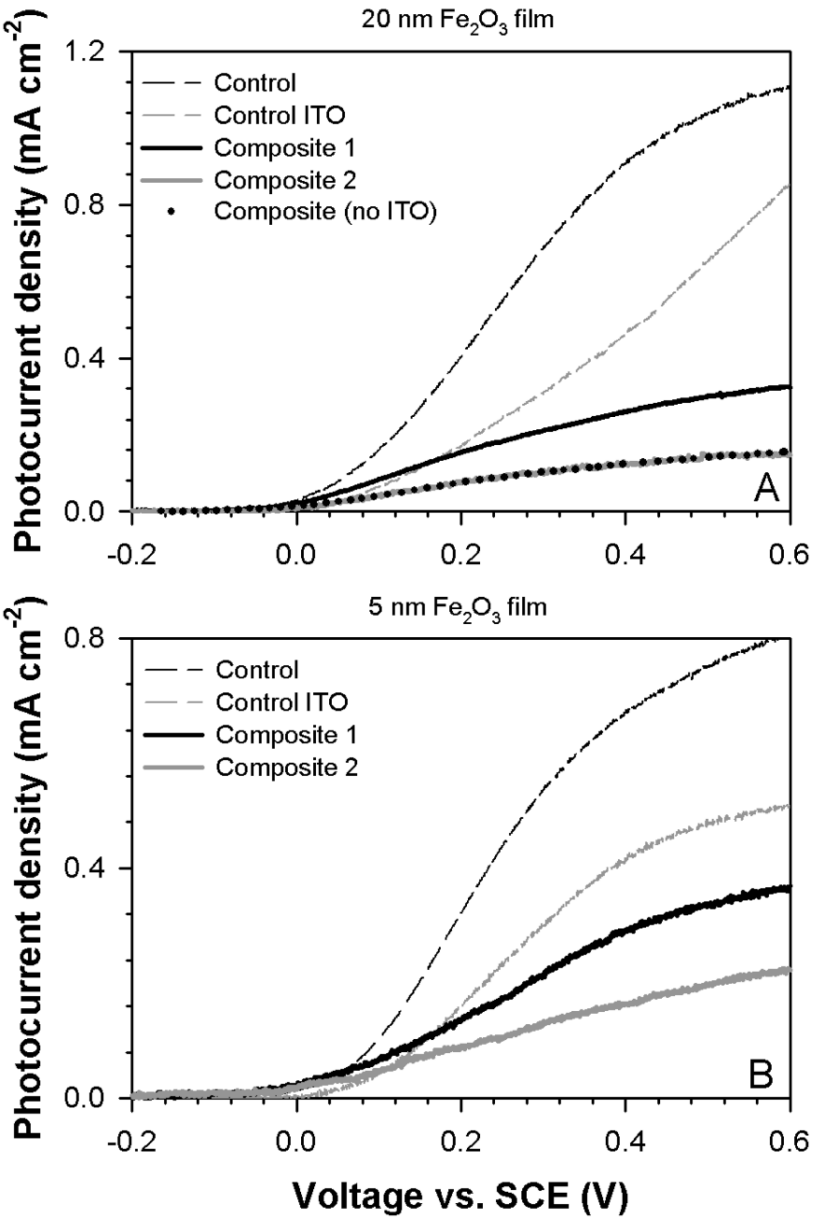

Figure 6.49: Photocurrent vs. voltage (V/SCE) for (A) the 20 nm α-Fe_2O_3 electrodes, and (B) the 5 nm α-Fe_2O_3 electrodes, compared to the planar control α-Fe_2O_3 films.

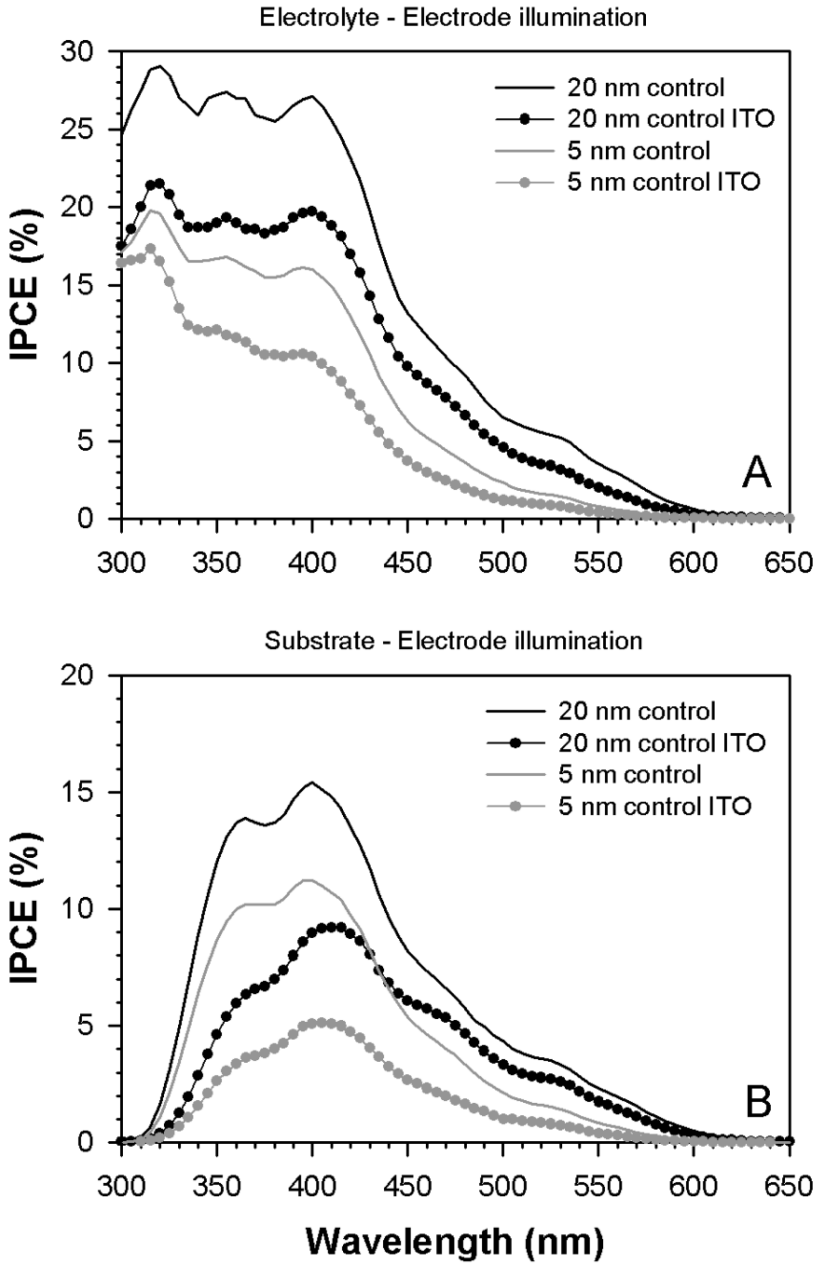

Figure 6.50: IPCE curves as functions of wavelength (0.5 V vs. SCE). (A) Electrolyte-electrode illumination measurements, and (B) substrate-electrode illumination measurements, for 270 nm thick (20 nm equivalent) and 65 nm thick (5 nm equivalent) planar α-Fe_2O_3 films used as controls for the composite electrode study.

photoactivity of the ZnO is undesirable as it complicates the interpretation of the photoelectrochemical measurements. When an ITO layer is deposited onto the ZnO nanowires, the IPCE decreases markedly, up to a factor of twenty at the shortest wavelengths. The photocatalytic reaction from the ZnO is being impeded by the presence of the ITO (absorbing incoming radiation as well as providing a barrier for the electrolyte). The characteristic peak of the ZnO at 380 nm is visible throughout the IPCE measurements of the composite electrodes, indicating that some electrolyte is penetrating the ITO film and reaching the ZnO. The IPCE values from the substrate-electrode illumination measurements did not show as large a decrease with the ITO film present as the light is absorbed in the ZnO film first.

The IPCE curves of the composite electrodes are compared to the α-Fe_2O_3 control films (with the ITO interlayer) and a ZnO nanowire substrate (with an ITO coating) in Figure 6.52. The IPCE curves of the composite electrodes have a similar shape to that of the control films (other than the ZnO peak at 380 nm), however the magnitude is significantly less. The IPCE values of the composite electrodes measured with SE illumination are very similar in shape to the ZnO control, but with obvious contribution from the α-Fe_2O_3 at long wavelengths.

The IPCE curves of a 20 nm α-Fe_2O_3 film deposited onto a ZnO nanowire array substrate (without an ITO interlayer), compared to a 20 nm α-Fe_2O_3 composite electrode, the ZnO control (no coating) and 270 nm thick (20 nm equivalent) α-Fe_2O_3 control film in Figure 6.53. Interestingly, the film deposited directly onto the ZnO nanowires has a similar $IPCE_{EE}$ to the better 20 nm composite electrode. This is suggesting that the addition of the ITO interlayer is not improving the electron transfer as expected. The $IPCE_{SE}$ data, Figure 6.53 (B), shows that the α-Fe_2O_3-ZnO electrode is performing better than the composite electrode when illuminated from the substrate side, particularly at long wavelengths where only the α-Fe_2O_3 is active. This is understandable as the ITO interlayer absorbs some of the incident radiation, as well as impedes the flow of charge carrier.

The ratios of various IPCE curves are shown in Figure 6.54, where (A) are $IPCE_{EE}$ and $IPCE_{SE}$ ratios of the composite electrodes to their respective control films. Figure 6.54 (B) is the ratio of the $IPCE_{SE}$ curves of the 20 nm composite

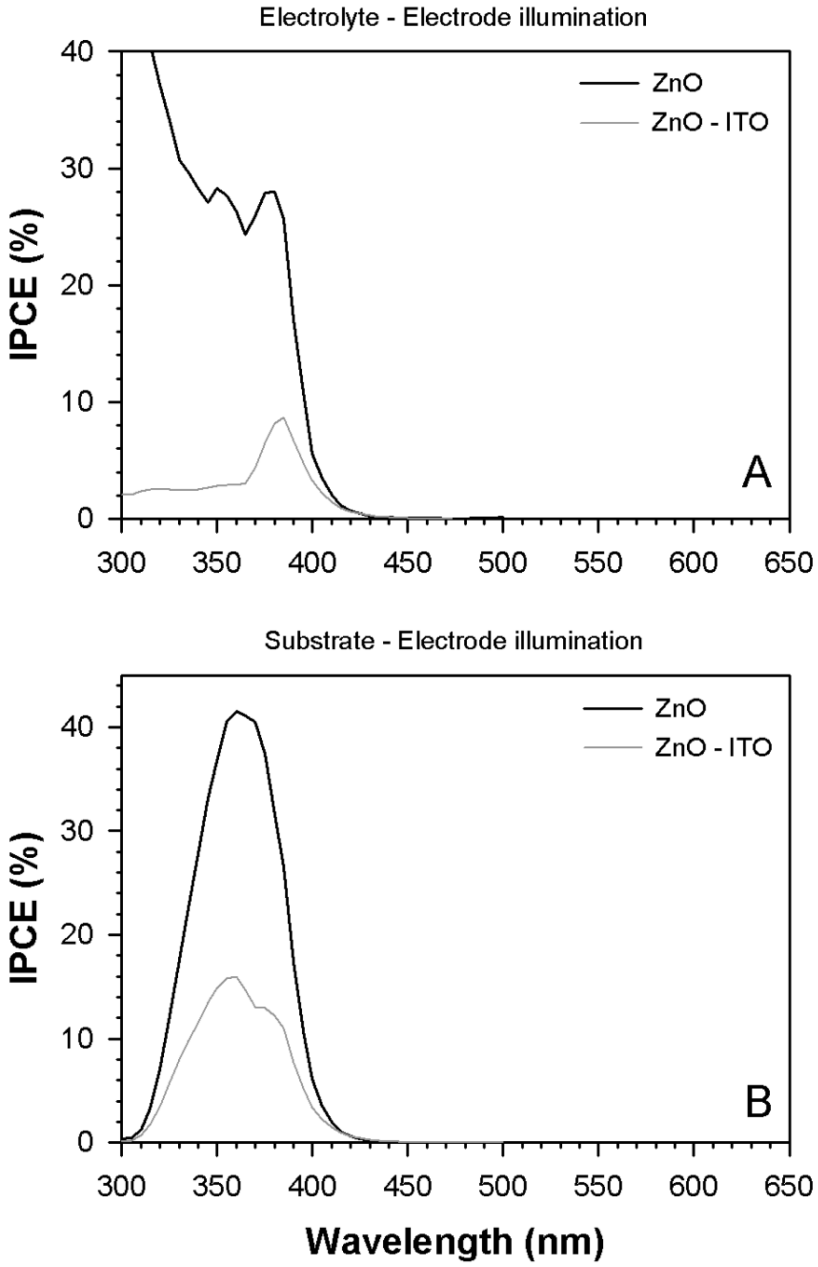

Figure 6.51: IPCE curves as functions of wavelength (0.5 V vs. SCE). (A) Electrolyte-electrode illumination measurements, and (B) substrate-electrode illumination measurements, for the ZnO nanowire array substrate, with and without an ITO film deposited on the nanowires.

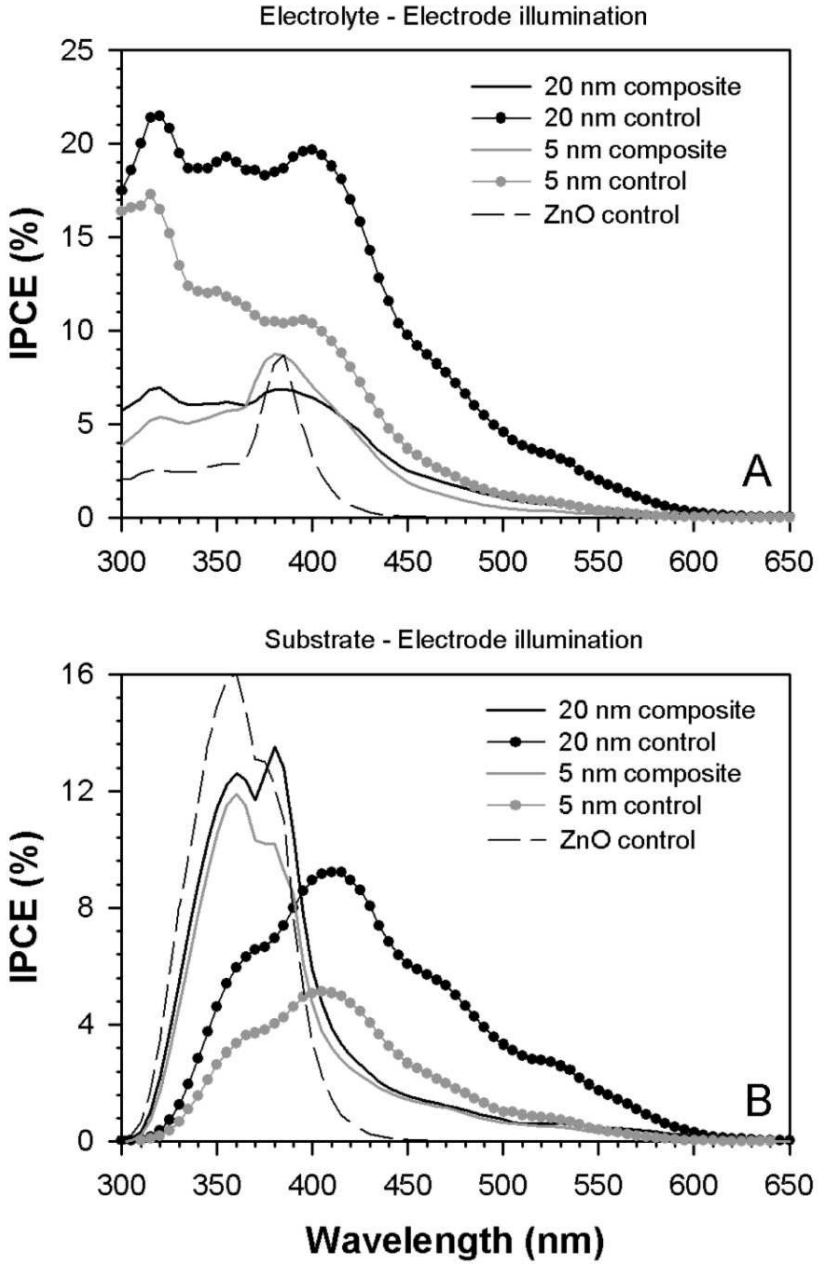

Figure 6.52: IPCE curves as functions of wavelength (0.5 V vs. SCE). (A) Electrolyte-electrode illumination measurements, and (B) substrate-electrode illumination measurements, for the composite electrodes and the planar α-Fe_2O_3 control films (deposited on ITO).

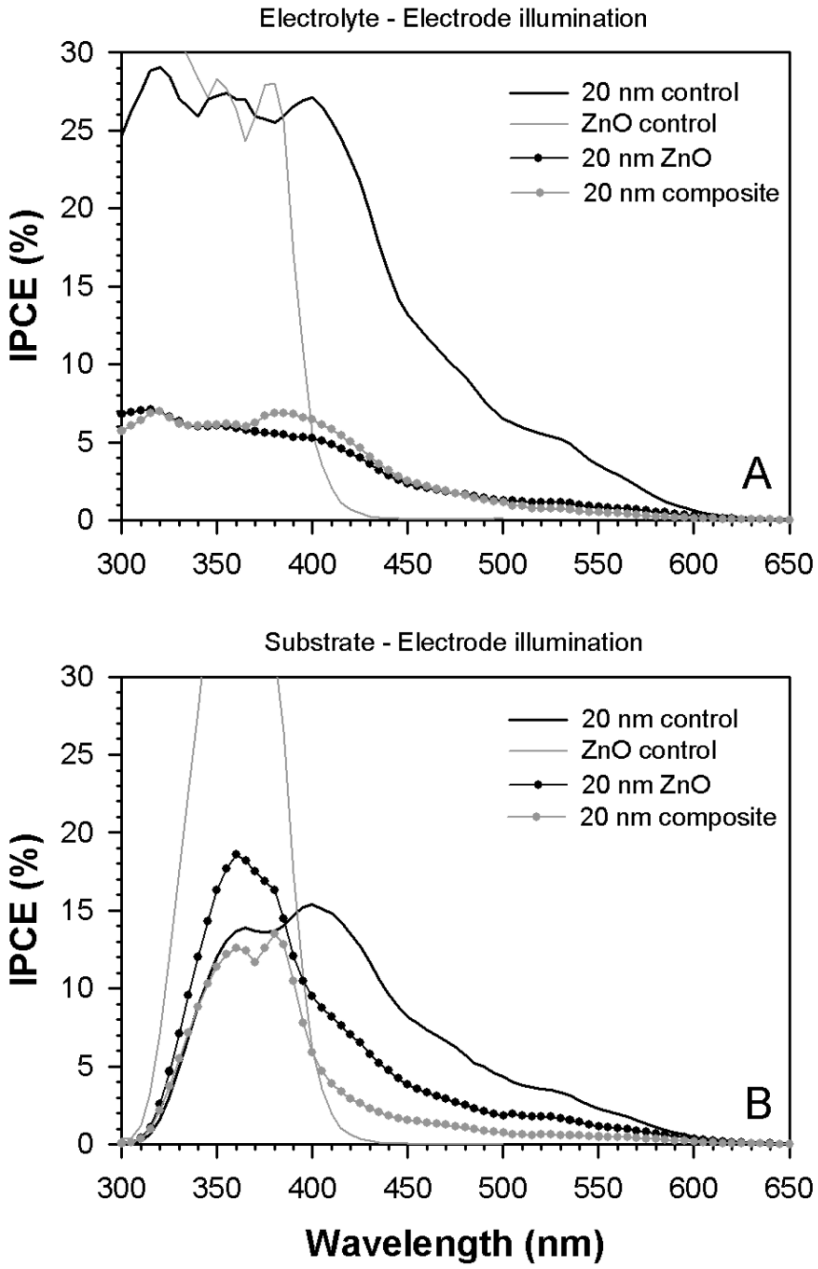

Figure 6.53: IPCE curves as functions of wavelength (0.5 V vs. SCE). (A) Electrolyte-electrode illumination measurements, and (B) substrate-electrode illumination measurements, for a 20 nm α-Fe_2O_3 film deposited onto a ZnO nanowire array substrate, compared to a 20 nm α-Fe_2O_3 composite electrode, the ZnO control (no coating) and 270 nm thick (20 nm equivalent) α-Fe_2O_3 control film.

to the 5 nm composite, where the $IPCE_{EE}$ ratio is very similar. These data are shown for wavelengths beyond 450 nm where the ZnO is not contributing to the photocurrent. The ratio of the 20 nm α-Fe_2O_3 composite and equivalent control film is 0.25 up to around 550 nm, but increases to around 0.8 at the 650 nm. For the 5 nm electrodes this ratio is relatively constant and around 0.5. Interestingly this ratio for the $IPCE_{SE}$ of the 20 nm (and equivalent control) films is very similar to the $IPCE_{EE}$ ratio. However in the case of the thinner film the ratio is significantly higher for SE illumination than for EE illumination, with the ratio approaching unity at long wavelengths. There is an obvious wavelength dependence of the IPCE ratios, with the values increasing at long wavelengths. This is a very encouraging result at is shows that the shape of the IPCE curve has been changed. The same volume of absorbing material is present for the composite electrodes and the control films, therefore the relative increase at longer wavelengths cannot be attributed to optical absorption, but must be due to enhanced collection of charge carriers.

Figure 6.55 shows SEM images of the three-layer composite electrode at each step of the coating the process. The upper row, (A) to (C), show edges of the nanowire arrays, imaged at an angle of 60°. The lower row are top-views of the electrodes. Figure 6.55 (A) and 6.55 (D) show the uncoated ZnO nanowire arrays. Successive increases in the diameter of the nanowires are obvious after the deposition of the ITO (Figure 6.55 (B)) and the α-Fe_2O_3 (Figure 6.55 (C)). The coating is not uniform though, with a small amount of coating material penetrating the array and reaching the base, leading to tapered nanowires. This effect is expected to be greater in the middle of the array than at the edge, as these images show. There appears to be preferential deposition onto the top of the nanowires, resulting in clumps of ITO being formed (Figure 6.55 (E)); this effect is increased after the α-Fe_2O_3 deposition (Figure 6.55 (F)). The development of these heads on the nanowires would further decrease the amount of material penetrating the array. It can be seen from Figure 6.55 that the parts of the nanowires down within the array have very little coating. Magnetron sputtering is a line-of-sight deposition technique, and shadowing is expected. A more uniform coating was achieved using the FAD system, where the substrate was able to be moved during deposition. However, the α-Fe_2O_3

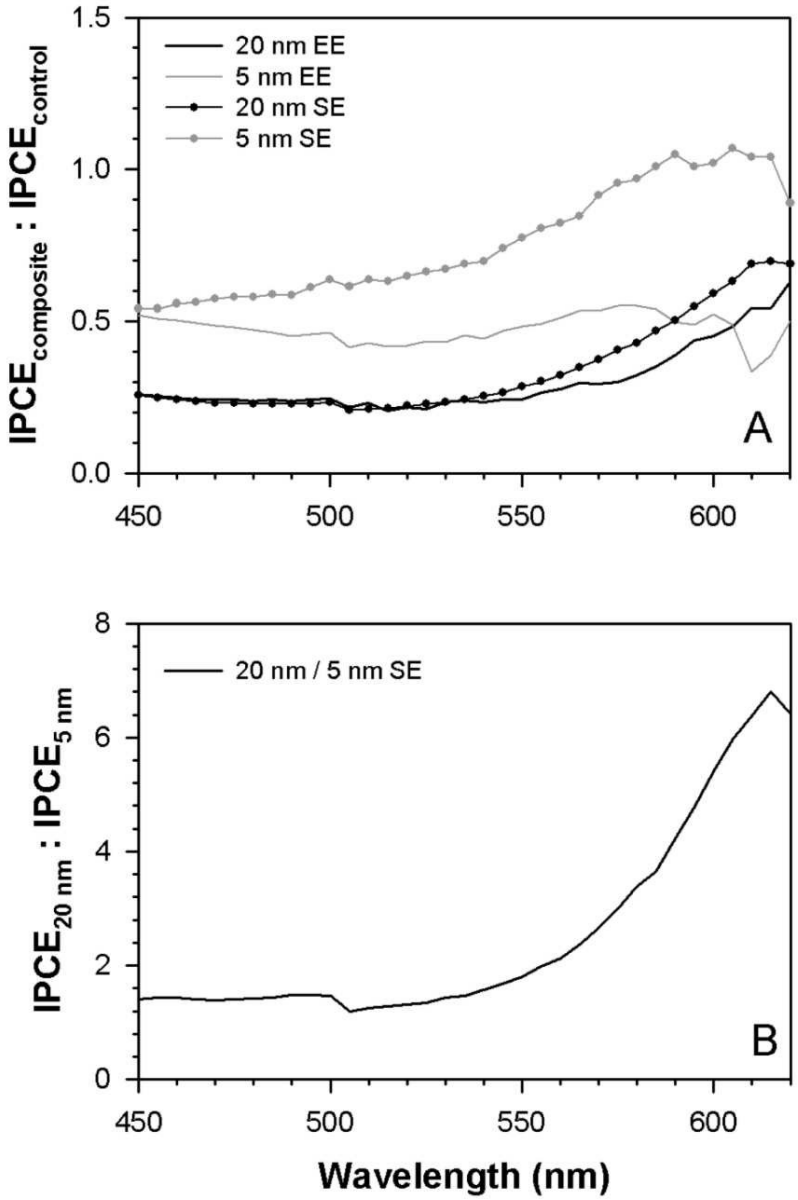

Figure 6.54: IPCE ratios (0.5 V vs. SCE). (A) $IPCE_{EE}$ and $IPCE_{SE}$ ratios of the composite electrodes to their respective control films. (B) $IPCE_{SE}$ ratio of the 20 nm composite electrode to the 5 nm composite electrode.

films deposited using FAD (Figure 6.48) were significantly thicker, so that it was not possible to view down within the array.

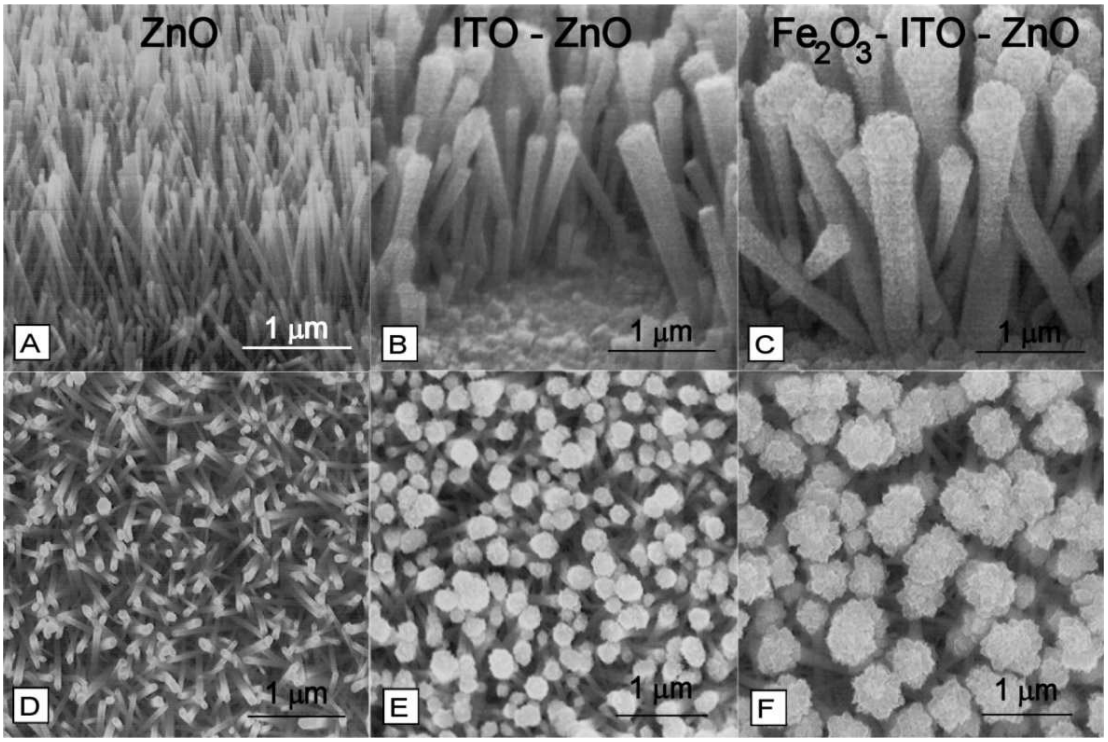

Figure 6.55: SEM images of ZnO nanowire arrays. The images on the top row (A, B, C) were collected at a angle of 60 ° (to the horizontal). The images on the bottom row (D, E, F) are top views, looking down into the arrays. The uncoated, ITO-coated and α-Fe_2O_3-ITO-coated ZnO nanowire arrays are shown in images (A, D), (B, E), and (C, F) respectively.

6.3.3 Discussion

The aim of the composite electrode design was to increase the quantum efficiency of α-Fe_2O_3, particularly in the long wavelength region where the IPCE curves usually drop off rapidly (Figure 4.1), and where there are significant gains to be made in terms of available photons (Figure 1.3). Although the overall IPCE values of the composite electrode were lower than that of the control α-Fe_2O_3 films, the relative response from the long wavelength region was enhanced. The ITO interlayer did

not improve the electron charge transfer as expected, in fact the quantum efficiency decreases when the interlayer is introduced. It appears that the ITO interlayer is producing a potential barrier to electron flow in a similar fashion to the ZnO. The overall quantum efficiency of the composite electrodes may be poor for a number of reasons, including the non-uniformity of the ITO and α-Fe_2O_3 films, the formation of potential barriers at material interfaces, and the possibility that the very thin films are not representative of the bulk material. When semiconductor films are very thin it is expected that the properties of the film will be different from that of bulk material. Band-bending, depletion widths and diffusion lengths may no longer hold for very thin films, as evidenced by the poor fit of our data to the Schottky barrier model based on these concepts. To complicate matters further, it is extremely difficult to characterise very thin films by such techniques as were used to investigate the α-Fe_2O_3 thin films in this study. Ideally a substrate that allowed epitaxial growth of the α-Fe_2O_3 would be used. The deposition of a film on a substrate with vastly different crystal structure will result in an interlayer that may consist of a different iron oxide phase, amorphous material or α-Fe_2O_3 with very different properties to the hematite we have characterised. This material may be photocatalytically inactive and of no use for water splitting. This may explain the poorer performance of the α-Fe_2O_3 films with the ITO interlayer. When the α-Fe_2O_3 is restricted to a very thin film, there is the risk that the majority of the film will be an intermediate, inferior material.

The fact that the shape of the IPCE curve of α-Fe_2O_3 was changed at long wavelengths by introducing a nanostructured substrate, suggests that the composite electrode concept is plausible and worthy of further study.

Significant findings from the nanostructured composite electrode study

- Modelling of nanostructured electrode showed that,
  - close-packed, high aspect ratio nanostructures are required to provide a high surface area for hematite deposition,
  - higher aspect ratios are required for thinner hematite films, and
  - a path length of over 500 nm is required to absorb all of the incident solar photons.
- The quantum efficiency of composite electrodes was lower than that of control films with an equivalent volume of absorbing material, most likely as a result of potential barriers to electron flow formed at the interfaces with the ITO interlayer/ZnO.
- A relative enhancement of the IPCE values at long wavelengths was observed for the composite electrodes, indicating a relative improvement in the collection of long wavelength carriers.
- The nanostructured composite electrode concept is plausible and worthy of further investigation.

Chapter 7

Conclusions and recommendations

"Great is the art of beginning, but greater is the art of ending"

L. Long

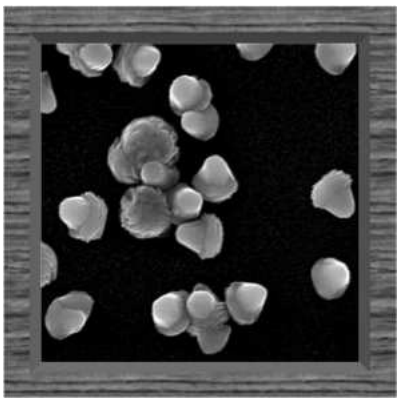

Nano-acorns

The objective of this study was to determine whether the water splitting efficiency of α-Fe_2O_3 could be improved by fabricating a nanostructured composite electrode to combat the reported short diffusion length of holes in this material. A thorough review of the literature indicated that the rate-limiting step for α-Fe_2O_3 is not yet well understood, in particular the relative effects of doping and (nano)structure. An extensive analysis of the photoelectrochemical, electrical, structural and optical properties of doped and undoped α-Fe_2O_3 films was undertaken in order to elucidate the role of the dopants and the predominant factor limiting the photoelectrochemical performance of α-Fe_2O_3. It was observed that doping was necessary to achieve significant photoelectrochemical activity. The crystallographic

orientation of the films does not appear to be a dominant factor affecting the photocurrent and also the reduced ohmic drop due to the change in conductivity with doping is insufficient to explain the observed changes in the photoelectrochemical activity. The undoped hematite is thought to have poor performance due to short diffusion lengths of charge carriers and/or poor surface charge transfer. The proposed mechanism for the enhanced photocurrent with doping is an improvement of the transfer rate coefficient at the surface and possibly also passivation of the grain boundaries by the dopants. The Si-doped hematite is thought to work less well than the Ti-doped material as the Si impurity appears to promote smaller grains and have a high level of surface states, enhancing recombination at the surface and at grain boundaries. Schottky barrier modelling of IPCE measurements showed that either the depletion layer width or the diffusion length is the dominant parameter, with a value around 30 nm. These results could not clearly distinguish between the diffusion length and the depletion layer width as the dominant factor. Calculated values of the surface transfer coefficient were similar to measured IPCE values, confirming that surface charge transfer is a major limitation for α-Fe_2O_3. Further surface modification experiments would be worthwhile.

SnO_2 and ZnO nanostructures were fabricated for use as nanostructured substrates for the α-Fe_2O_3 thin films. The growth of densely packed, well-aligned, high aspect ratio ZnO nanowire arrays was achieved by the deposition of seed layers, and the addition of a lateral growth restricting agent. The nanostructured arrays had a surface area per area of 12.5. Al-doping to improve the electrical properties of the ZnO had a detrimental effect on the geometry of the ZnO nanowires and hence the undoped material was used for the composite electrode study.

The composite electrode concept was investigated theoretically and experimentally. Modeling of nanostructured electrodes showed that: close-packed, high aspect ratio nanostructures are required to provide a high surface area for hematite deposition; higher aspect ratios are required for thinner hematite films; and a path length of over 500 nm is required to absorb all of the incident solar photons. The three-layer composite electrode concept was employed as is was thought that the ZnO - α-Fe_2O_3 interface would provide a large potential energy barrier to electron flow. Hence an

ITO interlayer was deposited between the ZnO and the α-Fe_2O_3. The quantum efficiency of the composite electrodes was lower than that of control films with an equivalent volume of absorbing material. However, a relative enhancement of the IPCE values at long wavelengths was observed for the composite electrodes, indicating a relative improvement in the collection of long wavelength carriers. These preliminary results are very encouraging as they indicate that the nanostructured composite electrode concept is a plausible route to improving the quantum effiency of α-Fe_2O_3 (and other low mobility materials).

The nanostructured composite electrode concept was based on the assumption that the diffusion length of carriers in α-Fe_2O_3 is short, and this is likely to be the case. However, despite decades of studying α-Fe_2O_3 for water splitting, the rate-limiting step in this material has not been satisfactorily explained. Hematite is a complex and interesting material, and further fundamental studies are required in order to design an electrode to overcome the shortcomings of the material. This study demonstrated that nanostructuring hematite has potential to increase the quantum efficiency of hematite and there is plenty of scope for exploring other substrate and interlayer materials. Also, hydrogen evolution and other photoelectrochemical studies would complement photocurrent and IPCE measurements. Lifetime and stability testing of the hematite electrodes would also need to be undertaken when an efficient material is developed. Further modelling of the charge transfer would be beneficial, particularly the investigation of models more suitable for thin films (e.g. diffusion models).

Appendix A

Crystal structure of α-Fe_2O_3

A brief description of the crystal structure of hematite is presented here as the electrical, magnetic and photoelectrochemical properties of α-Fe_2O_3 are determined by the crystal structure. Hematite has a corundum crystal type (isostructural to Al_2O_3, Cr_2O_3, V_2O_3 and Ti_2O_3) which forms a (slightly distorted) hexagonal close-packed (hcp) crystal structure. The hcp unit cell is shown in Figure A.1, where the balls represent the oxygen sites. The horizontal and vertical planes are referred to as *basal planes* and *prism planes* respectively. The distance between successive basal planes (length of the prism plane) is denoted by "c" where the c-axis intersects the basal planes orthogonally. The width of the prism planes (distance between adjacent vertical oxygen planes) is denoted by "a" and has the same magnitude for all planes due to the hexagonal symmetry.

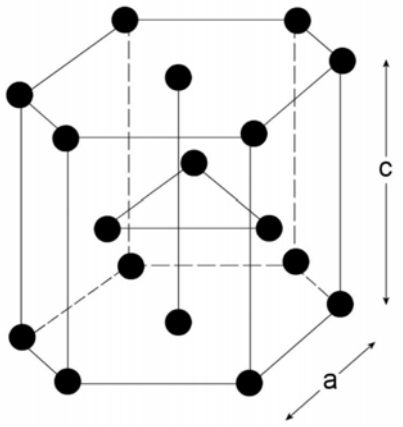

Figure A.1: Axes of the the hexagonal close-packed unit cell, showing the oxygen sites.

The Miller-Bravais index system is often used for describing hexagonal structures to account for the fourth lattice vector (three a axes and one c axis). A fourth index, i, is added to the general Miller index (hkl), to produce the Miller-Bravais general index (hkil) where i = -h-k. Directions in the crystal lattice can also be designated indices (enclosed in square brackets), where the direction [hkl] (or [hkil]) is orthogonal to the plane (hkl) (or (hkil)). A negative index is denoted by a bar above the value, for example $(0\bar{1}0)$. Both Miller and Miller-Bravais notation are used throughout the text.

The unit-cell of hematite is shown in Figure A.2, viewed in the [001] direction (looking down the c-axis, with the basal plane in the plane of the page), and in the [110] direction (looking at the prism planes). Note that the definition of the unit cell of α-Fe_2O_3 is different to that of the general hexagonal close-packed structure shown in Figure A.1. Since the hematite structure is a non-ideal version of the hcp structure, the unit cell of hematite is different to that shown in Figure A.1. In the hematite unit cell, the Fe ions lie in the basal planes, with only two of three sites intersecting the c-axis being occupied. These c-axis pairs form iron bilayers within the crystal and have the smallest cation-cation separation (205). The oxygen ions form distorted octahedra around the Fe ions. The deviation from the ideal hexagonal structure is visible when the unit cell is viewed in the [001] direction as in Figure A.2. The thermal,mechanical and charge transport properties of hcp structures can vary greatly in the c and a directions (40, 206).

The magnetic structure of hematite is linked to the crystal structure and is linked to the anisotropic conductivity of this material (43, 44, 205). Hematite can exhibit both ferromagnetic and antiferromagnetic behaviour. A ferromagnetic material has a spontaneous magnetic moment, with electron spins aligned in a regular fashion with neighbouring spins in one direction. In the case of antiferromagnetism, the electron spins are regularly aligned, but neighbouring spins point in opposite directions (3). The iron atoms in the (001) basal planes of hematite are coupled ferromagnetically, and iron atoms in successive planes in the [001] direction are coupled antiferromagnetically (43, 97, 205, 207). Between 260 K and 950 K, hematite exhibits weak ferromagnetism due to slight spin canting (spins nearly in the basal

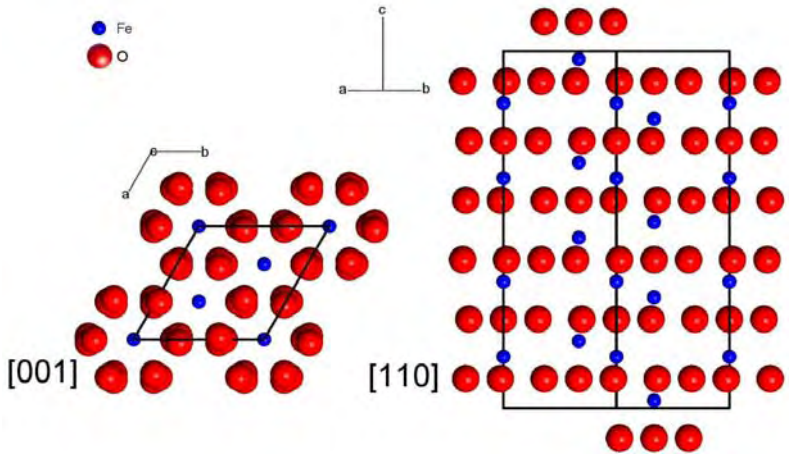

Figure A.2: Unit cell of hematite viewed in the [001] and [110] directions.

plane) (43, 205). Below 260 K hematite is antiferromagnetic with the spins parallel to the *c*-axis (42, 205). The Néel temperature (point at which the thermal energy is large enough to destroy the magnetic ordering of an antiferromagnetic material) is around 950 K for hematite (42, 89, 205). The Néel temperature is analogous to the Curie point, the temperature above which a ferromagnetic material loses its magnetic ordering (208).

Appendix B

Conductivity mechanisms in α-Fe_2O_3

This appendix provides further discussion of the conduction properties of α-Fe_2O_3, including the anisotropic nature and temeperature dependence of the conductivity and discussion of the intrinsic conduction mechanisms. Tables summarising experimental results from the conductivity measurments of doped and undoped α-Fe_2O_3 presented in the literature are also presented.

B.1 Anisotropic conductivity

The electrical conductivity of hematite is highly anisotropic, which can be explained by its antiferromagnetic structure. The low conductivity along the [001] direction has been attributed to spin-restricted transfer of electrons from one iron layer to another across an oxygen plane (43, 44, 205). Hematite has five $3d$ electrons per Fe^{3+} ion (one in each d orbital), with spins coupled ferromagnetically in the basal plane (001). Due to Pauli's exclusion principle, an extra electron (e.g. from a donor centre) would need to have a spin antiparallel to this plane. This electron can move easily along the basal plane in an environment of parallel spins. However, because successive basal planes are coupled antiferromagnetically, the donor electron will have the same spin as electrons already occupying d orbitals in adjacent iron layers, and hence electron transfer is restricted in the [001] direction. Conductivity along [001] is dominated by the movement of Fe^{4+} holes, which are thought to have a lower mobility than electrons in hematite (43).

The anistropy of the electrical conductivity has been observed experimentally (100, 201) and confirmed theoretically (43, 44, 202). Studies of single crystal hematite have shown anisotropic conductivity and activation energies for conduction. Nakau observed anistropy of the conductivity that was very dependent on the impurities (100). A sample containing 5.4 at.% Mg and 2.4 at.% Ca (both group II elements) showed less than an order of magnitude difference in conductivities between the [0001] and $[10\bar{1}0]$ directions, with similar activation energies (0.25 and 0.22 eV respectively). However, in the case of material containing 3.3 at.% Mg (II A) and 1.0 at.% Sn (IV B), the conductivity in the [0001] direction was five orders of magnitude lower than that measured in the $[10\bar{1}0]$ direction (at room temperature) where the activation energies were 0.74 eV and 0.17 eV respectively. Benjelloun *et al.* (201) measured the conductivity in the (001) plane and along the [001] axis and observed anisotropic behaviour up to around 1100 K (for undoped α-Fe_2O_3 with 5 ppm Pb and B and 3 ppm Sn impurities). The maximum difference in conductivity between the two crystallographic directions was around one order of magnitude (at 500 K). The hematite used in this study contained the following major impurities: 5 ppm Pb, 5 ppm B, and 3 ppm Sn.

Theoretical models have also shown anisotropic conduction in hematite (43, 44, 202). These authors often cite the experimental work of Nakau (100) and Benjelloun *et al.* (201), to which they compare their conductivity values. This may not be a meaningful comparison given that the experimental material was impure, and that the conductivity and degree of anisotropy was highly dependent on the doping (100, 201). Iordanova *et al.* (44) calculated mobilities that were approximately three orders of magnitude higher in the basal plane (001) than along the *c*-axis direction [001], due to an electronic coupling value five times larger in the basal plane compared to the [001] direction. The electron coupling value α is a measure of the strength of the electron-lattice interaction, as shown by Eq. B.1, where ω_L is the longitudinal optical phonon frequency and $\frac{1}{2}\alpha$ is the number of phonons surrounding a slow-moving electron in a lattice (3).

$$\frac{1}{2}\alpha = E_d/\hbar\omega_L \tag{B.1}$$

The larger Fe-Fe distance in the c direction is partly responsible for the smaller electronic coupling, however there exists three bridging oxygen atoms (compared to two in the basal plane) which should facilitate better coupling. The hole transfer rate was found to be around three times smaller than that of the electrons (for the (001) plane compared to along the [110] direction), which was attributed to the larger reorganisation energy for holes.

B.2 Conductivity measurements

The difficulties of making good conductivity measurements, summarised in Section 4.1.2, are discussed here in further detail.

Stoichiometric metal oxides are nearly always insulators. However, most metal oxides are non-stoichiometric, due to, deficiency or excess of cations or oxygen. Hematite is a metal-excess semiconductor with a small deviation from stoichiometry (39, 40, 98). Oxygen stoichiometry can be manipulated via oxidation or reduction reactions under controlled temperature and atmospheric conditions. The electrical conductivity and thermopower are often measured as functions of oxygen partial pressure. The conductivity of hematite has been shown to be independent of oxygen pressure at temperatures above 650 °C (38, 80, 98). The change in the sign of the thermopower (indicating p-type properties) is often observed at high temperatures ($\geq$ 800 °C) (38, 39, 80, 89) and has been shown to be dependent on the orientation of the sample (201).

During the heating of ceramic samples, such as hematite, oxygen vacancies can be formed. The level of reoxidation and defects frozen into the bulk upon cooling will depend on the defect structure, the microstructure of the sample, and the treatment conditions (such as heating and cooling rates and the atmosphere) (41, 80, 87). Reoxidation initially occurs at grain boundaries, producing high-resistivity grain boundary layers (41, 42). Even in single crystal material, stoichiometry and dopant concentrations of a surface layer can differ from the bulk (39, 42, 98). The effect of such layers can lead to the misinterpretation of the results of electrical measurements. Gleitzer *et al.* (39) present a temperature-composition phase diagram (as a

function of weight % oxygen) which shows that there is a very narrow region where bulk hematite is non-stoichiometric. Non-stoichiometry of the near-surface layer occurs over a wider region, however. Non-stoichiometry in the bulk was observed above 1400 K, and in the surface layer above around 900 K. Bevan *et al.* (209) commented that changes in the stoichiometry of the surface layer were sufficient to account for observed changes in conductivity, without changes to the bulk material. Grain boundary effects can be avoided by controlling the quench process. Cooling hematite in a nitrogen atmosphere with low oxygen partial pressure can suppress the formation of high-resistivity grain boundaries (42).

Gharibi *et al.* (98) have observed unusual behaviour of the conductivity at low temperatures. They attribute this effect to surface limitations, suggesting mechanisms such as non-stoichiometry (adsorbed oxygen), segregation of some impurities, and imperfect electrode contact.

Bosman *et al.* (42) provide an interesting example of the large effect of grain boundaries on d.c. resistivity measurements of Ti-doped polycrystalline ceramic samples. A sample in which grain boundary layers had an effect showed a resistivity up to several orders of magnitude higher than a sample with no contribution from grain boundaries. The temperature dependence of the resistivity is also different. In contrast, Tanner *et al.* (210) observed only a small difference between the conductivity of single crystal and polycrystalline samples. The samples used were impure but not intentionally doped. The synthetic and natural single crystals had large amounts of various impurities. The polycrystalline material had smaller amounts of impurities. de Wit *et al.* (211) have shown that the conductivity is not only dependent on high-resistivity grain boundaries, but also on inhomogeneous/non-stoichiometric grain structure.

When hematite is heated to high temperatures (under certain atmospheric conditions), other iron oxide phases can be formed. The γ-Fe_2O_3 (maghemite) to α-Fe_2O_3 (hematite) transition occurs around 600 °C. Any γ-Fe_2O_3 inclusions should be converted to hematite via heat treatment (e.g. annealing). Samples prepared and treated at temperatures below 600 °C could have residual maghemite present. The formation of magnetite has been observed at temperatures above 720 °C (209, 211),

consistent with the phase diagram presented by Gleitzer *et al.* (39). Small inclusions of the magnetite phase in hematite can have a large effect on the electrical properties (88, 95). Merchant *et al.* (88) introduced magnetite into hematite crystals by reduction and observed an increase in conductivity of four orders of magnitude. Magnetite is highly conductive, with conduction occuring via electron transfer from Fe^{2+} to Fe^{3+} sites. Only a surface layer of magnetite could be formed and when this layer was removed the conductivity of the samples decreased to that of the unreduced samples. The corundum crystal structure of the hematite has low tolerance for large inclusions of the magnetite spinel structure (88, 95, 106). Given the large effect of small inclusions of magnetite in hematite, electrical measurements need to be undertaken on doped samples that do not contain spinel phases. Sieber *et al.* (106) and Sanchez *et al.* (95) used magnetic susceptibility measurements to confirm that the samples (Ge-doped Fe_2O_3 and Ni-doped Fe_2O_3 respectively) were free of spinel inclusions.

The preparation of appropriate samples for conductivity measurements is important, so that the results are not dominated by the morphology or crystal structure of the material. Poor samples for conductivity measurements may be impure, porous, non-stoichiometric or inhomogeneous (4). There is a broad range of temperature and oxygen pressure regions over which equilibrium occurs; therefore the preparation of samples with a high level of stoichiometry should be achievable (4). However the bulk and gas phase equilibrate at a significant rate only at very high temperatures. If material prepared at lower temperatures equilibrium will not occur.

The conductivity of hematite is highly moisture-dependent,and hence the use of this material for humidity sensing applications (188, 212). This property may also be a source of measurement error for experiments performed under ambient conditions.

The low concentration of intrinsic defects in hematite means that the electrical properties of the material can be dependent on small concentrations of impurities. As a result, conclusions regarding the the conduction mechanisms of hematite from experiments involving low-purity samples have been questioned (38). The production of non-stoichiometric material by the introduction of vacancies or interstitials

(via reduction or oxidation) can give unreliable conductivity results. Hence most samples are deliberately doped (4). Undoped samples are rarely of high enough purity, and may be "self-doped" via impurities or defects.

B.2.1 Temperature dependence

Measurements of the conductivity of hematite as a function of temperature often exhibit a number of distinct conduction regions. These are shown by regions of the log σ vs. T^{-1} curves with different gradients (and hence activation energies) (38, 41, 80, 87, 98, 201, 210). The temperature regions and corresponding electrical properties such as activation energy and carrier mobility are shown in Table B.1 for selected studies of undoped Fe_2O_3.

The transition temperatures appear to be dependent on the sample type, the crystallographic orientation (201) and the atmosphere under which the conductivity measurement is performed (38, 98). The high-temperature region is often attributed to intrinsic conduction. The transition temperature for this region varies from 650 °C to 800 °C in the examples shown. The regions at lower temperature are controlled by extrinsic processes (dependent on dopants, or impurities in undoped samples). Often a third temperature region is present, which has been attributed to the effects of grain boundaries (41).

Gardner *et al.* (41, 80) describe three temperature regimes of 99.99 % hematite (as shown in Table B.1), with approximate temperature limits : (A) < 450 °C, (B) 450 °C- 800 °C and (C) > 800 °C, with activation energy values of 0.7 eV, 0.1 eV and 1.0 eV respectively. The conduction in region (A) was attributed to grain boundary effects (in the case of the undoped sample). When the Fe_2O_3 was doped, the conductivity was most affected in this region and the effects of the grain boundaries were over-ridden by that of the dopants (80). In region (B) it was postulated that during heating oxygen vacancies are formed and when the sample is cooled these donor centres are frozen into the lattice (due to the slow equilibrium with oxygen at these lower temperatures). Hence the carrier concentration (number of donor centres) in this region is constant and the change in conductivity is thought to be related to

the change in carrier mobility. Gardner *et al.* showed that their sintered powder samples were oxygen-deficient (excess metal) and observed an increase in oxygen loss with increasing firing temperature. Table B.1 shows the carrier concentration values at a number of different firing temperatures in region (B). It can be seen that the donor density values increase and activation energy values decrease with increasing firing temperature. Above 800 °C (region (C)), conduction is thought to be due to both oxygen vacancies and intrinsic processes. Both Gardner and Morin (89) concluded that at lower temperatures conduction is attributed to charge carrier mobility, whereas at higher temperatures the charge carrier concentration is more important than mobility. It must be stressed that the samples used by Gardner *et al.* were sintered polycrystalline powders, and the conductivity will depend on how well the particles are fused during sintering. These types of materials may behave very differently to polycrystalline thin films for example.

As discussed on Section 2.2, there is a high temperature region where intrinsic behaviour is observed for both doped and undoped hematite (38, 41, 80, 89, 96, 98, 201, 210) (as the intrinsic charge carrier concentration exceeds that of the extrinsic charge carriers). The transition temperature is the temperature at which the intrinsic region begins, and the slope of the log σ curve (activation energy) varies (as shown in Table B.1). The activation energy of the intrinsic region is often found to be around 1 eV. Theoretically the intrinsic activation energy should be equal to half of the band-gap (from the exponential term in Eq. 2.12).

It has been observed that the electrical conductivity of hematite is independent of oxygen partial pressure at high temperatures (38, 80, 89, 98) and has been used as an indicator of intrinsic behaviour. Dieckmann (40) suggests that this may be due to large thermal electronic disorder and/or impurity levels that are significantly larger than the defect concentration. This is only valid for samples with impurity levels below the deviation from stoichiometry due to the large effect of small levels of impurities on the conductivity of hematite (4, 38). Gardner *et al.* (41) predicted a small change (8 %) in conductivity with oxygen partial pressure above 1000 °C and a larger effect (20 %) at 700 °C.

The conduction mechanisms of hematite and the nature of the defects in the

high temperature regions are not yet well understood (40). The only experimental investigation of the conductivity of very high purity hematite was undertaken by Warnes *et al.* using 99.9997 % α-Fe_2O_3 (38). They concluded that α-Fe_2O_3 is an intrinsic semiconductor above 650 °C, with both electrons and holes contributing to intrinsic conductivity. The concentration of electrons is greater than that of holes above 650 °C, supporting previous conclusions (80, 98, 213) that hematite contains oxygen vacancies and iron interstitials. Dieckmann (40) similarly concluded that charge carriers are the majority defects, and oxygen vacancies the major ionic defect at high temperatures (99.998 % Fe_2O_3).

Gardner *et al.* (41, 80) presented extensive discussion of the possible conduction mechanisms (origin of charge carriers) of hematite at high temperatures using data from both pure (99.99 %) and doped material. At temperatures above 800 °C (region (C)) extrinsic effects were discounted due to the high purity of the material and the fact that the presence of dopant impurities had little effect at high temperatures. Gardner *et al.* postulate that negative charge carriers are generated by oxygen vacancies (O_2 loss during heating) as well as intrinsic transitions (leaving a hole in the O $2p$ band). In oxygen-deficient hematite the negative carriers are thought to be electrons on ferric ions. Generally holes in the O $2p$ band would be expected to have high mobility, whereas the the positive charge carriers in hematite have low mobility (80). Spectral data suggested that the width of the O $2p$ band is narrow (1 - 2 eV) and hence the low mobility for holes is reasonable. It was concluded that the electronic transition to produce a hole occurred by the process shown in Eq. B.2.

$$Fe^{3+} + O^{2-} \longrightarrow Fe^{2+} + O^{-} \tag{B.2}$$

B.2.2 Tables of experimental conductivity results

Table B.1 sumarises the experimental results from electrical measurements of undoped presented in the literature. Table B.2 and Table B.3 show selected electrical properties of, Ti-doped and Ge-doped hematite respectively, as presented in the literature.

Author	**Sample**	**Temperature regions °C**	**E_a (eV)**	**Carrier Concentration (cm^{-3})**
Warnes *et al.*, 1984 (38)	Polycrystalline, 99.9997 %	PO_2 1 atm		At 600, 1040 °C
		> 650	1.11	4 x 10^{20} (h) and 8 x 10^{20} (e),
		< 650	0.29*	1 x 10^{21} (h) and 7 x 10^{21} (e)
		PO_2 0.21 atm		
		> 620	1.11	
		450 - 620	0.81*	
		< 450	0.26*	
Gardner *et al.*, 1963 (41)	Polycrystalline, 99.99 %, air	> 800	1.0	
		450 - 800	0.1	
		< 450	0.7	
	Firing temp (°C)	450 - 800		
	1000		0.31	4.5 x 10^{18}
	1100		0.22	1.7 x 10^{19}
	1200		0.13	5.5 x 10^{19}
	1300		0.12	1.5 x 10^{20}
Dieckmann, 1993 (40)	Polycrystalline, 99.998 %	> 1000	1.18	
			1.30^{+}	
Morin, 1951 (89)	Polycrystalline, 99.0 %	< 1000	1.17	
Gharibi *et al.*, 1990 (98)	Single crystal (001), Air 0.21 atm	> 680	1.08	
		420 - 680	0.3	
		< 420	0.48	
Benjelloun *et al.*, 1984 (201)	Single crystal, air (001), [001]	> 700, > 640	0.6*, 0.6*	
		390 - 700, 500 - 640	0.1*, 0.06*	
		< 500, < 390	0.17*, 0.29*	

* E_a calculated from presented data.

$^{+}$ E_a from log σT vs. 1/T plot, rather than log σ vs. 1/T plot

Table B.1: Electrical properties of undoped hematite; experimental results from the literature.

Author	**Sample**	**Ti level**	**Resistivity, ρ (Ω cm)**	**Carrier Density (cm^{-3})**	**Mobility, μ ($cm^2V^-s^{-1}$)**	**E_a (eV)**
Morin, 1951, 1954 (89, 96)	Polycrystalline, ρ at 100 °C, carrier density and μ at 400 °C (O_2, reducing)	Undoped 0.05 % 0.2 % 1 %	$> 10^{11}$, 10^{11} 2 x 10^9, 10^6 10^6, 5 x 10^3 5, 3	10^{16}, 10^{17} 10^{18}, 6 x 10^{19} 5 x 10^{18}, 2 x 10^{19} 10^{19}, 10^{19}	1.5 x 10^{-4}, 2 x 10^{-3} 6 x 10^{-4}, 2 x 10^{-3} 2 x 10^{-2}, 2 x 10^{-2} 3 x 10^{-2}, 3 x 10^{-2}	1.17, 1.11* 1.05*, 0.63* 0.66*, 0.43* 0.18*, 0.23*
Gardner *et al.*, 1963 (80)	Polycrystalline μ at 25 °C	1 %			0.0158 (e) 1.24 × 10^{-9} (h)	
Bosman and van Daal, 1970 (42)	Polycrystalline Resistivity at 25 °C	2 %	0.4			
de Cogan and Lonergan, 1974 (87)	Polycrystalline, ρ at 100 °C	Undoped 0.01 % 0.1 % 1 %	6.9 x 10^5 2.7 x 10^3 5.1 < 1			0.73 0.56 0.19 0.16
Warnes *et al.*, 1984 (38)	Polycrystalline, ρ at 200, 400 °C	0.07 % 0.18 % 0.76 % Undoped (PO_2 0.21 atm) (PO_2 1 atm)	6.3 x 10^3, 500 500, 50 1, 0.63 ρ at 400, 1000 °C 6.3 x 10^6, 2 4.0 x 10^5, 2	At 600, 1040 °C 4 x 10^{20} (h) and 8 x 10^20 (e), 1 x 10^{21} (h) and 7 x 10^{21} (e)	At 50, 400 °C 0.8 (h) and 0.4 (e), 0.05 (h) and 0.16 (e)	0.17* 0.12* 0.03* 1.11 (int.)
Gharibi *et al.*, 1990 (98)	Single crystal (001), ρ at 400, 980 °C	2 %	0.75, 0.13			0.15, 0.08 (int.)

* E_a calculated from presented data.

All activation energy values are in the extrinsic region unless otherwise stated.

Table B.2: Electrical properties of Ti-doped hematite samples. Selected experimental results from the literature.

Author	**Ge level**	**Resistivity (Ω cm) at 25 °C**	**E_a (eV)**
H.L. Sanchez *et al.*, 1982 (105)	2 mole %	300	-
	Undoped	10^6	
Patterson, 1975 (107)	2 mole %	25	-
	Undoped	3.5 x 10^4	
Sieber *et al.*, 1985 (106)	2 mole %	5 ± 4	0.12
	Undoped	$> 10^6$	

Table B.3: Electrical properties of Ge-doped hematite samples. Selected experimental results from the literature.

Abbreviations and symbols

ACG	Aqueous chemical growth
AFM	Atomic force microscopy
AM1.5	Air-mass 1.5, solar radiation standard
FAD	Filtered arc deposition
FTIR	Fourier-transform infra-red spectroscopy
FTO	Fluorine-doped tin oxide
FWHM	Full-width-half-maximum
IPCE	Incident photon-to-current conversion efficiency
$IPCE_{EE}$	IPCE measured using illumination from the electrolyte-electrode side
$IPCE_{SE}$	IPCE measured using illumination from the substrate-electrode side
IR	Infrared
ITO	Indium-tin-oxide (tin-doped indium oxide)
NHE	Normal hydrogen electrode
PEC	Photoelectrochemical cell
RHE	Reversible hydrogen electrode
RMS	Reactive magnetron sputtering
SCE	Standard calomel (reference) electrode
SEM	Scanning electron microscopy
UV	Ultraviolet
XRD	X-ray diffraction

c	Speed of light in a vacuum (2.99793 x 10^8 m s^{-1})
C	Capacitance (F)
D	Diffusion coefficient
E_A	Activation energy for conductivity (eV)
E_b	Potential energy related to the bias (eV)
E_c	Conduction band energy (eV)
E_D	Donor energy level (eV)
E_F	Fermi energy (eV)
E_g	Band-gap energy (eV)
E_s	Total incident solar irradiance
E_v	Valence band energy (eV)
ΔG	Gibbs free energy ($kJ\,mol^{-1}$)
G	Surface transfer coefficient
h	Planck's constant (6.626 x 10^{-34} Js)
I	Current (A)

I_{ph}	Photocurrent
j_p	Photocurrent density ($\mathrm{mA\,cm^{-2}}$)
k	Boltzmann's constant (1.381×10^{-23} $\mathrm{m^2\ kg\ s^{-2}\ K^{-1}}$ or 8.617×10^{-5} $\mathrm{eV\ K^{-1}}$)
κ	Extinction coefficient
L	Charge carrier diffusion length (nm)
n	Electron concentration
n	Refractive index
N_C	Number of charge carriers in the conduction band
N_D	Carrier density
n_i	Intrinsic carrier concentration
N_{ss}	Surface state concentration
N_V	Number of charge carriers in the valence band
p	Hole concentration
R	Resistance
V_B	Band bending (V)
V_{bias}	Bias voltage (V)
V_{fb}	Flat-band potential (V)
$V_{Helmholtz}$	Potential drop across Helmholtz layer
V_{Photo}	Photo-voltage
V_{WC}	Potential of working electrode relative to counter electrode (V)
V_{WR}	Potential of working electrode relative to reference electrode (V)
V_{WS}	Water splitting potential (V)
w_d	Width of the depletion layer (nm)

α	Absorption coefficient ($\mathrm{m^{-1}}$)
η	Overpotential (V)
η_c	Photoconversion efficiency (%)
ϵ_0	Permittivity in a vacuum
ϵ_r	Relative permittivity
λ	Wavelength (nm)
λ_g	Wavelength corresponding to the energy gap (nm)
λ_D	Debye length (nm)
μ_n	Mobility of electrons ($\mathrm{cm^2\,V^{-1}\,s^{-1}}$)
μ_p	Mobility of holes ($\mathrm{cm^2\,V^{-1}\,s^{-1}}$)
ω	Frequency (Hz)
ρ	Resistivity ($\Omega\,\mathrm{m}$)
σ	Electrical conductivity (Ω^{-1} $\mathrm{cm^{-1}}$)
τ	Time constant (s)

Reference list

[1] Gerischer H. Semiconductor electrodes and their interaction with light. In *Photochemistry Photocatalysis and Photoreactors*, pages 39–106. D. Reidel, 1985.

[2] Kay A., Cesar I., and Grätzel M. New benchmark for water photooxidation by nanostructured alpha-Fe_2O_3 films. *J. Am. Chem. Soc.*, 128(49):15714–15721, 2006.

[3] Kittel C. *Introduction to solid state physics*. John Wiley and Sons, Inc., New York, third edition, 1953.

[4] Jonker G.H. Energy levels of impurities in transition metal oxides. In *Proc. Semicond. Phys. Conf.*, pages 864–867, 1961.

[5] Nozik A.J. and Memming R. Physical chemistry of semiconductor-liquid interfaces. *J. Phys. Chem.*, 100(31):13061–13078, 1996.

[6] Özdemir A.F., Türüt A., and Kokce A. The interface state energy distribution from capacitance-frequency characteristics of gold/n-type gallium arsenide schottky barrier diodes exposed to air. *Thin Solid Films*, 425(1-2):210–215, 2003.

[7] Cesar I., Kay A., Gonzalez Martinez J.A., and Grätzel M. Translucent thin film Fe_2O_3 photoanodes for efficient water splitting by sunlight: nanostructure-directing effect of Si-doping. *J. Am. Chem. Soc.*, 128(14):4582–4583, 2006.

[8] Momirlan M. and Veziroglu T.N. Current status of hydrogen energy. *Renewable Sustainable Energy*, 6(1-2):141–179, 2002.

[9] Dunn S. Hydrogen futures: Toward a sustainable energy system. *Int. J. Hydrogen Energy*, 27(3):235–264, 2002.

[10] Bolton J.R. Solar photoproduction of hydrogen: A review. *Sol. Energy*, 57(1):37–50, 1996.

[11] Bak T., Nowotny J., Rekas M., and Sorrell C.C. Photo-electrochemical hydrogen generation from water using solar energy: materials-related aspects. *Int. J. Hydrogen Energy*, 27(10):991–1022, 2002.

[12] Murphy A.B., Barnes P.R.F., Randeniya L.K., Plumb I.C., Grey I.E., Horne M.D., and Glasscock J.A. Efficiency of solar water-splitting using semiconductor electrodes. *Int. J. Hydrogen Energy*, 31:1999–2017, 2006.

[13] Tributsch H. *Photoelectrocatalysis*, pages 339–383. Photocatalysis Fundamentals and Applications. Wiley, New York, 1989.

[14] Asahi R., Morikawa T., Ohwaki T., Aoki K., and Taga Y. Visible-light photocatalysis in nitrogen-doped titanium oxides. *Science*, 293:269–271, 2001.

[15] Serpone N. Is the band gap of pristine TiO_2 narrowed by anion- and cation-doping of titanium dioxide in second-generation photocatalysts? *J. Phys. Chem. B*, 110(48):24287–24293, 2006.

[16] Kisch H. and Macyk W. Visible-light photocatalysis by modified titania. *ChemPhysChem*, 3(5):399–400, 2002.

[17] Li D., Haneda H., Hishita S., and Ohashi N. Visible-light-driven nitrogen-doped TiO_2 photocatalysts: effect of nitrogen precursors on their photocatalysis for decomposition of gas-phase organic pollutants. *Mater. Sci. Eng.: B*, 117(1):67–75, 2005.

[18] Lindgren T., Wang H., Beermann N., Vayssiéres L., Hagfeldt A., and Lindquist S.-E. Aqueous photoelectrochemistry of hematite nanorod array. *Sol. Energy Mater. Sol. Cells*, 71(2):231–243, 2002.

[19] Ohno T., Mitsui T., and Matsumura M. Photocatalytic Activity of S-doped TiO_2 Photocatalyst under Visible Light. *Chem. Lett.*, 32(4):364–365, 2003.

[20] Maeda K. and Domen K. New non-oxide photocatalysts designed for overall water splitting under visible light. *J. Phys. Chem. C*, 111(22):7851–7861, 2007.

[21] Gole J.L., Stout J.D., Burda C., Lou Y., and Chen X. Highly efficient formation of visible light tunable $TiO_{2x}N_x$ photocatalysts and their transformation at the nanoscale. *J. Phys. Chem. B*, 108(4):1230–1240, 2004.

[22] So W.-W., Kim K.-J., and Moon S.-J. Photo-production of hydrogen over the CdS-TiO_2 nano-composite particulate films treated with $TiCl_4$. *Int. J. Hydrogen Energy*, 29(3):229–234, 2004.

[23] Hodes G., Cahen D., and Manassen J. Tungsten trioxide as a photoanode for a photoelectrochemical cell (PEC). *Nature*, 260:312–313, 1976.

[24] Oh S.M. and Ishigaki T. Preparation of pure rutile and anatase TiO_2 nanopowders using RF thermal plasma. *Thin Solid Films*, 457(1):186–191, 2004.

[25] Sinha A.S.K., Sahu N., Arora M.K., and Upadhyay S.N. Preparation of eggshell type Al_2O_3-supported CdS photocatalysts for reduction of H_2O to H_2. *Catalysis Today*, 69(1-4):297–305, 2001.

[26] Kennedy J.H. and Frese K.W. Jr. Photooxidation of water at α-Fe_2O_3 electrodes. *J. Electrochem. Soc.*, 125(5):709–714, 1978.

[27] Dare-Edwards M.P., Goodenough J.B., Hamnett A., and Trevellick P.R. Electrochemistry and photoelectrochemistry of iron (III) oxide. *J. Chem. Soc. Faraday Trans. 1*, 79:2027–2041, 1983.

[28] Itoh K. and Bockris J. O'M. Stacked thin-film photoelectrode using iron oxide. *J. Appl. Phys.*, 56(3):874–876, 1984.

[29] Beermann N., Vayssieres L., Lindquist S.-E., and Hagfelt A. Photoelectrochemical studies of oriented nanorod thin films of hematite. *J. Electrochem. Soc.*, 147(7):2456–2461, 2000.

[30] Itoh K. and Bockris J.O. Thin films photoelectrochemistry: iron oxide. *J. Electrochem. Soc.*, 131(6):1266–1271, 1984.

[31] Könenkamp R., Boedecker K., Lux-Steiner M.C., Poschenrieder M., Zenia F., Levy-Clement C., and Wagner S. Thin film semiconductor deposition on free-standing ZnO columns. *Appl. Phys. Lett.*, 77(16):2575–2577, 2000.

[32] Yu Z.G., Pryor C.E., Lau W.H., Berding M.A., and MacQueen D.B. Core-shell nanorods for efficient photoelectrochemical hydrogen production. *J. Phys. Chem. B*, 109(48):22913–22919, 2005.

[33] Matsumoto Y. Energy positions of oxide semiconductors and photocatalysis with iron complex oxides. *J. Solid State Chem.*, 126(2):227–234, 1996.

[34] Robertson J., Xiong K., and Clark S.J. Band gaps and defect levels in functional oxides. *Thin Solid Films*, 496:1–7, 2006.

[35] Minami T. Transparent conducting oxide semiconductors for transparent electrodes. *Semicond. Sci. Technol.*, 20(4):S35–S44, 2005.

[36] Thursfield A., Metcalfe I.S., Kruth A., and Irvine J.T.S. *Defect chemistry and transport in metal oxides.* Metal oxides: chemistry and applications. CRC Press, Taylor and Francis Group, FL, USA, 2006.

[37] Finklea H.O. *Semiconductor electrode concepts and terminology.* Semiconductor Electrodes. Elsevier, 1988.

[38] Warnes B.F., Aplan F.F., and Simkovich G. Electrical conductivity and Seebeck voltage of Fe_2O_3 pure and doped as a function of temperature and oxygen partial pressure. *Solid State Ionics*, 12:271–276, 1984.

[39] Gleitzer C., Nowotny J., and Rekas M. Surface and bulk electrical properties of the hematite phase Fe_2O_3. *Appl. Phys. A: Solid Surfaces*, 53(4):310–316, 1991.

[40] Dieckmann R. Point defects and transport in hematite ($Fe_2O_{3-\epsilon}$). *Phil. Mag. A*, 68(4):725–745, 1993.

[41] Gardner R.F.G., Sweett F., and Tanner D.W. The electrical properties of alpha ferric oxide-II. Ferric oxide of high purity. *J. Phys. Chem. Solids*, 24:1183–1196, 1963.

[42] Bosman A.J. and van Daal H.J. Small-polaron versus band conduction in some transition-metal oxides. *Adv. Phys.*, 19(77):1–117, 1970.

[43] Rosso K.M., Smith D.M.A., and Dupuis M. An ab initio model of electron transport in hematite (α-Fe_2O_3) basal planes. *J. Chem. Phys.*, 118(14):6455–6466, 2003.

[44] Iordanova N., Dupuis M., and Rosso K.M. Charge transport in metal oxides: A theoretical study of hematite α-Fe_2O_3. *J. Chem. Phys.*, 122(14):1443051–14430510, 2005.

[45] Gerischer H. Electrochemical photo and solar cells. principles and some experiments. *Electroanal. Chem. Interfacial Electrochem.*, 58:263–274, 1975.

[46] Gerischer H. Electron-transfer kinetics of redox reactions at the semiconductor/electrolyte contact. A new approach. *J. Phys. Chem.*, 95:1356–, 1991.

[47] Wilson R.H. Electron transfer processes at the semiconductor-electrolyte interface. *CRC Crit. Rev. Solid State Mater. Sci.*, 10:1–41, 1980.

[48] Butler M.A. Photoelectrolysis and physical properties of the semiconducting electrode WO_3. *J. Appl. Phys.*, 48(5):1914–1920, 1977.

[49] Gärtner W.W. Depletion-layer photoeffects in semiconductors. *Phys. Rev.*, 116(1):84–87, 1959.

[50] Terman L.M. Spectral response of solar-cell structures. *Solid-State Elect.*, 2(1):1–7, 1961.

[51] Ghosh A.K., Morel D.L., Feng T., Shaw R.F., and Rowe C.A. Jr. Photovoltaic and rectification properties of Al/Mg phthalocyanine/Ag Schottky-barrier cells. *J. Appl. Phys.*, 45(1):230–236, 1974.

[52] Wilson R.H. A model for the current-voltage curve of photoexcited semiconductor electrodes. *J. Appl. Phys.*, 48(10):4292–4297, 1977.

[53] Reichman J. The current-voltage characteristics of semiconductor-electrolyte junction photovoltaic cells. *Appl. Phys. Lett.*, 36(7):574–577, 1980.

[54] Lindquist S.-E., Finnström B., and Tegnér L. Photoelectrochemical properties of polycrystalline TiO_2 thin film electrodes on quartz substrates. *J. Electrochem. Soc.*, 130(2):351–358, 1983.

[55] Södergren S., Hagfeldt A., Olsson J., and Lindquist S.-E. Theoretical models for the action spectrum and the current-voltage characteristics of microporous semiconductor films in photoelectrochemical cells. *J. Phys. Chem.*, 98:5552–5556, 1994.

[56] Maruska H.P. and Ghosh A.K. Photocatalytic decomposition of water at semiconductor electrodes. *Solar Energy*, 20:443–458, 1978.

[57] Ghosh A.K. and Maruska H.P. Photoelectrolysis of water in sunlight with sensitized semiconductor electrodes. *J. Electrochem. Soc.*, 124(10):1516–1522, 1977.

[58] Bisquert J., Garcia-Belmonte G., and Fabregat-Santiago F. Modelling the electric potential distribution in the dark in nanoporous semiconductor electrodes. *J. Solid State Electrochem.*, 3(6):337–347, 1999.

[59] Hagfeldt A. and Graetzel M. Light-induced redox reactions in nanocrystalline systems. *Chem. Rev.*, 95(1):49–68, 1995.

[60] Benkstein K.D., Kopidakis N., Lagemaat J.v.d., and Frank A.J. Influence of the percolation network geometry on electron transport in dye-sensitized titanium dioxide solar cells. *J. Phys. Chem. B*, 107(31):7759–7767, 2003.

[61] Khan S.U.M. and Akikusa J. Stability and photoresponse of nanocrystalline n-TiO_2 and n-TiO_2/Mn_2O_3 thin film electrodes during water splitting reactions. *J. Electrochem. Soc.*, 145(1):89–93, 1998.

[62] Tang J., Wu Y., McFarland E.W., and Stuckey G.D. Synthesis and photocatalytic properties of highly crystalline and ordered mesoporous TiO_2 films. *Chem. Commun.*, (14):1670–1671, 2004.

[63] Mishra P.R., Shukla P.K., Singh A.K., and Srivastava O.N. Investigation and optimization of nanostructured TiO_2 photoelectrode in regard to hydrogen production through photoelectrochemical process. *Int. J. Hydrogen Energy*, 28(10):1089–1094, 2003.

[64] Fujishima A. and Honda K. Electrochemical photolysis of water at a semiconductor electrode. *Nature*, 238:37–38, 1972.

[65] Nozik A.J. Photoelectrochemistry: Applications to solar energy conversion. *Ann. Rev. Phys. Chem.*, 29:189–222, 1978.

[66] Somorjai G.A., Hendewerk M., and Turner J.E. The catalyzed photodissociation of water. *Catal. Rev. Sci. Eng.*, 26(34):683–708, 1984.

[67] Getoff N. Photoelectrochemical and photocatalytic methods of hydrogen production: A short review. *Int. J. Hydrogen Energy*, 15(6):407–417, 1990.

[68] Bard A.J. and Fox M.A. Artificial photosynthesis: Solar splitting of water to hydrogen and oxygen. *Acc. Chem. Res.*, 28(3):141–145, 1995.

[69] Amouyal E. Photochemical production of hydrogen and oxygen from water: A review and state of the art. *Sol. Energy Mater. Sol. Cells*, 38(1-4):249–276, 1995.

[70] Hardee K.L. and Bard A.J. Semiconductor electrodes V. The application of chemically vapor deposited iron oxide films to photosensitized electrolysis. *J. Electrochem. Soc.*, 123(7):1024–1026, 1976.

[71] Marusak L.A., Messier R., and White W.B. Optical absorption spectrum of hematite αFe_2O_3 near IR to UV. *J. Phys. Chem. Solids*, 41:981–984, 1980.

[72] Sartoretti C.J., Alexer B.D., Solarska R., Rutkowska I.A., Augustynski J., and Cerny R. Photoelectrochemical oxidation of water at transparent ferric oxide film electrodes. *J. Phys. Chem. B*, 109(28):13685–13692, 2005.

[73] Sastri M.V.C. and Nagasubramian G. Studies on ferric oxide electrodes for the photo-assisted electrolysis of water. In *Proc. 3rd World Hydrogen Energy Conf.*, volume 2, 1980.

[74] Shinar R. and Kennedy J.H. Photoactivity of doped α-Fe_2O_3 electrodes. *Solar Energy Mater.*, 6:323–335, 1982.

[75] Sartoretti C.J., Ulmann M., Alexander B.D., Augustynski J., and Weidenkaff A. Photoelectrochemical oxidation of water at transparent ferric oxide film electrodes. *Chem. Phys. Lett.*, 376(1-2):194–200, 2003.

[76] Fredlein R.A. and Bard A.J. Semiconductor electrodes XXI: The characterization and behavior of n-type Fe_2O_3 electrodes in acetonitrile solutions. *J. Electrochem. Soc.*, 126(11):1892–1898, 1979.

[77] Kennedy J.H., Shinar R., and Ziegler J.P. α-Fe_2O_3 photoanodes doped with silicon. *J. Electrochem. Soc.*, 127(10):2307–2309, 1980.

[78] Kennedy J.H., Anderman M., and Shinar R. Photoactivity of polycrystalline α-Fe_2O_3 electrodes doped with group IVA elements. *J. Electrochem. Soc.*, 128(11):2371–2373, 1981.

[79] Turner J.E., Hendewerk M., Parmeter J., Neiman D., and Somorjai G.A. The characterization of doped iron oxide electrodes for the photodissociation of water. *J. Electrochem. Soc.*, 131(8):1777–1783, 1984.

[80] Gardner R.F.G., Sweett F., and Tanner D.W. The electrical properties of alpha ferric oxide-I. The impure oxide. *J. Phys. Chem. Solids*, 24:1175–1181, 1963.

[81] Morin F.J. Magnetic susceptibility of αFe_2O_3 and αFe_2O_3 with added titanium. *Phys. Rev.*, 78:819–820, 1950.

[82] Fu Y.Y., Wang R.M., Xu J., Chen J., Yan Y., Narlikar A.V., and Zhang H. Synthesis of large arrays of aligned α-Fe_2O_3 nanowires. *Chem. Phys. Lett.*, 379:373–379, 2003.

[83] Kim C.H., Chun H.J., Kim D.S., Kim S.Y., Park J., Moon J.Y., Lee G., Yoon J., Jo Y., Jung M.-H., Jung S., and Lee C.J. Magnetic anisotropy of vertically aligned α-Fe_2O_3 nanowire array. *Appl. Phys. Lett.*, 89(22):223103–1 – 223103–3, 2006.

[84] Wang R., Chen Y., Fu Y., Zhang H., and Kisielowski C. Bicrystalline hematite nanowires. *J. Phys. Chem. B*, 109(25):12245–12249, 2005.

[85] Wen X.G., Wang S.H., Ding Y., Wang Z.L., and Yang S.H. Controlled growth of large-area uniform vertically aligned arrays of alpha-Fe_2O_3 nanobelts and nanowires. *J. Phys. Chem B*, 109(1):215–220, 2005.

[86] Xu L., Guo Y., Liao Q., Zhang J., and Xu D. Morphological Control of ZnO Nanostructures by Electrodeposition. *J. Phys. Chem. B*, 109(28):13519–13522, 2005.

[87] de Cogan D. and Lonergan G.A. Electrical conduction in Fe_2O_3 and Cr_2O_3. *Solid State Commun.*, 15:1517–1519, 1974.

[88] Merchant P., Collins R., Kershaw R., Dwight K., and Wold A. The electrical, optical and photoconducting properties of $Fe_{2-x}Cr_xO_3$ ($0 \leq x \leq 0.47$). *J. Solid State Chem.*, 27:307–315, 1979.

[89] Morin F.J. Electrical properties of α-Fe_2O_3 and α-Fe_2O_3 containing titanium. *Phys. Rev.*, 83(5):1005–1010, 1951.

[90] Anderman M. and Kennedy J.H. *Iron Oxide (Fe_2O_3)*, volume 55 of *Semiconductor electrodes*. Elsevier, 1988.

[91] Glasscock J.A., Barnes P.R.F., Plumb I.C., and Savvides N. The enhancement of photoelectrochemical hydrogen production from hematite thin films by the introduction of Ti and Si. *J. Phys. Chem. C*, 111:16477–16488, 2007.

[92] Duret A. and Grätzel M. Visible light-induced water oxidation on mesoscopic α-Fe_2O_3 films made by ultrasonic spray pyrolysis. *J. Phys. Chem. B*, 109(36):17184–17191, 2005.

[93] Miller E.L., Paluselli D., Marsen B., and Rocheleau R.E. Low-temperature reactively sputtered iron oxide for thin film devices. *Thin Solid Films*, 466(1-2):307–313, 2004.

[94] Khan S.U.M. and Akikusa J. Photoelectrochemical splitting of water at nanocrystalline n-Fe_2O_3 thin-film electrodes. *J. Phys. Chem. B*, 103(34):7184 –7189, 1999.

[95] Sanchez C., Hendewerk M., Sieber K.D., and Samorjal G.A. Synthesis, bulk, and surface characterization of niobium-doped Fe_2O_3 single crystals. *J. Solid State Chem.*, 61:47–55, 1986.

[96] Morin F.J. Electrical properties of α-Fe_2O_3. *Phys. Rev.*, 93(6):1195–1199, 1954.

[97] Cox P.A. *Transition metal oxides: An introduction to their electronic structure and properties*. Oxford University Press, England, 1992.

[98] Gharibi E., Hbika A., Dupre B., and Gleitzer C. Electrical properties of pure and titanium-doped hematite single crystals in the basal plane at low oxygen pressure. *Eur. J. Solid State Inorg. Chem.*, 27:647–658, 1990.

[99] Kuratomi T., Yamaguchi K., Yamawaki M., Bak T., Nowotny J., Rekas M., and Sorrell C.C. Semiconducting properties of polycrystalline titanium dioxide. *Solid State Ion.*, 154, 2002.

[100] Nakau T. Electrical conductivity of α-Fe_2O_3. *J. Phys. Soc. Japan*, 15:727, 1960.

[101] Lide D.R. *CRC Handbook of Chemistry and Physics*. Taylor and Francis, Bocca Raton, FL, eighty seventh edition, 2007.

[102] Velev J., Bandyopadhyay A., Butler W.H., and Sarker S. Electronic and magnetic structure of transition-metal-doped alpha-hematite. *Phys. Rev.B: Cond. Matt. and Mater. Phys.*, 71(20):205208–7, 2005.

[103] Ingler W.B. Jr., Baltrus J.P., and Khan S.U.M. Photoresponse of p-type zinc-doped iron(III) oxide thin films. *J. Am. Chem. Soc.*, 126(33):10238–10239, 2004.

[104] Ingler W.B. Jr. and Khan S.U.M. Photoresponse of spray pyrolytically synthesized copper-doped p-Fe_2O_3 thin film electrodes in water splitting. *Int. J. Hydrogen Energy*, 30(8):821–827, 2005.

[105] Sanchez H.L., Steinfink H., and White H.S. Solid solubility of Ge, Si and Mg in Fe_2O_3 and photoelectric behaviour. *J. Solid State Chem.*, 41:90–96, 1982.

[106] Sieber K.D., Sanchez C., Turner J.E., and Samorjal G.A. Preparation, characterization and photoelectronic properties of germanium-substituted Fe_2O_3 single crystals. *J. Chem. Soc., Faraday Trans. 1*, 81:1263–1274, 1985.

[107] Patterson F.K. Semiconductive oxides. US patent: US3890251, 1975.

[108] Vayssiéres L. and Graetzel M. Highly ordered SnO_2 nanorod arrays from controlled aqueous growth. *Angewandte Chemie Int. Ed.*, 43(28):3666–3670, 2004.

[109] Limmer S.J., Cruz S.V., and Cao G.Z. Films and nanorods of transparent conducting oxide ITO by a citric acid sol route. *Appl. Phys. A: Solids Surfaces*, 79:421–424, 2004.

[110] Limmer S.J., Seraji S., Wu Y., Chou T.P., Nguyen C., and Cao G.Z. Template-based growth of various oxide nanorods by sol-gel electrophoresis. *Adv. Funct. Mater.*, 12(1):59–64, 2002.

[111] Limmer S., Chou T., and Cao G. A study on the influences of processing parameters on the growth of oxide nanorod arrays by sol electrophoretic deposition. *J. Sol-Gel Sci. Tech.*, 36(2):183–195, 2005.

[112] Yu D., Wang D., Yu W., and Qian Y. Synthesis of ITO nanowires and nanorods with corundum structure by a co-precipitation-anneal method. *Mater. Lett.*, 58(1-2):84–87, 2004.

[113] Lee C.H., Kim M., Kim T., Kim A., Paek J., Lee J.W., Choi S.-Y., Kim K., Park J.-B., and Lee K. Ambient pressure syntheses of size-controlled corundum-type In_2O_3 nanocubes. *J. Am. Chem. Soc.*, 128(29):9326–9327, 2006.

[114] Vayssiéres L., Hagfeldt A., and Lindquist S.-E. Purpose-built metal oxide nanomaterials. The emergence of a new generation of smart materials. *Pure Appl. Chem.*, 72(1):47–52, 2000.

[115] Vayssiéres L. Growth of arrayed nanorods and nanowires of ZnO from aqueous solutions. *Adv. Mater.*, 15(5):464–466, 2003.

[116] Vayssiéres L., Keis K., Lindquist S.-E., and Hagfeldt A. Purpose-built anisotropic metal oxide material: 3D highly oriented microrod array of ZnO. *J. Phys. Chem. B*, 105(17):3350–3352, 2001.

[117] Greene L.E., Law M., Goldberger J., Kim F., Johnson J.C., Zhang Y., Saykally R.J., and Yang P. Low-temperature wafer-scale production of ZnO nanowire arrays. *Angew. Chem. Int. Ed.*, 42(26):3031–3034, 2003.

[118] Greene L.E, Law M., Tan D.H., Montano M., Goldberger J., Somorjai G., and Yang P. General route to vertical ZnO nanowire arrays using textured ZnO seeds. *Nano Lett.*, 5(7):1231–1236, 2005.

[119] Greene L.E., Yuhas B.D., Law M., Zitoun D., and Yang P. Solution-grown zinc oxide nanowires. *Inorg. Chem.*, 45(19):7535–7543, 2006.

[120] Law M., Greene L., Johnson J.C., Saykally R., and Yang P. Nanowire dye-sensitized solar cells. *Nature Mater.*, 4:455–459, 2005.

[121] Cui J. and Gibson U.J. Enhanced nucleation growth rate and dopant incorporation in ZnO nanowires. *J. Phys. Chem. B*, 109(46):22074–22077, 2005.

[122] Ravirajan P., Peiró A.M., Nazeeruddin M.K., Graetzel M., Bradley D.D.C., Durrant J.R., and Nelson J. Hybrid polymer/zinc oxide photovoltaic devices with vertically oriented ZnO nanorods and an amphiphilic molecular interface layer. *J. Phys. Chem. B*, 110(15):7635–7639, 2006.

[123] Zhang X.T., Sato O., and Fujishima A. Water ultrarepellency induced by nanocolumnar ZnO surface. *Langmuir*, 20(14):6065–6067, 2004.

[124] Cembrero J., Elmanouni A., Hartiti B., Mollar M., and Marí B. Nanocolumnar ZnO films for photovoltaic applications. *Thin Solid Films*, 451:198–202, 2004.

[125] Jeong J.S., Lee J.Y., Cho J.H., Lee C.J., An S.J., Yi G., and Gronsky R. Growth behaviour of well-aligned ZnO nanowires on a Si substrate at low temperature and their optical properties. *Nanotechnol.*, 16(10):2455–2461, 2005.

[126] Meng X.Q., Zhao D.X., Zhang J.Y., Shen D.Z., Lu Y.M., Liu Y.C., and Fan X.W. Growth temperature controlled shape variety of ZnO nanowires. *Chem. Phys. Lett.*, 407(1-3):91–94, 2005.

[127] Zhao D., Andreazza C., Andreazza P., Ma J., Liu Y., and Shen D. Buffer layer effect on ZnO nanorods growth alignment. *Chem. Phys. Lett.*, 408(4-6):335–338, 2005.

[128] Huang M.H., Wu Y., Feick H., Tran N., Weber E., and Yang P. Catalytic growth of zinc oxide nanowires by vapor transport. *Adv. Mater.*, 13(2):113–116, 2001.

[129] Huang M.H., Mao S., Feick H., Yan H., Wu Y., Kind H., Weber E., Russo R., and Yang P. Room-temperature ultraviolet nanowire nanolasers. *Science*, 292(5523):1897–1899, 2001.

[130] Huang H., Yang S., Gong J., Liu H., Duan J., Zhao X., Zhang R., Liu Y., and Liu Y. Controllable assembly of aligned ZnO nanowires/belts arrays. *J. Phys. Chem. B*, 109(44):20746–20750, 2005.

[131] Ye C., Fang X., Hao Y., Teng X., and Zhang L. Zinc oxide nanostructures: Morphology derivation and evolution. *J. Phys. Chem. B*, 109(42):19758–19765, 2005.

[132] Zhu Z., Chen T.L., Gu Y., Warren J., and Osgood R.M. Zinc oxide nanowires grown by vapor-phase transport using selected metal catalysts: A comparative study. *Chem. Mater.*, 17(16):4227–4234, 2005.

[133] Thonke K. Nanostructures from ZnO and other semiconductors generated via self-organizing polymers. In *Physics of semiconductors: 27th International Conference on the Physics of Semiconductors*, volume 772, pages 831–834. American Institute of Physics, 2005.

[134] Park W.I., Kim D.H., Jung S.-W., and Yi G.-C. Metalorganic vapor-phase epitaxial growth of vertically well-aligned ZnO nanorods. *Appl. Phys. Lett.*, 80(22):4232–4234, 2002.

[135] Park J.Y., Lee D.J., and Kim S.S. Size control of ZnO nanorod arrays grown by metalorganic chemical vapour deposition. *Nanotechnol.*, 16(10):2044–2047, 2005.

[136] Park J.Y., Oh H., Kim J.J., and Kim S.S. Growth of ZnO nanorods via metalorganic chemical vapor deposition and their electrical properties. *J. Crystal Growth*, 287(1):145–148, 2006.

[137] Vayssieres L. Aqueous purpose-built nanostructured metal oxide thin films. *Int. J. Mater. Prod. Technol.*, 18(4-6):313–337, 2003.

[138] Vayssiéres L. On the design of advanced metal oxide nanomaterials. *Int. J. Nanotechnol.*, 1(1), 2004.

[139] Vayssiéres L., Keis K., Hagfeldt A., and Lindquist S.-E. Three-Dimensional Array of Highly Oriented Crystalline ZnO Microtubes. *Chem. Mater.*, 13(12):4395–4398, 2001.

[140] Guo M., Diao P., and Cai S. Hydrothermal growth of well-aligned ZnO nanorod arrays: Dependence of morphology and alignment ordering upon preparing conditions. *J. Solid State Chem.*, 178(6):1864–1873, 2005.

[141] Silva R.F. and Zaniquelli M.E.D. Aluminium-doped zinc oxide films prepared by an inorganic sol-gel route. *Thin Solid Films*, 449(1-2):86–93, 2004.

[142] Majumder S.B., Jain M., Dobal P.S., and Katiyar R.S. Investigations on solution derived aluminium doped zinc oxide thin films. *Mater. Sci. Eng.: B*, 103(1):16–25, 2003.

[143] Musat V., Teixeira B., Fortunato E., Monteiro R.C.C., and Vilarinho P. Al-doped ZnO thin films by sol-gel method. *Surface and Coatings Technology*, 180, 2004.

[144] Shan F.K. and Yu Y.S. Band gap energy of pure and Al-doped ZnO thin films. *J. Europ. Ceram. Soc.*, 24(6):1869–1872, 2004.

[145] Lee J.H. and Park B.O. Characteristics of Al-doped ZnO thin films obtained by ultrasonic spray pyrolysis: effects of Al doping and an annealing treatment. *Mater. Sci. Eng.: B*, 106(3):242–245, 2004.

[146] Paraguay D.F, Morales J., Estrada L.W., Andrade E., and Miki-Yoshida M. Influence of Al, In, Cu, Fe, and Sn dopants in the microstructure of zinc oxide thin films obtained by spray pyrolysis. *Thin Solid Films*, 366(1-2):16–27, 2000.

[147] Minami T., Suzuki S., and Miyata T. Transparent conducting impurity-c-doped ZnO:Al thin films prepared by magnetron sputtering. *Thin Solid Films*, 398, 2001.

[148] Hsu C.L., Chang S.J., Hung H.C., Lin Y.R., Huang C.J., Tseng Y.K., and Chen I.C. Well-aligned vertically Al-doped ZnO nanowires synthesized on ZnO:Ga/glass templates. *J.Electrochem.Soc.*, 152(5):G378–G381, 2005.

[149] He J.H., Lao C.S., Chen L.J., Davidovic D., and Wang Z.L. Large-scale Ni-doped ZnO nanowire arrays and electrical and optical properties. *J. Am. Chem. Soc.*, 127(47):16376–16377, 2005.

[150] Björksten U., Moser J., and Grätzel M. Photoelectrochemical studies on nanocrystalline hematite films. *Chem. Mater.*, 6:858–863, 1994.

[151] Kiwi J. and Grätzel M. Light-induced hydrogen formation and photo-uptake of oxygen in colloidal suspensions of α-Fe_2O_3. *J. Chem. Soc. Faraday Trans.*, 1(83):1101–1108, 1987.

[152] Hida Y. and Kozuka H. Photoanodic properties of sol-gel-derived iron oxide thin films with embedded gold nanoparticles: effects of polyvinylpyrrolidone in coating solutions. *Thin Solid Films*, 476(2):264–271, 2005.

[153] Watanabe A. and Kozuka H. Photoanodic properties of sol-gel-derived Fe_2O_3 thin films containing dispersed gold and silver particles. *J. Phys. Chem. B*, 107(46):12713–12720, 2003.

[154] Vayssiéres L., Guo J., and Nordgren J. Aqueous chemical growth of α-Fe_2O_3-α-Cr_2O_3 nanocomposite thin films. *J. Nanosci. Nanotech.*, 1(4):385–388, 2001.

[155] Mathur S., Veith M., Sivakov V., Shen H., Huch V., Hartmann U., and Gao H.B. Phase-selective deposition and microstructure control in iron oxide films obtained by single-source CVD. *Chem. Vapor Depos.*, 8(6):277–283, 2002.

[156] Martin P.J., Bendavid A., and Kinder T.J. *Surf. Coat. Technol.*, 49:239, 1991.

[157] Boxman R.L. and Zhitomirsky V.N. Vacuum arc deposition devices. *Rev. Sci. Instrum.*, 77(2):021101–021115, 2006.

[158] Tay B.K., Zhao Z.W., and Chua D.H.C. Review of metal oxide films deposited by filtered cathodic vacuum arc technique. *Mater. Sci. Eng. B*, 52(1-3):1, 2006.

[159] Savvides N. Deposition parameters and films properties of hydrogenated amorphous silicon prepared by high rate dc planar magnetron reactive sputtering. *J. Appl. Phys.*, 55:4232–4238, 1984.

[160] Thibeau R.J., Brown C.W., and Heidersbach R.H. Raman spectra of possible corrosion products of iron. *Appl. Spectroscopy*, 32:532, 1978.

[161] de Faria D.L.A., Venâncio Silva S., and de Oliveira M.T. Raman microspectroscopy of some iron oxides and oxyhydroxides. *J. Raman Spectrosc.*, 28(11):873–878, 1997.

[162] Bersani D., Lottici P.P., and Montenero A. Micro-Raman investigation of iron oxide films and micro-powders produced by sol-gel syntheses. *J. Raman Spectrosc.*, 30:355–360, 1999.

[163] Bell T.J., Bendeli A., Field J.S., Swain M.V., and Thwaite E.G. The determination of surface plastic and elastic properties by ultra micro-indentation. *Metrologia*, 28(6):463–469, 1991.

[164] Poelman D. and Smet P.F. Methods for the determination of the optical constants of thin films from single transmission measurements: a critical review. *J. Phys. D: Appl. Phys.*, 36(15):1850, 2003.

[165] Szczyrbowski J. Determination of optical constants of real thin films. *J. Phys. D: Appl. Phys.*, 11:583, 1978.

[166] Davids E.A. and Mott N.F. Conduction in non-crystalline systems v. Conductivity, optical absorption and photoconductivity in amorphous semiconductors. *Phil. Mag.*, 22:903, 1970.

[167] Moss T.S. *Optical properties of semi-conductors.* Butterworths, London, 1959.

[168] Hall L.H., Bardeen J., and Blatt J. Infrared absorption spectrum of germanium. *Phys. Rev.*, 95:559, 1954.

[169] Pankove J.I. *Optical processes in semiconductors.* Dove Publications Inc., New York, 1971.

[170] Barnes P.R.F., Blake D., Glasscock J.A., Plumb I.C., Vohralik P.F., Bendavid A., and Martin P.J. Optimizing charge transport in Fe_2O_3 films deposited

on nanowire arrays. In Vayssiéres L., editor, *Proc. SPIE Solar Hydrogen and Nanotechnology*, volume 6340, pages 6340P1–6430P8. SPIE, Bellingham, WA, USA, 2006.

[171] Aroutiounian V.M., Arakelyan V.M., Shahnazaryan G.E., Stepanyan G.M., Turner J.A., and Kocha S.S. Investigations of the $Fe_{1.99}Ti_{0.01}O_3$-electrolyte interface. *Electrochimica Acta*, 45(12):1999–2005, 2000.

[172] Bockris J.O'M. and Reddy A.K.N. *Modern Electrochemistry: Electrodics in Chemistry Engineering Biology and Environmental Science*. Kluwer Academic/Plenum Publishers, 2000.

[173] McCann J.F. and Badwal S.P.S. Equivalent circuit analysis of the impedance response of semiconductor/electrolyte/counterelectrode cells. *J. Electrochem. Soc.*, 129(3):551–559, 1982.

[174] Nicolian E.H. and Brews J.R. *MOS Physics and Technology*. Wiley, New York, 1982.

[175] Glasscock J.A., Barnes P.R.F., Plumb I.C., Bendavid A., and Martin P.J. Structural, optical, and electrical properties of undoped polycrystalline hematite thin films produced using filtered arc deposition. *Thin Solid Films (in press)*, 2007.

[176] Harris L.A., Gerstner M.E., and Wilson R.H. Characterized semiconductor electrodes. II. Room temperature diffusion in a single crystal rutile electrode. *J. Electrochem. Soc.*, 126(5):850–855, 1979.

[177] Mörl K., Röpke U., Knappe B., Lehmann J, Perthel R., and Schr oder H. Optical properties of sputtered Fe_2O_3 films. *Thin Solid Films*, 60:49–53, 1979.

[178] Kaye G.W.C. and Laby T.H. *Table of physical and chemical constants*. Longman Group, London, tenth edition, 1995.

[179] Fischer-Cripps A.C. Review of analysis and interpretation of nanoindentation test data. *Surf. Coat. Technol.*, 200(14-15):4153–4165, 2006.

[180] Laetsch T. and Downs R.T. Software for identification and refinement of cell parameters from powder diffraction data of minerals using the RRUFF poject and American mineralogist crystal structure databases. In *Proc. 19th Gen. Meet. Int. Mineral. Assoc., Kobe, Japan*, 2006.

[181] Beattie I.R. and Gilson T.R. The single-crystal Raman spectra of nearly opaque materials. Iron (III) oxide and chromium oxide. *J. Chem. Soc.*, A:980–986, 1970.

[182] Pérez León C., Kado L., Zhang M., and Müller A.H.E. In-situ laser-induced formation of α-Fe_2O_3 from Fe^{3+} ions in a cylindrical core-shell polymer brush. *J. Raman Spectrosc.*, 35:165, 2004.

[183] Bendavid A., Martin P.J., and Takikawa H. Deposition and modification of titanium dioxide thin films by filtered arc deposition. *Thin Solid Films*, 360:241–249, 2000.

[184] National Institute for Standards Technology. NIST standard reference database 20, Version 3.4: x-ray photoelectron spectroscopy database, http://srdata.nist.gov/xps, accessed Jan 2007. Website, http://dirs.cis.rit.edu/ rvrpci/dirs/mie/refindx.dat, accessed Dec 2006, 2003.

[185] Qian X., Zhang X., Bai Y., Li T., Tang X., Wang E., and Dong S. Photoelectrochemical Characteristics Of α-Fe_2O_3 Nanocrystalline Semiconductor Thin Film. *J. Nanoparticle Res.*, 2(2):191–198, 2000.

[186] Comini E., Guidi V., Frigeri C., Riccó I., and Sberveglieri G. CO sensing properties of titanium and iron oxide nanosized thin films. *Sens. Actuat. B: Chem.*, 77(1-2):16, 2001.

[187] Huo L., Li Q., Zhao H., Yu L., Gao S., and Zhao J. Sol-gel route to pseudocubic shaped alpha-Fe_2O_3 alcohol sensor: preparation and characterization. *Sens. Actuat. B.: Chem.*, 107(2):915, 2005.

[188] Sun H.T., Cantalini C., Faccio M., Pelino M., Catalano M., and Tapfer L. Porous silica-coated α-Fe_2O_3 ceramics for humidity measurement at elevated temperature. *J. Am. Ceram. Soc.*, 79(4):927, 1996.

[189] Zhou H.S., Mito A., Kundu D., and Honma I. Nonlinear optical susceptibility of Fe_2O_3 thin film synthesized by a modified sol-gel method. *J. Sol-Gel Sci. Technol.*, 19(1/3):539, 2000.

[190] Özer N. and Tepehan F. Optical and electrochemical characteristics of sol-gel deposited iron oxide films. *Sol. Energy Mater. Solar Cells*, 56(2):141, 1999.

[191] Sokolik I.N. and Toon O.B. Incorporation of mineralogical composition into models of the radiative properties of mineral aerosol from UV to IR wavelengths. *J. Geophys. Res.*, 104:9423, 1999.

[192] Tanaka T. Optical constants of polycrystalline 3d transition metal oxides in the wavelength region 350 to 1200 nm. *Jap. J. Appl. Phys.*, 18(6):1043–1047, 1979.

[193] Longtin D.R., Shettle E.P., Hummel J.R., and Pryce J.D. A wind dependent desert aerosol model: radiative properties. Technical report, US Air Force Geophysics Laboratory Report, 1988.

[194] Kerker M., Scheiner P., Cooke D.D., and Kratohvil J.P. Absorption index and color of colloidal hematite. *J. Colloid Interface Sci.*, 71(1):176–187, 1979.

[195] Galuza A.I., Eremenko V.V., and Kirichenko A.P. Analysis of hematite reflection spectrum by the Kramers-Kronig method. *Sov. Phys. Solid State*, 21(4):654–656, 1979.

[196] Akl A.A. Optical properties of crystalline and non-crystalline iron oxide thin films deposited by spray pyrolysis. *Appl. Surf. Sci.*, 233(1-4):307–319, 2004.

[197] Quinn R.K., Nasby R.D., and Baughman R.J. Photoassisted electrolysis of water using single crystal α-Fe_2O_3 anodes. *Mat. Res. Bull.*, 11:1011, 1976.

[198] Papaioannou J.C., Patermarakis G.S., and Karayianni H.S. Electron hopping mechanism in hematite (alpha-Fe_2O_3). *J. Phys. Chem. Solids*, 66:839, 2005.

[199] Kulkarni S.S. and Lokhande C.D. Structural optical electrical and dielectrical properties of electrosynthesized nanocrystalline iron oxide thin films. *Mater. Chem. Phys.*, 82(1):151–156, 2003.

[200] Bedwell I.R. and McCartney E.R. The use of semiconducting oxide ceramics in solar energy conversion. *Mater. Sci. Monogr.*, 6:1159–1172, 1980.

[201] Benjelloun D., Bonnet J.-P., Doumerc J.-P., Launay J.-C., Onillon M., and Hagenmuller P. Anisotropie des Proprietes Electriques de l'Oxyde de fer Fe_2O_3. *Mater. Chem. Phys.*, 10:503–518, 1984.

[202] Kerisit S. and Rosso K.M. Computer simulation of electron transfer at hematite surfaces. *Geochimica et Cosmochimica Acta*, 70(8):1888–1903, 2006.

[203] Khan S.U.M. and Bockris J.O.'M. A model for electron transfer at the illuminated p-type semiconductor-solution interface. *J. Phys. Chem.*, 88:2504–2515, 1984.

[204] Rahachou A.I. and Zozoulenko I.V. Light propagation in nanorod arrays. *J. Opt. A: Pure Appl. Opt.*, 9(3):265–270, 2007.

[205] Adler D. *Insulating and metallic states in transition metal oxides*, volume 21 of *Solid State Physics*, pages 1–111. Academic Press, 1968.

[206] Wirth B.D. Crystal structures. Website, http://iron.nuc.berkeley.edu/ bdwirth/NE120/documents/Chap2.crystals.pdf, accessed 28/09/2006.

[207] Townsend Smith T. The mangetic properties of hematite. *Phys. Rev.*, 8:721–738, 1916.

[208] Selwood P.W. *Magnetochemistry*. Interscience Publishers, Inc., New York, second edition, 1956.

[209] Bevan D.J.M., Shelton J.P., and Anderson J.S. Properties of some simple oxides and spinels at high temperatures. *J. Chem. Soc*, pages 1729–1741, 1948.

[210] Tanner D.W., Sweett F., and Gardner R.F.G. Electrical conductivity of single crystal alpha ferric oxide. *Brit. J. Appl. Phys.*, 15:1041–1043, 1964.

[211] de Wit J.H.W. and Broesma A.F. and Stroband M. Surface stability and nonstoichiometry of α-Fe_2O_3. *J. Solid State Chem.*, 37:242–247, 1981.

[212] Cantalini C., Faccio M., Ferri G., and Pelino M. Microstructure and electrical properties of Si-doped α-Fe_2O_3 humidity sensor. *Sens. Act. B*, 15(16):293–298, 1993.

[213] Chang R.H. and Wagner J.B. Direct-current conductivity and iron tracer diffusion inhematite at high temperatures. *J. Amer. Ceram. Soc.*, 55(4):211–213, 1972.